



A University of Sussex PhD thesis

Available online via Sussex Research Online:

<http://sro.sussex.ac.uk/>

This thesis is protected by copyright which belongs to the author.

This thesis cannot be reproduced or quoted extensively from without first obtaining permission in writing from the Author

The content must not be changed in any way or sold commercially in any format or medium without the formal permission of the Author

When referring to this work, full bibliographic details including the author, title, awarding institution and date of the thesis must be given

Please visit Sussex Research Online for more information and further details



University of Sussex

Quantum gravity with higher curvature interactions and the Standard Model

Gustavo Medina Vazquez

Submitted for the degree of Doctor of Philosophy

University of Sussex

August 2020

Declaration

I hereby declare that this thesis has not been and will not be submitted in whole or in part to another University for the award of any other degree.

The work in this thesis has been done at University of Sussex between September 2016 and August 2020 in collaboration with Daniel Litim. The results of Chapter 4, Chapter 5 and Chapter 7 will appear in papers currently in preparation. A part of the results discussed in Section 2.2 has been published as:

1. Bond, A. D., Litim, D. F., Medina Vazquez, G., & Steudtner, T. (2018). UV conformal window for asymptotic safety. *Physical Review D*, 97(3), 036019. <https://doi.org/10.1103/PhysRevD.97.036019>

Signature:

Gustavo Medina Vazquez

UNIVERSITY OF SUSSEX

GUSTAVO MEDINA VAZQUEZ, DOCTOR OF PHILOSOPHY

QUANTUM GRAVITY WITH HIGHER CURVATURE INTERACTIONSAND THE STANDARD MODELSUMMARY

The quest for a fundamental quantum theory of gravity compatible with the Standard Model of particle physics continues to offer challenges. The asymptotic safety conjecture offers a promising direction, stipulating the non-perturbative renormalisability of gravity through an interacting ultraviolet fixed point. Strong circumstantial evidence for asymptotic safety of gravity has accumulated over the past decades with the help of functional renormalisation. However, matter quantum fluctuations may destabilise a gravitational fixed point. Since the observable universe contains matter, it becomes important to understand whether an asymptotically safe version of gravity is compatible with matter.

This thesis investigates the impact of quantised non-selfinteracting matter fields and the prospect for a combined fixed point for gravity with matter. The focus is on Standard Model matter, though asymptotic limits such as matter domination ($N \rightarrow \infty$), where N denotes the number of matter fields, or the absence of matter ($N \rightarrow 0$) are also investigated. A novelty of this study is introducing higher order Ricci scalar, Ricci tensor and Riemann tensor interactions beyond the Einstein-Hilbert action to ensure stability and convergence of findings.

A bootstrap search strategy is performed to high polynomial order in curvature, alongside functional renormalisation and high performance computing tools to identify ultraviolet fixed points. Additionally, heat kernel and spectral sum techniques are compared, providing improved approximations for the latter. Results include new gravitational fixed points with matter and higher curvature invariants, tests of stability and convergence, universal scaling dimensions and eigenperturbations. Notably, matter influences the types of higher order interactions required for asymptotic safety. Moreover, Standard Model matter may increase the dimensionality of the UV critical surface. Finally, a new scaling limit is found in the large- N regime, characterised by an enhancement of fourth-order interactions. Results are established both numerically and analytically in a $1/\sqrt{N}$ expansion. The relevance of these findings for the asymptotic safety conjecture is discussed.

Acknowledgements

I would not have been able to complete this challenge without the help and support of many people around me.

I would like to thank my supervisor Daniel Litim for his guidance, constant support and encouragement. His enthusiasm and passion for physics were always present in our conversations, which motivated me to push forward with this monumental endeavour.

I was lucky to have been surrounded by amazing people in the Theoretical Particle Physics group who created a great working atmosphere. Thanks to Andy, Ibere, Tom, Yannick and Charlie, from whom I have learned a lot through many interesting conversations and with whom I shared plenty of memorable evenings at the pub. To Dan and John for being wonderful officemates and friends. Thanks to Sonali for always being one to lend an ear, being fun to hang out with and being a great friend. To Luke, Basem, Tugba, Chris, Jack, Wissarut, Folkert and all the TPPeeps for all the great moments, conversations, parties and all the fun we had during this time.

Thanks to Diana, who could always make me feel like I was a little bit closer to home in a foreign country. To Paty, for being my very first friend when I arrived in this distant land and remaining one for such a long time now. To Raul, for his constant support and contagious optimism, and for always being like a true brother to me. To Rafael, for all the memes, anecdotes and interesting conversations.

I am indebted to my family for always being so supportive and believing in me. Without their continuous encouragement and reassurance, I would not have been able to get to where I am now. To my mom, dad and brother, my heartfelt thank you.

Lastly, I would like to thank Jolly for being the light of my life when I needed a light, for being an oak when the tempests came, and for being the best friend anyone could ever hope for. I could not have come this far without her.

This work was supported by the Consejo Nacional de Ciencia y Tecnología (CONACyT).

so many things to do, so little time . . .

Contents

List of Tables	x
List of Figures	xv
1 Introduction	1
2 Preliminaries	4
2.1 Basics of asymptotic safety	4
2.2 Asymptotic safety in particle physics	8
2.3 Functional renormalisation group	13
2.3.1 Wilson renormalisation	13
2.3.2 Effective Average Action	14
2.3.3 Flow equations	17
2.3.4 Approximations	18
2.4 Renormalisation group for quantum gravity	19
2.4.1 Metric fluctuations	19
2.4.2 Gauge fixing and ghosts	20
2.4.3 York decomposition	22
2.4.4 Flow equation of gravity	24
2.4.5 Background field approximation	25
2.4.6 Trace evaluation	26
2.4.7 Types of cut-offs	26
2.4.8 Excluded modes	27
2.4.9 Approximations	28
2.5 State-of-the-art in asymptotically safe gravity	31
3 Quantum Gravity	37
3.1 Introduction	37

3.2	Methodology	38
3.2.1	Gravitational action	38
3.2.2	Vertical and horizontal searches	40
3.2.3	Fixed point search	41
3.3	Fixed points of quantum gravity	43
3.3.1	Coupling values	43
3.3.2	Critical behaviour	45
3.3.3	Convergence	48
3.3.4	Action and equation of motion	50
3.3.5	Another family of solutions	51
3.4	Conclusions	52
4	Including Matter	54
4.1	Introduction	54
4.2	Functional renormalisation group	56
4.3	Operator traces	59
4.3.1	Heat kernel	59
4.3.2	Spectral sum	61
4.3.3	Smoothed sums and optimum average	64
4.3.4	Smooth step function	68
4.3.5	Comparison of matter bounds I. Large N	72
4.3.6	Comparison of matter bounds II. Supersymmetry	73
4.4	Gravitational fixed points with matter	75
4.5	Conclusions	77
5	Quantum gravity and the Standard Model	80
5.1	Introduction	80
5.2	Methodology	81
5.2.1	Renormalisation Group	81
5.2.2	Search strategy	82
5.2.3	Computational algorithms	83
5.3	Gravitational fixed points with the Standard Model	84
5.3.1	Accuracy	85
5.3.2	Fixed point coordinates	86
5.3.3	Scaling dimensions	87

5.3.4	Relevant directions	89
5.3.5	Convergence	92
5.3.6	Beyond the polynomial approximation	94
5.3.7	UV-IR connecting trajectories	96
5.4	A first peek beyond the Standard Model	97
5.5	Conclusions	98
6	Impact of SM matter on quantum gravitational fixed points	100
6.1	Introduction	100
6.2	Methodology	101
6.3	Impact of matter on couplings	102
6.4	Impact of matter on scaling dimensions	104
6.5	Relevant directions	107
6.6	Convergence	109
6.7	Conclusions	110
7	Gravitational fixed points in the large N limit	112
7.1	Introduction	112
7.2	Conformal window of matter-induced asymptotic safety	113
7.3	Fixed points of the large matter regime	116
7.3.1	Enhanced quantum gravity fluctuations	116
7.3.2	Fixed points in the infinite N limit	118
7.3.3	Fixed points beyond the infinite N limit	119
7.4	Critical behaviour	120
7.4.1	Beta functions	121
7.4.2	Scaling dimensions	121
7.4.3	UV-IR connecting trajectories	123
7.5	Scheme and parametrisation independence	125
7.5.1	Higher order matter contributions	125
7.5.2	Parametrisation of graviton fluctuations	126
7.6	Conclusions	127
8	Conclusions	129
	Bibliography	132
A	Flow equation of $f(X) + R z(X)$	153

B	Flow equation of $f(R)$	156
C	Additional figures for Chapter 3	158
D	Additional figures for Chapter 5	166
E	Tables for Chapter 6	174

List of Tables

3.1	Coupling values of gravitational fixed points at $N = 101$	45
3.2	Eigenvalues of the gravitational fixed points at $N = 101$	47
3.3	Scaling dimensions of the fixed point at $(a, b, c) = (2/5, 3/5, 0)$. This fixed point displays only four pairs of complex values, all others are real.	47
3.4	Fixed points of $f(R, Riem^2)$ in pure gravity, the dimensionality of their critical surface, coupling values and their fate when translated to other projections of the action. The points (a, b, c, m) are as defined in Figure 3.1.	52
4.1	The eigenspectrum of the Laplace operator $-\nabla^2$ acting on scalars, transverse vectors and spinors in S^d . The first column indicates the spin, λ_n^s indicates the eigenvalues and m_n^s , the multiplicity of eigenvalues.	59
4.2	The first three heat kernel coefficients for the operator $\Delta_i = -\nabla^2 + \alpha_i \bar{R}$ acting on the fields $i = \{\phi, A_\mu^T, \psi\}$ in S^4 . Note the spin-1 field is a transverse vector.	61
4.3	Fixed point search in polynomial $f(R)$ with SM matter in two scenarios. The columns indicate the technique employed to compute the matter quantum corrections, the dimensionality of the UV critical surface, the maximum approximation order, the nature of the boundary and the values of couplings.	74
4.4	Coupling values of a fixed point solution in polynomial $f(R)$ with SM matter using the averaged interpolation of the spectral sum in the matter traces.	75
4.5	Eigenvalues of a fixed point solution in polynomial $f(R)$ with SM matter using the averaged interpolation of the spectral sum in the matter traces.	76
5.1	Fixed points of gravity with SM matter indicating: projection of the action, dimensionality of the UV critical surface, coupling values, scaling dimensions, radius of convergence r_R and rate of convergence r_N . The Einstein-Hilbert theory with SM matter is included in the first row for comparison.	84

5.2	Coupling values of gravitational fixed points with SM matter at order $N = 101$	86
5.3	Real part of the eight most relevant scaling dimensions of fixed points with SM matter at order $N = 101$	87
5.4	Projections of the RG flows around the fixed points in the doubly-normalised eigenvector matrix ranked from relevant to irrelevant directions.	91
5.5	Radius of convergence of the polynomial theory from the ratio test r_R , and value at which the numerical integration encounters a singularity r_S	93
5.6	BSM matter configurations and whether they support gravitational fixed points or not. All solutions have negative Newton's constant and therefore, they do not possess RG flows connecting the theory continuously to General Relativity in the IR.	98
6.1	Qualitative behaviour of couplings between the pure gravity and the SM scenario.	104
7.1	Boundary of the conformal window of the large N fixed point where solutions annihilate through a fixed point merger. The third row indicates the maximum proportion of fermions with the given scalar and gauge boson ratios. No real solution is available for the given ratios even in the formal $N \rightarrow \infty$ limit, as indicated by the LO solution, eq. (7.9).	116
7.2	Schematic impact on the fixed point due to matter terms of order R^3 and higher. E indicates that matter explicitly appears in the equation of the corresponding term. I indicates that matter corrections appear implicitly through other couplings.	126
E.1	Couplings values of the non-Gaussian fixed point interpolated from pure gravity to the SM matter configuration at $N = 101$	175
E.2	Real part of the scaling dimensions of the non-Gaussian fixed point interpolated from pure gravity to the SM matter configuration at $N = 101$	176
E.3	Imaginary part of the scaling dimensions of the non-Gaussian fixed point interpolated from pure gravity to the SM matter configuration at $N = 101$	177

List of Figures

- 2.1 Phase portrait of an asymptotically safe gauge-Yukawa model with a finite number of matter fields. Arrows point towards the IR. Black dots indicate, from left to right, the Gaussian fixed point, the gauge-Yukawa UV fixed point and an interacting IR sink. The two trajectories emanating from the UV fixed point define quantum field theories which are either free (left) or interacting (right) at low energies. 9
- 2.2 Left: Profile functions R_k plotted in units of k^2 . The bottom line is the optimised regulator (2.28) (black), the other three correspond to the exponential one (2.29) with $(a, b) = (2, 1)$ (blue), $(a, b) = (1, 1)$ (green) and $(a, b) = (1, 2)$ (red) from bottom to top. Right: Modified propagators G_k in units of k^2 . The order is inverted from bottom to top in this plot, the colour coding matches that of the left panel. 16
- 3.1 Map of the theory space of pure gravity showing the paths explored in this study. The sides of the triangle form a set of orthogonal axes in this projection. The labels correspond to: $a = (1, 0, 0)$, $b = (0, 1, 0)$, $c = (0, 0, 1)$, $m = (1, 1, 1)$ 41
- 3.2 Map of normalised couplings $\lambda_n X_0^{[n/2]}$ of the fixed point in the theory space from $n = 0$ (violet) to $n = 100$ (red) at approximation order $N = 101$ 43
- 3.3 Product of the cosmological and Newton's constant at the fixed point in the theory space in the Einstein-Hilbert approximation $N = 2$ (violet) and at order $N = 101$ (red). 44
- 3.4 Map of the real part of the scaling dimensions associated with the fixed point in the pure gravity theory space at $N = 101$ 46

3.5	Left axis, violet solid line: radius of convergence R_c from the root test. Right axis, red data points: Rate of convergence of scaling dimensions in number of orders required to achieve a further digit of accuracy. Error bars indicate the 95% confidence interval.	49
3.6	Rate of convergence of scaling dimensions for two configurations. Left: the point of fastest convergence and largest radius R_c . Right: The solution found at $f(R, Riem^2)$, where convergence has stopped. The black line indicates the linear fit of ϑ_0 . The red, the average fit of the data shown for $N \geq 61$	50
3.7	Eigenvalues of the $f(R, Riem^2)$ fixed points translated to $f(R, Ric^2)$	51
4.1	Coefficients of the matter multiplicities appearing in the traces of each field as a function of p . Left: matter coefficient linear in R only. Middle and right: sum of coefficients representing the total contribution of each matter field evaluated at $R = 1$ and $R = 10^6$, respectively. Curves are normalised to heat kernel values. For any value of R , there are always two points where the traces can be matched with the results from the heat kernel expansion. The endomorphism parameters are fixed to eq. (4.10). The middle of the staircase interpolation corresponds to $p = -1/2$, the averaged interpolation to $p = \{-1, 0\}$, the optimised interpolation to $p = p_{opt.} \approx \{-0.79, -0.21\}$	68
4.2	Coupling values λ_n for each polynomial approximation of the fixed points in the averaged interpolation from $N = 2$ (violet) up to $N = 51$ (red). Left: Real part of the couplings. Note that all couplings are positive. Right: Complex phase of couplings. The imaginary part is non-zero only for even values of N	71
4.3	Eigenspectrum of fixed point in the averaged interpolation with optimised boundary conditions. All values are real.	73
4.4	Rate of convergence of the eigenspectrum with vanishing boundary conditions. The negative vertical axis indicates the number of digits of accuracy. The black line indicates the linear fit of the most relevant eigenvalue. The red line, the mean fit of the curves shown. The fits are performed for $N \geq 31$	78
5.1	Accuracy of the fixed point FP_4^c at increasing polynomial orders as a function of the curvature R	85

5.2	Absolute values of couplings λ_n of FP_4^c , with the index n in the horizontal axis, at each approximation order from $N = 2$ (violet) to $N = 101$ (red). . .	86
5.3	First eight eigenvalues of FP_5^c at each approximation. Thick red lines indicate the value at $N = 101$ while black lines are used for all other orders. All relevant eigenvalues are real. The gap between the least relevant and the most irrelevant values is $\Delta_{gap} \approx 1.90$	88
5.4	Eigenvalues of the stability matrix at each order N for FP_4^c . Negative values are UV relevant directions. The eigenspectrum shows stability towards higher polynomial orders.	89
5.5	Eigenvectors of the stability matrix for FP_4^c	90
5.6	Left: Action of the polynomial solution FP_4^c from $N = 7$ (violet) to $N = 101$ (red). Right: Number of digits of accuracy in the scaling dimensions of FP_4^c taking as reference value $N = 101$. The black line is the linear fit of ϑ_0 , the red line is the averaged fit for the shown data. The fits are performed for $N \geq 61$	92
5.7	Equation of motion obtained by numerical integration of the action from fixed point FP_4^c at order $N = 101$. The region of integration is bounded by a singularity. No de Sitter solutions are found in the range of the integration.	94
5.8	Phase portrait of the Einstein-Hilbert theory also showing UV-IR connecting trajectories.	95
5.9	Renormalisation group flow of couplings in $(0, 0, 1)$ from the UV (FP_4^c) to the IR (right to left) at $N = 4$. Higher order couplings are set to their fixed point values at $N = 101$. Along this trajectory, the cosmological constant smoothly crosses the zero and changes sign at $k \approx 5.973$ GeV.	96
6.1	Absolute value of couplings λ_n at the fixed point. Left: Variation with respect to N_{mat} from pure gravity ($N_{mat} = 0$) to the SM ($N_{mat} = 1$) at $N = 101$ for λ_0 (violet) to λ_{100} (red). Right: variation with respect to N at the SM ($N_{mat} = 1$ fixed). Each vertical observation is a coupling with data points from $N = 2$ (violet) to $N = 101$ (red).	103
6.2	Eigenvalues of the stability matrix at the SM matter content at increasing order N . The left panel shows the trend of the eigenvalues ranked from relevant to irrelevant towards higher N . The right panel shows the variation of each eigenvalue at all orders from $N = 2$ (violet) to $N = 101$ (red).	105

6.3	Scaling dimensions along the numerical variation at $N = 101$. The left panel shows the upper end (most relevant) of the scaling dimensions. The right panel shows the lower end (most irrelevant) of the scaling dimensions.	106
6.4	Eigenvectors of the stability matrix at the SM matter configuration and $N = 101$. The first five are relevant and the rest, irrelevant. The data points in each column indicate the elements of each eigenvector, associated with operators in the actions. The index i refers to the R^i operator.	108
6.5	Polynomial action as a function of the scalar curvature at approximations $N = 51$ (violet) to $N = 101$ (red). The left panel shows the theory without matter, the right one, with SM matter.	109
6.6	Rate of convergence of the scaling dimensions associated with the fixed point at the SM matter configuration.	110
7.1	Real and imaginary parts of the couplings values of FP_2 , in a matter configuration with only gauge bosons, at $N = 11$.	114
7.2	Real and imaginary parts of the eigenvalues of FP_2 , in a matter configuration with only gauge bosons, at $N = 11$.	115
7.3	RG trajectory connecting the FP_2 with a Gaussian regime in the IR with $N_{mat} = 10^6$ gauge bosons. Only the first seven couplings are shown. The factors of N_{mat} have been extracted from the couplings in this plot to aid visualisation.	123
C.1	Fixed points of pure gravity in various projections of the action.	159
C.2	Real part of scaling dimensions of gravitational fixed points in various projections of the action (view 1).	160
C.3	Real part of scaling dimensions of gravitational fixed points in various projections of the action (view 2).	161
C.4	Polynomial action as a function of R for various projections of the action in pure gravity.	162
C.5	Polynomial equation of motion as a function of R for various projections of the action in pure gravity.	163
C.6	Rate of convergence of scaling dimensions in various projections of the action in pure gravity with vanishing boundary conditions. The black line is the linear fit of ϑ_0 . The red line is the mean fit of the data shown for $N > 60$.	164

C.7	Rate of convergence of scaling dimensions in various projections of the action in pure gravity with optimised boundary conditions. The black line is the linear fit of ϑ_0 . The red line is the mean fit of the data shown for $N > 60$.	165
D.1	Residuals of the polynomial solutions as a function of R with SM matter.	167
D.2	Absolute value of effective couplings $ \lambda_n X^{\lfloor n/2 \rfloor} $ at the fixed point with SM matter.	168
D.3	Eigenvalues of the stability matrix for fixed points with SM matter. Negative values indicate relevant RG directions.	169
D.4	Eigenvalues of the stability matrix superimposed at increasing N for fixed points with SM matter.	169
D.5	Elements of the doubly-normalised eigenvectors of the stability matrix for fixed points with SM matter.	170
D.6	Polynomial action for fixed points with SM matter.	171
D.7	Rate of convergence of scaling dimensions for fixed points with SM matter. The black line is the linear fit of ϑ_0 . The red line is the mean fit of the data shown for $N > 50$.	172
D.8	RG flows connecting UV fixed points with SM matter to a Gaussian IR regime.	173

Chapter 1

Introduction

The Standard Model of particle physics and General Relativity provide the most advanced description of the universe up to date. The Electroweak theory [1–3], the Higgs mechanism [4] and Asymptotic Freedom of the strong force [5, 6] are the cornerstones of our current understanding of physics at the microscopic scale [7]. On the other hand, gravity is best described by Einstein’s theory, which inextricably intertwines time and space into a dynamical spacetime. Both frameworks have passed extensive tests, such as the discovery of the Higgs boson [8, 9] and the detection of gravitational waves [10]. However, both still have their shortcomings. Issues such as matter-antimatter asymmetry [11], non-zero neutrino masses [12, 13] and the apparent meta-stability of the Higgs potential [14, 15] remain unexplained. On the gravity side, the theory predicts spacetime singularities, plus there is the cosmological constant problem [16], a.k.a. the worst prediction in the entire history of physics. Thus, both can be understood to be effective field theories valid up to a finite energy scale. Moreover, while the former describes quantum matter, a consistent theory of quantum spacetime is yet to be found. While the effective field theory approach has been useful in constraining predictions of new physics, the holy grail of physicists since the advent of modern physics has been finding a unified fundamental theory of everything, capable of describing all aspect of nature at any scale, and is still the main motivation for many physicists in present day. Thus, one of the most monumental open questions in physics nowadays is obtaining a consistent quantum theory of gravity compatible with the Standard Model and extensions thereof.

The problem starts from the fact that Einstein’s gravity is not perturbatively renormalisable above two dimensions. The latter is the critical dimension of the theory and can be inferred from counting the superficial degree of divergence in graviton loop integrals. This failure of perturbative renormalisability can also be understood from the fact that

Newton's coupling has a negative canonical mass dimension above two dimensions. This indicates that the classical power counting argument valid for perturbatively renormalisable theories fails. Thus, barring exceptional cancellations at all loop orders, an infinite number of divergences, and thus free parameters, appears in the theory.

Explicit calculations show that gravity is renormalisable only at one-loop in the absence of matter [17, 18], however this breaks down at two-loops [19, 20]. The situation is even worse if matter is included, as already at one-loop the theory is non-renormalisable [17, 21–23]. Matter fields further induce new divergences up to fourth-derivative order that do not vanish on-shell nor for any physical matter configuration [24–27]. These divergences of quadratic curvature order naturally lead to extending Einstein's gravity with higher derivative terms. Higher derivative interactions become important at high energies and can play a role in resolving singularities and in inflation, thus they cannot be ignored. Indeed, the situation improves in quadratic gravity as the theory becomes renormalisable, although unphysical ghosts appear then [28–31]. Thus, matter introduces a further layer of complexity and must be considered in a formulation of quantum gravity from the start.

This thesis is concerned with reconciling the matter and metric degrees of freedom in a single quantum gravitational theory. The central paradigm on which this thesis is constructed is the asymptotic safety conjecture of gravity. This poses that the theory can be rendered non-perturbatively renormalisable by an interacting ultraviolet (UV) fixed point of the renormalisation group (RG) [32]. This idea entails that the running couplings take a constant finite value at high energies, restoring scale-invariance in the UV and rendering the theory predictive and fundamental at all energy scales [33, 34]. This can be realised in $d = 2 + \epsilon$, where a perturbative interacting fixed point arises [35–38]. In four dimensions, matter could even mediate a fixed point in the large N limit, rendering the theory weakly coupled [39, 40]. The development of the functional renormalisation group has allowed this idea to be further explored in a non-perturbative framework, finding results in support for the existence of such a fixed point [41].

The aim of this thesis is to investigate the impact of matter on gravitational fixed points with different types of higher order curvature interactions using functional renormalisation and numerical analysis techniques. In particular, the prospect of fixed points of quantum gravity compatible with the Standard Model will be the focus of the study. Additionally, other matter regimes are also investigated to further understand the influence of matter quantum fluctuations in fixed points of gravity. The investigation is carried out according to the following outline. Chapter 2 introduces the basic concepts, notation and technical

tools necessary for the study and offers a literature review of progress in the field. Chapter 3 searches for fixed points of quantum gravity in theories without matter studying different types of higher curvature interactions. Chapter 4 introduces non-interacting matter fields and illustrates some technical subtleties involved in the computation of matter quantum fluctuations. Chapter 5 offers a dedicated analysis of gravitational fixed points compatible with Standard Model matter to high order in curvature. Critical exponents, tests of convergence and UV-IR connecting trajectories are discussed. Chapter 6 considers the impact of matter fields on fixed points of pure gravity and studies how couplings and scaling dimensions are modified. Chapter 7 then investigates the limit of many matter fields both numerically and analytically, finding a new scaling regime where fixed points can appear in an expansion on a small parameter from a competition between metric and matter fluctuations. Finally, Chapter 8 presents a summary of the findings and the conclusions of this thesis.

Chapter 2

Preliminaries

This chapter introduces the concepts, notation and technical tools necessary for the investigation in this thesis. The paradigm of asymptotic safety is first explained in general terms. Then, instances of asymptotic safety in particle physics are given, outlining its relevance for high-energy physics. While the particle physics scenarios discussed here can be treated perturbatively, gravity, a non-perturbative force, requires different tools. Thus, the functional renormalisation group is introduced next, which provides a framework for studying non-perturbative physics. Afterwards, additional technicalities regarding the functional renormalisation of gravity, its subtleties and approximations are discussed. This chapter concludes with a literature review outlining the state-of-the-art in research in the asymptotic safety programme in gravity.

2.1 Basics of asymptotic safety

The concept behind asymptotic safety is simple and elegant. It requires no further tools than the renormalisation group developed more than 50 years ago and, at the level of the equations, amounts to a generalisation of asymptotic freedom. The basics of asymptotic safety are explained in this section.

The paradigm of asymptotic safety traces its roots back to 1974 when Wilson put forward the block-spin integration technique applied to the Kondo problem and introduced the concept of a UV fixed point of the action [33,34]. Through his seminal work in critical phenomena, Wilson offered an intuitive physical interpretation of renormalisation as an averaging of field fluctuations, beyond it just being an abstract mathematical tool to remove infinities in loop integrals. At a critical point, where a phase transition occurs, the correlation lengths and the order parameters of a dynamical system follow a power-law

scaling characterised by critical exponents. These critical points are fixed points of the renormalisation group. Different physical systems that exhibit the same scaling behaviour near a phase transition belong to the same universality class, meaning that they have the same critical exponents. Thus, fixed points of a system and their critical exponent carry profound universal information of nature.

Asymptotic safety is the realisation of a non-trivial ultraviolet fixed point of the renormalisation group that controls the high-energy behaviour of the theory. The conjecture of asymptotically safe gravity states that such a fixed point exists which renders the gravitational theory non-perturbatively renormalisable [32]. Thus, divergences are avoided and the theory is truly fundamental, being able to describe physics at any energy scale. In quantum field theory, renormalisation reveals that couplings constants characterising interactions are actually not constant but running couplings that depend on the scale at which they are measured. The renormalisation group equations take the form of the beta functions β_{g_i} [42, 43], equations that describe the running of dimensionless couplings g_i with respect to the renormalisation scale k :

$$k \frac{dg_i}{dk} = \beta_{g_i}(g_n) \quad (2.1)$$

where the subindex n indicates that the running of g_i in general depends on all couplings g_n in the theory.

The beta function for g_i consists of a classical part and a quantum part. The former is given by the canonical mass dimension of the coupling, while the latter is determined by the quantum fluctuations of the fields in the theory:

$$\beta_{g_i} = -[\bar{g}_i]g_i + f_i(g_n) \quad (2.2)$$

where $[\bar{g}_i]$ is the canonical mass dimension of the dimensionful coupling \bar{g}_i . The quantum contributions to the running of the coupling is given by the function $f_i(g_n)$. In perturbation theory, this takes the form of a series expansion in powers of small couplings. In non-perturbative settings, other techniques are required to compute the quantum corrections. One of such frameworks, the functional renormalisation group will be introduced in Section 2.3.

The renormalisation group flow vanishes at a fixed point and therefore couplings stop running with the energy and obtain a constant value:

$$\beta_{g_i}(g_n^*) \equiv \beta_{g_i}^* = 0 \quad (2.3)$$

where the star notation (*) indicates evaluation at the fixed point. At the fixed point, there is no notion of scale anymore, the physics becomes scale-invariant and conformal symmetry is restored.

The evolution of the system is determined by the initial conditions of the parameters at a given reference scale. Each initial condition defines a renormalisation group flow trajectory that describes how the couplings run with energy. Ultraviolet trajectories are those that flow into a fixed point at higher energies. The hypersurface of all UV attractive directions is known as the UV critical surface of the fixed point. To understand the relevance of this surface, it is instructive to study the flow around a fixed point.

Very close to a fixed point, the RG flow must be asymptotically vanishing. Demanding analyticity of the flow, the beta function can be expressed as a power expansion of couplings shifted from the fixed point by a small amount:

$$\beta_{g_i}(g_n - g_n^*) = \beta_{g_i}^* + \sum_{i,n} \left. \frac{\partial \beta_{g_i}}{\partial g_n} \right|_* (g_n - g_n^*) + \mathcal{O}(g_n - g_n^*)^2 \quad (2.4)$$

The first term vanishes by definition. Neglecting quadratic and higher order terms, the solution of this equation is:

$$g_i(k) = g_i^* + \sum_n c_n V_i^n \left(\frac{k}{\mu} \right)^{\vartheta_n} \quad (2.5)$$

where μ is a reference energy scale, c_n are constants that define the initial conditions, and ϑ_n and V_n are the eigenvalues and eigenvectors of the stability matrix, respectively:

$$M_{ij} \equiv \left. \frac{\partial \beta_{g_i}}{\partial g_j} \right|_* \quad (2.6)$$

These eigenvalues have a classical part given by the canonical mass dimension and a quantum part given by the anomalous dimensions η :

$$\vartheta_i = -[\bar{g}_i] + \eta(g_i^*) \quad (2.7)$$

The quantum corrections are zero at a trivial fixed point where the theory is free, while they are non-vanishing at a non-trivial fixed point. Each eigenvector represents an orthogonal direction in the space of operators. If a direction is associated with a positive eigenvalue, then evolving towards increasing energy k would drive the couplings away from the fixed point. These are irrelevant directions for which the free parameters must vanish, thus $c_n = 0$ for $\vartheta_n > 0$. In the opposite case, if the eigenvalue is negative, then the flow drives the couplings into the fixed point and the constants c_n remain to be determined.

In summary:

$$c_n = \begin{cases} 0, & \vartheta_n > 0 \\ \text{free}, & \vartheta_n < 0 \end{cases} \quad (2.8)$$

This is where the predictive power of asymptotic safety lies and constitutes one of its most promising features. Although the symmetries of the theory may allow infinitely many interactions, in asymptotic safety it is sufficient to measure only a finite number of couplings to completely determine the rest. The number of free parameters is equal to the number of relevant directions, this is the dimensionality of the UV critical surface. The irrelevant directions, in turn, are predictions of the theory.

The phase portrait of a certain type of gauge theory is shown in Figure 2.1 as an illustrative example. The arrows point towards the IR. Three fixed points appear in the phase diagram, from left to right, a Gaussian fixed point, an interacting UV fixed point with one UV attractive direction and an interacting fixed point which is fully IR attractive. The latter type of points is also sometimes called an IR *sink*. The red trajectories emanating from the UV fixed point define quantum field theories which are both UV and IR finite. In this diagram, there is only one pair of opposing trajectories leaving the UV fixed point, thus, the dimensionality of the UV critical surface is one (this plot shows a projection on a two-parameter space, the full theory has four interactions, however it remains true that the UV critical surface is one-dimensional for this particular example). Depending on the initial conditions, the theory ends up being either free (left) or interacting and finite (right) at low energies.

The scaling dimensions, or critical exponents, encode information about the power-law behaviour of order parameters close to a critical point. They are given by the eigenvalues mentioned above with the sign reversed. In this thesis, the terms *scaling dimensions*, *critical exponents* and *eigenvalues* (of the stability matrix) will be used interchangeably, where the appropriate sign will be made clear from the context. These quantities are universal numbers that can in principle be measured by experiment and define universality classes in critical systems. As universal quantities, they are invariant under redefinitions of the fields and transformations in the theory space. This can be checked by considering a general linear transformation of the couplings

$$Z = \frac{\partial \lambda'_n}{\partial \lambda_n} \quad (2.9)$$

The beta functions transform as a vector under such transformation

$$\beta_n \rightarrow \beta'_n = Z \beta_n \quad (2.10)$$

leading to the following transformation rule for the stability matrix:

$$M' = \frac{\partial(Z\beta_i)}{\partial\lambda'_j} = \frac{\partial(Z\beta_i)}{\partial\lambda_j} \frac{\partial\lambda_j}{\partial\lambda'_j} = \frac{\partial Z}{\partial\lambda_j} \beta_i Z^{-1} + Z M Z^{-1} \quad (2.11)$$

In the last expression, the first term vanishes at the fixed point as per the definition of the beta functions. The second term is a similarity transformation which leaves the eigenvalues unchanged. Note, however, that eigenvectors are not universal and do change under transformations in the theory space.

As a final interesting remark, note that although the scaling dimensions are universal numbers which in principle could be measured in experiment and therefore should be real-valued, complex scaling dimensions can also appear, giving rise to interesting behaviour. In a phase diagram, the real part of these numbers describes the magnitude and direction of the flows around the fixed point, while the imaginary part gives rise to curved spiral trajectories around it. An interesting case is that of closed loops known as limit-cycles, they indicate discrete scale invariance, a weaker form of scale invariance, and are associated with log-periodic corrections to scaling. This is a feature usually found in fractals [44] but which is also relevant in condensed matter systems giving rise to Efimov states of bound bosons [45–48]. Such closed RG trajectories have also been found in a minisuperspace approximation in gravity [49].

2.2 Asymptotic safety in particle physics

Although the term ‘asymptotic safety’ was coined by Weinberg in 1979 in the context of gravity [32], the idea behind it is a fundamental concept that is applicable to any quantum field theory. The notion of a UV fixed point was first introduced by Wilson in scalar theories [50, 51]. The Wilson-Fisher fixed point is the best-known example, it is a UV fixed point of the scalar $O(N)$ theory in $d = 4 - \epsilon$ [52], while non-trivial stationary points can also arise in other types of scalar theories [53–58]. Interacting fixed points can also be found in fermionic theories as in Gross-Neveu models [59–65]. In gauge theories, the Banks-Zaks fixed point is an IR non-trivial stationary point bounding the conformal window of QCD just below a critical number of fermions [66]. The existence of a conjectured interacting UV fixed point of QCD beyond the Banks-Zaks has also been put forward [67]. Other solutions can also appear in Yang-Mills theories away from four dimensions [68, 69].

A recent breakthrough was the realisation of asymptotic safety in non-abelian gauge-Yukawa theories with fermions and complex scalars in four dimensions. The theory put

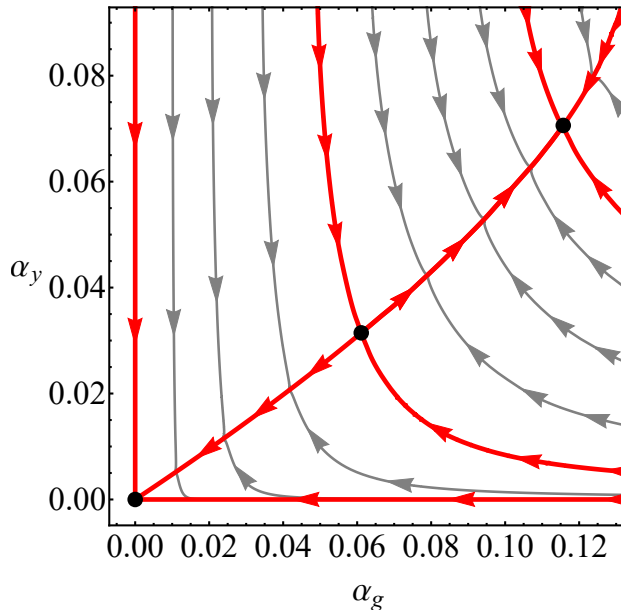


Figure 2.1: Phase portrait of an asymptotically safe gauge-Yukawa model with a finite number of matter fields. Arrows point towards the IR. Black dots indicate, from left to right, the Gaussian fixed point, the gauge-Yukawa UV fixed point and an interacting IR sink. The two trajectories emanating from the UV fixed point define quantum field theories which are either free (left) or interacting (right) at low energies.

forward in ref. [70] is perturbatively renormalisable with a weakly coupled ultraviolet fixed point under strict perturbative control in a large N limit. It is instructive to understand the mechanism through which this stationary point arises. A general theory is introduced next and the conditions under which asymptotic safety appears will be specified. Consider a four-dimensional gauge theory with a gauge group \mathcal{G} with N_F Dirac fermions ψ and complex meson-like scalars H with the following Lagrangian:

$$\begin{aligned}
L = & -\frac{1}{2} \text{Tr} (F_{\mu\nu} F^{\mu\nu}) - \text{Tr} (\bar{\psi} i \not{D} \psi) \\
& + \text{Tr} (\partial_\mu H^\dagger \partial^\mu H) + y \text{Tr} (\bar{\psi}_L H \psi_R + \bar{\psi}_R H^\dagger \psi_L) \\
& - u \text{Tr} ((H^\dagger H)^2) - v (\text{Tr} (H^\dagger H))^2
\end{aligned} \tag{2.12}$$

where $F_{\mu\nu}$ is the field strength of the gauge bosons, $\psi = \psi_L + \psi_R$ are chiral fermions which can be separated in left-handed and right-handed components, and H is a $N_F \times N_F$ matrix of complex scalar fields. The trace runs over the colour and flavour indices. The scalars are uncharged, carry two flavour indices and couple to the fermions through a Yukawa interaction. The theory has a global $SU(N_F)_L \times SU(N_F)_R$ flavour symmetry. In the following, only one gauge interaction is assumed although the formulation can be extended to semi-simple groups, under which only the fermions are charged [71]. Introducing $\alpha_g =$

$g^2/(4\pi)^2$ for the gauge coupling and similarly for α_y , the beta functions describing the flow of the gauge and Yukawa couplings to two and one-loop in perturbation theory can be schematically written as:

$$\beta_g = -B\alpha_g^2 + C\alpha_g^3 - D\alpha_g^2\alpha_y \quad (2.13)$$

$$\beta_y = E\alpha_y^2 - F\alpha_g\alpha_y \quad (2.14)$$

In the absence of scalars, i.e. no Yukawa term, the gauge coupling has a non-trivial solution given by $\alpha_g^* = B/C$, the Banks-Zaks fixed point [66]. Requiring loss of asymptotic freedom implies that the solution is UV attractive if $B < 0$ and $C < 0$. The key observation is that these coefficients can never have the correct signs simultaneously, i.e. this can only be an IR fixed point. This has been shown unambiguously for all simple and semi-simple gauge groups in any fermion representation [72]. It is only through Yukawa interactions that a UV solution can appear. The flow of the Yukawa interaction defines a nullcline where this beta function vanishes,

$$\alpha_y^* = \frac{F}{E}\alpha_g^* \quad (2.15)$$

Along this nullcline, the two-loop coefficient of the gauge coupling is shifted to

$$C \rightarrow C' = C - D\frac{F}{E}\alpha_g \quad (2.16)$$

such that the gauge beta function is also shifted,

$$\beta_g = -B\alpha_g^2 + C'\alpha_g^3 \quad (2.17)$$

This differential equation has the non-trivial solution:

$$\alpha_g^* = \frac{B}{C'} \quad (2.18)$$

If the fermions transform under the fundamental representation of $SU(N_C)$, then both $B < 0$ and $C' < 0$ can be realised leading to a physical UV fixed point. Conversely, no interacting fixed point can appear in weakly coupled theories in four dimensions without gauge interactions [73]. Thus, cooperation between all three types of fields, fermions, gauge bosons and scalars, is necessary to source a physical UV solution. The fixed point cascades into the scalar sector, meaning that all couplings remain finite at high energies.

The fixed point is weakly coupled in a particular type of large N limit where it can be studied within perturbation theory. This can be observed by introducing a control parameter ϵ , defined as:

$$\epsilon = \frac{N_F}{N_C} - \frac{11}{2} \quad (2.19)$$

This quantity becomes continuous in the Veneziano limit, where both N_F and N_C are set to infinity while their ratio is kept fixed. This limit reduces the number of parameters in the theory from two to one. Having the fermions transforming under the fundamental representation of $SU(N_C)$, the one-loop coefficient of the gauge beta function is proportional to this parameter, $B \propto \epsilon$ and thus, $\alpha_g^* \propto \epsilon$. Therefore, taking ϵ to be vanishingly small, the fixed point can be written in a perturbative expansion around ϵ whose coefficients can be systematically computed order by order. Moreover, this stationary point possesses a single relevant direction flowing to the Gaussian towards the IR. Thus, the theory is maximally predictive as it has only one free parameter.

This model has been investigated up to next-to-next-to-leading order in perturbation theory where constraints in the parameter space have been derived, finding that the conformal window is bounded by vacuum instability considerations [74, 75]. In ref. [76], the author and collaborators have further investigated this model in the finite N regime, where in spite of the lack of a strictly perturbative parameter, the fixed point can remain weakly coupled for finite values of N_F and N_C . In this setting, the conformal window is narrowed towards smaller values of N_C but matter configurations still exist which allow for a UV complete theory. The fixed point retains one relevant direction and renormalisation group flows connect the interacting theory in the ultraviolet to a free theory in the IR, such that the physics is well-defined at all energy scales. Moreover, this setting also suggests the existence of a non-trivial IR sink bounding the phase diagram of the theory beyond the UV fixed point. Then, all flows terminate in the IR either in a free theory or in a strongly interacting but finite regime that could describe a confinement phase. The phase portrait of the α_g - α_y system at finite ϵ and N_C is shown in Figure 2.1 [76]. The UV fixed point is shown in the middle with trajectories pointing towards the IR. The flows leaving this fixed point end at either a free theory (left) or an interacting one (right) in the IR. Note that an interacting IR sink would render all trajectories IR finite.

A stream of research has followed this discovery expanding this model to other interesting settings. For example, the theory has been investigated away from four dimensions [77], where quantum fluctuations at one-loop can balance with canonical scaling dimensions to source a fixed point, which is either UV attractive or repulsive above or below four dimensions, respectively. The supersymmetric case has been explored where a partially-interacting fixed point arises with fields charged under two gauge groups [78]. The impact of canonically irrelevant scalar operators has also been studied, finding that they remain irrelevant and weakly coupled in the UV, indicating that vacuum instabil-

ity bounds are not further modified by higher order operators [79]. Moreover, the gauge symmetry can be extended to semi-simple groups finding a variety of non-trivial solutions, phase diagrams and RG flows [71]. Furthermore, a recent investigation has found that there are two more asymptotically safe models like this one, both with Majorana fermions, one with $SO(N_C)$ and the other with $Sp(N_C)$ gauge groups. All three theories form a *triviality* as they are in the same universality class and are equivalent even away from the fixed point due to negative dimensionality theorems and orbifolding [80].

The perturbative realisation of asymptotic safety in the model described above has also generated much interest in phenomenology and model-building applications. Formulations for UV-complete extensions of the Standard Model have been put forward and their phenomenological implications have been explored [81–85]. In addition, recent investigations have used this mechanism to explain the discrepancies in both the muon and electron anomalous magnetic moments [86]. It is highly non-trivial that the same model can explain both anomalies as they appear with opposite signs.

A similar approach to asymptotic safety has also been pursued in the large N_F limit, where resummation techniques for all-orders beta functions have been put forward (see e.g. [87–92] and refs. within). In this setting, a fixed point can potentially arise from poles in the expressions of these beta functions in a large $1/N_F$ expansion. Note that this is a qualitatively different mechanism from the one in the model previously explained, as the fixed point arises non-perturbatively. This idea has also been the starting point of numerous investigations on BSM extensions [93–99], although it has come under closer scrutiny as of lately [100, 101].

Finally, note that quantum gravitational effects will become important at around the Planck scale and lead to modifications in the beta functions of the matter interactions. The leading gravitational corrections to the perturbative beta functions are of order α , i.e., the same as the canonical mass dimension of the couplings. For canonically marginal interactions, this term takes precedence over the quantum corrections and can be interpreted as modifying the mass dimension of couplings. For the running of gauge interactions, this correction is gauge and regularisation dependant but is strictly non-positive for both abelian and non-Abelian gauge groups, resulting in an effective dimensional reduction and thus pushing towards Asymptotic Freedom [102–113]. This should change the current understanding regarding triviality in the $U(1)$ sector [114–116]. On the other hand, the contribution to the running of the Yukawa coupling appears with a positive sign [117–121]. The gravitational coupling may also run into a fixed point, as studies in the pure gravity

theory suggest [41] (see Section 2.5). However, if this occurs at a large value for Newton's coupling, this could destabilise the interacting fixed point in the matter sector [122, 123].

The paradigm of asymptotic safety is also applicable to the theory of gravity, which is the main subject of this study. However, as gravity is perturbatively non-renormalisable, a different toolset is required to study the realisation of asymptotic safety in this theory. The next section introduces the functional renormalisation group, which will be used throughout this thesis in the search for gravitational fixed points.

2.3 Functional renormalisation group

This section provides a succinct introduction to the functional renormalisation group and is based on the following textbooks, to which the reader is referred for a detailed pedagogical introduction to the framework and its applications in condensed matter and gravity [124–126].

2.3.1 Wilson renormalisation

The functional renormalisation group, or exact renormalisation group, is a framework for implementing renormalisation in the sense of Wilson. In Wilsonian renormalisation, the momentum integration in the path integral is not carried out all at once but in an iterative manner by performing a coarse-graining over field fluctuations. Conceptually, the fluctuations of the field are separated into low and high-energy modes according to their momentum k :

$$\Phi = \Phi^- + \Phi^+ \tag{2.20}$$

The coarse-graining procedure consists of two steps. In the first step, the high-energy fluctuations are integrated out leaving behind a partially integrated action:

$$\begin{aligned} \mathcal{Z} &= \int \mathcal{D}[\Phi] e^{-S[\Phi;g]} = \int \mathcal{D}[\Phi^-] \int \mathcal{D}[\Phi^+] e^{-S[\Phi^- + \Phi^+;g]} \\ &= \int \mathcal{D}[\Phi^-] e^{-S_k^-[\Phi^-;g']} \end{aligned} \tag{2.21}$$

with S^- defined as:

$$e^{-S_k^-[\Phi^-;g']} = \int \mathcal{D}[\Phi^+] e^{-S[\Phi^- + \Phi^+;g]} \tag{2.22}$$

This is now an effective action which describes the theory with the high-energy fluctuations integrated out. Note that the interactions g' in S_k^- are different from the ones in the original action g . In the second step, the fields and all scale-dependent quantities are rescaled so

they can be related to the original quantities. These two steps can be repeated until all fluctuations have been integrated out.

A well-known approach to Wilsonian renormalisation is the Polchinski equation [127], which is a flow equation for the Wilsonian effective action S_k valid up to a UV cut-off. The same equation has also been shown to be satisfied by the generators of the connected amputated Green's functions with an IR regulator [128, 129]. A different formulation in terms of the Legendre transform is given in the next section and will prove to be more convenient to work with.

2.3.2 Effective Average Action

Consider the generator of the connected Green's functions in a quantum field theory:

$$W[J] = \log \mathcal{Z}[J] = \log \int \mathcal{D}[\Phi] e^{-(S_0[\Phi] + S_I[\Phi] - J, \Phi)} \quad (2.23)$$

The action contains a free part S_0 and interaction terms S_I . The collective field Φ contains all fields in the theory $\Phi = \{\phi_1, \dots, \phi_n\}$ and to each of them corresponds a source $J = \{J_1, \dots, J_n\}$, with the following notation introduced for convenience:

$$J, \Phi = \int d^d x \Phi J \quad (2.24)$$

In the first step of Wilson's renormalisation, the field fluctuations of momentum higher than an IR scale k must be integrated out. This can be implemented by adding an IR regulator to this action that plays the role of a mass term for the low momentum modes. The regulator must be quadratic in the fields and takes the general form:

$$\Delta S_k = \frac{1}{2} \int d^d x \Phi \mathcal{R}_k(q^2) \Phi \quad (2.25)$$

This regulator is a function of the momentum of the fields q^2 and the integration scale k so it can distinguish between modes with momentum above and below this scale. Its main purpose is to modify the propagators acting as a mass term for the low momentum modes so they are suppressed or weighed down in the path integral, leading to the modified propagator:

$$G_k = \frac{1}{q^2 + \mathcal{R}_k} \quad (2.26)$$

At the same time, the contributions from high-energy fluctuations should remain unaffected by this modification to the action. In addition, the regulator must disappear when all modes have been integrated out, that is, when the IR scale is set to zero. Thus, the properties that the regulator must possess to achieve its goal can be summarised as follows:

1. It vanishes quickly for large momentum, $\lim_{q^2/k^2 \rightarrow \infty} \mathcal{R}_k = 0$
2. It is positive and large (possibly infinite) for small momentum. In particular, $\lim_{q^2/k^2 \rightarrow 0} \mathcal{R}_k \propto k^2$ is convenient
3. It vanishes uniformly in the IR, $\lim_{k \rightarrow 0} \mathcal{R}_k = 0$
4. It is monotonically decreasing in q at fixed k and increasing in k at fixed q .

The last condition has been included as it is desirable that the regulator acts in a consistent manner on modes of different momenta and when the integration scale is varied. In the limit of vanishing momentum, the regulator should induce a mass gap which depends on k^2 to suppress these modes in the path integral. The low momentum modes completely drop out if the regulator diverges at this point, however, this singular behaviour may complicate working with such an expression. Finally, note that the second condition implies that the regulator diverges if the IR scale is set to infinity with $q^2 \ll k^2$. Any regulator that complies with the asymptotic behaviour described by these conditions will work and there is freedom in choosing how the modes are regulated in between. This is determined by the dimensionless profile function R_k :

$$\mathcal{R}_k = k^2 R_k(z) \tag{2.27}$$

Two examples are the optimised and the exponential profiles [130, 131]:

$$R_k(z) = (1 - z)\Theta(1 - z) \tag{2.28}$$

$$R_k(z) = \frac{az^b}{e^{az^b} - 1} \tag{2.29}$$

with free positive parameters $a > 0$ and $b \geq 1$. These *cut-off* profiles and the corresponding modified propagators are shown in the panels of Figure 2.2 in units of k^2 . As mentioned above, this leads to a mass gap in the regulated propagators removing any IR divergences. Note that while the optimised profile treats all momentum modes below the IR scale equally (with a mass gap of k^2), the other choices lead to a different weighting of these modes. This freedom leads to some regulator dependence on the quantities associated with the fixed point and is briefly addressed in Section 2.5.

It is convenient to work with dimensionless fields and couplings so that the second step in the coarse-graining procedure is automatically accounted for. Note that the regulator has introduced an explicit scale dependence on the action, so the scale-dependent functional is now:

$$W_k[J] = \log \int \mathcal{D}[\Phi] e^{-(S_0[\Phi] + \Delta S_k + S_I[\Phi] - J, \Phi)} \tag{2.30}$$

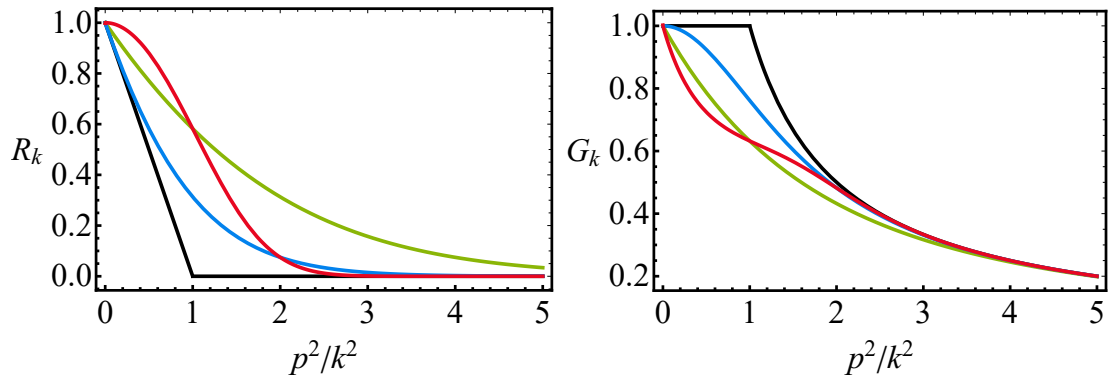


Figure 2.2: Left: Profile functions R_k plotted in units of k^2 . The bottom line is the optimised regulator (2.28) (black), the other three correspond to the exponential one (2.29) with $(a, b) = (2, 1)$ (blue), $(a, b) = (1, 1)$ (green) and $(a, b) = (1, 2)$ (red) from bottom to top. Right: Modified propagators G_k in units of k^2 . The order is inverted from bottom to top in this plot, the colour coding matches that of the left panel.

The Legendre transform of the generator of connected Green's functions is the effective action $\Gamma[\hat{\Phi}]$. In the scale-dependent functional, this has to be compensated by subtracting the regulator, leading to the definition of the Effective Average Action Γ_k :

$$\Gamma_k[\hat{\Phi}] = J_k \hat{\Phi} - W_k[J_k[\hat{\Phi}]] - \frac{1}{2} \int d^d x \hat{\Phi} \mathcal{R}_k(\Delta) \hat{\Phi} \quad (2.31)$$

where $\hat{\Phi}$ is the expectation value of the fields $\hat{\Phi} = \delta W_k / \delta J$. From now on, the regulator is written as a function of the coarse-graining operator Δ that appears in the propagator of the fields and measures their momentum. This is typically the Laplacian and it may include additional terms that appear in the potential of the field. This Γ_k is the scale-dependent version of the effective action Γ and satisfies the following integro-differential equation:

$$\begin{aligned} \exp(-\Gamma_k) &= \int \mathcal{D}\phi \exp\left(-S + \int d^d x (\phi - \hat{\phi}) \frac{\delta \Gamma_k}{\delta \hat{\phi}}\right) \\ &\times \exp\left(-\frac{1}{2} \int d^d x (\phi - \hat{\phi}) \mathcal{R}_k(\Delta) (\phi - \hat{\phi})\right) \end{aligned} \quad (2.32)$$

where the quantum equation of motion for non-zero source $\delta \Gamma_k / \delta \hat{\Phi} = J_k$ has been used. This scale-dependent functional is the central object of the functional renormalisation group and defines an effective action which describes physics at a variable energy scale. In the IR limit $k \rightarrow 0$, the regulator vanishes by construction and the quantum effective action Γ is recovered, where all field fluctuations have been integrated out. In the UV limit $k \rightarrow \infty$, all modes are suppressed as the regulator becomes k^2 . Then, the second exponential in eq. (2.32) approaches a delta functional, the integration over the quantum fields can be

performed trivially and the bare action S is recovered. Thus, the Γ_k interpolates between both functionals in the low and high-energy limits, respectively:

$$\Gamma \xleftarrow{k \rightarrow 0} \Gamma_k \xrightarrow{k \rightarrow \infty} S \quad (2.33)$$

2.3.3 Flow equations

The iterative coarse-graining steps can be taken continuously by performing the integration in infinitesimal thin momentum shells. This amounts to taking the momentum derivative of Γ_k . It is convenient to work with dimensionless quantities, so the log-momentum derivative is employed, $\partial_t = \partial_{\log k} = k\partial_k$, yielding:

$$\partial_t \Gamma_k = \frac{1}{2} \text{STr} \left[\left(\Gamma_k^{(2)} + R_k \right)^{-1} \partial_t R_k \right] \quad (2.34)$$

This is the form of the equation first derived by Wetterich [132] and then by Ellwanger [133] and Morris [129] independently, while Bonini et al. give an equivalent formula [134]. The trace stands for integration in spacetime and momentum, and sum over any discrete indices such as flavour or colour. A negative sign is implied for Grassman fields. The notation $\Gamma_k^{(2)}$ refers to the second variation of Γ_k with respect to the fields, the Hessian. This is an exact equation which describes the flow of the scale-dependent effective action with respect to the renormalisation scale. This equation is free from divergences both in the IR and in the UV due to the presence of the regulator.

The relation between this flow equation and Polchinski's equation is a Legendre transform [58, 129, 135]. Polchinski's equation is formulated in terms of the low energy modes of the fields, this is an effective theory valid up to a finite energy scale and agnostic to the physics above that scale, thus, it makes reference to a UV cut-off. The Legendre transform switches the point of view. The flow equation of Γ_k is formulated in terms of the high-energy modes, which are sequentially integrated down to lower scales until the quantum effective action is recovered. Thus, this equation depends on an IR cut-off.

The structure of this flow equation is similar to the one-loop effective action if the replacement $\Gamma_k \rightarrow S$ is applied on the right-hand side of the equation. This amounts to neglecting the running of the couplings and recovers the one-loop effective action supplemented by the IR regulator. Looking at it from the other way around, the exact flow equation represents an improvement from the one-loop effective action as the running of couplings is correctly accounted for. This is sometimes referred to as the *RG improvement* in the literature.

2.3.4 Approximations

The effective average action Γ_k describes the physics at some energy scale k and in general, will contain all the operators allowed by the symmetries of the theory. Even if some of these operators are turned off at a certain scale, they will generically be generated by the renormalisation group flow:

$$\Gamma_k[\hat{\Phi}] = \sum_n \lambda_n(k) \mathcal{O}_n[\hat{\Phi}] \quad (2.35)$$

It is impossible to keep track of this infinite set of operators, thus, some approximations are required. Two such approximations are discussed next, the derivative expansion and the vertex expansion.

The derivative expansion consists of making an ansatz for the form of the Γ_k arranging the operators in a series in increasing powers of momenta, where the kinetic term is counted separately:

$$\Gamma_k = Z_{\hat{\Phi}} (\nabla \hat{\Phi})^2 + U(\hat{\Phi}) + V(\hat{\Phi}, p^2) + \dots \quad (2.36)$$

The first term in this expression stands for the kinetic term of the fields, here written schematically as that of a scalar field. The second term contains all operators in the theory space that respect the symmetries and involve no derivatives of the fields. The third one contains interactions with two derivatives, while higher order functions follow this pattern. Operators of higher-derivative order can be dropped if they are not relevant for the physics. However, note that it is not a priori known which operators are relevant at an interacting fixed point, as interactions can turn canonically irrelevant operators into relevant ones. The local potential approximation consists of truncating this expression to include only the kinetic and the potential U term and ignoring the running of the wavefunction renormalisation constant. This approach is commonly used in quantum and statistical field theory where one is interested in large wavelength phenomena [136–138]. In gravity, this is usually replaced by the operator expansion, where the ordering is made in powers of curvature invariants [139] (see Section 2.4.9).

The vertex expansion consists instead on writing the generator of the 1PI correlation functions as a Taylor expansion of the n-vertex functions:

$$\Gamma_k = \sum_{n=0}^{\infty} \frac{1}{n!} \Gamma_k^{(n)} \prod_j^n \hat{\Phi}_j \quad (2.37)$$

where the functional variations are taken with respect to the fields $\hat{\Phi}_j$. Taking the log-momentum derivative leads to a system of integro-differential equations that couple the

flow of the n -point function to that of other functions up to $n + 2$. Since the flow of a given vertex depends on all operators contributing to that interaction, this approach can in principle retain effects from higher derivative orders. This means that it can track the momentum dependence of the correlation functions. The vertex expansion has been commonly employed in condensed matter physics, although it is currently also been used in gravity, where it has made it possible to disentangle background and dynamical couplings [129, 140–145].

Approximations should be guided by an underlying physical principle that allows them to be systematic and reliable. In strongly interacting systems, it is not guaranteed that a certain truncation will leave the qualitative features of the full system unaffected. In general, a fixed point of the full theory may not be visible in certain projections of the action on a truncated theory space. The converse is also true, spurious solutions may arise as artefacts of truncations which do not correspond to a physical solution of the full theory. This is a point of uncertainty and one should keep in mind that results may reflect some dependence on the projection and truncation of the Γ_k .

2.4 Renormalisation group for quantum gravity

This section describes some additional elements required for the formulation of the path integral of gravity. It introduces some technical developments useful for quantising the theory and constructs the flow equation of the gravitational theory. The section outlines some of the additional complications that make gravity such a unique theory. Afterwards, the following section ends this chapter with a review of the state of the art on the research of asymptotic safety in gravity.

2.4.1 Metric fluctuations

Calculations in curved spacetime require the use of the background field approach, decomposing the metric into a background field and a fluctuating field. The reason for this is that when spacetime is dynamical, there is no preferred definition of coarse-graining operators, lengths scales are dynamical and thus there is no unique way to measure momentum. The introduction of a fixed background field helps alleviate this issue as then differential operators can be defined in the background. There are at least two ways in which this decomposition can take place.

The first is the linear parametrisation, where the full metric is a superposition of the

background metric and a fluctuating field,

$$g_{\mu\nu} = \bar{g}_{\mu\nu} + h_{\mu\nu} \quad (2.38)$$

where the bar notation denotes the background field and from now on, this notation will be used to denote operators constructed with the background metric. This split is widely used in the literature because of its simple interpretation and because it makes computations manageable. This is the parametrisation that will be used throughout this thesis.

The second is the exponential parametrisation, where the dynamical metric is given by a background metric weighted by a fluctuation of the form:

$$g_{\mu\nu} = \bar{g}_{\mu\rho}(e^h)^\rho{}_\nu = \bar{g}_{\mu\nu} + h_{\mu\nu} + \frac{1}{2}h_\mu{}^\lambda h_{\lambda\nu} + \dots \quad (2.39)$$

This split has the advantage of manifestly preserving the signature of the metric, in addition to making it easy to pick out the conformal mode of the metric. Furthermore, this choice allows a formulation which leads to an explicit separation between the physical and gauge degrees of freedom which also works off-shell. [146]. A generalised approach has also been put forward that interpolates between these two splits, highlighting the parametrisation dependence of the results and that different families of fixed points may exist [147–150].

2.4.2 Gauge fixing and ghosts

The symmetry of gravity is diffeomorphism invariance, resulting in the invariance of general coordinate transformations of the metric:

$$\delta_\epsilon g_{\mu\nu} = \mathcal{L}_\epsilon g_{\mu\nu} = \nabla_\mu \epsilon_\nu + \nabla_\nu \epsilon_\mu = \epsilon_\rho \partial^\rho g_{\mu\nu} + \partial^\rho \epsilon_\nu g_{\mu\rho} + \partial^\rho \epsilon_\mu g_{\rho\nu} \quad (2.40)$$

In quantum gauge transformations, the fluctuation absorbs all changes while the background remains unchanged:

$$\delta_\epsilon h_{\mu\nu} = \mathcal{L}_\epsilon g_{\mu\nu}, \quad \delta_\epsilon \bar{g}_{\mu\nu} = 0 \quad (2.41)$$

The metric has ten degrees of freedom in four dimensions, however, the graviton has only two polarisations, meaning that eight of those are unphysical (in d dimensions, this is $d(d-3)/2$ physical degrees of freedom). Diffeomorphism invariance gets rid of these additional degrees of freedom by imposing constraints on the equations. Just like in gauge theories, the gauge fixing can be implemented using the Fadeev-Popov procedure, ensuring that the path integration is performed only over the physical degrees of freedom. A general

gauge condition is of the form:

$$F_\mu = 0 \quad (2.42)$$

where F_μ is a differential operator on the fluctuation field to be specified. To embed this condition in the path integral, the partition function can be multiplied by the following identity:

$$1 = \Psi(h; \bar{g}) \int (df) \delta(F_\mu(h^f; \bar{g})) \quad (2.43)$$

where the integration is over diffeomorphisms f , δ is a functional Dirac delta and a quantum gauge transformation acting on the field is denoted as $h^f = h + \delta_f h$. Inserting this in the partition function, the integration over the diffeomorphism group can be factored out and absorbed into an overall normalisation. This is possible because the action is itself gauge invariant under quantum gauge transformations, such that a shift of variables in the integration gets rid of the dependence on f . Then, the partition function reads:

$$\mathcal{Z} = \int (dh) \Psi(h; \bar{g}) \delta(F_\mu(h; \bar{g})) e^{iS(h; \bar{g})} \quad (2.44)$$

The overall normalisation factor Ψ and the delta function can be absorbed into the action in the exponential. Through the usual Fadeev-Popov trick, the normalisation Ψ turns out to be the determinant of the Fadeev-Popov operator, denoted as Δ_{FP} . This can be rewritten as a Gaussian integral introducing anti-commuting fields \bar{C} and C ,

$$\Psi = \det \Delta_{FP} = \int d\bar{C} dC e^{iS_{GH}(h, \bar{C}, C; \bar{g})} \quad (2.45)$$

with ghost action

$$S_{GH}(h, \bar{C}, C; \bar{g}) = \int dx \sqrt{\bar{g}} \bar{C}^\mu (\Delta_{FP})_{\mu\nu} C^\nu \quad (2.46)$$

and the Fadeev-Popov operator defined as

$$(\Delta_{FP})_{\mu\nu} = \frac{\delta F_\mu}{\delta h_{\rho\sigma}} (g_{\sigma\nu} \nabla_\rho + g_{\rho\nu} \nabla_\sigma) \quad (2.47)$$

The delta function can be implemented by defining

$$\delta(F_\mu(h; \bar{g})) = \lim_{\alpha \rightarrow 0} e^{iS_{GF}(h; \bar{g})} \quad (2.48)$$

with gauge fixing action

$$S_{GF}(h; \bar{g}) = \frac{1}{2\alpha} \int d^d x \sqrt{\bar{g}} \bar{g}^{\mu\nu} F_\mu F_\nu \quad (2.49)$$

Putting everything together, the partition function is:

$$Z = \int dh d\bar{C} dC e^{i(S(h;\bar{g})+S_{GF}(h;\bar{g})+S_{GH}(h,\bar{C},C;\bar{g}))} \quad (2.50)$$

A convenient choice is to let the gauge fixing condition be linear in the fluctuation $F(h;\bar{g}) = 0$:

$$F_\mu(h;\bar{g}) = \bar{\nabla}_\rho h^\rho{}_\mu - \frac{1+\delta}{d} \bar{\nabla}_\mu h = 0 \quad (2.51)$$

In this expression, δ is a free parameter, not to be confused with a Dirac delta. The Fadeev-Popov operator corresponding to (2.51) is

$$(\Delta_{FP})_{\mu\nu} = \bar{\nabla}^\rho \bar{g}_{\mu\nu} \nabla_\rho + \bar{\nabla}^\rho \bar{g}_{\rho\nu} \nabla_\mu - 2 \frac{1+\delta}{d} \bar{\nabla}_\mu \bar{g}^{\rho\sigma} \bar{g}_{\rho\nu} \nabla_\sigma \quad (2.52)$$

The harmonic (de Donder) gauge condition corresponds to $\delta = d/2 - 1$, while the geometric gauge condition is $\delta = 0$. Taking the limit $\alpha \rightarrow 0$ not only enforces the gauge fixing condition but is also a fixed point of the renormalisation group of this gauge fixing parameter [151]. Moreover, this limit is convenient as computations greatly simplify. Finally, note that studies of quadratic gravity usually employ a gauge fixing term which contains four background derivatives, which proves convenient to cancel nonminimal fourth-order terms in the kinetic operator of the fluctuation $h_{\mu\nu}$ [152–155].

2.4.3 York decomposition

It is advantageous to separate the metric fluctuation into its components disentangling its degrees of freedom. This is done in curved spacetimes through the York decomposition [156]:

$$h_{\mu\nu} = h_{\mu\nu}^{TT} + \bar{\nabla}_\mu \xi_\nu + \bar{\nabla}_\nu \xi_\mu + \bar{\nabla}_\mu \bar{\nabla}_\nu \sigma - \frac{1}{d} \bar{g}_{\mu\nu} \bar{\nabla}^2 \sigma + \frac{1}{d} \bar{g}_{\mu\nu} h \quad (2.53)$$

The first term is transverse and traceless and carries the physical spin-2 degrees of freedom of the graviton. The vector ξ_μ is transverse and carries the spin-1 component, while σ and h carry the scalar modes, the last one being the trace part of the metric. These fields obey the conditions:

$$\bar{\nabla}^\mu h_{\mu\nu}^{TT} = 0, \quad \bar{g}^{\mu\nu} h_{\mu\nu}^{TT} = 0, \quad \bar{\nabla}^\mu \xi_\nu = 0, \quad h = \bar{g}_{\mu\nu} h^{\mu\nu} \quad (2.54)$$

This decomposition has the further advantage that the propagator turns almost diagonal when evaluated on a spherical background so that it becomes easier to invert.

It should be noted that some of the eigenmodes of these components may need to be excluded from the calculations. This is because when the metric is decomposed, the

components may have eigenmodes which are zeromodes and thus do not give a physical contribution. For example, on spherical backgrounds, the two lowest modes of a scalar field do not contribute to the propagation of a rank-2 tensor. Similarly, if the vector field ξ_μ contains killing vectors, these should also be removed.

This transformation is, in essence, a change of variables which in Einstein spaces gives rise to a Jacobian of the form:

$$J = \left(\det_{(1T)} \left(-\bar{\nabla}^2 + \frac{\bar{R}}{d} \right) \right)^{1/2} \left(\det_{(0)} \left(\frac{d-1}{d} \right) (-\bar{\nabla}^2) \left(-\bar{\nabla}^2 + \frac{\bar{R}}{d-1} \right) \right)^{1/2} \quad (2.55)$$

The first term arises from identifying the kinetic operator of the spin-1 transverse field ξ_μ , while the second one, from that of the scalar σ field. The other components do not induce any further terms.

There are two non-equivalent ways to treat this Jacobian. First, in all similarity to the Fadeev-Popov trick, the determinants can be rewritten as Gaussian integrals over new auxiliary fields. The one arising due to the scalar modes introduces a pair of complex Grassmann scalars and one real scalar. Similarly, the one appearing due to the vector mode results in a pair of complex Grassmann transverse vectors and one real transverse vector field [157]. This is the treatment that will be employed throughout this thesis.

The second method is to note that ξ_μ and σ do not have the same mass dimension as the metric from which they originate. In a spherical background, a field redefinition can be performed to make these fields canonically massless by rescaling them with suitable differential operators [158]:

$$\hat{\xi}_\mu = \sqrt{-\bar{\nabla}^2 - \frac{\bar{R}}{d}} \xi_\mu, \quad \hat{\sigma} = \sqrt{(-\bar{\nabla}^2) \left(-\bar{\nabla}^2 - \frac{\bar{R}}{d-1} \right)} \sigma \quad (2.56)$$

This change of variables induces a new Jacobian which exactly cancels that from the York decomposition, such that the transformation $h_{\mu\nu} \rightarrow (h^{TT}, \hat{\xi}, \hat{\sigma}, h)$ does not induce any overall factors. It is important to note that such non-local field redefinitions are only admissible for non-physical fields. In this case, it is understood that ξ_μ and σ carry gauge degrees of freedom, while only h^{TT} is physical. Note that this approach may not work in general spaces, where the Jacobians from the York decomposition would be more complicated expressions.

It should be noted that these two treatments are not equivalent and can lead to finding slightly different results. In the case of the linear split, field redefinitions lead to very mild differences, while in combination with the exponential split, qualitative differences in the results have been observed [147].

Similarly, the vector ghosts can be separated into their transverse and longitudinal parts:

$$\bar{C}_\mu = \bar{C}_\mu^T + \bar{\nabla}_\mu \bar{\eta}, \quad C_\mu = C_\mu^T + \bar{\nabla}_\mu \eta \quad (2.57)$$

This transformation gives rise to a new Jacobian from the longitudinal modes:

$$J_{GH} = (\det(-\bar{\nabla}^2))^{-1} \quad (2.58)$$

As before, this can be either rewritten as additional auxiliary fields, yielding a pair of complex scalar fields, or it can be cancelled by a redefinition of the longitudinal mode.

2.4.4 Flow equation of gravity

The construction of the effective action for gravity follows that of the Section 2.3 with the insertion of the gauge fixing and ghost terms, as well as a regulator for the ghosts. In a slight abuse of notation, from now on the expectation value of the fields $h_{\mu\nu}, \bar{C}, C$ appearing in Γ_k will be denoted by the same name as the quantum fields.

An important remark is that under the split of the metric in background and fluctuation, the coarse-graining operator of the regulator term must be constructed using the background metric, i.e. $\Delta S_K(\Delta) \rightarrow \Delta S_K(\bar{\Delta})$. This is unavoidable as momentum must be measured with respect to a fixed background for a proper regularisation. Following the same steps as before, the flow equation for Γ_k in gravity is:

$$\partial_t \Gamma_k(h, \bar{C}, C; \bar{g}) = \frac{1}{2} \text{Tr} \left[\left(\Gamma_k^{(2)} + \mathcal{R}_k \right)_{hh}^{-1} (\partial_t \mathcal{R}_k)_{hh} \right] - \text{Tr} \left[\left(\Gamma_k^{(2)} + \mathcal{R}_k \right)_{\bar{C}C}^{-1} (\partial_t \mathcal{R}_k)_{\bar{C}C} \right] \quad (2.59)$$

The h in this equation refers to the full fluctuation field. As before, this equation is finite both in the UV and the IR due to the regulator which satisfies the requirements previously listed. Note that this equation depends on two metrics, the full dynamical metric $g_{\mu\nu}$ and the background metric $\bar{g}_{\mu\nu}$. This is because the gauge fixing and regulator terms introduce an additional dependence on the background on top of the one defined by the metric fluctuation $h_{\mu\nu} = g_{\mu\nu} - \bar{g}_{\mu\nu}$. This additional background dependence makes it impossible to write a flow equation in terms of a single metric. Moreover, this seemingly introduces a non-trivial background dependence on the functional. However, physical observables must be background-independent. The information on diffeomorphism invariance and background independence of Γ_k is carried by the split Ward identities and Nielsen identities. These identities relate derivatives with respect to the fluctuation field and those with respect to the background field, and encode the amount of *additional* background

dependence of the functional. For a detailed review, the reader is referred to ref. [159] and references therein.

2.4.5 Background field approximation

A first approximation to treat this problem is offered by noting that Γ_k can, in general, be written as:

$$\Gamma_k(g, \bar{g}, \bar{C}, C) = \bar{\Gamma}_k(g) + \hat{\Gamma}_k(g, \bar{g}, \bar{C}, C) \quad (2.60)$$

The first term depends only on the full dynamical metric and is defined by setting all fluctuations to zero $\bar{\Gamma}_k(g) \equiv \Gamma_k(g, g, 0, 0)$. In the absence of fluctuations, $g_{\mu\nu} = \bar{g}_{\mu\nu}$ and $\bar{\Gamma}_k$ satisfies diffeomorphism invariance. Then, functional derivatives with respect to $\bar{g}_{\mu\nu}$ and $h_{\mu\nu}$ coincide in the linear split and the Ward identity is satisfied to leading order [41], implying for the second term:

$$\hat{\Gamma}_k(\bar{g}, \bar{g}, 0, 0) = 0 \quad (2.61)$$

This term contains the gauge fixing, ghosts and possibly auxiliary fields arising from field redefinitions, as explained in Section 2.4.3. The background field approximation, or single-metric approximation, consists of approximating the effective action via $\bar{\Gamma}_k$ and neglecting the running of the gauge fixing and the ghosts' wavefunction renormalisation constant. Then, the running of the couplings contained in $\bar{\Gamma}_k$ can be obtained by evaluating the Hessian at vanishing fluctuation. Note that this approximation is only exact in the case of scalar fields. The assumption is that $\bar{\Gamma}_k$ carries the physical information of the theory while $\hat{\Gamma}_k$ includes quantum corrections to the gauge fixing. The background field approximation will be employed throughout the rest of this study, thus:

$$\Gamma_k = \bar{\Gamma}_k + S_{GF} + S_{GH} + S_{AUX} \quad (2.62)$$

Note that this also reproduces the one-loop effective action replacing $\Gamma_k \rightarrow S$ on the right hand side of (2.59).

The flow equation can now be computed setting field fluctuations to zero at the end. The first term in (2.59) encodes quantum corrections due to metric fluctuations and can be computed either taking derivatives of $h_{\mu\nu}$ as was done originally in ref. [41] or by using the York decomposition and adding regulators for each mode independently. The advantage of the latter approach is that this choice helps to disentangle the mixing of physical and unphysical degrees of freedom leading to a nearly diagonal propagator. If the method of auxiliary fields is used, additional traces over these fields need to be added to the equation.

2.4.6 Trace evaluation

Two mathematical techniques are commonly used to evaluate the traces in the right-hand side of (2.59), the early time heat kernel expansion and the smoothed spectral sum. Both methods are discussed in detail in Chapter 4 so an explanation is deferred until then. In that chapter, the calculations are performed explicitly for free matter fields.

It is worth to mention that the result of the computations depend on the profile function and on the coarse-graining operator used to regulate the field fluctuations. It is only the traces of canonically marginal couplings that do not depend on the regulator, thus they are scheme independent [125,160]. This regulator dependence introduces some uncertainty on the results regarding the flow of canonically dimensionful couplings. For instance, the contributions to the flow equation from free fermions can appear with different signs depending on how these fields are regularised [161]. This dependence concerns not only the choice of the profile function but also the choice of the coarse-graining operator employed to regularised the fields. Further details are given in the following section.

2.4.7 Types of cut-offs

The coarse-graining operator Δ of the profile function $R_k(\Delta)$ is supposed to measure the momentum of the fields being regularised. A natural choice is to let it be a function of the Laplacian constructed with the background metric, $-\bar{\nabla}^2$. In the following, it is understood that all quantities are constructed with the background metric $\bar{g}_{\mu\nu}$ and the bar notation is dropped for readability. A general form for this operator in spherical backgrounds can be written as:

$$\Delta = -\nabla^2 + \sum_n \alpha_n f_n(R) + \sum_n g_n(k) h_n(R, \Phi) \quad (2.63)$$

The first term is the bare Laplacian which appears in the kinetic operator of all the fields. The second term includes linear curvature scalars encoded by $f_n(R)$ with free constant parameters α_n . These curvature terms may appear in the propagator due to the generalised definition of the Laplacian on curved spacetime acting on tensors of rank-1 and above or spinors. The third term contains any other interactions with spacetime or other fields which are accompanied by momentum-dependent couplings $g_n(k)$. Three types of cut-offs can be defined depending on which of these terms are included in the coarse-graining operator for any given field. These are now listed following the nomenclature introduced in [160].

The type I cut-off is defined by fixing $\alpha_n = g_n = 0$ dropping any k dependence in

the regulator. This is suitable for free massless scalar fields where the kinetic operator is just the bare Laplacian but is also commonly used for the components of the metric in the York decomposition. The type II cut-off is characterised by including potential terms with constant coefficients, such that $\alpha_n \neq 0$ and $g_n(k) = g_n$. This is suitable for vectors, tensors and spinors, where the kinetic operator can include terms linear in curvature with constant coefficients. The constant g_n can be zero for free fields, or can be non-zero if there are interactions but their running is neglected. For example, one may wish to investigate the impact of mass or a non-minimal coupling to curvature in a simplified approximation where these couplings are taken as free parameters. The type III cut-off is the most general scenario and is defined by including momentum-dependent couplings. This implies that the spectrum of the coarse-graining operator also evolves with the RG flow. For this reason, this is also known as the spectrally adjusted cut-off and is useful when the momentum-dependence of interactions must be retained, for example, when computing the running of wavefunction renormalisation constants or investigating the momentum dependence of correlation functions.

2.4.8 Excluded modes

The decomposition of the spin-1 and spin-2 fields into their irreducible components of the Lorentz group entails that some unphysical contributions to the eigenspectrum of these fields must be removed. Consider the decomposition of a vector field into its transverse and longitudinal parts:

$$A_\mu = A_\mu^T + \nabla_\mu \phi \quad (2.64)$$

The transverse part contains the physical field while the longitudinal part carries the gauge degrees of freedom. However, the constant mode of ϕ is not a physical degree of freedom of A_μ and thus should be excluded from any computations. This is usually denoted by using a prime notation ($'$) to indicate how many of the lowest modes must be removed. For example:

$$\text{Tr}'_\phi W(-\nabla^2) \quad (2.65)$$

indicates that the lower eigenmode of the differential operator $-\nabla^2$ acting on ϕ is to be excluded. The same applies in the York decomposition of the metric. The spin-1 component ξ_μ may contain Killing vectors which must be excluded from the traces. This depends on the choice of metric so it must be checked each time. Likewise, the spin-0 component σ may carry modes which do not contribute to the metric. All calculations in this thesis

will take place on a spherical background, where these spurious modes correspond to the two lowest modes of σ and the lowest mode of ξ_μ .

2.4.9 Approximations

The effective action generically contains any number of operators allowed by the symmetries of the theory accompanied by a running coupling:

$$\Gamma_k(g, \bar{g}, \Phi) = \int d^d x \sqrt{\bar{g}} \sum_n \lambda_n(k) \mathcal{O}_n(g, \bar{g}, \Phi) \quad (2.66)$$

where all the fields in the theory are collected in Φ and it is implied that the operators can contain any possible combination of these fields that respect diffeomorphism invariance and any other symmetries of the theory. The beta functions describing the flow of these couplings are obtained by projecting the right-hand side of the flow equation on each of the operators and comparing with the left-hand side, thus:

$$\int d^d x \sqrt{g} \beta_n \mathcal{O}_n = P_{\mathcal{O}_n} \partial_t \Gamma_k \quad (2.67)$$

With $P_{\mathcal{O}_n}$ a projection operator that picks out the terms in the flow equation proportional to \mathcal{O}_n . As discussed already in Section 2.3, an ansatz for Γ_k can be chosen by limiting the set of operators appearing in Γ_k to a truncated theory space. Then the projection of the flow equation is made on the basis of operators present in the action.

A simple starting point is the derivative expansion introduced in 2.3. In the following, the notation \mathcal{O}_n^m indicates an operator with m derivatives and the subindex n is just a label to distinguish all the possible ones. The zeroth and second derivative-order contain only one operator each, the vacuum energy and the Einstein-Hilbert term:

$$\mathcal{O}_1^0 = \mathbb{I}, \quad \mathcal{O}_1^2 = R, \quad (2.68)$$

At fourth derivative-order, there are four curvature invariants constructed with the curvature tensors and covariant derivatives. On a manifold without boundary, total derivatives can be ignored and this number reduces to three independent terms. They may be written either on the Ricci basis, in terms of $(R^2, R_{\mu\nu}^2, R_{\mu\nu\rho\sigma}^2)$ or equivalently in the Weyl basis, (R^2, E, C^2) , where E is the integrand of the Gauss-Bonnet term and C^2 is the square of the Weyl tensor:

$$\mathcal{O}_1^4 = R^2, \quad \mathcal{O}_2^4 = C_{\mu\nu\rho\sigma} C^{\mu\nu\rho\sigma}, \quad \mathcal{O}_3^4 = E \quad (2.69)$$

with:

$$\begin{aligned} E &= R^2 - 4R_{\mu\nu}R^{\mu\nu} + R_{\mu\nu\rho\sigma}R^{\mu\nu\rho\sigma}, \\ C^2 &= R_{\mu\nu\rho\sigma}R^{\mu\nu\rho\sigma} - \frac{4}{d-2}R_{\mu\nu}R^{\mu\nu} + \frac{2}{(d-1)(d-2)}R^2 \end{aligned} \quad (2.70)$$

At the sixth order, there are already ten different operators, which reduce to eight independent invariants in four dimensions due to geometrical relations between them. However, this expansion becomes very complicated as the number of curvature invariants blows up very quickly with increasing derivative-order. Furthermore, computing the Hessians for each different operator in a general background becomes a very complicated task as the number of curvature invariants increases. Moreover, constructing suitable projection operators to disentangle the running of all different couplings is a highly non-trivial task. A simpler alternative is available by truncating to a subspace of operators.

The derivative expansion is usually replaced by the operator expansion in the study of gravity. This involves truncating the theory space of the derivative expansion to include only a subset of the possible curvature invariants. The approach is structurally simpler as it is effectively an expansion in powers of a given basis of operators. Note this is not a true derivative expansion, as operators outside of the truncated theory space are neglected at each order in momentum. Nonetheless, it is useful as it permits investigations on the effect of higher derivative-order operators. These operators can, in principle, become relevant at an interacting fixed point and cannot be ignored. The predictivity of the theory can be spoiled if an infinite number of operators become relevant.

An example is given by the $f(R)$ approximation, where the Γ_k is assumed to be a general function of the Ricci scalar only.

$$\Gamma_k = \int d^d x \sqrt{g} f_k(R) \quad (2.71)$$

In maximally symmetric spaces, this approximation leads to a partial differential equation which can be solved to find global solutions of the theory. Then, the limits of small and large curvature, corresponding to the UV and IR, respectively, can both be studied. A further approximation is given by assuming that the function can be written in polynomial form, leading to a sum of monomials of increasing power in R :

$$\Gamma_k = \int d^d x \sqrt{g} \sum_n^N \lambda_n(k) R^n \quad (2.72)$$

with N being the order of the approximation. In this case, the basis of the operators is given solely by the Ricci scalar and results in a system of ordinary differential equations that can be solved algebraically at the fixed point. This expansion is justified by the bootstrap hypothesis which is explained next.

The bootstrap hypothesis assumes that operators can be ordered in a power series according to their canonical mass dimension. Moreover, it states that if higher derivative

curvature invariants are introduced in the action, the additional RG directions in the expanded theory space are less and less relevant. This implies that there is a finite number of relevant directions (free parameters) associated with a UV fixed point and thus the theory is predictive. This is not necessarily true at an interacting fixed point and the hypothesis must be checked a posteriori. Based on this assumption, the polynomial approach looks for fixed points by gradually incorporating higher derivative operators. This bootstrap search strategy will be used throughout this thesis to find gravitational fixed points including operators up to 100th curvature-order.

Similar polynomial approximations have been explored more recently, e.g. the $f(R, Ric^2)$ and $f(R, Riem^2)$ approximations, where the basis of operators is $(R, R_{\mu\nu}^2)$ and $(R, R_{\mu\nu\rho\sigma}^2)$, respectively. This study will consider a generalised version of these polynomial approximations where the action will be projected on a subspace spanned by linear combinations of $(R^2, Ric^2, Riem^2)$. This is discussed first in the theory without matter in Chapter 3 and then in the presence of Standard Model matter in Chapter 5.

Another approximation is given by the so-called form factors:

$$\Gamma_k = \Gamma_k^{(EH)} + \int d^d x \sqrt{\bar{g}} (C_{\mu\nu\rho\sigma} W_k^C(\Delta) C^{\mu\nu\rho\sigma} + R W_k^R(\Delta) R) \quad (2.73)$$

with the first term denoting the Einstein-Hilbert action. This expansion captures terms which are not included in $f(R)$ -like truncations. Moreover, these form factors are momentum-dependent and quadratic in the metric fluctuations, thus they include non-trivial contributions to the propagator of the tensor and scalar mode of the graviton. Terms of this form but of higher curvature order also encode the momentum-dependence of the running couplings. This approach has been used to compute non-perturbative IR corrections to the Newtonian potential [162] and to compute graviton mediated scattering amplitudes of scalar fields [163, 164]. For a detailed review of this approach, see ref. [165].

In addition, the vertex expansion already introduced in Section 2.3 carries over to the gravitational case. This approach recognises the bi-metric structure of Γ_k , disentangling background and dynamical fluctuations and allowing to investigate the momentum dependence of correlation functions. This results in a distinction between background and dynamical couplings, related to each other by modified Slavnov-Taylor identities. Moreover, this implies that each n-point vertex carries a different interaction coupling and respective graviton mass parameters. The next section includes a review of progress in this approach.

2.5 State-of-the-art in asymptotically safe gravity

Now that the necessary concepts and technical tools have been introduced, a literature review is presented summarising significant advancements in asymptotic safety in gravity up to date. Although this section is aimed to provide a broad scope of the advances in the field and highlight the many difficulties and implications of asymptotically safe gravity, it is by no means an exhaustive review and some important developments may have been neglected. References for more complete review papers are provided throughout as a supplement for the reader.

Einstein-Hilbert gravity. The development of the functional renormalisation group offered a breakthrough in the asymptotic safety programme by providing a framework to study non-perturbative physics. The seminal paper that started renewed efforts applied this framework to the Einstein-Hilbert theory [41]. In this setting, an interacting fixed point is found with two relevant directions and well-defined RG flows connecting the interacting and finite theory in the UV to a Gaussian regime in the IR [166, 167]. Since then, this approximation has been extensively studied providing strong support for the existence of the fixed point in four dimensions [166–170] and above [170–172]. The conformally reduced theory has also been explored, finding similar results as the full theory in the Einstein-Hilbert theory [173–176], while actions with non-local terms have also been considered finding they decouple from the RG flow [157, 177]. Moreover, the theory remains asymptotically safe upon inclusion of the two-loop Goroff-Sagnotti term [178]. For a broader review of the progress in the field, the reader is directed to refs. [160, 179–181].

Quadratic gravity. The derivative expansion has been consistently explored up to fourth order in momentum. The quadratic gravity approximation was first studied in a spherical background with the RG improvement [168, 182] as well as in general backgrounds at one-loop [152, 154]. Later, the use of Einstein backgrounds allowed to identify the running of two distinct couplings with the RG improvement, finding a non-trivial fixed point for these couplings [153]. This result has also been reproduced in perturbation theory [183, 184]. It is only recently that a computation in a general background using the RG improvement was performed, disentangling the running of all three independent couplings [155]. All these studies agree on finding three relevant directions. In the general background, the Gauss-Bonnet integrand remains exactly marginal in the UV. This is consistent with this term being a total derivative in four dimensions and hence having no

influence in the physics.

Operator expansion. Meanwhile, the operator expansion has mainly featured $f(R)$ theories, where necessary conditions for global solutions have been investigated [139, 176, 185–189]. The polynomial approximation has similarly been explored putting forward the bootstrap hypothesis. As previously explained, this conjectures that canonical power counting remains a valid ordering principle for operators in the UV. The implication is that a fixed point of the theory has only a finite number of relevant directions, ensuring that the theory remains predictive [187]. Studies up to high polynomial orders have all confirmed this notion finding three relevant directions [157, 190–194]. Additionally, the theory space has been extended to include operators of the form $R_{\mu\nu}^2$ finding qualitatively similar results [195]. Moreover, models including terms $R_{\mu\nu\rho\sigma}^2$ have found solutions with up to four relevant directions, indicating that the contributions from other higher derivative curvature invariants could play an important role in determining the UV critical surface of the fixed point [196].

Form factors. An approximation in terms of form-factors was recently put forward within the background field approach, which carry information about the momentum dependence of propagators and correlation functions [165]. This approach has been used to compute non-perturbative quantum corrections to the Newtonian potential, which differ from the perturbative EFT approach [162]. It has also been used to compute finite gravity-mediated scattering amplitudes of non-minimally coupled scalars [163, 164].

Dynamics of the ghost sector. Another direction of research beyond the local potential approximation has investigated the dynamics of the ghost sector. The backreaction of these ghosts appears explicitly in the beta functions of the gravitational couplings, thus modifying the fixed point. Moreover, self-interactions and interactions with matter could in general lead to additional relevant RG flows. This has been explored in the Einstein-Hilbert action finding that the fixed point survives without major modification, while the ghost self-interaction becomes asymptotically free [197–199]. On the other hand, their interaction with scalars is non-vanishing and could become relevant for large values of the ghost and scalar anomalous dimensions [200]. Furthermore, the running of the graviton and ghost anomalous dimensions have also been computed beyond the background field approximation in the Einstein-Hilbert theory [201].

Vertex expansion. In parallel to the background field approximation, bi-metric treatments have been put forward where the functional is recognised to depend on two metrics separately. This makes it possible to keep track of background and fluctuation dependent quantities and to verify that background independence is restored in the IR as encoded by split Ward identities [143, 202–204]. This allows for a vertex expansion where dynamical and background running couplings have been extracted from the flow of up to the 4-point correlation functions [144, 145, 205–207]. Each vertex contains a different *avatar* of Newton’s coupling and a graviton mass parameter. The dynamical Newton’s couplings are in agreement with each other leading to a sort of *effective universality*, providing further support for the asymptotic safety conjecture [207, 208]. Minimally coupled matter has also been studied in this approach, finding that the difference between background and dynamical fixed points becomes more significant once matter is included, with the dynamical one showing a weak matter and curvature dependence with near-perturbative behaviour [209–212]. These computations have included fourth-derivative operators finding that higher derivative operators can source a third relevant RG direction, in agreement with the findings in the background field approach. Most computations have been performed around a flat background but studies in curved backgrounds have also been undertaken [213]. Besides from the linear and exponential splits mentioned in Section 2.4.1, the geometric DeWitt-Vilkovisky parametrisation has also been investigated in these bi-metric approaches [214, 215]. For a more complete review on the vertex expansion, see ref. [159].

Lorentzian gravity. Although most computations in the continuum approach are performed in Euclidean spaces, the causal structure of spacetime can also be reconciled with the asymptotic safety conjecture. To achieve this, a flow equation using the ADM decomposition of the metric has been derived, which allows connecting Euclidean with Lorentzian computations [216–219]. This has been used to explore Horava-Lifshitz gravity with the functional renormalisation group finding an imprint of the fixed point found in Euclidean space [220]. These foliated spacetimes exhibit points with the same qualitative features as the Euclidean computations mentioned above. In the presence of matter, a fixed point with suitable RG flows compatible with General Relativity in the IR has also been found [221]. Breaking of Lorentz invariance in the UV may be visible in the IR which can be used to constrain Lorentz invariance violation in gravity and the matter sector [222, 223].

Parametrisation dependence. The approximations to the exact flow equation introduce a degree of uncertainty. Lacking a perturbative parameter, it is important to keep

track of how significant the impact of this freedom in parametrisation can be. Previous studies have investigated the dependence on gauge fixing parameters, metric fluctuation and regulator parametrisation [146–150]. The guiding principle of least variation suggests that choices which lead to large variations in quantities like scaling dimensions under a small variation of the parameter may lead to unreliable results. This statement should be taken with caution, however, as choices which are physically motivated should be preferred. More recently, an approach towards a background independent formalism has been put forward [224]. In terms of the theory space of truncations, dependence on the projection of the action can be compared across $f(R)$ [192], $f(R, Ric^2)$ [195] and $f(R, Riem^2)$ settings [196]. Chapter 3 of the present study expands the literature by providing an analysis of the variation of the gravitational fixed point in an interpolation between these three settings, showing that a fixed point that is considered physical under a certain projection can appear spurious under a different projection. Moreover, it will be explicitly shown throughout the different chapters of this thesis that physical solutions need not be continuously connected in the space of parameters.

Large N matter. The theory of gravity displays a matter-mediated stationary point in the large N regime with many matter fields. This was first observed in perturbation theory [30, 39] and was later revisited with the RG improvement including higher derivative-order terms [225, 226]. To leading order, the gravitational quantum corrections are neglected and a fixed point for the canonically relevant couplings is found, with higher order ones being asymptotically free. This scenario will be the subject of Chapter 7, where the computations will be revisited and extended to next-to-leading order. It will be shown that there exists a scaling regime in which gravitational interactions compete with matter fluctuations and generate a non-trivial fixed point for the marginal coupling. This, in turn, cascades into all higher derivative interactions, which at the fixed point can be resummed into a Coleman-Weinberg type gravitational potential, defining a general solution of the fixed point functional.

Fermions and chiral symmetry breaking. Fermion interactions in curved spacetime can be affected by the gravitational couplings. Similar to the confinement phenomenon in QCD, strong gravitational couplings could break chiral symmetry at the Planck scale, leading to large fermion masses which are not observed. However, studies have found that chiral symmetry breaking is avoided in the asymptotic safety scenario [227–229]. Moreover, fermions pose an additional ambiguity as their contribution to the flow can appear with

different signs depending on the choice of regulator. The case for regularisation with a type II cut-off has been made for non-interacting fermions [161]. A more recent study suggests that this may just be an artefact of neglecting fermion interactions, showing that regulator dependence can be mild for non-minimally coupled fermions [230].

Matter impact on gravity. Matter interactions can influence the gravitational fixed point and could in principle modify the dimensionality of the UV critical surface. It then becomes important to understand the impact of self-interactions and gravity-matter interactions. Plenty of investigations have been made augmenting either the Einstein-Hilbert theory or the quadratic gravity scenario with interacting scalars [231–240], fermions [120, 230, 241], considering the Higgs-Yukawa sector [117, 118] and also with Majorana fermions [242], delimiting restrictions on the matter content of the theory. Minimally coupled matter is also compatible with the Lorentzian formulation [221]. Qualitatively, a large number of fermion fields drives the cosmological constant towards negative values and can annihilate the gravitational fixed point. Meanwhile, gauge bosons tend to stabilise the fixed point and result in more perturbative coupling values [243]. Moreover, the backreaction of matter could impose further restrictions. This has been explored in an improved background field setting finding narrow constraints due to large anomalous dimensions [244, 245] while leading to weaker bounds in the vertex expansion [208–210, 212]. In the operator expansion, studies on $f(R)$ with minimally coupled matter have found that the SM field content is only compatible with a gravitational fixed point to high derivative order in particular settings showing strong parametrisation and regulator dependence [243, 246, 247]. This last point will be further discussed in Chapter 4, illustrating two scenarios in $f(R)$ for which different technical choices lead to either the absence or presence of a gravitational fixed point. Furthermore, this analysis will be extended to an expanded theory space in Chapter 5, discussing fixed points compatible with SM matter under the presence of higher order curvature invariants.

Gravity impact on matter. As already discussed in Section 2.2, quantum gravitational effects will impact the matter sector close to the Planck scale leading to non-trivial modifications of the running of matter couplings in the UV. This can lead to predictions for low energy physics, such as the prediction for the Higgs boson mass [248] and estimates on the Top and Bottom quark masses [249, 250]. Moreover, gravity induces an effective dimensional reduction on the gauge couplings which can change the prospect regarding triviality in the $U(1)$ sector [110, 113, 114]. For more complete reviews of matter

UV completions and the impact of gravity in the matter sector, the reader is referred to refs. [123, 251–253]

Observables. An important challenge is accessing observables that can support or falsify the asymptotic safety conjecture in gravity. The dynamical nature of spacetime makes it difficult to formulate such observables contrary to conventional flat-space quantum field theory. Quantum gravitational effects are expected to kick-in close to the Planck scale and can impact high-energy processes such as black hole physics [254–256]. However, it is unlikely that experiments will ever be able to access such high energies directly. Instead, one could consider that UV physics effects can percolate to lower energies and leave imprints of asymptotic safety in experimentally accessible scales. This could occur in the matter sector and is closely related to the discussion in the previous paragraph, leading to predictions of the Higgs [248] and the Top mass [249] and measurements of gauge couplings [114]. Furthermore, cosmology can offer another window to probe strong gravitational effects in the early universe, such as inflation [257–259] and provide further bounds on the matter content [260]. See refs. [261, 262] for reviews on implications of asymptotic safety for cosmology.

Chapter 3

Quantum Gravity

3.1 Introduction

The asymptotic safety conjecture for gravity has been extensively investigated with the functional renormalisation group, as outlined in the previous literature review. Beyond the Einstein theory, fourth derivative-order curvature invariants induce deviations on the coupling values and critical exponents. However, higher derivative-order operators are found to stabilise the fixed point as these variations become smaller. Previous studies have investigated operator expansions on the Ricci scalar [192, 263], Ricci tensor [195] and Riemann tensor [196] separately. While most studies of pure gravity suggest the existence of a fixed point with three relevant renormalisation group (RG) directions, solutions with four can appear if higher order interactions of the Riemann tensor are considered. This difference on the dimensionality of the UV critical surface suggests that such interactions can play an important role in quantum gravity. Thus, it becomes important to understand how fixed points of the theory depend on such higher order terms.

Moreover, numerical convergence of the fixed point seems to be subject to the types of interactions present in the theory. In the first case of the previously mentioned studies, convergence is slow and it is necessary to go to high orders in curvature to establish numerical reliability. The second case has a fixed point with faster convergence, while in the last case, fixed points with either fast or limited convergence appear. Therefore, to properly assess the numerical reliability and convergence of solutions, it may be necessary to consider very high curvature orders. The present analysis extends the current understanding of these theories by considering cases where the three independent quadratic curvature invariants appear simultaneously in the action. Moreover, this study will consider models up to order $N = 101$ in a curvature expansion. Fixed points are searched for by performing

a scan of the theory space where these three operators appear in a linear combination.

The outline of this study is as follows. Section 3.2 introduces the theoretical framework and explains the methodology employed in the fixed point search. Section 3.3 presents the results of the search and discusses how the characteristics of the fixed point vary in different points of the theory space. Finally, Section 3.4 summarises the results and gives the conclusions.

3.2 Methodology

3.2.1 Gravitational action

The general form of the action for the types of models that will be studied here is

$$\Gamma_{grav} = \int d^4x \sqrt{g} [\bar{F}_k(\bar{X}) + \bar{R} \bar{Z}_k(\bar{X})] \quad (3.1)$$

The bar notation indicates dimensionful quantities. The functions \bar{F}_k and \bar{Z}_k contain the gravitational interactions including the Einstein action,

$$\bar{F}_k(0) = \frac{\Lambda_k}{8\pi G_k}, \quad \bar{Z}_k(0) = -\frac{1}{16\pi G_k} \quad (3.2)$$

as well as higher order interactions. The action should be supplemented by the appropriate gauge fixing and ghost operators as outlined in Chapter 2. \bar{F}_k and \bar{Z}_k are functions of \bar{X} , defined as a linear combination of the three independent quadratic curvature invariants,

$$\bar{X} = a \bar{R}^2 + b \bar{R}_{\mu\nu} \bar{R}^{\mu\nu} + c \bar{R}_{\mu\nu\rho\sigma} \bar{R}^{\mu\nu\rho\sigma} \quad (3.3)$$

The free constant parameters $\{a, b, c\} \in \mathbb{R}^3$ determine the projection of the action on the subspace of linear combinations of these operators. Thus, the theory space is spanned by the basis operators $(R^2, Ric^2, Riem^2)$, with (a, b, c) defining points in this subspace. Introducing some notation, the $f(R)$ theory is contained in this approach and corresponds to setting $(a, b, c) = (1, 0, 0)$, $f(R, Ric^2)$ corresponds to $(a, b, c) = (0, 1, 0)$, while $f(R, Riem^2)$, to $(a, b, c) = (0, 0, 1)$. Interactions involving the Ricci and Riemann tensors induce additional quantum corrections to the flow equation which are not present in the well-studied $f(R)$ theory. The aim of this study is to understand how these interactions affect the asymptotic safety scenario in pure gravity by scanning for fixed points across regions of this parameter space.

It is convenient to switch to dimensionless quantities in the following, thus, the dimensionless functions f_k and z_k are introduced as

$$f(X) = \frac{\bar{F}_k(\bar{X})}{16\pi k^d}, \quad z(X) = \frac{\bar{Z}_k(\bar{X})}{16\pi k^{d-2}} \quad (3.4)$$

The k notation has been dropped but it is implied that these functions are scale-dependent as they include renormalised couplings. The dimensionless X is $X = k^{-2}\bar{X}$.

This type of theories has been studied in the background field approximation with a spherical background S^d . Note that in this background, the Ricci and Riemann tensors are proportional to the Ricci scalar via:

$$R_{\mu\nu} = \frac{1}{d}g_{\mu\nu}R, \quad R_{\mu\nu\rho\sigma} = \frac{g_{\mu\rho}g_{\nu\sigma} - g_{\mu\sigma}g_{\nu\rho}}{d(d-1)}R \quad (3.5)$$

As a result, it is impossible to distinguish the three operators appearing in X and the running of the couplings associated to them is conflated into a single coupling per canonical mass dimension. Nonetheless, this approach is useful for probing the general behaviour of higher order couplings and understanding if relevant RG directions can arise at higher curvature-orders.

The quantum corrections for these type of models have been previously computed in the literature employing the functional renormalisation group. This thesis does not attempt to reproduce these computations and just borrows the results obtained in refs. [195, 196], to which the reader is directed for details on the derivation. The flow equation of this theory takes the general form:

$$\partial_t f + R \partial_t z + 4f + 2Rz - 4X(f' + Rz') = I_Q \quad (3.6)$$

The prime notation indicates derivative with respect to the argument X , which is omitted in this expression for clarity. The left-hand side is the classical part of the flow driven by canonical mass dimensions, while the right-hand side encodes the corrections due to quantum fluctuations of the metric. Explicit expressions for I_Q are given in Appendix A taken from refs. [195, 196, 263].

This thesis assumes that the UV fixed point of gravity admits a Taylor expansion in small curvature and makes use of the polynomial approximation, where f and z are expressed as a power series of X ,

$$f(X) = \sum_{n=0}^{\lfloor \frac{N-1}{2} \rfloor} \lambda_{2n} X^n, \quad z(X) = \sum_{n=0}^{\lfloor \frac{N-2}{2} \rfloor} \lambda_{2n+1} X^n \quad (3.7)$$

The parameter N is the order of the approximation and counts the number of curvature invariants in the action. These models contain the Einstein-Hilbert theory at $N = 2$, with the dimensionless cosmological constant $\lambda_c = k^{-4}\Lambda_K$ and Newton's coupling $g_N = k^2 G_k$ given by:

$$\lambda_c = -\frac{\lambda_0}{2\lambda_1}, \quad g_N = -\frac{1}{\lambda_1} \quad (3.8)$$

From the relations (3.5), X evaluated on a four-dimensional spherical background reduces to:

$$X|_{S^4} = \frac{12a + 3b + 2c}{12} R^2 \quad (3.9)$$

As each type of interaction yields different contributions to the flow equation, (a, b, c) appear explicitly in the expressions for I_Q given in Appendix A.

The full set of points that can be covered within this approximation is given by the surface:

$$a + \frac{b}{4} + \frac{c}{6} = X_0 \quad (3.10)$$

where $X_0 \neq 0$ is an arbitrary constant. Points lying in different surfaces intersected by rays emanating from the origin are equivalent. For example, the point $(a, b, c) = (1, 0, 0)$ describes the same theory as $(a, b, c) = (2, 0, 0)$ modulo constants multiplying the couplings. The three theories previously mentioned are identified by the following points:

$$(a, b, c) = \begin{cases} (1, 0, 0), & f(R) \\ (0, 1, 0), & f(R, Ric^2) \\ (0, 0, 1), & f(R, Riem^2) \end{cases} \quad (3.11)$$

These correspond to projections where the action is completely aligned with the direction of each of the quadratic operators mentioned above. The theory is defined for any real values of (a, b, c) for which $X_0 \neq 0$. In principle this can also include linear combinations with negative parameters, however, for simplicity, this analysis is limited to positive values only. Moreover, note that as the Weyl squared tensor vanishes in a spherical background in four dimensions, it is not possible to study actions in the Weyl basis in the present approximation.

3.2.2 Vertical and horizontal searches

This section briefly introduces some terminology that is used through the text and explains the basic idea behind the search strategy employed in this study.

In the present analysis, a vertical search will refer to a fixed point search where the parameters are kept fixed and the order of the approximation N is systematically increased. These searches are motivated by the bootstrap hypothesis, which states that higher order curvature invariants do not induce new relevant RG directions once the fixed point has stabilised. Separate vertical searches can be performed at different points in the parameter

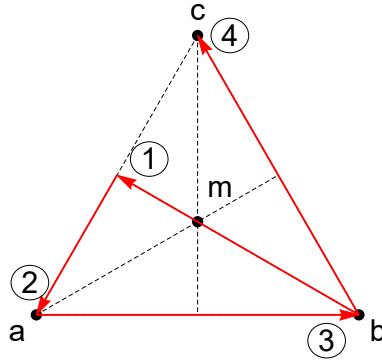


Figure 3.1: Map of the theory space of pure gravity showing the paths explored in this study. The sides of the triangle form a set of orthogonal axes in this projection. The labels correspond to: $a = (1, 0, 0)$, $b = (0, 1, 0)$, $c = (0, 0, 1)$, $m = (1, 1, 1)$.

space, such as the previously mentioned studies $f(R)$ [191, 192, 263], $f(R, Ric^2)$ [195] and $f(R, Riem^2)$ [196].

A horizontal search will refer to a fixed point search where the parameters are continuously varied while the approximation order is kept fixed. Horizontal searches can only be performed if the flow equation is a continuous function of the parameters to investigate. This category of searches includes any analysis that investigates dependence on the parameters of the theory, such as gauge fixing and metric parametrisation dependence [147–150], as well as matter content and regularisation-dependence [160, 244, 246]. Just as multiple vertical searches can be performed at different points of the parameter space, multiple horizontal searches can be performed at increasing approximation orders. This study will perform many horizontal searches in parallel at increasing approximation order.

3.2.3 Fixed point search

The parameters (a, b, c) are left open and multiple points of the theory space are explored looking for fixed points. The strategy is to start from a pre-defined point and make a small variation on (a, b, c) . Then, a fixed point of the flow is searched for at the new point in the vicinity of the original fixed point. If a solution is found, this process can be repeated many times between any two given points in the theory space.

The first step is to define the starting point and perform a vertical search to high curvature order. The initial point is chosen to be $(0, 1, 0)$ because of the high level of convergence, accuracy and stability of the fixed point found in that theory [195]. The vertical search had been previously performed up to order $N = 21$ in the literature and

has been extended to order $N = 101$ for this analysis.

The second step is to define a path in the theory space specifying the end points and how they are connected. The number of free parameters is reduced to two by demanding the normalisation:

$$a + b + c = 1 \tag{3.12}$$

A further constraint is imposed by setting one of the parameters to either a constant value or equating it to one of the other two along any path. This uniquely defines a straight line connecting two points in the \mathbb{R}^3 theory space. Note that this normalisation cuts through different surfaces, as defined in (3.10). However this does not matter, as any point in these lines can always be mapped to a reference surface $X_0 = 1$.

The present analysis consists of four such paths, connecting seven points in the theory space, the seven 3-tuples that can be formed with 0 and 1, excluding the trivial case $(0, 0, 0)$. The route chosen to sequentially visit these points is the following:

1. $(0, 1, 0) \implies (1, 1, 1) \implies (1, 0, 1)$
 2. $(1, 0, 1) \implies (1, 0, 0)$
 3. $(1, 0, 0) \implies (1, 1, 0) \implies (0, 1, 0)$
 4. $(0, 1, 0) \implies (0, 1, 1) \implies (0, 0, 1)$
- (3.13)

This is illustrated in Figure 3.1 where the circuit is drawn on a two-dimensional representation of (a, b, c) . In this projection of the parameter space, the edges of the triangle in the plot form a set of orthogonal axes. The vertices labeled as a , b , and c represent configurations $(1, 0, 0)$, $(0, 1, 0)$ and $(0, 0, 1)$, respectively, while the centre-point $(1, 1, 1)$ is labelled as m . The point $(0, 1, 0)$ is repeated as the initial trajectory bisects the triangle in order to visit all seven points. Infinitely many other parametrisations are available covering the same points and other points that have been neglected in this study.

This variation analysis is performed numerically. A dedicated computational toolkit has been developed for this purpose using the *Wolfram Mathematica* software. The paths are segmented in finite steps with small variations on (a, b, c) . At each step, a numerical root finding algorithm is employed to look for fixed points of the flow equation using as initial search value the fixed point at the previous step. The horizontal search is performed at each order from $N = 2$ to $N = 101$. As these searches are independent from each other, they were implemented in parallel and were performed in the high performance computing cluster *Apollo* from University of Sussex. Each of the four paths was explored in 201 steps at each order except at $N = 101$, where 1001 steps were used to ensure the quality of

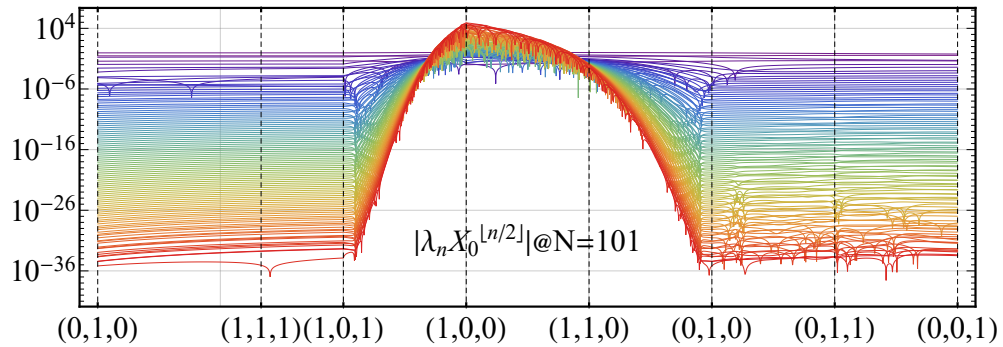


Figure 3.2: Map of normalised couplings $\lambda_n X_0^{[n/2]}$ of the fixed point in the theory space from $n = 0$ (violet) to $n = 100$ (red) at approximation order $N = 101$.

the data. For the same reason, the root search was performed demanding 100 digits of working accuracy in *Mathematica*. The critical exponents are found as the eigenvalues of the stability matrix which is evaluated numerically. As this computation becomes very demanding at high orders, critical exponents were computed every five steps. A posterior analysis of the data identified regions of large fluctuations, where critical exponents were re-calculated at each step to obtain further resolution.

One of the highlights of the present study is that up to now, only a handful of models had been explored to high orders in the polynomial approximation. The algorithms developed here allow an efficient parallelisable search of many models. At the highest approximation order, this effectively corresponds to searching for fixed points of 1001 models of pure gravity at up to 100th order in curvature.

3.3 Fixed points of quantum gravity

This section presents the results of the horizontal search starting from the $f(R, Ric^2)$ theory and discusses important characteristics of the fixed point and how they vary along the chosen paths. A separate analysis starting from the $f(R, Riem^2)$ theory is also briefly explored at the end of this section.

3.3.1 Coupling values

A meaningful comparison between different scenarios can be obtained from the normalised couplings $\lambda_n X_0^{[n/2]}$, which take into account the numerical factors appearing due to projecting the operators in the sphere. The map of normalised couplings at order $N = 101$ is shown in Figure 3.2 where the colour coding indicates the index from $n = 0$ (violet)

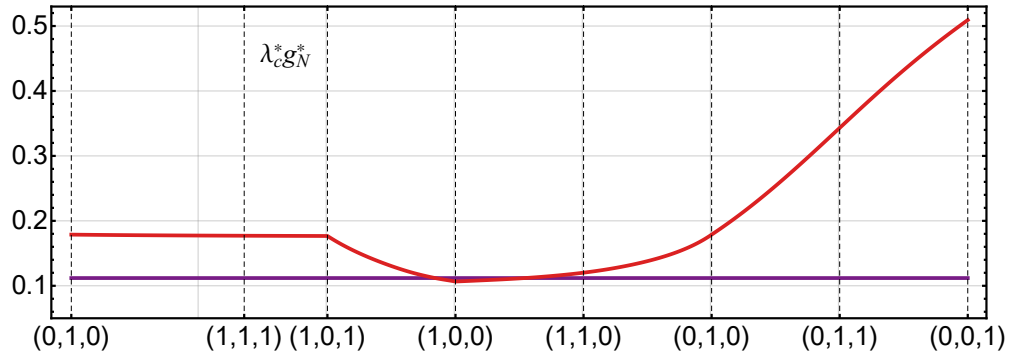


Figure 3.3: Product of the cosmological and Newton’s constant at the fixed point in the theory space in the Einstein-Hilbert approximation $N = 2$ (violet) and at order $N = 101$ (red).

to $n = 100$ (red). The most important features are discussed now. The circuit can be roughly divided into three regions according to the behaviour of couplings. The first region is composed of the first trajectory bisecting the triangular parameter space. It spans a line which enjoys great stability in the coupling values, as virtually no variation takes place. The second region encompasses the second and third trajectories, which describe lines connecting $(1,0,1)$ to $f(R)$ and then to $(0,1,0)$, respectively. These lines see a sharp increase in values as $f(R)$ is approached from either side. These first three trajectories form a closed loop, returning to the original point in $f(R, Ric^2)$. The fourth and final trajectory leaves $f(R, Ric^2)$ towards $f(R, Riem^2)$ and sees relatively little variation in the magnitude of couplings, although sign changes are present in the higher order ones.

The product of the cosmological and the Newton’s constant is shown in Figure 3.3, where the colour coding indicates the Einstein-Hilbert theory $N = 2$ (violet) and approximation order $N = 101$ (red). The individual behaviour of λ_c and g_N follows the same trend as their product so they have been omitted. The values are the smallest around $f(R)$, moderate when Ric^2 is the predominant direction and they are the largest projecting towards $Riem^2$. The numerical values at specific points in the interpolation are given in Table 3.1 and are now compared with previous results for these projections. The fixed point previously identified in $f(R)$ studies appeared with $\lambda_c^* g_N^* \approx 0.1210(0.1060)$ with a type I (II) cut-off [192, 243, 263], while the present study finds $\lambda_c^* g_N^* \approx 0.1066$ using the type II cut-off. This indicates that the solution found by the horizontal search in $f(R)$ is not exactly the same as that found by a vertical search. The solutions are continuously connected only at low orders up to $N = 11$. Above this number, the couplings approach different values in $f(R)$, with large differences in the values of higher order couplings.

Action	λ_c^*	g_N^*	$\lambda_c^* g_N^*$
(1, 0, 0)	0.11460	0.93017	0.10660
(1, 1, 0)	0.12375	0.97125	0.12019
(0, 1, 0)	0.16175	1.1054	0.17880
(0, 1, 1)	0.24275	1.4135	0.34313
(0, 0, 1)	0.29757	1.7111	0.50918
(1, 0, 1)	0.16048	1.1010	0.17669
(1, 1, 1)	0.16089	1.1024	0.17737

Table 3.1: Coupling values of gravitational fixed points at $N = 101$.

Many solutions may appear at high orders in the polynomial approximation, thus, the horizontal search, which is based on a numeric root-finding algorithm, is most likely probing the basin of attraction of other solutions than the vertical search. Similarly, previous searches found $\lambda_c^* g_N^* \approx 0.1638 - 0.2228$ for $f(R, Riem^2)$ [196], while the present study arrives at $\lambda_c^* g_N^* \approx 0.5092$, a value which is notably higher. The solutions in $f(R, Ric^2)$ and $f(R, Riem^2)$ are not connected at any order.

A transposed view is offered in Figure C.1 in Appendix C, where the plots in each panel show the couplings λ_n at different points with the index n in the horizontal axis. The spread of the data points in the plots is a qualitative indicator of the rate of convergence of the couplings. All points show a relatively small spread, except (1,0,0) and (1,1,0), which have large couplings and poorer convergence, as do (0,1,1) and (0,0,1). Not visible in the plots, the values appear with alternating sign for every other coupling, except on (1,0,0) and (1,1,0), where they show a mix of 6-8-fold sign periodicity. The sign periodicities are related to the location of poles of the flow equation in the complex plane [186], and could be understood as a general feature of solutions in $f(R)$ [192].

3.3.2 Critical behaviour

The flow in the neighbourhood of a fixed point can be described to linear order by the stability matrix evaluated at the fixed point value:

$$M_{ij} = \left. \frac{\partial \beta_i}{\partial \lambda_j} \right|_* \quad (3.14)$$

The critical exponents are given by the eigenvalues of this matrix with the opposite sign. These describe the directions and the magnitude of the RG flows surrounding the fixed

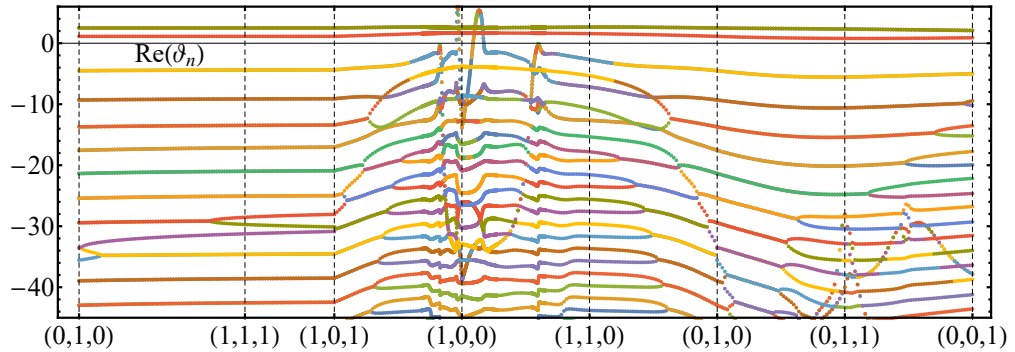


Figure 3.4: Map of the real part of the scaling dimensions associated with the fixed point in the pure gravity theory space at $N = 101$.

point. The predictability of an Asymptotically Safe theory is determined by the number of attractive UV directions, which correspond to free parameters of the theory.

The map of the eigenvalues in the interpolation is shown in Figure 3.4 at order $N = 101$, with the numerical values provided in Table 3.2. The eigenspectrum is virtually unchanged along the first trajectory with little to no variation. Around $f(R)$, in the second and third trajectories, the spectrum undergoes sudden changes as most complex irrelevant eigenvalues become real and fluctuate in value. In particular, an irrelevant eigenvalue becomes relevant and then immediately becomes irrelevant again as $f(R)$ is approached from either side. This change in sign does not signal a fixed point merger, as the solution remains real. This erratic behaviour is concerning and may indicate some issue with the procedure. At order $N = 101$, the interpolation has been performed in 1001 steps keeping 100 digits of accuracy to ensure appropriate resolution, reducing the probability of this being a numeric issue. This behaviour could also be attributed to the paths chosen and may not appear if $f(R)$ is approached from a different direction.

The third trajectory leaves this point towards $f(R, Ric^2)$ and sees the eigenspectrum stabilising again. There is a region where most of the spectrum is real before these values collapse again into complex pairs. As a representative example, the point $(2/5, 3/5, 0)$ is identified and is included in the figures in the appendix. This point has only four pairs of complex eigenvalues, shown in Table 3.3, while the remaining are real.

The relevant eigenvalues do not change much in the fourth trajectory, however the irrelevant ones undergo substantial variations reaching very large magnitudes (not pictured). These variations are different at every order and do not show a specific pattern. It would remain to be seen whether other trajectories approaching this point also display such large fluctuations.

Action	ϑ_0	ϑ_1	ϑ_2	ϑ_3	ϑ_4	ϑ_5	ϑ_6	Δ_{gap}
(1, 0, 0)	2.5501	2.5501	1.7107	-3.8316	-8.5647	-9.0935	-9.0935	2.1209
(1, 1, 0)	2.6454	2.6454	1.5731	-2.6639	-2.6639	-5.3385	-7.1712	1.0909
(0, 1, 0)	2.4963	2.4963	1.1244	-4.5080	-4.5080	-9.3085	-9.3085	3.3837
(0, 1, 1)	2.3248	2.3248	0.78993	-5.5375	-5.5375	-10.590	-10.590	4.7476
(0, 0, 1)	2.0883	2.0883	0.89829	-5.0043	-5.0043	-9.4400	-10.175	4.1060
(1, 0, 1)	2.5045	2.5045	1.1261	-4.3630	-4.3630	-9.0984	-9.0984	3.2369
(1, 1, 1)	2.5029	2.5029	1.1259	-4.3886	-4.3886	-9.1354	-9.1354	3.2626

Table 3.2: Eigenvalues of the gravitational fixed points at $N = 101$.

	ϑ_0	ϑ_1	ϑ_2	ϑ_3	ϑ_4	ϑ_5
Re	2.6512	2.6512	1.5115	-3.3389	-3.3389	-6.2289
Im	2.0758	-2.0758	0	5.0900	-5.0900	0
	ϑ_6	ϑ_7	ϑ_8	ϑ_9	ϑ_{10}	ϑ_{11}
Re	-7.8580	-7.8580	-11.887	-12.890	-12.890	-15.765
Im	4.0956	-4.0956	0	1.5521	-1.5521	0

Table 3.3: Scaling dimensions of the fixed point at $(a, b, c) = (2/5, 3/5, 0)$. This fixed point displays only four pairs of complex values, all others are real.

The transposed view of the eigenspectrum is offered in Figure C.2 where each panel shows the real part of the eigenvalues for several points at each approximation order. Apparent convergence is observed for all points with the exception of (1,0,0), (0,1,1) and (0,0,1) which show large fluctuations. Likewise, Figure C.3 offers a complementary view where the values are superimposed at each polynomial order. This view confirms, once more, the bootstrap hypothesis, as each subsequent eigenvalue is less relevant than the previous one. Moreover, they all also fall close to the classical values, indicating that anomalous scaling dimensions are small. The gap between adjacent relevant and irrelevant values is also shown in Table 3.2, where projecting on $R_{\mu\nu\rho\sigma}^2$ leads to a larger gap on average, while the projections around (1,0,0) have a smaller one. It is also on (0,1,1) and (0,0,1) that the smallest relevant scaling dimensions are closer to zero. This indicates that quantum fluctuations from $R_{\mu\nu\rho\sigma}^2$ operators shift the eigenspectrum towards more irrelevant values.

3.3.3 Convergence

There are two main aspects regarding convergence of the polynomial solutions, the first being the radius of convergence and the second being the rate of convergence. The first relates to the maximum value of the scalar curvature R for which the polynomial approximation converges, while the second relates to how fast numeric quantities stabilise. This section attempts to uncover how these quantities change with respect to the projection of the action.

The radius of convergence R_c can be computed applying the root test for power series on the coupling values at the highest order $N_{max} = 101$. This is shown in Figure 3.5 by the violet solid line, measured by the primary axis. R_c has a minimum at $f(R)$ of $R_c \approx 0.8922$ and increases away from this point reaching a global maximum of $R_c \approx 2.1912$ achieved at $(1/20, 19/20, 0)$. This point is of special interest as it also features the fastest convergence rate, as is shown next, and is included in the figures in the appendix. From this point, R_c slowly decreases to reach $R_c \approx 2.1379$ at $f(R, Riem^2)$. This directly establishes that quantum contributions from $R_{\mu\nu}^2$ and $R_{\mu\nu\rho\sigma}^2$ can expand the radius of convergence of the polynomial approximation. Note that this radius is saturated away from $f(R)$, as it extends beyond the singularity of the flow equation found at $R = 2.006$ which is independent of the choice of action.

The rate of convergence can be measured by the number of digits in the eigenspectrum that stabilise at higher orders. Two examples are shown in the panels of Figure 3.6 plotted on the negative axis taking $N = 101$ as reference value, where the data points indicate every other of the first twelve eigenvalues. Note that the behaviour changes above $N = 51$, thus, it is necessary to consider high polynomial orders to capture the true asymptotic behaviour of these solutions. The slope of the linear fit shown in the plot indicates the number of digits of accuracy gained per order. The inverse of this is the number of orders required to achieve a further digit of accuracy. The left panel shows $(1/20, 19/20, 0)$, the projection with the fastest rate of convergence, gaining a further digit every 8-10 orders. In contrast, the right panel shows $(0, 0, 1)$, where the convergence rate stagnates at a maximum of 3 digits of accuracy.

A global picture can be obtained by repeating this analysis for a sample of points along the lines of the interpolation. This is shown in Figure 3.5 as the red data points where the error bars denote the 95% confidence interval and the values are measured by the secondary axis. Large error bars indicate that the estimate is not significant, while the absence of data points indicate that no meaningful inference can be made; this occurs

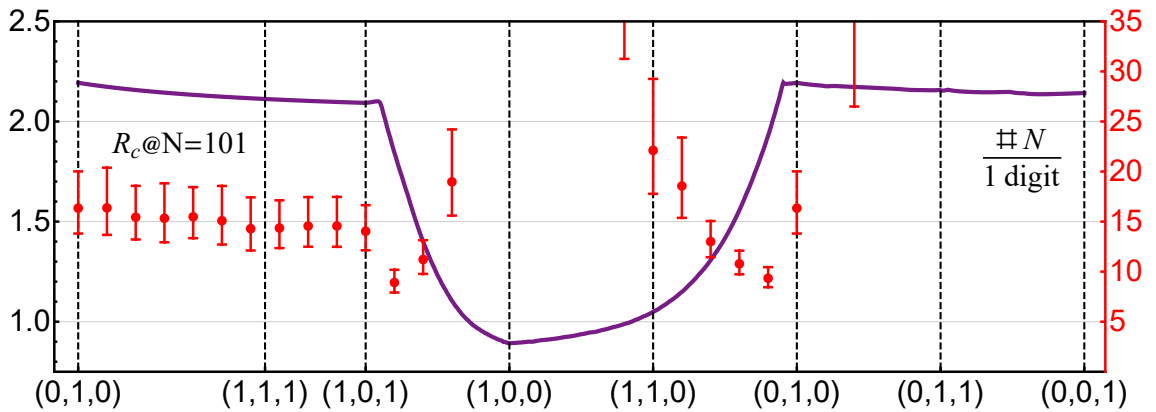


Figure 3.5: Left axis, violet solid line: radius of convergence R_c from the root test. Right axis, red data points: Rate of convergence of scaling dimensions in number of orders required to achieve a further digit of accuracy. Error bars indicate the 95% confidence interval.

when the rate of convergence is very close to zero or non-existent.

The rate of convergence does not change substantially along the first trajectory. It decreases around $(1,0,1)$ in the second line but greatly deteriorates as $f(R)$ is approached, coming to a stop altogether near this point. This indicates that the eigenvalues only converge to a finite number of digits around $f(R)$ and no further precision is gained by extending the approximation order. This can be related to the large fluctuations observed in Figure 3.4, suggesting that the results in those regions of the plot may not be reliable.

As the third trajectory approaches $f(R, Ric^2)$, the rate of convergence improves again, with $(1/20, 19/20, 0)$ reaching the fastest rate of convergence and the largest radius of convergence. Towards $f(R, Riem^2)$ in the fourth trajectory, the rate quickly deteriorates and once again comes to a stop. Thus, in these regions, the polynomial solutions may not really be approaching a true fixed point at infinite order and their validity is not guaranteed. It is intriguing to find that, although the solutions connecting $f(R, Ric^2)$ and $f(R, Riem^2)$ enjoy a large radius of convergence and share similar coupling values and eigenspectrum, it is only within a small region of the parameter space that they show a fast convergence rate.

As a final remark, these estimates were generated using vanishing boundary conditions, with higher order couplings set to zero. Optimised boundary conditions, where the higher order couplings are set to their asymptotic values at each order, may improve the situation in some cases. However, this amounts to a re-computation of the eigenspectrum at each order at each point in the interpolation. Due to time-efficiency, this has only

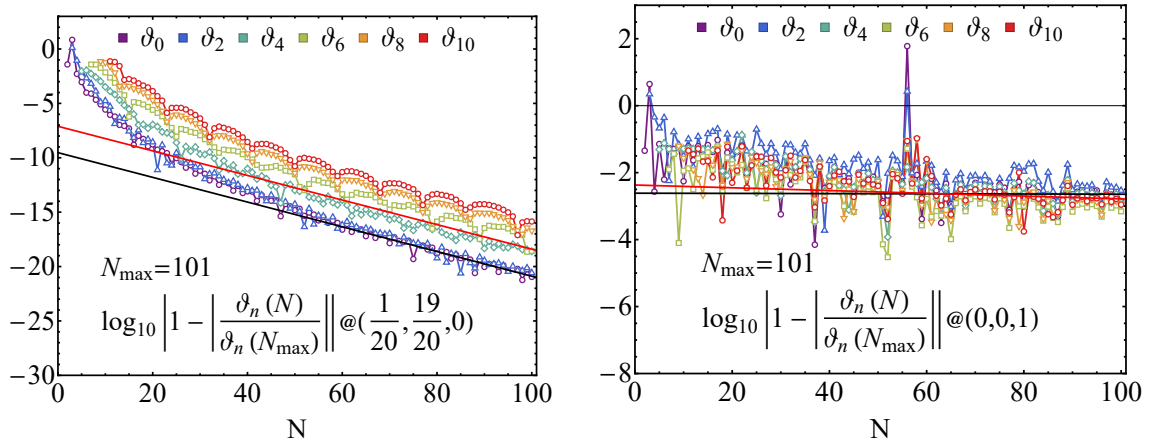


Figure 3.6: Rate of convergence of scaling dimensions for two configurations. Left: the point of fastest convergence and largest radius R_c . Right: The solution found at $f(R, Riem^2)$, where convergence has stopped. The black line indicates the linear fit of ∂_0 . The red, the average fit of the data shown for $N \geq 61$.

been performed in nine projections and the corresponding plots are shown in Figure C.7 in the appendix. In the case of $(0,0,1)$, the projection shows a small but positive rate of convergence, while for $(1,0,0)$, the picture is much worse showing no convergence at all. Thus, it is not clear whether the solutions can be trusted in these regions.

3.3.4 Action and equation of motion

The polynomial action is plotted as a function of the scalar curvature in Figure C.4 in Appendix C. The solutions take a few orders to stabilise before the lines fall on top of each other. In the plots, the first two orders have been excluded from the points $(0,1,0)$, $(1,1,1)$, $(1,0,1)$, $(1,1,0)$, the first three from $(1,0,0)$ and $(0,1,1)$ and the first four from $(0,0,1)$. Note that the curves in $(1,0,0)$, $(1,1,0)$ and $(2/5, 3/5, 0)$ show alternating tails for negative curvature, while in the other projections, the tails consistently point upwards for negative R . In the latter case, this indicates the existence of a pole for real negative values of R bounding the radius of convergence of the solution. In the former, the pole lies in the imaginary plane. All points show qualitatively similar behaviour.

The equation of motion of the action in vacuum is plotted in Figure C.5 for each projection. A solution appears at $R > 1$ in $(0,1,1)$ and $(0,0,1)$, while it is located at $R < 1$ in the other cases, except $(1,0,0)$, where no solution is visible within the radius of convergence. Thus, the $R_{\mu\nu}^2$ and $R_{\mu\nu\rho\sigma}^2$ operators can induce a de Sitter solution to appear, describing a universe with small positive curvature. Some of these solutions lie close to the radius of convergence and more refined methods can be employed to check

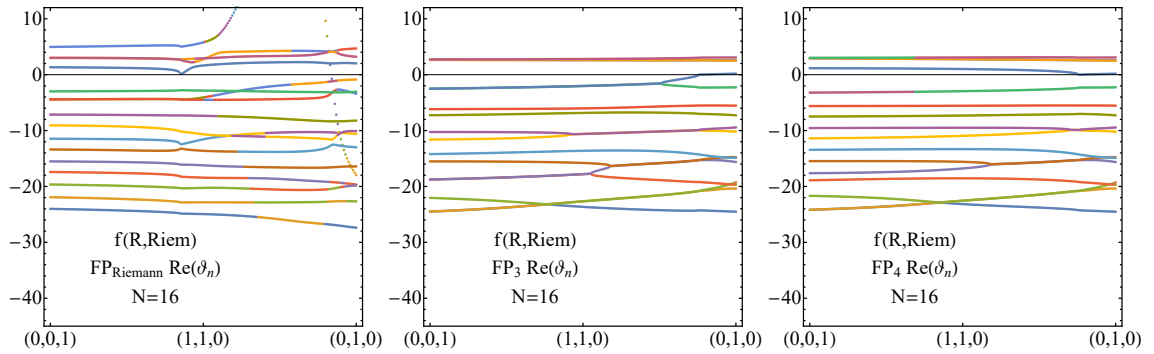


Figure 3.7: Eigenvalues of the $f(R, Riem^2)$ fixed points translated to $f(R, Ric^2)$.

whether they can be trusted.

3.3.5 Another family of solutions

The results presented so far concern solutions which are continuously connected to the original point from the $f(R, Ric^2)$ theory. The analysis can be repeated starting from other initial points and can lead to finding different results. A brief example can be considered starting from the $f(R, Riem^2)$ theory instead. Three solutions had been previously identified in that theory stable to high polynomial order [196]. None of these solutions were reached in the interpolation starting from $f(R, Ric^2)$, indicating that these fixed points are not continuously connected along the path specified here. A separate interpolation is performed starting from these solutions, labelled $FP_{Riemann}$, FP_3 and FP_4 following the naming convention of that study. This interpolation is performed only up to order $N = 16$ and consists of three paths, all starting from $(0,0,1)$ and connecting the theory to $(0,1,0)$, $(1,1,1)$ and $(1,0,0)$. The results are summarised in Table 3.4 and are explained next.

The analysis finds that the higher order couplings, which are initially small at $(0,0,1)$, increase to large magnitudes towards $f(R, Ric^2)$ and the fixed points become complex before arriving at $(0,1,0)$. The two solutions which are closer to each other, FP_3 and FP_4 merge, while $FP_{Riemann}$ annihilates with a further spurious solution. The merger between FP_3 and FP_4 can be seen in Figure 3.7 which shows the eigenvalues along this trajectory. The merger is signalled by a pair of relevant and irrelevant eigenvalues in the middle and right panel, respectively, meeting at the zero towards the end of the plots.

Along the second line, going from $(0,0,1)$ to the centre-point $(1,1,1)$, FP_3 and FP_4 remain real, while $FP_{Riemann}$ becomes complex conjugate. The third trajectory, heading towards $(1,0,0)$, finds that the higher order couplings increase in magnitude at such an accelerated rate that the root search method fails to find a solution shortly before arriving

$f(R, Riem^2)$	d_{UV}	λ_c^*	g_N^*	$\lambda_c^* g_N^*$	$c \implies b$	$c \implies m$	$c \implies a$
FP _{Riemann}	4	0.07843	2.840	0.2228	$\lambda_n \in \mathbb{C}$	$\lambda_n \in \mathbb{C}$	accelerated growth
FP ₃	3	0.1392	1.029	0.1431	$\lambda_n \in \mathbb{C}$	✓	accelerated growth
FP ₄	4	0.1484	1.103	0.1637	$\lambda_n \in \mathbb{C}$	✓	accelerated growth

Table 3.4: Fixed points of $f(R, Riem^2)$ in pure gravity, the dimensionality of their critical surface, coupling values and their fate when translated to other projections of the action. The points (a, b, c, m) are as defined in Figure 3.1.

at $f(R)$. If the solution can really be translated to that point, its couplings have a very large magnitude, $\sim 10^8$, much larger than the those found at the same point in the original interpolation. This would place harsh constraints on its radius of convergence and possibly in the numerical stability of the fixed point. A more detailed analysis with higher resolution or using different methods would be required to further explore approaching this point.

3.4 Conclusions

This study has performed a numerical search of fixed points of pure gravity. The theory space has been scanned to understand how small variations in the interactions of Ricci and Riemann tensors modify the theory. A line of stability has been identified, where the coupling values and critical exponents of the $f(R, Ric^2)$ fixed point show little variation. In this path, linear combinations of the R^2 , $R_{\mu\nu}^2$ and $R_{\mu\nu\rho\sigma}^2$ interactions are present in the action. This finding suggests that the combined effect of the three types of interactions is to further stabilise the pure gravity fixed points.

Additionally, lines of instability appear close to the $f(R)$ and $f(R, Riem^2)$ models. Close to these points, scaling dimensions have a limited convergence, stabilising to only three digits of accuracy. This could be an indication that the polynomial approximation does not converge to a physical solution of the full theory and could explain large fluctuations of the critical exponents in the vicinity of these points. Convergence can be also assessed using optimised boundary conditions finding mixed results. Other techniques, such as expanding around a different field value could shed further light on this observation.

The fixed points previously found in separate polynomial studies are not continuously connected beyond the Einstein theory through the paths explored here. Moreover, models

where the critical exponents are mostly real have been identified involving either only R^2 and $R_{\mu\nu}^2$, or R^2 and $R_{\mu\nu\rho\sigma}^2$. Thus, these interactions could play a role in lifting the degeneracy of scaling dimensions found in current models of pure gravity.

Under the premise that there is a physical fixed point of the full gravitational theory, the solutions found in approximated theory spaces can be considered as shadows of this fixed point projected on some subspace of operators. The fact that these shadows do not appear to be continuously connected is not necessarily a problem, as long as a suitable fixed point is available in the region of parameter space that can describe our universe. A *suitable* solution entails physical coupling values, reasonable (and possibly real) critical exponents and finite UV-IR RG flows connecting the theory to General Relativity in the IR. From this perspective, different families of solutions determine the UV-completion of the theory in different regions of the parameter space. These different families may be unified in some form in a more complete theory than the approximation considered here.

Chapter 4

Including Matter

4.1 Introduction

Fixed points of pure gravity have been studied in the Einstein theory and at high curvature orders. The previous chapter investigated gravitational models which feature fixed points that are numerically stable and display fast convergence in coupling values and critical exponents. Equally important is to reconcile a quantum theory of gravity with the Standard Model (SM). Investigations of the impact of matter on gravity, and vice versa, find non-trivial dynamics that suggest that the mutual influence of both sectors should be considered when building a UV-complete theory from the ground up [107, 110, 111, 161, 210, 221, 225, 227, 244].

Progress towards an asymptotically safe description of gravity has been aided by the development of the functional renormalisation group [129, 132] and its application to gravity [41, 153, 157, 158, 160, 166, 167, 169, 178, 182]. Quantum corrections to the renormalisation group equations can be computed non-perturbatively under this framework and the calculations involve evaluating the trace of functionals of differential operators. This formidable task requires advanced tools such as the heat kernel expansion [264, 265]. Alternatively, the spectral sum of these operators may also be carried out explicitly under suitable regularisation schemes that simplify the calculations. However, the latter approach leads to expressions containing non-analytical terms, which encumbers the analytic treatment of the equations. Prescriptions for removing these terms are given in the literature and call for smoothing-out the sums, albeit they introduce some degree of arbitrariness as there is not a unique way to do this [139, 174, 246]. While physical observables should be independent of regularisation details, the results may be obscured if unsuitable choices are made. It thus becomes important to have an understanding of the parametrisation dependence

introduced by this smoothing procedure to facilitate further progress towards a consistent theory of gravity and matter.

The purpose of this study is two-fold. First, to provide a comparative analysis of the heat kernel and spectral sum methods and disambiguate the freedom in regularisation in the latter approach. Second, to introduce the quantum effects of matter fields in the theory of gravity and set the stage for the subsequent chapters of this thesis, where various matter regimes will be explored. While the technique of smoothed spectral sums has been investigated in the literature, studies making use of this method have been mainly restricted to the purely gravitational setting. Namely, this technique has been used to study conformally reduced Einstein-Hilbert gravity in $d = 4$ [174], topologically massive gravity in $d = 3$ [266], Einstein-Hilbert gravity on-shell [267], global solutions of $f(R)$ in $d = 4$ [139] as well as in $d = 3$, in a conformally reduced setting [176], it has also been used in conjunction with the exponential parametrisation in $f(R)$ theories [188, 189], $f(R)$ on-shell [268], and in the vertex expansion in the Einstein-Hilbert theory [213]. However, its use has been largely absent in the matter sector, with limited studies making use of this technique so far to explore gravity-matter settings [246, 247]. This chapter provides a comparative analysis of the computations in the matter sector finding that the freedom in the smoothing procedure can result in tangible qualitative changes in the UV behaviour of the theory. To resolve this, an optimised smoothing procedure is put forward which reproduces known results from the heat kernel expansion without introducing further ambiguities.

The present analysis is organised as follows. Section 4.2 introduces the main framework for the computations and the particle content of the theory. Some concepts that were already explained in previous chapters are re-introduced for completeness. Section 4.3 comprises the bulk of this analysis and is further subdivided into three parts of two subsections each. The first part explains how the heat kernel expansion and the spectral sums techniques are used to compute the traces of the matter sector. The second part illustrates the necessity for smoothing out the sums, introduces a generalised averaging procedure and identifies an optimised average for which the results of both techniques agree. An alternative derivation of the trace is also offered, where the smoothing is performed before computing the sum. The third part briefly assesses the impact of the difference in these results in two interesting simplified settings of the parameter space. Section 4.4 further showcases the impact of this ambiguity in the smoothing procedure by performing a comparative analysis of fixed points in $f(R)$, finding that each method leads to a qualitatively

different picture of gravity in the UV. Finally, the findings are summarised and conclusions are given in section 4.5.

4.2 Functional renormalisation group

The functional renormalisation group is a framework for studying quantum field theories beyond perturbation theory. The central object is the effective average action, a scale-dependent functional which describes the theory at an integration scale k , where all field modes with momentum higher than k are integrated out. This scale is varied from the UV to the IR, resulting in a momentum-shell integration thus incorporating Wilson renormalisation. This action interpolates between the bare action S in the UV and the full quantum effective action Γ in the IR.

The flow equation of the action is an exact equation which describes the flow of all running couplings [129, 132]:

$$\partial_t \Gamma_k(\Phi) = \frac{1}{2} \text{STr} \frac{\partial_t \mathcal{R}_k^{\Phi\Phi}}{\Gamma_{\Phi\Phi}^{(2)} + \mathcal{R}_k^{\Phi\Phi}} \quad (4.1)$$

The field Φ collectively denotes all the fields in the theory. The derivation is with respect to the logarithmic energy scale $\partial_t = \partial \log k$. The super trace involves a momentum integration as well as a sum over all discrete indices, like flavour and gauge indices. A negative sign is implied for anti-commuting fields. The notation $\Gamma_{\Phi\Phi}^{(2)}$ stands for the second variation of the action with respect to the fields Φ , which is the inverse propagator of the field. This equation is free of divergences both in the UV and in the IR through the use of a regulator \mathcal{R}_k .

A common ansatz for the action is given by $f(R)$ theories. These are gravitational theories living in a subset of the space of diffeomorphic-invariant operators composed of curvature invariants that depend only on the scalar curvature.

$$\Gamma_k = \int d^d x \sqrt{g} \bar{f}_k(\bar{R}) = \int d^d x \sqrt{g} \sum_n \bar{\lambda}_n \mathcal{O}_n(\bar{R}) \quad (4.2)$$

In this expression, \bar{R} is the dimensionful Ricci curvature and $\bar{\lambda}_n$, the dimensionful running couplings. This action must be supplemented by the usual gauge fixing and ghost terms. Then, the beta function for the dimensionless running couplings is obtained by identifying the prefactors of each operator on both sides of (4.1). In a polynomial expansion in a fixed background, for example, these can be obtained in terms of dimensionless quantities as:

$$\partial_t \lambda_n = \beta_n = \frac{1}{n!} \frac{1}{V} \left. \frac{\delta^n \partial_t \Gamma_k}{\delta R^n} \right|_{R=0} \quad (4.3)$$

where the dimensionless Ricci scalar is $R = k^{-2}\bar{R}$, the dimensionless couplings are $\lambda_n = k^{d-2n}\bar{\lambda}_n$ and V is the volume of spacetime. Introducing the dimensionless function $f(R) = k^{-4}\bar{f}(R)/(16\pi)$, the flow equation for this theory has the general form:

$$\partial_t f + 4f - 2Rf' = I_Q \quad (4.4)$$

In this expression, a prime denotes derivative with respect to the argument and I_Q contains the quantum corrections due to fluctuations of the metric. The right hand side of the flow equation involves evaluating traces of differential operators in curved spacetime. The computations are manageable by embedding the theory in a maximally symmetric background, like S^d . Then, the traces can be computed and explicit expressions for I_Q are available in the literature (for details on the derivation, see refs. [157, 185, 189, 192, 194, 263]). Note also that this same flow equation is recovered by setting $(a, b, c) = (1, 0, 0)$ in the equation introduced in Chapter 3 and found in Appendix A). This class of theories has been widely studied both in the polynomial approximation, where fixed points are identified to high approximation order [157, 160, 192, 263], as well as for general $f(R)$ actions, where searches for global solutions have been performed [139, 176, 185, 186, 189].

The present study focuses on the computation of the quantum corrections due to the presence of matter fields and its introduction into the working framework is explained in this section. Gaussian matter is easily incorporated by adding the kinetic terms to the effective action:

$$\begin{aligned} \Gamma_{matter} = \int d^d x \sqrt{g} & \left(\frac{1}{2} g^{\mu\nu} \sum_i^{N_S} \partial_\mu \phi^i \partial_\nu \phi^i + \sum_i^{N_D} \bar{\psi}^i \not{D} \psi^i + \sum_i^{N_M} \frac{1}{4} g^{\mu\nu} g^{\rho\sigma} F_{\mu\rho}^i F_{\nu\sigma}^i \right. \\ & \left. + \frac{1}{2} \sum_i^{N_M} (\nabla^\mu A_\mu^i)^2 - \sum_i^{N_M} \bar{c}_i \square c_i \right) \end{aligned} \quad (4.5)$$

This action describes N_S real scalar fields ϕ , N_M Maxwell vectors A_μ with their corresponding ghosts (\bar{c}, c) and N_D Dirac spinors $(\bar{\psi}, \psi)$. All fields are massless and their interactions and wavefunction renormalisation constants are neglected for simplicity. For the spectral sums, it will be useful to further decompose the vector fields into their transverse and longitudinal parts $A_\mu = A_\mu^T + \nabla_\mu \varphi$ (although this is not strictly necessary for the computation using the heat kernel method, as results for unconstrained fields are known). The flow equation (4.4) is then modified by adding a term I_M on the right hand side which accounts for fluctuations due to matter fields. This term is then given by the following

traces:

$$\begin{aligned} \partial_t \Gamma_{k(\text{matter})} = & \frac{N_S}{2} \text{Tr}_{(0)} \frac{\partial_t \mathcal{R}_k^S}{\Gamma_{\phi\phi}^{(2)} + \mathcal{R}_k^S} - \frac{N_D}{2} \text{Tr}_{(1/2)} \frac{\partial_t \mathcal{R}_k^D}{\Gamma_{\bar{\psi}\psi}^{(2)} + \mathcal{R}_k^D} \\ & + \frac{N_M}{2} \left(\text{Tr}_{(1)} \frac{\partial_t \mathcal{R}_k^{MT}}{\Gamma_{A_\mu^T A_\mu^T}^{(2)} + \mathcal{R}_k^{MT}} + \text{Tr}'_{(0)} \frac{\partial_t \mathcal{R}_k^{ML}}{\Gamma_{\varphi\varphi}^{(2)} + \mathcal{R}_k^{ML}} - 2 \text{Tr}_{(0)} \frac{\partial_t \mathcal{R}_k^{GH}}{\Gamma_{\bar{c}c}^{(2)} + \mathcal{R}_k^{GH}} \right) \end{aligned} \quad (4.6)$$

The sub-index notation for the traces in this expression denotes the spin of the matter fields. The prime notation indicates that the constant mode of the longitudinal component of the vector fields must be excluded as it is not a degree of freedom of A_μ . Note the negative sign for the ghosts as they are anti-commuting fields. The Hessians for the matter fields are:

$$\Gamma_{\phi\phi}^{(2)} = -\nabla^2, \quad \Gamma_{\bar{\psi}\psi}^{(2)} = -\nabla^2 + \frac{R}{4}, \quad \Gamma_{A_\mu^T A_\mu^T}^{(2)} = -\nabla^2 + \frac{R}{d}, \quad \Gamma_{\varphi\varphi}^{(2)} = -\nabla^2, \quad \Gamma_{\bar{c}c}^{(2)} = -\nabla^2 \quad (4.7)$$

where the one for the fermions corresponds to the square of the Dirac operator, as implied by the factor of 1/2 in front of the N_D trace. These Hessians are second-order differential operators known as coarse-graining operators and will also be denoted as Δ in the present analysis. At this point, the regulators \mathcal{R}_k must be specified to obtain the regulated propagators. These regulators should be chosen according to the replacement $\Delta \rightarrow \Delta + R_k(\Delta)$ in the traces, where R_k is a profile function specifying how the low momentum modes are suppressed. It is convenient to use the optimised regulator as computations greatly simplify [131]:

$$R_k(\Delta_i) = (k^2 - \Delta_i) \Theta(k^2 - \Delta_i) \quad (4.8)$$

where the index runs over the matter fields and Δ_i has the general form:

$$\Delta_i = -\nabla^2 + \alpha_i \bar{R} \quad (4.9)$$

with α_i being free parameters that should be chosen accordingly for each field. Setting them all to zero specifies a type I cut-off while giving them some non-zero value defines a type II cut-off. A third type is available where the potential term is allowed to vary with the energy scale and is known as spectrally adjusted, or type III, cut-off. The correct treatment of minimally coupled spinors calls for employing a type II cut-off [161] (this regulator dependence has been recently discussed in the presence of non-minimal coupling in ref. [230]). Moreover, choosing values of α_i to cancel the potential appearing in the propagator removes unnecessary poles in the flow equation from the onset. Nonetheless,

Spin	λ_n^s	m_n^s
0	$\frac{n(n+d-1)}{d(d-1)}\bar{R}$	$\frac{(n+d-2)!(2n+d-1)}{(d-1)!n!}$
1T	$\frac{(n(n+d-1)-1)}{d(d-1)}\bar{R}$	$\frac{(n+d-3)!(2n+d-1)(n+d-1)n}{(d-2)!(n+1)!}$
1/2	$\frac{(n^2+dn+\frac{d}{4})}{d(d-1)}\bar{R}$	$2^{\lfloor d/2+1 \rfloor} \frac{(n+d-1)!}{(d-1)!n!}$

Table 4.1: The eigenspectrum of the Laplace operator $-\nabla^2$ acting on scalars, transverse vectors and spinors in S^d . The first column indicates the spin, λ_n^s indicates the eigenvalues and m_n^s , the multiplicity of eigenvalues.

these coefficients could also be chosen to overcome movable singularities of the flow equation, so retaining them as free parameters in the equations can be useful in the search of global solutions [188, 247]. In this study, the values of α are left as open parameters in the equations but note that the following are preferred values which cancel the potential term in the propagator:

$$\alpha_S = 0, \quad \alpha_D = \frac{1}{4}, \quad \alpha_{MT} = \frac{1}{d}, \quad \alpha_{ML} = 0, \quad \alpha_{GH} = 0 \quad (4.10)$$

4.3 Operator traces

There are currently two main approaches for evaluating the traces appearing on the right hand side of the flow equation (4.1). The first one is based on an early time heat kernel expansion, while the second is based on an explicit sum over the eigenspectrum of differential operators. The first two subsections in this section introduce both techniques and reproduce results known in the literature. The next two put forward a novel parametrisation for the smoothing procedure in the spectral sums, as well as an alternative formulation where the smoothing is performed before taking the sum. This section ends with a comparison of results obtained in both approaches and their impact on the gravitational flow equation.

4.3.1 Heat kernel

The trace over a function of a differential operator can be written as the sum of the function evaluated on the eigenvalues λ_n of that operator:

$$\text{Tr } W(\Delta) = \sum_n W(\lambda_n) \quad (4.11)$$

where the lower and upper boundaries of the summation are defined by the eigenspectrum of the operator. Note that if there are negative or zero modes, these should be subtracted on an ad hoc basis. In the case at hand, it is useful to recall the eigenspectrum of the Laplace operator in a spherical background S^d , given in Table 4.1. To obtain the eigenvalues of the coarse-graining operator Δ , it is enough to add the endomorphism term to the values displayed in the table. Degenerate eigenvalues are counted separately in the sum (4.11).

It is convenient to introduce the Laplace anti-transform \overline{W} , so the trace can be written as:

$$\mathrm{Tr} W(\Delta) = \int_0^\infty dt \sum_n e^{-t\lambda_n^{(\Delta)}} \overline{W}(t) \quad (4.12)$$

where $\lambda_n^{(\Delta)}$ are the eigenvalues of the differential operator Δ . The sum over n can be identified as the trace of the heat kernel of the operator Δ :

$$\mathrm{Tr} K_\Delta(t) = \sum_n e^{-t\lambda_n^{(\Delta)}} \quad (4.13)$$

The heat kernel satisfies the heat equation, which smooths out the profile of an initial scalar field distribution over time. In this context, small values of t correspond to high energies or small curvature. In the early time heat kernel expansion, this trace is:

$$\mathrm{Tr} K_\Delta(t) = \frac{1}{(4\pi t)^{d/2}} (B_0(\Delta) + tB_2(\Delta) + t^2B_4(\Delta) + \dots) \quad (4.14)$$

where $B_{2n}(\Delta)$ are the heat kernel coefficients. Then, the trace of W is given by the series expansion:

$$\mathrm{Tr} W(\Delta) = \frac{1}{(4\pi)^{d/2}} (Q_{d/2}(W)B_0(\Delta) + Q_{d/2-1}(W)B_2(\Delta) + \dots) \quad (4.15)$$

The heat kernel coefficients depend on the spin on the field that is being acted on by the differential operator and the background. Computing these coefficients in curved backgrounds is a complicated task, see refs. [264,265] for computations in general backgrounds and [269] for the spherical background. Meanwhile, the integration on t is encoded in the functionals $Q_n(W)$, which carry the dependence on the profile function used to regulate the traces:

$$Q_n(W) = \frac{(-1)^k}{\Gamma(n+1)} \int_0^\infty dz z^{n+k-1} W^{(k)}(z) \quad (4.16)$$

with k an arbitrary positive integer such that $n+k > 0$. Using the optimised regulator (4.8) results in the particularly simple expression:

$$Q_n(W) = \begin{cases} \frac{2}{n!} k^{2n}, & n \geq 0 \\ 0, & n < 0 \end{cases} \quad (4.17)$$

Spin	B_0	B_2	B_4
0	1	$\left(\frac{1}{6} - \alpha_S\right) \bar{R}$	$\left(\frac{29}{2160} - \frac{1}{6}\alpha_S + \frac{1}{2}\alpha_S^2\right) \bar{R}^2$
1T	3	$\left(\frac{1}{4} - 3\alpha_M\right) \bar{R}$	$\left(-\frac{7}{1400} - \frac{1}{4}\alpha_M + \frac{3}{2}\alpha_M^2\right) \bar{R}^2$
1/2	4	$\left(\frac{2}{3} - 4\alpha_D\right) \bar{R}$	$\left(\frac{101}{2160} - \frac{2}{3}\alpha_D + 2\alpha_D^2\right) \bar{R}^2$

Table 4.2: The first three heat kernel coefficients for the operator $\Delta_i = -\nabla^2 + \alpha_i \bar{R}$ acting on the fields $i = \{\phi, A_\mu^T, \psi\}$ in S^4 . Note the spin-1 field is a transverse vector.

This directly implies that the series expansion is truncated at a finite order, such that only a finite number of heat kernel coefficients is needed. The coefficients relevant to the present study are given in Table 4.2.

The matter traces (4.6) in four dimensions and in terms of dimensionless quantities are then given by:

$$\text{Tr}_S = \frac{N_S}{32\pi^2} \frac{1}{1 - \alpha_S R} \left(1 + \left(\frac{1}{3} - 2\alpha_S\right) R + \left(\frac{29}{1080} - \frac{1}{3}\alpha_S + \alpha_S^2\right) R^2 \right) \quad (4.18)$$

$$\begin{aligned} \text{Tr}_M = & \frac{N_M}{32\pi^2} \left[\frac{1}{1 + \left(\frac{1}{4} - \alpha_T\right) R} \left(3 + \left(\frac{1}{2} - 6\alpha_T\right) R + \left(-\frac{7}{720} - \frac{1}{2}\alpha_T + 3\alpha_T^2\right) R^2 \right) \right. \\ & + \frac{1}{1 - \alpha_L R} \left(1 + \left(\frac{1}{3} - 2\alpha_L\right) R + \left(-\frac{61}{1080} - \frac{1}{3}\alpha_L + \alpha_L^2\right) R^2 \right) \\ & \left. - \frac{2}{1 - \alpha_{GH} R} \left(1 + \left(\frac{1}{3} - 2\alpha_{GH}\right) R + \left(\frac{29}{1080} - \frac{1}{3}\alpha_{GH} + \alpha_{GH}^2\right) R^2 \right) \right] \quad (4.19) \end{aligned}$$

$$\text{Tr}_D = -\frac{N_D}{32\pi^2} \frac{1}{1 + \left(\frac{1}{4} - \alpha_D\right) R} \left(4 + \left(\frac{4}{3} - 8\alpha_D\right) R + \left(\frac{101}{1080} - \frac{4}{3}\alpha_D + 4\alpha_D^2\right) R^2 \right) \quad (4.20)$$

where the volume element has already been extracted. These coefficients agree with the one-loop matter divergences computed in the literature [24, 27].

4.3.2 Spectral sum

The traces can also be computed by taking a direct sum of the function evaluated at the operators' eigenvalues, i.e. computing the spectral sum of the differential operator Δ . In the general case, this implies an infinite sum over the eigenmodes, the sum can then be approximated using numerical methods. Using the optimised regulator (4.8), however, the sum simplifies and can be carried out analytically:

$$\frac{1}{2} \text{Tr} \frac{\partial_t \mathcal{R}_k(\Delta)}{\Gamma^{(2)} + \mathcal{R}_k(\Delta)} = \sum_{n=n_{min}}^{\infty} m_n \Theta(k^2 - \bar{\lambda}_n) = \sum_{n=n_{min}}^{n_{max}} m_n \quad (4.21)$$

In this expression, $\bar{\lambda}_n$ refers to the dimensionful eigenvalues of the coarse-graining operator Δ , and m_n , to the multiplicities of these eigenvalues. In the last equality, the upper boundary of the sum is made finite by enforcing the step function. The maximum mode that contributes to the sum is found by setting $\bar{\lambda}_{n_{max}}^{(s)} = k^2$ and solving for n_{max} . Using the expressions given in Table 4.1, the maximum modes for matter fields of each spin are:

$$n_{max}^{(0)}(\alpha) = \frac{d-1}{2} \left(-1 + \sqrt{1 + \frac{4d}{(d-1)} \left(\frac{k^2}{\bar{R}} - \alpha \right)} \right) \quad (4.22)$$

$$n_{max}^{(1/2)}(\alpha) = -\frac{d}{2} + \sqrt{d(d-1) \left(\frac{k^2}{\bar{R}} + \frac{1}{4} - \alpha \right)} \quad (4.23)$$

$$n_{max}^{(1)}(\alpha) = \frac{d-1}{2} \left(-1 + \sqrt{1 + \frac{4d}{(d-1)} \left(\frac{k^2}{\bar{R}} + \frac{1}{d(d-1)} - \alpha \right)} \right) \quad (4.24)$$

In the sum, one should now replace $n_{max} \rightarrow \lfloor n_{max} \rfloor$, as n is a discrete variable. After computing the sums, this would give rise to a staircase profile as the sums are a function of R , which introduces non-analyticities in the flow equation. There are some prescriptions for treating these non-analyticities but before addressing this issue, the sums will be computed explicitly.

Consider the sum where the Heaviside theta function appears explicitly:

$$S_1 = \sum_{n=n_{min}}^{\infty} m_n \Theta(k^2 - \bar{\lambda}_n) \quad (4.25)$$

This is the form of the sum used in refs. [161, 266]. No closed expression is available for this infinite sum but it must be finite since the step function will cut off contributions from eigenmodes above k^2 . Nonetheless, it can be approximated with the Euler-Maclaurin approximation of the sum:

$$\sum_{i=a}^b f(i) = \int_a^b dx f(x) + \frac{1}{2} (f(a) + f(b)) + \sum_{k=2}^n \frac{B_k}{k!} \left(f^{(k-1)}(x) \right) \Big|_a^b - r \quad (4.26)$$

This formula consists of an integral, the mean value of the function between the boundaries, a sum of derivatives and a remainder r . In this expression, n is the order of the approximation. Applying this formula to S_1 results in the general form:

$$\begin{aligned} S_1 &= \int_{n_{min}}^{\infty} dn m_n \Theta(k^2 - \bar{\lambda}_n) \\ &+ \frac{1}{2} (m_{n_{min}} \Theta(k^2 - \bar{\lambda}_{n_{min}}) + m_{\infty} \Theta(k^2 - \bar{\lambda}_{\infty})) \\ &+ \sum_{i=2}^j \frac{B_i}{i!} \left(\frac{\partial^{(i-1)}}{(\partial n)^{(i-1)}} (m_n \Theta(k^2 - \bar{\lambda}_n)) \right) \Big|_{n_{min}}^{\infty} - r \end{aligned} \quad (4.27)$$

The step function brings down the upper limit of the integration to $\lfloor n_{max} \rfloor$. The second term evaluated at $\bar{\lambda}_{\infty}$ vanishes for $\bar{\lambda}_{\infty} > k^2$. The only non-zero contributions in the last

term are those where the derivatives act on m_n evaluated at the lower boundary. As the multiplicities m_n are a polynomial of degree $d - 1$, the sum of derivatives is finite with upper limit $j = d$. Replacing $[n_{max}]$ for the dummy variable x , the sums in four dimensions result in:

$$\text{Tr}_S = \frac{N_S R^2}{384\pi^2} \frac{1}{1 - \alpha_S R} \left(\frac{1}{12} (1 + x_S)^2 (2 + x_S)^2 - \frac{1}{90} \right) \quad (4.28)$$

$$\begin{aligned} \text{Tr}_M = & \frac{N_M R^2}{384\pi^2} \left[\frac{1}{1 + (\frac{1}{4} - \alpha_T) R} \left(\frac{1}{4} x_T^2 (3 + x_T)^2 - \frac{11}{30} \right) \right. \\ & + \frac{1}{1 - \alpha_L R} \left((1 + x_L)^2 (2 + x_L)^2 - \frac{91}{90} \right) \\ & \left. - \frac{2}{1 - \alpha_{GH} R} \left(\frac{1}{12} (1 + x_{GH})^2 (2 + x_{GH})^2 - \frac{1}{90} \right) \right] \end{aligned} \quad (4.29)$$

$$\text{Tr}_D = \frac{N_D R^2}{384\pi^2} \frac{1}{1 + (\frac{1}{4} - \alpha_D) R} \left(\frac{1}{3} (1 + x_D)^2 (3 + x_D)^2 - \frac{19}{90} \right) \quad (4.30)$$

where the volume element has also been factored out for comparison. The sub-index in x indicates which values of $[n_{max}]$ and α_i should be used, with S denoting the scalars, T and L the transverse and longitudinal modes of the vectors, respectively, GH the ghosts and D the Dirac fermions. Working with this expression is still difficult as the discrete nature of n_{max} gives rise to a staircase profile in the flow equation. This is just a reflection of the non-analytic nature of the regulator employed and the fact that the eigenspectrum of the Laplacian is discrete on spheres, therefore the low energy modes in the integration are suppressed on a discrete basis. Thus, one may dare to drop the requirement of taking the floor of n_{max} . This allows to expand the products of x and, remarkably, the coefficients turn out just right to cancel the square roots contained in n_{max} . Moreover, the expressions exactly coincide with those obtained from the early time heat kernel expansion, given in (4.18)-(4.20). Note, however, that the sums are only exact for discrete n ; relaxing this restriction is already an approximation.

For comparison, consider now the last equality in (4.21) where the step function is enforced and the upper limit of the sum is finite:

$$S_2 = \sum_{n=n_{min}}^{[n_{max}]} m_n \quad (4.31)$$

This is the form of the sum used in refs. [139, 174, 176, 189, 246, 267]. Using once more the Euler-Maclaurin formula, the sum can be approximated as:

$$S_2 = \int_{n_{min}}^{[n_{max}]} dn m_n + \frac{1}{2} (m_{n_{min}} + m_{[n_{max}]}) + \sum_{k=2}^d \frac{B_k}{k!} \left(m_n^{(k-1)} \right) \Big|_{n_{min}}^{[n_{max}]} - r \quad (4.32)$$

While the integration term will yield the same result as in S_1 , it is clear that the evaluation at $\lfloor n_{max} \rfloor$ in the other terms does not vanish, resulting in:

$$\text{Tr}_S = \frac{N_S R^2}{384\pi^2} \frac{1}{1 - \alpha_S R} \frac{1}{12} (1 + x_S)(2 + x_S)^2(3 + x_S) \quad (4.33)$$

$$\begin{aligned} \text{Tr}_M = \frac{N_M R^2}{384\pi^2} & \left[\frac{1}{1 + (\frac{1}{4} - \alpha_T) R} \frac{1}{R} \frac{1}{4} x_T(1 + x_T)(3 + x_T)(4 + x_T) \right. \\ & + \frac{1}{1 - \alpha_L R} \left(\frac{1}{12} (1 + x_L)(2 + x_L)^2(3 + x_L) - 1 \right) \\ & \left. - \frac{2}{1 - \alpha_{GH} R} \frac{1}{12} (1 + x_{GH})(2 + x_{GH})^2(3 + x_{GH}) \right] \end{aligned} \quad (4.34)$$

$$\text{Tr}_D = \frac{N_D R^2}{384\pi^2} \frac{1}{1 + (\frac{1}{4} - \alpha_D) R} \frac{1}{R} \frac{1}{3} (1 + x_D)(2 + x_D)(3 + x_D)(4 + x_D) \quad (4.35)$$

Comparing this with (4.28)-(4.30) it is evident that the Euler-Maclaurin approximation returns different results for S_1 and S_2 .

A more straightforward variant to compute (4.31) is to notice that, on S^d , the multiplicities of the eigenvalues are relatively simple polynomial expressions, such that the sums can be performed exactly. Denoting once again the upper limit as x , the exact summed expressions are:

$$S_2^{(0)} = \frac{(2n + d)\Gamma(n + d)}{\Gamma(d + 1)\Gamma(n + 1)} = \frac{2n + d}{d!} \prod_{x=0}^{d-2} (n + d - x - 1) \quad (4.36)$$

$$\begin{aligned} S_2^{(1T)} &= 1 + \frac{(2n + d)(n(n + d) - 1)\Gamma(n + d - 1)}{d\Gamma(d - 1)\Gamma(n + 2)} \\ &= 1 + \frac{(d - 1)(2n + d)(n(n + d) - 1)}{\Gamma(d + 1)} \prod_{x=1}^{d-4} (n + d - x - 2) \end{aligned} \quad (4.37)$$

$$S_2^{(1/2)} = \frac{2^{\lfloor 1+d/2 \rfloor} \Gamma(n + d + 1)}{\Gamma(d + 1)\Gamma(n + 1)} = \frac{2^{\lfloor 1+d/2 \rfloor}}{d!} \prod_{x=0}^{d-1} (n + d - x) \quad (4.38)$$

Evaluating at $d = 4$ exactly reproduces (4.33)-(4.35). This directly implies that the Euler-Maclaurin approximation is exact for S_2 .

4.3.3 Smoothed sums and optimum average

The expressions obtained from S_2 are exact, however, they suffer from an important drawback which makes them somewhat cumbersome to work with. Even if the discreteness condition on n is dropped, the upper limit n_{max} contains square roots that give rise to non-analytic terms in the flow equation. While in S_1 the coefficients turn out exactly such that the square roots cancelled, this is not the case for S_2 . There are several prescriptions to treat these terms, which can be generalised to an artificial smoothing of the sum by taking the mean of two sums with different upper limits.

Consider shifting the maximum mode of the sum by a constant parameter p , then n_{max} is schematically written as:

$$n_{max} = a + p + \sqrt{b} \quad (4.39)$$

where the values of a and b can be read-off from (4.22)-(4.24). Taking the average of two sums with shift parameters p_1 and p_2 would result in a trace which, in four dimensions for scalars and vectors, contains terms of the form:

$$(4 + 2a + p_1 + p_2) c b^{1/2} + (4 + 2a + p_1 + p_2) b^{3/2} \quad (4.40)$$

where the overall factor counting the number of fields has been omitted and c is a function of a , p_1 and p_2 . For the case of fermions, the 4 is replaced by a 5. The prefactor in front of the non-analytic terms $b^{1/2}$ and $b^{3/2}$ defines a condition on the shift parameters such that these terms vanish. For any type of matter field in four dimensions, this is:

$$p_1 + p_2 = -1 \quad (4.41)$$

This prescription gets rid of the non-analytic terms for any values of p_1 and p_2 obeying this relation. For example, the values $p_1 = 0$ and $p_2 = -1$ correspond to the so-called averaged interpolation, which is the mean of two sums up to the two highest modes allowed. Similarly, setting $p_1 = p_2 = -1/2$ results in the middle of the staircase interpolation. This is a single sum where the upper limit is set between the two highest modes.

Note, however, that infinitely many other interpolations are available. Moreover, the terms that remain in the trace depend on the product $p_1 p_2$, not on their sum. Therefore, results will not coincide for different choices of these parameters. This means that the averaged interpolation does not yield the same results as the middle of the staircase one, as was already pointed out in ref. [246].

Setting $p_2 = -1 - p_1$, renaming $p_1 \rightarrow p$, and introducing the auxiliary function:

$$\begin{aligned} \tau(\alpha, x, y, z) = & \left(1 - \left(-\frac{1}{4} + \alpha\right) R\right) \left(1 - \left(-\frac{1}{6} + \alpha\right) R\right) + \left(\frac{x}{6} + \frac{p(1+p)}{2}\right) R \\ & + \frac{1}{72} \left(y + \frac{(z + 13 - 72\alpha + p(1+p))p(1+p)}{2}\right) R^2 \end{aligned} \quad (4.42)$$

the matter traces (4.6) employing this method are:

$$\text{Tr}_S = \frac{N_S}{32\pi^2} \frac{\tau(\alpha_S, 0, 0, 0)}{1 - \alpha_S R} \quad (4.43)$$

$$\begin{aligned} \text{Tr}_M = & \frac{N_M}{32\pi^2} \left[\frac{3 \tau(\alpha_T, -1, 2(-1 + 6\alpha_T), 2)}{1 + \left(\frac{1}{4} - \alpha_T\right) R} \right. \\ & \left. + \frac{\tau(\alpha_L, 0, -6, 0)}{1 - \alpha_L R} - \frac{2 \tau(\alpha_{GH}, 0, 0, 0)}{1 - \alpha_{GH} R} \right] \end{aligned} \quad (4.44)$$

$$\text{Tr}_D = -\frac{N_D}{32\pi^2} \frac{4 \tau(\alpha_D, 0, 0, 3)}{1 + \left(\frac{1}{4} - \alpha_D\right) R} \quad (4.45)$$

Note that the first term in (4.42) can cancel with the denominator in the trace of the transverse part of the vectors and the fermions. The averaged interpolation is recovered by setting $p = 0$ in these expressions. In that case, all R^2 terms vanish for the fermions, so the trace contains only a constant and a linear term in this interpolation. Furthermore, in that case, the linear term of the fermions then appears with a factor of one half compared to the heat kernel result (4.30). This means that the averaged interpolation cuts down the number of spinors in the system by half. The impact of this effective reduction in the number of fermionic degrees of freedom is explored in the subsequent sections.

By direct comparison with (4.28)-(4.30), there is a value of p for which the linear term matches with the results from the heat kernel expansion, which are considered reliable in the small curvature regime. Denoting this shift as $p_{\text{opt.}}$:

$$p_{\text{opt.}} = -1/2 \pm \sqrt{1/12} \quad (4.46)$$

for all three types of matter fields and independent of the endomorphism parameters. If, instead, it is the quadratic terms that are matched, the corresponding expressions $p_{\text{opt.}}^{(2)}$ depend on α_i :

$$(p_{\text{opt.}}^{(2)})_S = \frac{1}{2} \left(-1 \pm \sqrt{-25 + 144\alpha_S \pm 2\sqrt{\frac{2407}{15} + 96\alpha_S(-19 + 54\alpha_S)}} \right) \quad (4.47)$$

$$(p_{\text{opt.}}^{(2)})_M = \frac{1}{2} \left(-1 \pm \left[-(31 + 72(2\alpha_{GH} - \alpha_L - 3\alpha_T)) \right. \right. \\ \left. \left. \pm 2\sqrt{2} \left(-\frac{79}{15} + 4(-3(2\alpha_{GH} - \alpha_L - 3\alpha_T)) \right. \right. \right. \\ \left. \left. \left. + 2(4 + 9(2\alpha_{GH} - \alpha_L - 3\alpha_T))^2 \right) \right]^{1/2} \right)^{1/2} \quad (4.48)$$

$$(p_{\text{opt.}}^{(2)})_D = \frac{1}{2} \left(-1 \pm \sqrt{-31 + 144\alpha_D \pm 2\sqrt{\frac{3682}{15} + 48\alpha_D(-47 + 108\alpha_D)}} \right) \quad (4.49)$$

The sign notation implies that all four combinations of positive and negative signs are allowed in these expressions. However, setting the cut-off parameters to those given in (4.10), two of these four shifts come out only slightly different to $p_{\text{opt.}}^{(1)}$. The differences between these two matchings are:

$$(p_{\text{opt.}}^{(2)})_S - p_{\text{opt.}} = \pm 0.00075865 \quad (4.50)$$

$$(p_{\text{opt.}}^{(2)})_M - p_{\text{opt.}} = \pm 0.00085026 \quad (4.51)$$

$$(p_{\text{opt.}}^{(2)})_D - p_{\text{opt.}} = \pm 0.00414955 \quad (4.52)$$

This means that matching at order R produces a very close but imperfect match at order R^2 and vice versa. In general, there is no reason why a single parameter would be able

to match both orders, so it is interesting that these values come out very close. In this calculation, the same shift was assumed for the transverse, longitudinal and ghost part of the sum counting N_M . Although each sum could in principle be performed with different shifts, this does not significantly reduce the error.

The dependence of the traces on the shift parameter p is illustrated in Figure 4.1 for all three types of fields. The plots show the relative deviation of the averaged traces (4.43)-(4.45) with respect to eqs. (4.28)-(4.30) as a function of p . The short-dashed vertical lines indicate the optimum interpolation (4.46), the long-dashed lines, the averaged interpolation and the dot-dashed line, the middle of the staircase one. The range stops at $p = -1$ as further values correspond to averages between modes below and above the IR scale k . The left panel shows the coefficient of the traces linear in R which appears explicitly in the beta function of Newton's constant (see eqs. (4.70)-(4.72)). The averaged interpolation, $p = \{-1, 0\}$ inflates the number of scalars while underestimating the number of vectors and fermions, while the opposite is true in the middle of the staircase, $p = -1/2$. Two special points can be distinguished where all coefficients match simultaneously, these correspond to the optimum interpolation (4.46). The middle and the right panels show the traces for fixed values of dimensionless scalar curvature. The three traces do not match simultaneously but the error is so small that it is imperceptible in the plots. There is always at least a pair of points where the traces can be matched for any value of R . For large R , this point does not differ too much from (4.46), while for vanishing curvature all expressions automatically agree. Note that at large curvature (right panel), the averaged interpolation stops seeing fermions compared to the heat kernel. This is because, as was previously mentioned, the R^2 term vanishes in this case.

A third shift parameter could be introduced by averaging over three sums instead of two. This would naively make it possible to match both linear and quadratic orders exactly. However, in that case, eq. (4.41) which sets the conditions to remove the squared root terms gets replaced by two restrictions, thus, there is still only one free parameter.

Finally, it is briefly noted that there is another method to match the averaged interpolation with the heat kernel expansion at linear order. However, while the smoothing procedure outlined in this section amounts to shifting the maximum mode n_{max} , the alternative matching procedure corresponds to introducing a shift in the eigenvalues $\bar{\lambda}_n$ without shifting the eigenfunctions. It's not immediately clear that such a shift can have a physical justification. Alternatively, this shift can be absorbed in the value of α_i , although this could introduce artificial poles in the flow equation.

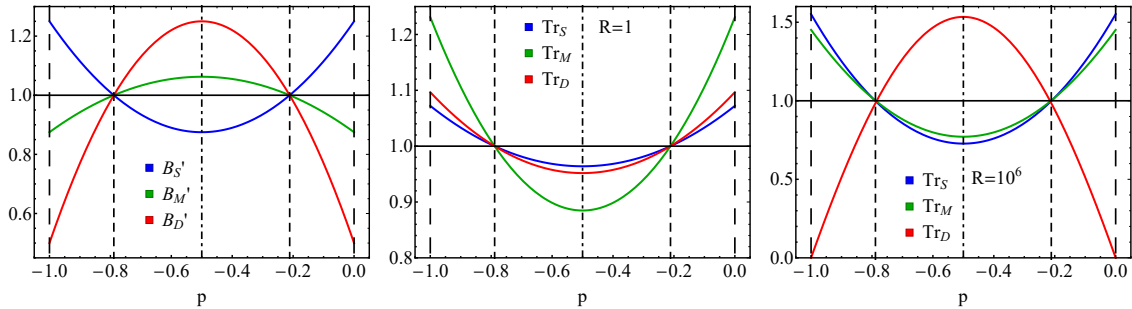


Figure 4.1: Coefficients of the matter multiplicities appearing in the traces of each field as a function of p . Left: matter coefficient linear in R only. Middle and right: sum of coefficients representing the total contribution of each matter field evaluated at $R = 1$ and $R = 10^6$, respectively. Curves are normalised to heat kernel values. For any value of R , there are always two points where the traces can be matched with the results from the heat kernel expansion. The endomorphism parameters are fixed to eq. (4.10). The middle of the staircase interpolation corresponds to $p = -1/2$, the averaged interpolation to $p = \{-1, 0\}$, the optimised interpolation to $p = p_{\text{opt.}} \approx \{-0.79, -0.21\}$.

4.3.4 Smooth step function

The sums S_1 (4.25) and S_2 (4.31) should be equivalent, thus there is evidently an incongruence in the results. Direct comparison between (4.28)-(4.30) and (4.33)-(4.35) shows that this has nothing to do with the smoothing procedure, nor with whether n_{max} is discrete or continuous. The difference seems to stem on whether the Heaviside theta function is evaluated prior to or after using the Euler-Maclaurin formula. Consider, instead, using a smeared-out version of it:

$$\Theta(k^2 - \bar{\lambda}_n) = \lim_{c \rightarrow \infty} \frac{1}{1 + e^{-c(1 - \bar{\lambda}_n/k^2)}}, \quad \text{for } c > 0, \bar{\lambda}_n \geq 0 \quad (4.53)$$

where c is a free parameter that controls the sharpness of the function. This can be understood as performing a smoothing *before* evaluating the sum, instead of after. In this case, the sum becomes:

$$S_3 = \sum_{n=n_{\text{min}}}^{\infty} \left(m_n \lim_{c \rightarrow \infty} \frac{1}{1 + e^{-c(1 - \bar{\lambda}_n/k^2)}} \right) \quad (4.54)$$

The point of doing this is to first compute the sum to obtain a result for general c and only take the limit $c \rightarrow \infty$ at the last step. The infinite sum is itself a limit, so it must be checked beforehand whether the limits $c \rightarrow \infty$ and $n \rightarrow \infty$ can be exchanged. Rewriting n_m in terms of the eigenvalues, the argument of the sum is a function of only one variable:

$$\frac{m(n)}{1 + e^{-c(1 - \bar{\lambda}_n/k^2)}} = \frac{(1 + 6(\frac{\lambda_n}{R} - \alpha)) \sqrt{1 + \frac{16}{3}(\frac{\lambda_n}{R} + \alpha)}}{1 + e^{-c(1 - \lambda_n)}} = f_c(\lambda_n) \quad (4.55)$$

written in terms of the dimensionless eigenvalues $\lambda_n = k^{-2}\bar{\lambda}_n$ and dimensionless Ricci scalar $R = k^{-2}\bar{R}$. Taking n as a continuous variable, the product vanishes for large n independent on the order of the limits:

$$\lim_{n \rightarrow \infty} \lim_{c \rightarrow \infty} f_c(\lambda_n) = \lim_{c \rightarrow \infty} \lim_{n \rightarrow \infty} f_c(\lambda_n) = 0 \quad (4.56)$$

Since there are no singularities and the functions are continuous in the whole domain, the limits can be exchanged. The sum can then be computed using the Euler-Maclaurin formula:

$$\begin{aligned} S_3 &= \lim_{c \rightarrow \infty} \left[\int_{n_{min}}^{\infty} m(n) \frac{1}{1 + e^{-c(1-\bar{\lambda}(n)/k^2)}} \right. \\ &\quad \left. + \frac{1}{2} \left(m(n_{min}) \frac{1}{1 + e^{-c(1-\bar{\lambda}(n_{min})/k^2)}} + m(\infty) \frac{1}{1 + e^{-c(1-\bar{\lambda}(\infty)/k^2)}} \right) \right] \\ &\quad + \sum_{i=2}^j \frac{B_i}{i!} \left[\left(m(n) \frac{1}{1 + e^{-c(1-\bar{\lambda}(n)/k^2)}} \right)^{(i-1)} \right] \Big|_{n_{min}}^{\infty} - r \end{aligned} \quad (4.57)$$

where $\bar{\lambda}(n) = \bar{\lambda}_n$ is implied. Note that the sum in the derivatives is unbounded from above, as the continuous step function is infinitely differentiable. The mean, derivatives and integral term are computed next, in that order.

The smooth step function vanishes as $\bar{\lambda}_n \rightarrow \bar{\lambda}_{\infty}$ in the mean term as long as $c > 0$. The evaluation at the lower boundary yields the multiplicity of the lowest mode times a constant. In the limit $c \rightarrow \infty$, this constant weight takes a value of one as long as $\bar{\lambda}(n_{min}) < k^2$ (including any endomorphism). Thus, the mean term yields the same result as that obtained from S_1 .

In the third term, the derivatives are acting on a product of functions, so a binomial series appears:

$$d^n(f \cdot g) = \sum_{k=0}^n \binom{n}{k} \cdot d^{n-k}(f) \cdot d^k(g) \quad (4.58)$$

Consider first the terms where at least one derivative acts on the continuous step function. By the chain rule, the derivative is:

$$\frac{d}{dn} \left(\frac{1}{1 + e^{-c(1-\bar{\lambda}(n)/k^2)}} \right) = \frac{\partial}{\partial \bar{\lambda}} \left(\frac{1}{1 + e^{-c(1-\bar{\lambda}(n)/k^2)}} \right) \frac{d\bar{\lambda}}{dn} \quad (4.59)$$

The first derivative of the smeared-out step function with respect to the argument is a smeared-out delta function centred around the inflection point k^2 . Further derivatives result in multiple smeared-out delta functions, each centred around the inflection points of their antiderivative, and overall centred around k^2 . Meanwhile, $\bar{\lambda}(n)$ is a polynomial of order two, so its derivatives are of linear and constant order. Since the boundary points

are taken to be far away from k^2 , the delta functions vanish exponentially and thus the whole product vanishes at the boundaries. The higher order derivatives decay faster, thus, the infinitely many derivatives arising from these terms can be neglected. This holds as long as $c > 0$ and $\bar{\lambda}(n_{min}) < k^2$ for rapidly decaying smooth delta functions. Therefore, the only terms that can be non-zero are those where the derivative is acting on $m(n)$ only. This is exactly as with sum S_1 , so this term matches as well.

The computation of the integral term is more easily performed in the domain of the eigenvalues $\lambda(n)$:

$$\text{Int.} = \lim_{c \rightarrow \infty} \int_{\lambda(n_{min})}^{\lambda(\infty)} d\lambda \frac{m(n)}{\lambda'(n)} \frac{1}{1 + e^{-c(1-\lambda(n))}} \quad (4.60)$$

For notational simplicity the dimensionless eigenvalues are used in the following calculations. The Jacobian of this coordinate transformation, $m(n)/\lambda'(n)$, depends on the specific trace under consideration. From now on the case of scalar fields is taken as an example but it is straightforward to reproduce the calculation for all the other fields. For scalar fields in d dimensions, this is:

$$\int_{\lambda(n_{min})}^{\lambda(\infty)} d\lambda \frac{d}{\Gamma(d-1)R} \left(\prod_{x=0}^{d-3} (n+d-2-x) \right) \frac{1}{1 + e^{-c(1-\lambda(n))}} \quad (4.61)$$

this expression still depends on n which must be replaced by $\lambda(n)$. This can be done by inserting n_{max} (4.22) with the substitution $k^2/\bar{R} \rightarrow \lambda/R$. Setting $d = 4$, the integral simplifies to:

$$\begin{aligned} \text{Int.} &= \int_{\lambda(n_{min})}^{\lambda(\infty)} d\lambda \left(\frac{4(1-6\alpha)}{R} + \frac{24\lambda}{R^2} \right) \frac{1}{1 + e^{-c(1-\lambda)}} \\ &= \left[-4(1-6\alpha) \frac{\log(1 + e^{c(1-\lambda)})}{c} \frac{1}{R} \right. \\ &\quad \left. + 24 \left(-\lambda \frac{\log(1 + e^{c(1-\lambda)})}{c} + \frac{\text{Li}_2(-e^{c(1-\lambda)})}{c^2} \right) \frac{1}{R^2} \right] \Big|_{\lambda(n_{min})}^{\lambda(\infty)} \end{aligned} \quad (4.62)$$

where $\text{Li}_s(z)$ is the polylogarithm of order s with argument z :

$$\text{Li}_s(z) = \sum_{j=1}^{\infty} \frac{z^j}{j^s} \quad (4.63)$$

and can also be defined iteratively as:

$$\text{Li}_{s+1}(z) = \int_0^z \frac{\text{Li}_s(t)}{t} dt \quad (4.64)$$

with base value:

$$\text{Li}_1(z) = -\log(1-z) \quad (4.65)$$

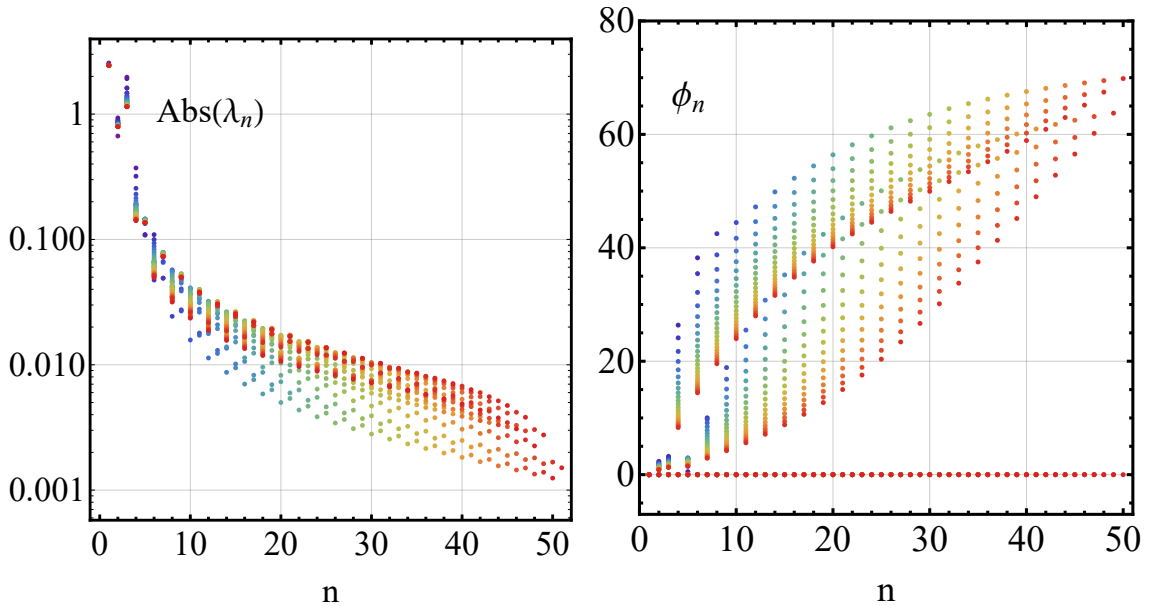


Figure 4.2: Coupling values λ_n for each polynomial approximation of the fixed points in the averaged interpolation from $N = 2$ (violet) up to $N = 51$ (red). Left: Real part of the couplings. Note that all couplings are positive. Right: Complex phase of couplings. The imaginary part is non-zero only for even values of N .

Evaluating at the upper and lower boundary points and then applying the limit $c \rightarrow \infty$ yields:

$$\text{Int.} = \frac{4(3 + (1 - 3\alpha)R)(1 - \alpha R)}{R^2} \quad (4.66)$$

for $\alpha\bar{R}/k^2 < 1$. Extracting the volume element, this exactly matches the result obtained from the infinite sum S_1 .

Thus, the sum S_3 (4.54) which employs a smooth version of the step function matches term by term with S_1 (4.25) and with the results obtained from the heat kernel expansion. Had any other regulator been employed from the start, the spectral sum would necessarily be infinite, such that a truncation of the sum would not be possible and a procedure similar to S_3 would have to be adopted, besides from numerical evaluation methods. Thus, any other regulator profile $R_k(z)$ which vanishes for $z/k^2 \gg 1$ and tends to a constant for $z \rightarrow 0$ should reproduce qualitatively similar results. It would be interesting to verify then, that both techniques match for an analytic profile, such as the exponential regulator, not only for matter fields but in the gravitational sector as well. This is left for future work.

4.3.5 Comparison of matter bounds I. Large N

The coefficient counting the number of matter fields can have a tangible impact in the search for gravitational fixed points. Given that spin-1/2 fields are the most abundant of matter fields in the SM, and in virtually all BSM extensions up to date, it becomes of paramount importance to get the count right or at least get an understanding of the error in the counting methods. As an example, consider the large N matter limit, where gravitational quantum corrections can be neglected at leading order and the flow equation of $f(R)$ in the sphere reduces to [225]:

$$\partial_t f + 4f - 2Rf' = I_M N \quad (4.67)$$

where all matter field multiplicities are proportional to a large positive number N and the matter quantum term contains only up to quadratic contributions in curvature with the optimised regulator:

$$I_M = A + B R + C R^2 \quad (4.68)$$

This setting supports a matter-generated fixed point, with the value of Newton's constant determined as:

$$g_N^* \propto -\frac{1}{B N} \quad (4.69)$$

In this limit, the sign is directly dictated by the coefficient B which depends on the matter content. Using a type II cut-off with the values given in (4.10), the B coefficient for each approximation is:

$$B_{HK} = 4N_S - 16N_M + 8N_D \quad (4.70)$$

$$B_{AVG} = 5N_S - 14N_M + 4N_D \quad (4.71)$$

$$B_{MID} = \frac{7}{2}N_S - 17N_M + 10N_D \quad (4.72)$$

The first line is the result of the heat kernel expansion, which coincides with S_1 and S_3 . The second and third line result from smoothing the spectral sum S_2 using the averaged and the middle of the staircase interpolation, respectively. As explained in section 4.3.3, the averaged interpolation cuts down the effective number of fermions by half compared to the heat kernel result. Meanwhile, the middle of the staircase overestimates this number. In a scenario with N SMs, (4.70) supports only 44 of the 45 Weyl fermions in the SM, while (4.71) can comfortably account for 74 before g_N becomes negative. Moreover, the destabilising effect of fermions is not limited to the Einstein-Hilbert theory

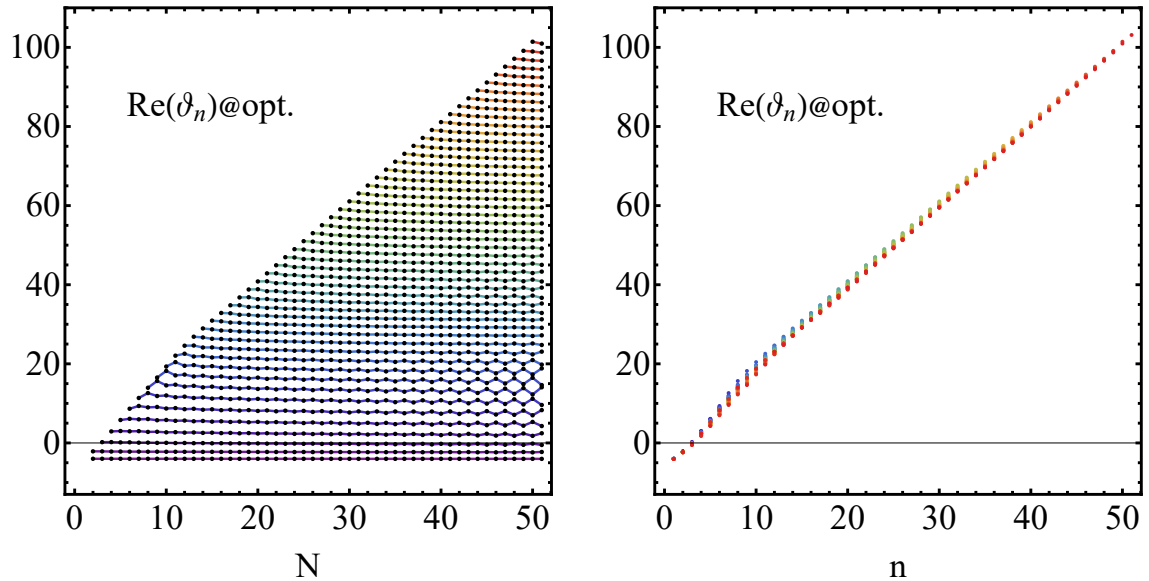


Figure 4.3: Eigenspectrum of fixed point in the averaged interpolation with optimised boundary conditions. All values are real.

and also affects fixed points of models with higher curvature interactions. In Chapter 5, fixed points with the SM content will be discussed, however, a large number of fermions may represent a challenge when BSM scenarios are discussed. Thus, the expression for the matter contributions to the running of Newton’s coupling, B , can qualitatively modify the behaviour of the gravitational theory in the UV. If the effective number of fermion degrees of freedom is greatly underestimated, this could lead to finding solutions of the flow which may not otherwise be physical.

4.3.6 Comparison of matter bounds II. Supersymmetry

As a final remark, note that both expressions agree to quadratic order in supersymmetric (SUSY) matter configurations. In SUSY, the number of physical fermionic and bosonic degrees of freedom is the same, thus there is a relation between the matter field multiplicities:

$$2N_W^{(SUSY)} = N_S^{(SUSY)} + 2N_M \quad (4.73)$$

Where the total number of fields including superpartners is included in the count. In terms of the fields present below the SUSY scale (i.e. without superpartners), these counts are:

$$N_W^{(SUSY)} = N_W + N_S + N_M, \quad N_S^{(SUSY)} = 2(N_W + N_S) \quad (4.74)$$

where N_W are two-component Weyl spinors, N_S counts real scalar degrees of freedom and N_M , the number of gauge bosons. This restriction can be used to eliminate the multiplicity

$\text{Tr}_{\text{matter}}$	d_{UV}	N_{max}	Bound	λ_c	g_N	$\lambda_c g_N$
H.K.	2	17	$\vartheta_0 \gg 4$	-5.6867	4.3739	-24.873
	3	15	$\lambda_n \in \mathbb{C}$	-19.365	16.367	-316.96
Avg.Int.	2	13	$\lambda_n \in \mathbb{C}$	-2.9845	2.3607	-7.0455
	3	> 51	$\lambda_n \in \mathbb{C}$ for N even	-1.5428	1.2607	-1.9450

Table 4.3: Fixed point search in polynomial $f(R)$ with SM matter in two scenarios. The columns indicate the technique employed to compute the matter quantum corrections, the dimensionality of the UV critical surface, the maximum approximation order, the nature of the boundary and the values of couplings.

of the scalar fields from the equations. Thus, in SUSY-like matter configurations (still neglecting matter interactions), the matter traces expanded around vanishing curvature are:

$$\begin{aligned} \text{Tr}_{\text{matter}}^{(S_1)} = & \left(6(1 + 4(\alpha_D - \alpha_S))(N_S + N_W) \right. \\ & \left. - 3(3 - 4(2\alpha_D - 3\alpha_T + 2\alpha_{GH} - \alpha_L))N_M \right) R \\ & + \frac{1}{12} (7(N_S + N_W) - 9N_M) R^2 + \dots \end{aligned} \quad (4.75)$$

$$\begin{aligned} \text{Tr}_{\text{matter}}^{(S_2)} = & \left(6(1 + 4(\alpha_D - \alpha_S))(N_S + N_W) \right. \\ & \left. - 3(3 - 4(2\alpha_D - 3\alpha_T + 2\alpha_{GH} - \alpha_L))N_M \right) R \\ & + \frac{1}{2} ((2 + 5(1 + p)p)(N_S + N_W) - (2 + 3(1 + p)p)N_M) R^2 + \dots \end{aligned} \quad (4.76)$$

The first expression corresponds to the heat kernel expansion and the second one, to the averaged spectral sum. The constant term cancels in this setting. The linear term in the trace using S_2 comes out independent of the shift parameter and thus matches with S_1 for any value of p and α_i . The quadratic term matches in both sums only for the optimised average (4.46) and for any α_i . The trace finishes at this order if the endomorphism parameters are set to the values given in eq. (4.10). Otherwise, the higher-order terms depend on p . Inserting the optimum value yields a near-perfect match between both expressions at order R^3 , just as in (4.50)-(4.52). In this setting, the averaged interpolation maximises the count of all three types of matter fields in the quadratic coefficient, while the middle of the staircase one minimises it.

	$N = 51$	$N = 50$	$N = 49$	$N = 48$	$N = 47$
λ_0	-2.4476	$-2.4476 - 0.0003I$	-2.4476	$-2.4477 - 0.0003I$	-2.4476
λ_1	-0.7932	$-0.7942 - 0.0118I$	-0.7937	$-0.7948 - 0.0122I$	-0.7943
λ_2	1.1444	$1.1464 + 0.0255I$	1.1458	$1.1479 + 0.0263I$	1.1473
λ_3	0.1411	$0.1419 + 0.0207I$	0.1419	$0.1428 + 0.0215I$	0.1428
λ_4	0.1359	$0.1358 + 0.0035I$	0.1360	$0.1360 + 0.0036I$	0.1362
λ_5	0.0495	$0.0500 + 0.0129I$	0.0500	$0.0506 + 0.0134I$	0.0505

Table 4.4: Coupling values of a fixed point solution in polynomial $f(R)$ with SM matter using the averaged interpolation of the spectral sum in the matter traces.

4.4 Gravitational fixed points with matter

Results using the explicit spectral sums in the purely gravitational setting are reported to be qualitatively independent of how the smoothing is performed [139, 176, 189]. However, these differences can have a significant influence in the matter sector, particularly due to the abundance of fermions in the SM. This has been first investigated in [246] making use of the averaged interpolation. However, the focus of that study was to show that qualitatively different solutions can appear using a type I or type II cut-off and that these families of fixed points are not necessarily connected. The present study fixes the cut-off as a control variable and provides a comparative analysis of fixed points found using different expressions for the matter traces.

Two scenarios are investigated, taking either the heat kernel results (4.28)-(4.30) or the spectral sum results with the averaged interpolation (4.43)-(4.45). To isolate the effect of the matter sector, a mixed approach is adopted, where the traces of the gravitational sector are obtained from the heat kernel expansion in both scenarios. The results for the gravitational traces are borrowed from refs. [192, 263], where the linear parametrisation of the metric is employed in a spherical background. Explicit expressions for this equation are provided in Appendix B. A mix of type I and type II cut-off is employed for the gravitational sector to remove technical singularities arising from unphysical degrees of freedom (see ref. [263] for details), while a type II cut-off with the parameters given in eq. (4.10) is fixed for the matter sector. The polynomial approximation is employed where the dimensionless action takes the form:

$$f(R) = \sum_{n=0}^{N-1} \lambda_n R^n \quad (4.77)$$

	$N = 51$	$N = 50$	$N = 49$	$N = 48$	$N = 47$
ϑ_0	4.0261	$4.0254 - 0.0056I$	4.0259	$4.0252 - 0.0058I$	4.0256
ϑ_1	2.2770	$2.2767 + 0.0013I$	2.2771	$2.2769 + 0.0014I$	2.2773
ϑ_2	0.5124	$0.5134 + 0.0002I$	0.5134	$0.5145 - 0.0001I$	0.5146
ϑ_3	-2.4479	$-2.4415 + 0.1296I$	-2.4418	$-2.4348 + 0.1345I$	-2.4350
ϑ_4	-4.2739	$-4.2685 + 0.0677I$	-4.2705	$-4.2649 + 0.0698I$	-4.2669
ϑ_5	-8.3011	$-8.2786 + 0.3104I$	-8.2849	$-8.2609 + 0.3207I$	-8.2676

Table 4.5: Eigenvalues of a fixed point solution in polynomial $f(R)$ with SM matter using the averaged interpolation of the spectral sum in the matter traces.

The bootstrap search strategy is adopted where higher derivative operators are gradually incorporated in a step by step basis. In the following, N refers to the order of the truncation and denotes the number of operators included in the action, with the initial value $N = 2$ being the Einstein-Hilbert action. The search finds three spurious solutions and one fixed point candidate only when the averaged interpolation spectral sum is employed. The findings are summarised in Table 4.3 and briefly explained next.

The first scenario using the heat kernel expansion yields two solutions at low polynomial order, with a two and three-dimensional UV critical surface each. However, they disappear when the truncation order is increased. The first one develops very large relevant and irrelevant eigenvalues of order $\vartheta \sim 100$ at $N > 17$. These values have large fluctuations and do not show signs of convergence at higher orders. The second one is strongly coupled, becomes complex for even-numbered truncations starting at $N = 8$ and completely disappears into the complex plane, developing large scaling dimensions at $N > 15$.

The second scenario using the averaged interpolation of the spectral sum also features two solutions, with two and three relevant directions each. The first one becomes complex at $N > 13$. The second one becomes complex for even-numbered truncations starting at $N = 6$ while it remains real for odd-numbered ones. The absolute value of the couplings and their phase in the complex plane are shown in Figure 4.2. For any single coupling, the phase becomes smaller at higher-order approximations. All couplings come out positive in their real values, except λ_0 and λ_1 , yielding the values reported in Tables 4.3 and 4.4.

The scaling dimensions of this solution show relative stability towards higher orders. The eigenvalues of the stability matrix are all real for odd N and for all N when optimised

boundary conditions are used. This means that the couplings whose running is neglected at each order are set to their asymptotic values, instead of vanishing values. This is shown in Figure 4.3, where the two panels offer transposed views of the eigenspectrum. Notice the fluctuations in the values towards higher orders, which seem to indicate that even and odd-numbered truncations converge separately. Numerical values for the most relevant eigenvalues are reported in Table 4.5 with vanishing boundary conditions.

The rate of convergence can be assessed by measuring how many approximation orders are necessary to gain a further digit of accuracy in the eigenspectrum. This is shown in the negative axis in Figure 4.4 with vanishing boundary conditions. In the figure, the black line indicates the linear fit for data points of the most relevant eigenvalue, while the red line indicates the mean linear fit of all data points shown for $N \geq 31$. The plot shows that the most relevant eigenvalue has stabilised to four digits of accuracy at order $N = 51$. Note that the curves become steeper above $N > 40$, slightly deviating from the fit. This would naively suggest a faster rate of convergence, however, this behaviour is expected to change as values continue adjusting at higher orders. In other words, higher orders would need to be computed to verify if this is the asymptotic behaviour. For now, ignoring this deviation provides a more conservative estimate. On average, a further digit of accuracy is gained every 15.1 – 23.3 orders. Convergence is slower with optimised boundary conditions (not pictured), mostly due to the even and odd orders tending to different asymptotic values. Keeping only the odd-numbered points, the rate comes out as 19.9 – 34.7 orders for a further digit.

The ratio test predicts a radius of convergence of $R_C \approx 1.0306$ for the polynomial approximation at $N = 51$. Since all higher-order couplings have a positive sign, convergence is probably bounded by a pole in the real axis, indicating this is most likely not a global solution. Remembering that the fixed singularity of this flow equation occurs at $R \approx 2.006$ [186], the bound found here must be arising from a movable singularity. The equation of motion admits no solutions whatsoever within the radius of convergence of the approximation.

4.5 Conclusions

The freedom in performing the smoothing of the spectral sum through an average has been parametrised by the introduction of a shift parameter p . This averaging defines how the modes near the cut-off scale are being regulated and can be understood as an indirect form of regulator dependence. In other words, this process is a further step of

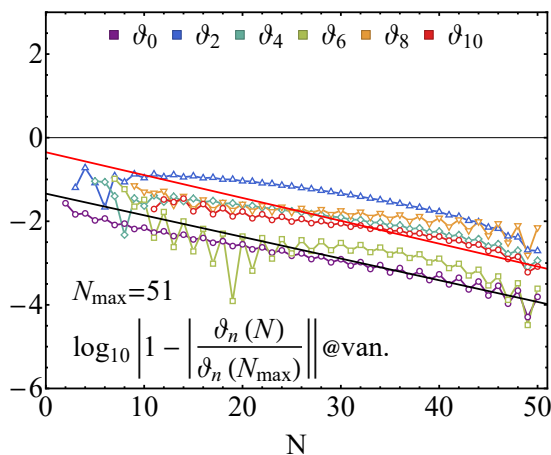


Figure 4.4: Rate of convergence of the eigenspectrum with vanishing boundary conditions. The negative vertical axis indicates the number of digits of accuracy. The black line indicates the linear fit of the most relevant eigenvalue. The red line, the mean fit of the curves shown. The fits are performed for $N \geq 31$.

regularisation. However, it is not guaranteed that an arbitrary choice of p produces flows that stem from any suitably-chosen regulator R_k . All the possible choices are depicted in Figure 4.1 as a function of p , this is one of the main results of this study. The averaged and the middle of the staircase interpolation can now be recognised as the boundaries of the allowed region, being the cases that introduce the largest deviation compared to the heat kernel results. The former minimises the counting of spin-1 and spin-1/2 fields and maximises that of spin-0 fields, while the latter takes the opposite role. The preferred optimised average described by p_{opt} is identified as the one inducing the least deviation in the flows, resulting in a perfect match with the heat kernel expansion at linear order and a near-perfect match at quadratic order for all matter fields. This is the only choice which has been proven to date to reproduce known results in the small curvature regime beyond constant order without introducing further ambiguities. Although the heat kernel is an asymptotic expansion in even dimensions with unknown radius of convergence, it is expected to be reliable for small curvature values. Note this is a general argument that applies beyond the treatment of matter fields, i.e., the optimised average can also be adopted for the computation of traces in the gravitational sector.

The case study of fixed points in polynomial $f(R)$ with SM matter in section 4.4 makes a further point on the tangible impact of understanding how the matter fields are counted. This is another main result of the study and provides a prime example of a theory without stationary solutions which develops a candidate fixed point as the effective number of fermions is effectively reduced by the averaging procedure. Although the identified

solution has some non-standard features compared to findings from other polynomial $f(R)$ studies [157, 160, 192], a fluctuating behaviour between even and odd approximations is not unheard of in the literature, see refs. [139, 176]. As previously explained, this numerical instability may very well be due to using flawed boundary conditions to close the system of equations and the behaviour can improve using more accurate non-vanishing conditions. Convergence in the eigenspectrum towards higher truncation orders is favourable up to the orders checked, although with a limited radius of convergence in the scalar curvature. This clearly illustrates the parallels between smoothing and regulator dependence as solutions may appear or disappear depending on these choices.

Replacing the Heaviside theta distribution by a smooth step function sheds some light on the ambiguity encountered in the computation of the traces. Then, the sum extends to infinity and the result of the spectral sum ultimately matches with the heat kernel expansion. In that case, the averaging step is exchanged for the smoothing of the regulator. This is indeed how the computation would have to be performed for any analytic regulator that vanishes asymptotically. Then, it is expected that both techniques coincide for small curvature if any smooth profile function is employed.

This study has aimed to clarify some of the ambiguities around the use of the spectral sum technique and has taken the matter sector as a simple example. It is left for future work to verify that the value of the optimum shift p_{opt} remains the same for the traces in the gravitational sector and to evaluate the impact of other choices in the traces of spin-2 fields. Similarly, this analysis has adopted many simplifications and it would be desirable to see that results generalise to other settings such as, computations in a general number of dimensions, in other curved backgrounds or considering matter anomalous dimensions or non-minimal matter interactions which would explicitly modify the matter traces.

Chapter 5

Quantum gravity and the Standard Model

5.1 Introduction

The previous chapters have established two key aspects of asymptotic safety in quantum gravity. On the one hand, interactions of the Ricci and Riemann and tensors squared lead to quantum corrections to the flow equation that can stabilise fixed points to very high curvature-order. This leads to improved numerical stability and faster convergence where these operators appear simultaneously. On the other hand, matter quantum fluctuations can destabilise the gravitational fixed point, with the SM field content potentially annihilating the solution beyond the Einstein theory. Thus, quantum matter fluctuations impose constraints on the field content for asymptotic safety of a given gravitational theory. However, the converse point of view is also true. For a given matter content, constraints are imposed on the type of gravitational models that allow a stable UV fixed point. Then, it seems conceivable that models which allow for higher order interactions of the aforementioned tensors could stabilise a fixed point with SM matter at high curvature-order.

This study builds on the results of the previous two chapters and performs a fixed point search to high curvature-order in the presence of the SM field content. The theory space is the one introduced in Chapter 3, which incorporates $(R^2, R_{\mu\nu}^2, R_{\mu\nu\rho\sigma}^2)$ operators to high polynomial order. The quantum matter fluctuations were determined in Chapter 4 and modify the flow equation leading to potentially new families of solutions. The seven points of the theory space previously identified are revisited, finding that only three of them host UV fixed points stable up to 100th curvature-order.

The analysis is organised in the following manner. Section 5.2 introduces the theoretical

framework combining the results from the previous chapters. The important equations are re-introduced for completeness and convenience of the reader. The parameter space is described and the search strategy is explained. Section 5.3 presents the results of the analysis and discusses characteristics of the fixed points such as coupling values, critical exponents, relevant directions, convergence and RG flows. Section 5.4 considers some Beyond the Standard Model scenarios and outlines general properties of solutions found in those settings. Finally, Section 5.5 summarises the results and gives the conclusions.

5.2 Methodology

5.2.1 Renormalisation Group

The gravitational theory considered in this study is of the same form as that already introduced in Chapter 3. Additionally, minimally coupled matter is added as in Chapter 4. The matter action is not repeated in here but it is recalled that N_S is the field multiplicity of the real scalar fields, N_M that of the Maxwell bosons and N_D , of Dirac spinors. The flow equation of this theory takes the following form:

$$\partial_t f + R \partial_t z + 4f + 2Rz - 4X(f' + Rz') = I_Q + I_M \quad (5.1)$$

Explicit expressions for the metric quantum corrections I_Q are given in Appendix A, while expressions for the matter contributions I_M are computed using the heat kernel method as introduced in Chapter 4. The functions $f(X)$ and $z(X)$ contain the gravitational interactions including the Einstein theory and higher derivative operators. Their argument is the linear combination of the three independent quadratic curvature invariants

$$X = aR^2 + bR_{\mu\nu}^2 + cR_{\mu\nu\rho\sigma}^2 \quad (5.2)$$

These are the three basis operators which define the theory space in this model. The coefficients (a, b, c) are free parameters that define the projection of the action on this subspace of operators. Unlike in the analysis of Chapter 4, the introduction of the Ricci and Riemann tensors leads to further quantum corrections in the flow equation. Thus, I_Q is a function of (a, b, c) , such that different fixed point can be found in different points of the theory space.

The polynomial approximation is assumed in this analysis, where f and z are written as a power series of X ,

$$f(X) = \sum_{n=0}^{\lfloor \frac{N-1}{2} \rfloor} \lambda_{2n} X^n, \quad z(X) = \sum_{n=0}^{\lfloor \frac{N-2}{2} \rfloor} \lambda_{2n+1} X^n \quad (5.3)$$

The upper limit of the sums is such that N counts the total number of operators in the action and is referred to as the approximation order. The approximation of order N retains the running of the first N couplings while ignoring the rest. The result is a system of coupled differential-algebraic equations which can be solved to find beta functions and fixed points. In this analysis, the system is closed by setting the higher order couplings to a constant vanishing value. The dimensionless cosmological constant $\lambda_c = k^{-4}\Lambda_c$ and Newton's coupling $g_N = k^2 G_N$ are related to the leading order couplings at $N = 2$ via:

$$\lambda_c = -\frac{\lambda_0}{2\lambda_1}, \quad g_N = -\frac{1}{\lambda_1} \quad (5.4)$$

5.2.2 Search strategy

This section outlines the strategy for the fixed point search. First, the free parameters of the theory are fixed. Then, the methodology of the search is explained.

Besides from the approximation order N , the flow equation has six free parameters, three describing the projection of the gravitational action (a, b, c) and three specifying the matter content (N_S, N_M, N_D) . The bulk of this analysis considers SM matter only, i.e. $(N_S, N_M, N_D) = (4, 12, 45/2)$. The methods developed for this study can be used to explore other matter configurations and Section 5.4 will briefly explore some scenarios beyond the Standard Model.

The theory space, and hence the interactions present in the action, is defined by (a, b, c) . For simplicity, only seven projections are studied in here:

$$(a, b, c) \in \{(1, 0, 0), (0, 1, 0), (0, 0, 1), (1, 1, 0), (1, 0, 1), (0, 1, 1), (1, 1, 1)\} \quad (5.5)$$

The first line projects the theory on actions where only one of $(R^2, R_{\mu\nu}^2, R_{\mu\nu\rho\sigma}^2)$ appears, while the second line, on actions where two or three of these operators appear simultaneously. Note that it is not the absolute value of these parameters that is important but their relative ratios, i.e. $(a, b, c) = (x a, x b, x c)$ with x a real constant. The seven scenarios chosen here serve only as representative examples, many other points are available as was already explained in Chapter 3. Lastly, recall that the squared of the Weyl tensor vanishes on the four-dimensional background. Therefore, it is not possible to study gravitational actions with curvature invariants on the Weyl basis in this approach.

The fixed point search adopts the bootstrap hypothesis. This assumes that canonical mass dimension is a valid ordering principle for higher derivative-order operators and justifies a curvature expansion in the theory space. Moreover, the hypothesis claims that

introducing higher order operators in the action induces new RG directions which are only less and less relevant. Thus, the number of relevant RG directions of a UV fixed point is finite. This is where the power of asymptotic safety lies, even though the theory may include infinitely many interactions, there is a only finite number of free parameters, ensuring the theory remains predictive. In general, this hypothesis may not be true as anomalous scaling dimensions are non-zero at an interacting fixed point and may turn canonically irrelevant operators into relevant ones in the UV. Thus, this hypothesis must be confirmed a posteriori.

Under this assumption, the analysis starts at an initial approximation order N and looks for stationary points of the flow. This results in a system of algebraic equations coupled at all orders. To close the system of equations within the theory, the higher order couplings whose running is neglected can be set to an arbitrary constant value, chosen to be zero in this analysis. The resulting system of equations can then be solved numerically.

5.2.3 Computational algorithms

The fixed point search makes use of further algorithms developed in the computational toolkit mentioned in Chapter 3. Vertical searches are performed at each of the seven points. Starting at an initial order N_i , a numeric root finding algorithm solves the flow equation at each order using 100 digits of working precision in *Wolfram Mathematica* up to $N = 101$. Critical exponents are calculated as the eigenvalues of the stability matrix which is numerically evaluated. Additional subroutines have been implemented which compare coupling values and critical exponents, automatically discarding fixed points with large jumps in these values and unphysically large magnitudes of the critical exponents.

A further technical complication is encountered, as some solutions only show numerical stability after several orders have been included. This means that starting at $N_i = 2$ may result in wrongly discarding some solutions which become well-behaved at higher orders. This is qualitatively similar to the findings in the $f(R, Riem^2)$ theory without matter, where a fixed point is only stable above $N \geq 9$ [196]. To account for this, multiple vertical searches are performed at each point starting from different initial orders N_i up to $N_i = 20$. As the searches are independent of each other, they were implemented in parallel in the high performance computing cluster *Apollo* from University of Sussex. However, the landscape of roots of the flow equation rapidly increases at higher orders. Therefore, each search is initialised with 500 random points serving as seeds for the root search algorithm.

Suitable solutions with real-valued couplings and reasonable critical exponents have

FP	(a, b, c)	d_{UV}	g_N^*	$\lambda_c^* g_N^*$	ϑ_0	ϑ_1	ϑ_2	r_R	r_N
FP_2^{EH}	(0, 0, 0)	2	4.4290	-25.489	3.9628	1.9043	—	—	—
FP_4^c	(0, 0, 1)	4	3.8849	-19.277	3.9012	2.1771	1.7228	2.0060	14.9
FP_5^c	(0, 0, 1)	5	4.1580	-22.152	3.8688	2.7985	2.5150	1.6133	18.6
FP_4^{ab}	(1, 1, 0)	4	1.1536	-1.7651	4.2331	3.1531	3.1531	0.43449	9.61
FP_5^{ab}	(1, 1, 0)	5	0.92466	-1.0937	4.0632	2.4983	2.4983	0.40101	12.4
FP_4^{bc}	(0, 1, 1)	4	3.9578	-20.122	3.9259	2.0914	1.8218	1.6858	—
FP_7^{bc}	(0, 1, 1)	7	4.2512	-23.319	3.9094	2.7049	2.7049	1.0056	—

Table 5.1: Fixed points of gravity with SM matter indicating: projection of the action, dimensionality of the UV critical surface, coupling values, scaling dimensions, radius of convergence r_R and rate of convergence r_N . The Einstein-Hilbert theory with SM matter is included in the first row for comparison.

been identified and are discussed in the next section.

5.3 Gravitational fixed points with the Standard Model

Although a wide variety of solutions can be found at low orders, many are not reliable as they show no or poor convergence towards higher orders. Nonetheless, three of the seven points of the theory space host six solutions which are candidates for physical fixed points of the theory. The nomenclature FP_x^y is introduced for these fixed points, where the subscript will denote the number of relevant RG directions associated with them and the superscript, the point in theory space where these solutions are found. There are only three superscripts, $c = (0, 0, 1)$, $ab = (1, 1, 0)$ and $bc = (0, 1, 1)$, with the letters indicating which of (a, b, c) are set to a value of one. Thus, FP_4^c and FP_5^c appear in scenario $(0, 0, 1)$, FP_4^{ab} and FP_5^{ab} in $(1, 1, 0)$, and FP_4^{bc} and FP_7^{bc} in scenario $(0, 1, 1)$.

Table 5.1 offers a summary presenting some important features of the solutions and comparing them to the Einstein-Hilbert theory with SM matter. Each of these aspects is discussed in detail in the coming sections. In the following, visualisations for only one solution are presented at a time. The corresponding plots for all six solutions can be found in Appendix D and they are discussed whenever relevant in the text. The solutions fluctuate more strongly at low approximation order and start showing signs of stability and convergence from order $N = 7$ onwards. For this reason, approximation orders below seven are dropped from the analysis.

No stable solution manifests itself in the $f(R)$ theory. This was already observed in

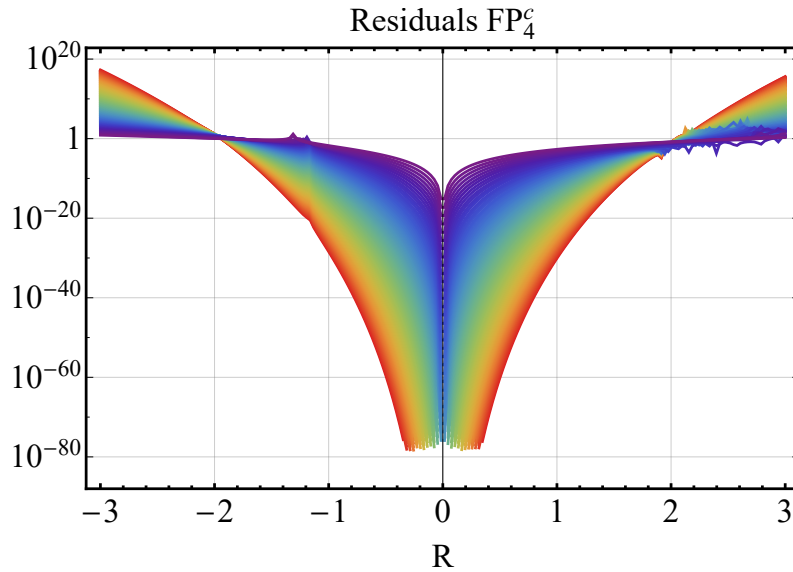


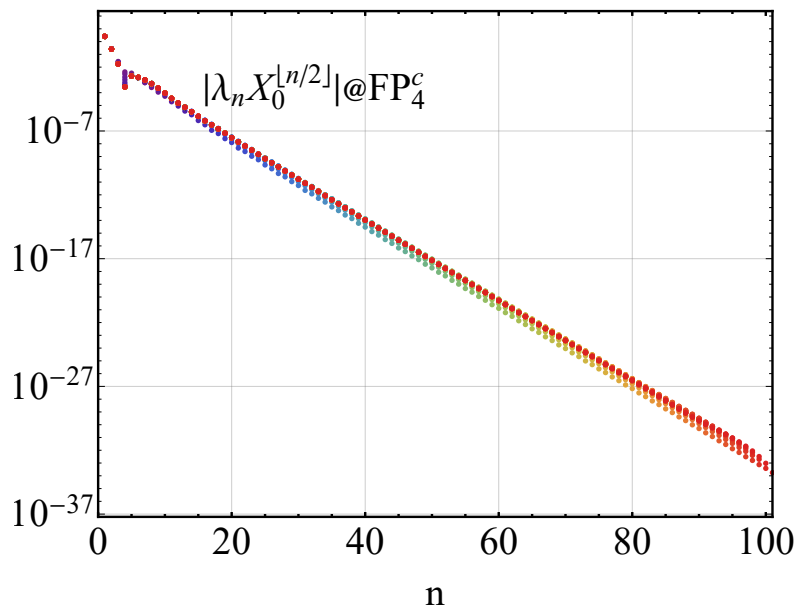
Figure 5.1: Accuracy of the fixed point FP_4^c at increasing polynomial orders as a function of the curvature R .

the analysis of Chapter 4. It is only when the action acquires a non-trivial projection in the direction of the other quadratic curvature invariants that stable solutions arise. Thus, these interactions can play a pivotal role in sourcing a fixed point of gravity with matter.

5.3.1 Accuracy

The solutions are determined to high numerical accuracy employing 100 digits of working precision in the calculations in *Wolfram Mathematica*. The residual of the polynomial solution in the flow equation is shown in Figure 5.1 as a function of the scalar curvature for FP_4^c , where the colour-coding indicates the order of the polynomial approximation from $N = 2$ (violet) up to $N = 101$ (red). The flow equation vanishes to order 10^{-80} for small curvature values, indicating that the polynomial approximation is a good solution. The radius of convergence, r_R , is estimated by the ratio test of the polynomial couplings at $N = 101$ and is given in Table 5.1. In the figure, this corresponds to the point where the lines cross. Beyond this point, increasing N returns less accuracy, indicating that the polynomial approximation breaks down. Plots relating to the other solutions are given in Figure D.1 in Appendix D and likewise show high accuracy, with the main difference being a substantial reduction in the radius of convergence of FP_5^{ab} and FP_4^{bc} .

FP	(a, b, c)	λ_c^*	g_N^*	λ_2^*	λ_3^*	λ_4^*	λ_5^*
FP_4^c	(0, 0, 1)	-4.9620	3.8849	0.10656	-0.0017246	0.072011	-0.056817
FP_5^c	(0, 0, 1)	-5.3275	4.1580	0.086866	0.030719	0.18870	-0.21747
FP_4^{ab}	(1, 1, 0)	-1.5301	1.1536	-1.1324	-4.0195	-3.9164	-1.6889
FP_5^{ab}	(1, 1, 0)	-1.1828	0.92466	-0.65704	-5.6558	-1.3648	-3.8781
FP_4^{bc}	(0, 1, 1)	-5.0842	3.9578	0.061175	-0.0068104	0.017822	-0.014004
FP_7^{bc}	(0, 1, 1)	-5.4854	4.2512	0.036245	0.023126	0.098100	-0.11644

Table 5.2: Coupling values of gravitational fixed points with SM matter at order $N = 101$.Figure 5.2: Absolute values of couplings λ_n of FP_4^c , with the index n in the horizontal axis, at each approximation order from $N = 2$ (violet) to $N = 101$ (red).

5.3.2 Fixed point coordinates

The solutions feature a negative cosmological constant and positive Newton's coupling, with the numerical values given in Table 5.2. In the Einstein-Hilbert theory, a large number of fermions turns the gravitational coupling negative. Therefore, it may be inferred that the higher curvature-order interactions are countering this effect. In the Einstein theory, the universal product of these couplings is $\lambda_c^* g_N^* \approx 0.10 - 0.18$ without matter [192, 195, 263] and $\lambda_c^* g_N^* \approx -25.5$ with SM matter. Meanwhile, the present solutions have $\lambda_c^* g_N^* \approx -20$ ($FP_4^c, FP_5^c, FP_4^{bc}, FP_7^{bc}$) and $\lambda_c^* g_N^* \approx -1$ (FP_4^{ab}, FP_5^{ab}). This indicates that while the former solutions do not deviate much from the Einstein-Hilbert approximation, the latter become more weakly coupled, although not as much as the theory without matter. In the former case, this can be attributed to the projection on $R_{\mu\nu\rho\sigma}^2$ leading to a larger value of Newton's

FP	(a, b, c)	ϑ_0	ϑ_1	ϑ_2	ϑ_3	ϑ_4	ϑ_5	ϑ_6	ϑ_7
FP_4^c	(0, 0, 1)	3.9012	2.1771	1.7228	1.1805	-0.66207	-2.0710	-4.1466	-6.0250
FP_5^c	(0, 0, 1)	3.8688	2.7985	2.5150	1.7398	0.45897	-1.4421	-2.9185	-5.1393
FP_4^{ab}	(1, 1, 0)	4.2331	3.1531	3.1531	1.9626	-1.8025	-1.8025	-3.9476	-6.3145
FP_5^{ab}	(1, 1, 0)	4.0632	2.4983	2.4983	1.3754	1.3754	-2.2270	-2.2270	-5.7377
FP_4^{bc}	(0, 1, 1)	3.9259	2.0914	1.8218	0.39502	-1.6498	-3.2924	-5.4692	-5.4692
FP_7^{bc}	(0, 1, 1)	3.9094	2.7049	2.7049	1.7735	0.98417	0.042973	0.042973	-1.4363

Table 5.3: Real part of the eight most relevant scaling dimensions of fixed points with SM matter at order $N = 101$.

coupling, a result which was already observed in the pure gravity analysis of Chapter 3.

On the spherical background, the couplings appearing in the action are weighted by factors of X . These effective coupling values are given in Figure 5.2 for FP_4^c from $N = 2$ (violet) to $N = 101$ (red), with the index n of the couplings λ_n in the horizontal axis. For all solutions, this is shown in Figure D.2. The trend of the values is to decrease in magnitude at higher orders for all solutions except FP_4^{ab} and FP_5^{ab} , where values increase. This can be directly associated with the smaller radius of convergence of these solutions as displayed in Table 5.1. The spread of the data points in the plots gives an indication of how fast couplings approach their asymptotic values. The solutions show good convergence except for FP_4^{bc} and FP_7^{bc} , where the spread is much wider. A quantitative measure for this rate of convergence is given subsequently in this section.

5.3.3 Scaling dimensions

The scaling dimensions associated with each solution are given in Table 5.3. Solutions FP_4^c , FP_4^{ab} and FP_4^{bc} have four relevant RG directions, FP_5^c and FP_5^{ab} have five, and FP_7^{bc} , has seven. Theories of pure gravity without Riemann interactions have fixed points with three relevant directions. Riemann interactions can induce a further one [196]. As a fifth relevant value appears in some of the solutions with SM matter, it may be inferred that quantum matter fluctuations shift the scaling dimensions towards more relevant values, possibly turning an irrelevant operator into a relevant one. In the case of FP_7^{bc} which has seven directions, it should be noted that two of them are very close to zero. As these quantities are bound to have some systematic error due to the approximations employed, it cannot be taken for granted whether these values are relevant or irrelevant.

The relevant scaling dimensions range from a value of four to near zero, meaning that

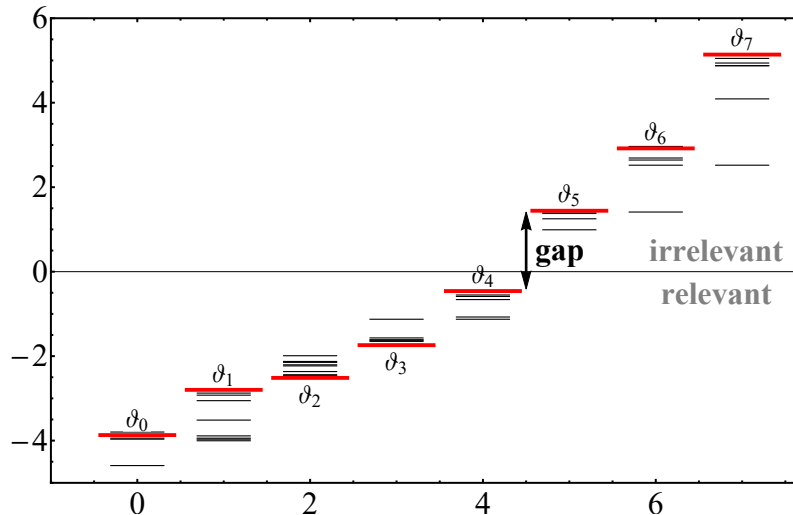


Figure 5.3: First eight eigenvalues of FP_5^c at each approximation. Thick red lines indicate the value at $N = 101$ while black lines are used for all other orders. All relevant eigenvalues are real. The gap between the least relevant and the most irrelevant values is $\Delta_{\text{gap}} \approx 1.90$

although the solutions are more strongly coupled compared to the pure gravity theory, the critical exponents do not show a substantial deviation from canonical scaling among the relevant values. These values are all real for FP_4^c , FP_5^c and FP_4^{bc} , indicating that SM matter has lifted the degeneracy of the critical exponents encountered in the theory without matter. The gap between the adjacent relevant and irrelevant values is shown in Figure 5.3 for FP_5^c and is close to two for this and all other solutions, except FP_4^{ab} and FP_5^{ab} , where it is closer to four. The larger difference in these cases is mostly due to the irrelevant values being complex conjugate, increasing the gap with the relevant ones.

An overview of the critical exponents is depicted in Figure 5.4 for FP_4^c . The left panel shows the values ϑ_n as a function of the approximation order N and illustrates that the scaling dimensions quickly tend to their asymptotic values. The right panel offers the transposed view, where the data points depict the values from order $N = 7$ (violet) to $N = 101$ (red) with the index n in the horizontal axis. This view directly confirms the bootstrap hypothesis, as higher order scaling dimensions are increasingly less relevant. The narrow spread of the data points shows quick convergence once more. Moreover, the distribution mostly follows a linear trend, fitted by the solid black line in the plot, indicating that matter quantum effects result in an overall uniform shift of the scaling dimensions. Reading from higher to lower n , this trend is broken by a pair of irrelevant complex values at $n = \{10, 11\}$.

The eigenspectrum of the other solutions is shown in Figures D.3 and D.4, and show

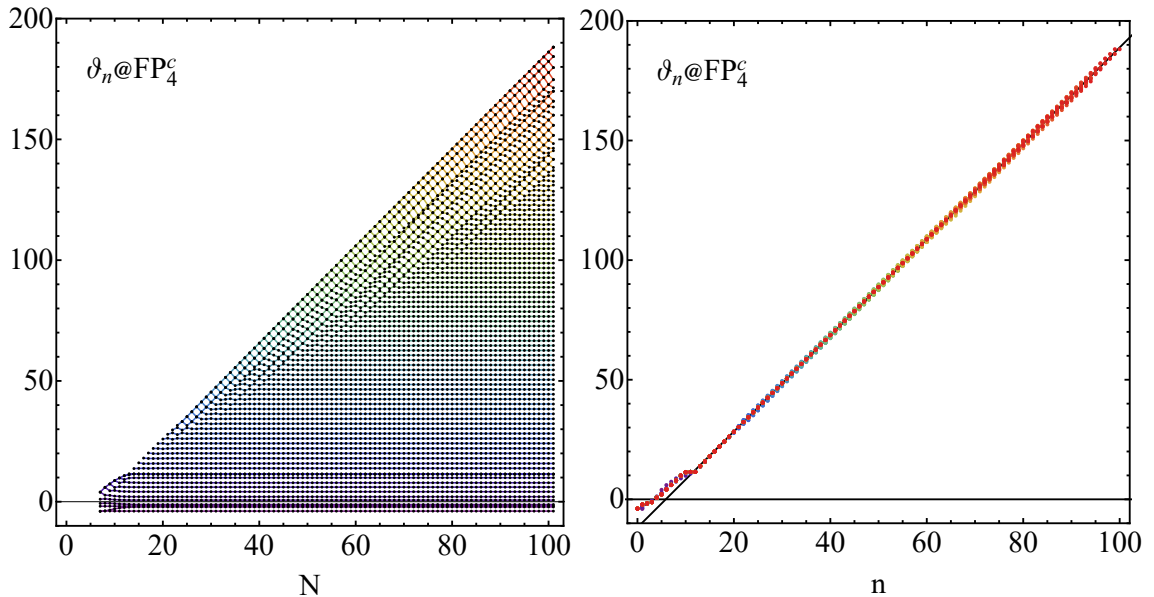


Figure 5.4: Eigenvalues of the stability matrix at each order N for FP_4^c . Negative values are UV relevant directions. The eigenspectrum shows stability towards higher polynomial orders.

qualitatively similar results although with three slight differences. First, two pairs of complex values ϑ_n appear between different positions $n = [3 - 12]$ in the solutions, excepting FP_4^{ab} with only one irrelevant complex pair and one relevant complex pair. Second, the intercept of the fitted linear trend is different between the solutions. This means that although the overall impact of matter is a pull towards more relevant values, the extent of this effect depends on the interactions present in the action. Third, the data points show a larger spread for FP_7^{bc} in Figure D.4, indicating that this solution has a slower rate of convergence compared to the others.

5.3.4 Relevant directions

The solutions found here have from five to seven relevant scaling dimensions, while the theory without gravity has been found to have only three. A natural question is then, what are the new RG directions appearing in the vicinity of the UV fixed point? This information is encoded in the eigenvectors associated to eigenvalues of the stability matrix. In the following, a brief technical review of this eigensystem is offered before analysing these vectors to provide an answer.

The eigenvalue equation for the stability matrix is:

$$M[V]^n = \vartheta_n[V]^n \quad (5.6)$$

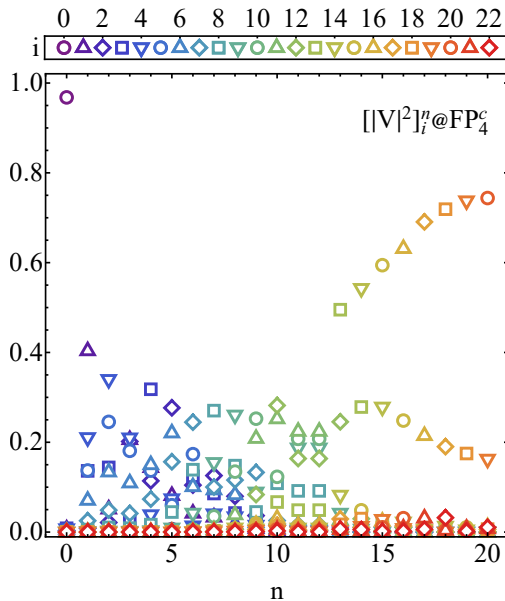


Figure 5.5: Eigenvectors of the stability matrix for FP_4^c .

The matrix of eigenvectors V of the stability matrix M contains in its columns the eigenvectors $[V]^n$ associated with the eigenvalues ϑ_n of M . The components $[V]_i^n$ are related to each of the running couplings λ_i that parametrise the interactions present in the action. The operators associated to these couplings define the theory space where RG flows live in. We put forward the interpretation that the components of the eigenvectors are the projections in the space of operators which the RG trajectories going into and out of the fixed point are associated with. In other words, the absolute value of the eigenvectors $||V|^2|^n$ define the direction that RG flows point towards, around the fixed point, in the phase diagram of the theory.

To further disentangle the mixing of components due to large differences in the magnitude of couplings, V is transformed into a doubly-stochastic matrix, effectively projecting the eigenvectors into the unit sphere S^N , such that:

$$\sum_{i=0}^{N-1} [||V|^2|_i^n = \mathbf{1}^\top, \quad \sum_{n=0}^{N-1} [||V|^2|_i^n = \mathbf{1} \quad (5.7)$$

where $\mathbf{1}$ is a vector of all ones with N elements, the subscript denotes row and superscript denotes column, and the convention of taking the initial index as zero is adopted. This is equivalent to a similarity transformation of the stability matrix, corresponding to a linear transformation of the couplings, which is always allowed. This double normalisation is implemented heuristically as a series of iterative rescalings of the matrix of eigenvectors.

The eigenvectors associated with the first twenty-one scaling dimensions, ranked from relevant to irrelevant, are shown in Figure 5.5 for FP_4^c at $N = 101$. The data points are

	\mathcal{O}_0	\mathcal{O}_1	\mathcal{O}_2	\mathcal{O}_3	\mathcal{O}_4	\mathcal{O}_5	\mathcal{O}_6
FP_4^c	\mathbb{I}	R	X^2	$X^2/R/X$	RX	X	RX^3
FP_5^c	\mathbb{I}	RX/X^2	X^2	R	RX^2	X^3/X	RX^3
FP_4^{ab}	\mathbb{I}	R/X	R/X	R	RX	RX	X^3
FP_5^{ab}	\mathbb{I}	R	R	X^2	X^2	RX/RX^2	RX/RX^2
FP_4^{bc}	\mathbb{I}	R/X^2	R	X	RX	X^2	RX^4
FP_7^{bc}	\mathbb{I}	RX	RX	R	X^3	X^3/RX^2	X^3/RX^2

Table 5.4: Projections of the RG flows around the fixed points in the doubly-normalised eigenvector matrix ranked from relevant to irrelevant directions.

the i components of each doubly-normalised squared eigenvector $[|V|^2]_i^n$, with the index n of the vector in the horizontal axis. The legend on the top associates data markers with the order in scalar curvature of the operators in the action. The plot reveals that the most relevant flow points in the direction of the vacuum energy operator (cosmological constant), the second one in the direction of R , the third in the direction of X^2 , and the fourth on a combination of X^2 , R and X . The eigenvectors show mixed contributions up to $n = 12$, while for $n \geq 13$, there is a clear dominant direction. Plots for the other solutions are given in Figure D.5 in Appendix D, showing a similar trend.

The dominant directions are summarised in Table 5.4 ranked from relevant to irrelevant for each solution. The RG flow associated with the largest eigenvalue is mostly projected on the direction of the cosmological constant in all cases. The rest of the eigenvectors have a mix of contributions from different operators and, in some cases, near-equal projections in different directions, which have been indicated as A/B in the table. The operators R and X appear interspersed in the table, with contributions of up to RX^4 , corresponding to curvature order nine, also appearing.

To conclude, it should be noted that eigenvectors are not universal quantities as they are not invariant under linear transformations of the couplings. The doubly-stochastic normalisation is employed as it is the projection that allows the most equitable representation, balancing the fact that couplings take values separated by many orders of magnitude. However, there is nothing universal about this normalisation. Hence, the mixture of directions found among the relevant RG directions may be further disentangled using other methods.

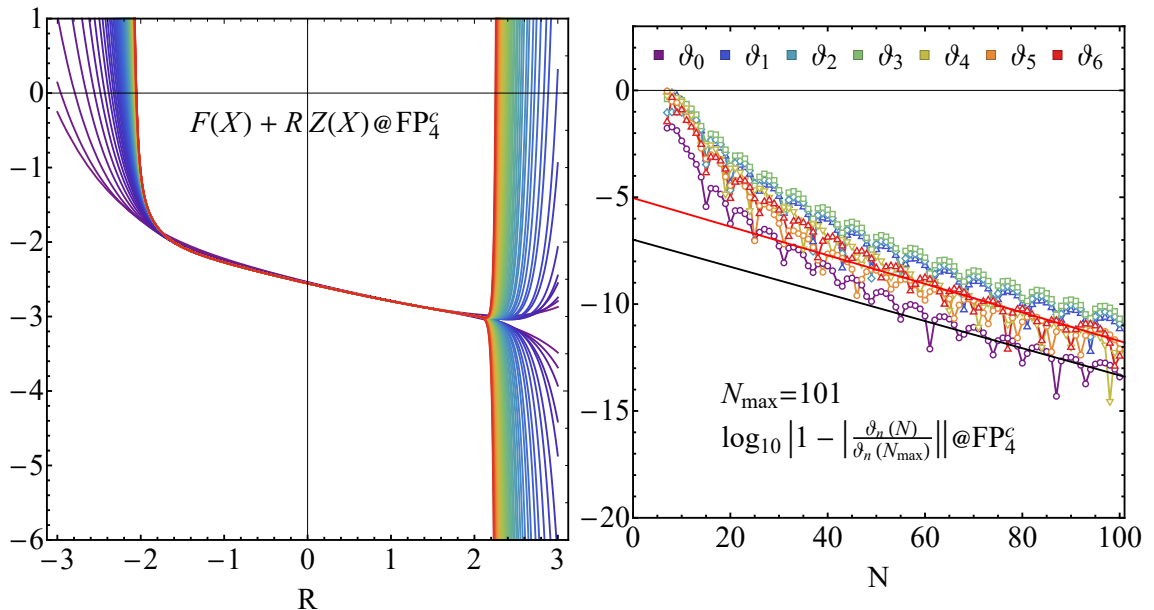


Figure 5.6: Left: Action of the polynomial solution FP_4^c from $N = 7$ (violet) to $N = 101$ (red). Right: Number of digits of accuracy in the scaling dimensions of FP_4^c taking as reference value $N = 101$. The black line is the linear fit of ϑ_0 , the red line is the averaged fit for the shown data. The fits are performed for $N \geq 61$

5.3.5 Convergence

The polynomial action is plotted in the left panel of Figure 5.6 for FP_4^c . The lines fall on top of each other indicating quick convergence, where the curves for $N < 7$ are dropped as the solutions are not stable yet at those orders. The tails of the curves consistently point upwards for negative curvature values and alternate for positive ones. This suggests that the radius of convergence, r_R may be bounded by a pole on the real negative axis. Noting that the flow equation has a pole at $R = 2.006$ (independent of (a, b, c)), this plot suggests that the radius of convergence of FP_4^c saturates this bound.

The corresponding plots for the other solutions can be found in Figure D.6. Solutions FP_4^c , FP_5^c and FP_4^{bc} have a large radius of convergence r_R . For the latter two, the tails at negative curvature values appear to start alternating in sign at high orders. Solution FP_5^{ab} has alternating tails for positive curvature and a smaller radius of convergence, suggesting the presence of a movable singularity at negative curvature values bounding this solution. Meanwhile, FP_4^{ab} and FP_7^{bc} show alternating tails on both sides, meaning that their radius of convergence, which is also smaller, is bounded by a pole in the complex plane.

The rate of convergence r_N , describing how fast the asymptotic behaviour is approached, can be measured by counting the number of digits that become stable in the

FP	(a, b, c)	r_R	r_S
FP_4^c	(0, 0, 1)	2.0060	2.0065
FP_5^c	(0, 0, 1)	1.6133	1.6932
FP_4^{ab}	(1, 1, 0)	0.43449	0.69352
FP_5^{ab}	(1, 1, 0)	0.40101	0.40500
FP_4^{bc}	(0, 1, 1)	1.6858	1.7135
FP_7^{cb}	(0, 1, 1)	1.0056	1.2518

Table 5.5: Radius of convergence of the polynomial theory from the ratio test r_R , and value at which the numerical integration encounters a singularity r_S .

scaling dimensions as the order N increases. This is shown on the negative axis for FP_4^c in the right panel of Figure 5.6. The plot illustrates that at order $N = 101$, ϑ_0 has stabilised to 13 digits of accuracy. The trend in the curves changes as N increases until about $N = 60$, above which the slope remains constant. This is interpreted as the onset of the asymptotic behaviour and would not have been visible had the analysis stopped at lower orders, leading to an exaggerated prediction for r_N ; this observation highlights the necessity for pushing the polynomial expansion to such high orders. The linear fit of ϑ_0 is shown as a black line and the averaged fit of the data, as a red line. The negative inverse of the slope of the fit is a quantitative measure of the rate of convergence. For the solution shown in the plot, a further digit of accuracy is gained every 13.8 orders on average.

The corresponding plots for the other solutions can be found in Figure D.7 in Appendix D, with the rate of convergence listed in Table 5.1. Solution FP_5^c has similar behaviour as FP_4^c , while FP_4^{ab} and FP_5^{ab} display a linear trend for all values of N . In contrast, FP_4^{bc} and FP_7^{cb} show only limited convergence, gaining a maximum of five digits of accuracy in ϑ_0 . This would seem to suggest that these polynomial solutions are not converging to a fixed point of the full theory. This picture could change if other methods are used, such as expanding around a different field value or using optimised boundary conditions. The average rate of convergence is summarised in Table 5.1 and is 14.9, 18.6, 9.61 and 12.4 for FP_4^c , FP_5^c , FP_4^{ab} and FP_5^{ab} , respectively, while no statistically meaningful inference can be drawn for FP_4^{bc} and FP_7^{cb} . To put these figures into context, the convergence rate in the $f(R)$ theory without matter was of 1 digit per 20 orders measured on the three leading coupling values [192], while for $f(R, Ric^2)$ without matter, it was of 1 digit per 2-3 orders measured using the critical exponents [195].

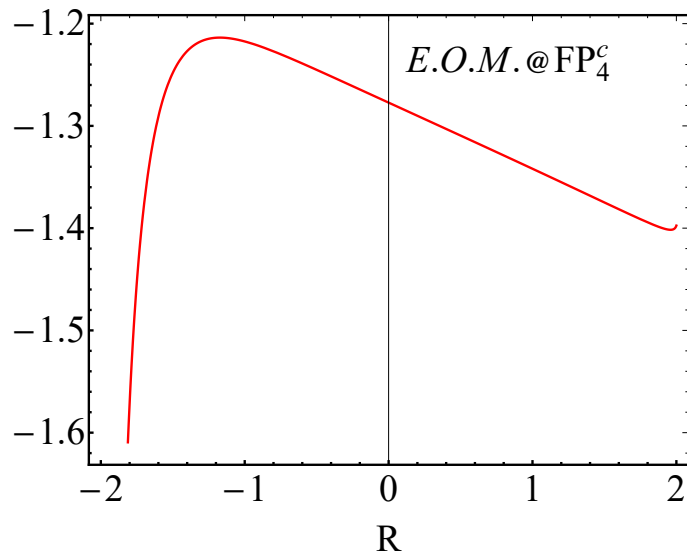


Figure 5.7: Equation of motion obtained by numerical integration of the action from fixed point FP_4^c at order $N = 101$. The region of integration is bounded by a singularity. No de Sitter solutions are found in the range of the integration.

5.3.6 Beyond the polynomial approximation

The polynomial solutions are only valid within their radius of convergence r_R . To go beyond, general solutions can be obtained by solving the flow equation for the action $f(X) + Rz(X)$ at the fixed point. This is a third order differential equation and can be solved numerically using the polynomial couplings to fix the initial conditions. The equation is separated into even and odd parts, defining independent equations for f and z , which can be solved in the domain $X > 0$:

$$4(f - X f') = I_{qg}^{(even)} + I_{qm}^{(even)} \quad (5.8)$$

$$2(Rz - 2X R z') = I_{qg}^{(odd)} + I_{qm}^{(odd)} \quad (5.9)$$

Solutions of these equations can diverge at the poles of the flow equation, found at:

$$R = -9.99855, \quad R = 0, \quad R = 2.00648 \quad (5.10)$$

independent of (a, b, c) . Additionally, movable singularities can also appear at varying values of R depending on the initial conditions of the action. A global solution is one which remains finite at these points and is valid for arbitrary values of R . Whether such a solution can be obtained depends on the initial conditions and thus on the polynomial couplings. Using the values of FP_4^c , the numerical integration is bounded by the pole of the flow equation at $R = 2.006$, making it impossible to go beyond with the initial

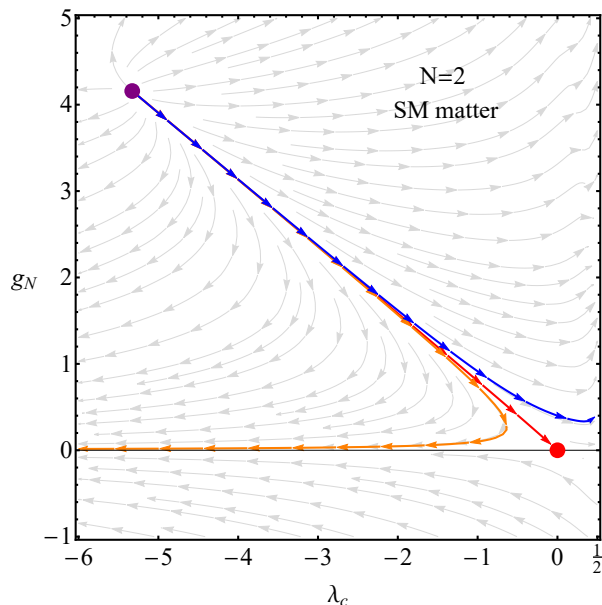


Figure 5.8: Phase portrait of the Einstein-Hilbert theory also showing UV-IR connecting trajectories.

conditions provided. As FP_4^c saturates the radius of convergence, the action obtained from this method is identical to the polynomial action of this solution.

For the other fixed points, the action can be extended beyond the radius of convergence of the polynomial approximations but not by much, as a singularity is shortly encountered, forcing the numerical integration to end. This is shown in Table 5.5 which compares the radius r_R of the polynomial approximation from the ratio test and the point where the numerical integration encounters a singularity. Thus, the solutions identified in here do not lead to global solutions of the action.

Using the result from the numerical integration of the action, one can also look for solutions to the equation of motion. Taking the variation of the action with respect to the metric leads to the equation of motion:

$$\frac{1}{2}f - \frac{1}{4}R \partial_R(X)f' + \frac{1}{4}Rz - \frac{1}{4}R^2 \partial_R(X)z' = 0 \quad (5.11)$$

This equation is plotted in Figure 5.7 for FP_4^c , showing that no solution is found within the domain of integration. This is mainly due to the negative cosmological constant which shifts the overall curve downwards, while the negative slope at small R is a consequence of having a positive g_N . As a result, the fixed points do not support de Sitter nor anti-de Sitter spacetime solutions.

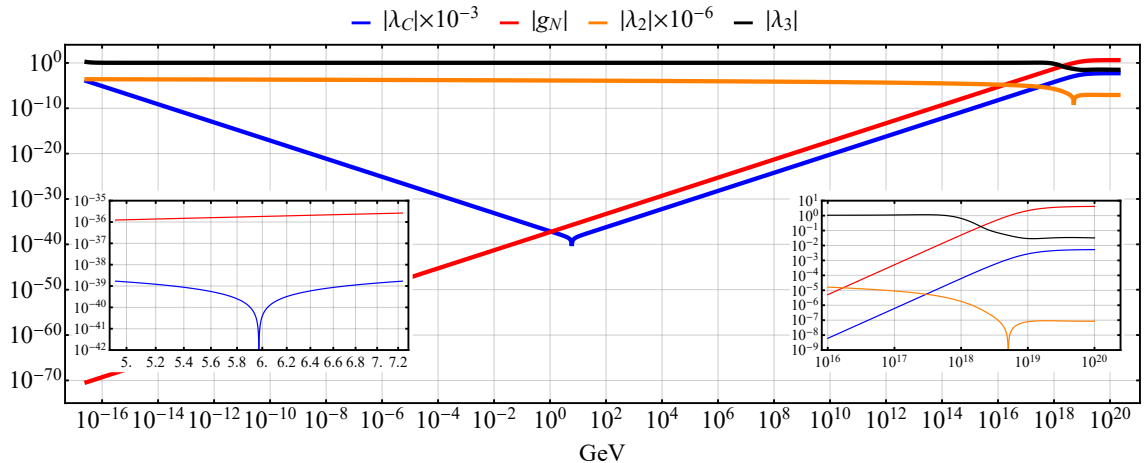


Figure 5.9: Renormalisation group flow of couplings in $(0, 0, 1)$ from the UV (FP_4^c) to the IR (right to left) at $N = 4$. Higher order couplings are set to their fixed point values at $N = 101$. Along this trajectory, the cosmological constant smoothly crosses the zero and changes sign at $k \approx 5.973$ GeV.

5.3.7 UV-IR connecting trajectories

A fundamental theory should have well-defined RG trajectories connecting the fixed point in the UV with a Gaussian regime compatible with General Relativity in the IR. Such trajectories can be found by numerically integrating the running of the couplings down to low energies. A simple phase portrait is available in the Einstein-Hilbert theory by setting higher order couplings to their fixed point values and neglecting their running. This is illustrated in Figure 5.8 for FP_5^c , showing trajectories emanating from the fixed point with the arrows pointing towards the IR. The critical exponents are real in this approximation and this is reflected in the flows around the fixed point which appear as straight lines. The trajectory highlighted in red runs exactly into the Gaussian in the IR, with λ_c remaining negative along the flow. Trajectories where the cosmological constant becomes positive are also available, with the one highlighted in blue as an example.

Next, the approximation is upgraded to $N = 4$ where suitable RG trajectories can also be found. One such trajectory is shown in Figure 5.9 for FP_5^c , which depicts the value of the running couplings as a function of the energy scale. A brief explanation of this plot is given now. At high energies in the rightmost part of the plot, the flow is very slow as this is the vicinity of the UV fixed point. As the energy decreases towards the left of the plot, a crossover region appears where the couplings runs faster. A zoom-in to this region is shown in the inset on the lower right. Both cosmological constant and Newton's coupling decrease in magnitude approaching vanishing values. The cosmological constant smoothly

crosses the zero and becomes positive at $k \approx 5.973$ GeV in the trajectory shown. The inset on the lower left provides a zoom-in of this region, where the sign change is signalled by a spike on the logarithmic plot. At the same time, Newton's coupling continues tending toward zero asymptotically. In the deep IR in the leftmost part of the plot, the flow approaches a pole of the flow equation close to $\lambda_c^* = 1/2$ where the numerical integration stops. Many other qualitatively similar trajectories are available where the couplings can flow either faster or slower. Similar trajectories are available for the other solutions and are depicted in Figure D.8 showing qualitatively the same behaviour.

Reproducing this task at higher orders becomes very challenging very quickly, not only because the numerical integration is more time-consuming but also because it is more difficult to find suitable initial conditions leading to UV-IR finite trajectories. As the flow of λ_c and g_N did not change drastically from $N = 2$ to $N = 4$, it may be reasonable to assume that higher derivative-order operators do not qualitatively modify the behaviour of these couplings and that finite trajectories may exist to all orders.

5.4 A first peek beyond the Standard Model

The analysis can be extended to matter configurations corresponding to Beyond the Standard Model (BSM) scenarios. However, such models tend to include more additional fermions and scalars than gauge bosons in the matter content. From the Einstein-Hilbert case, one can expect that a high number of fermions would lead to negative cosmological constant and a negative Newton's coupling. This is indeed what is found for all the cases explored in here.

A list of interesting BSM models that have been considered in this analysis is given in Table 5.6 along with their matter content. The first three correspond to well-known BSM models. The models AS-GY-A/B refer to the asymptotically safe gauge-Yukawa model proposed in ref. [70]. The next two, AS-SUSY-A/B, are the supersymmetric version, discussed in [78]. The last three, AS-ST-A/B/C, refer to a type of minimal SM extensions which are made asymptotically safe via Yukawa couplings to three BSM Dirac spinors and nine complex scalars [84, 86]. The matter content is determined by the free parameters of the theories, for which representative examples have been chosen according to the appropriate constraints in each case.

No stable solutions are found in SO(10) GUT, AS-GY-B and AS-ST-A. In the other models, solutions are found where the cosmological constant can obtain either a positive or a negative value, however, Newton's constant consistently appears with a negative value

Model	N_S	N_M	N_D	FP	d_{UV}	UV-IR RG
MSSM	98	12	61/2	✓	4	✗
SU(5) GUT	124	24	24	✓	2	✗
SO(10) GUT	97	45	24	✗	–	✗
AS-GY-A	578	8	51	✓	6	✗
AS-GY-B	1568	24	140	✗	–	✗
AS-SUSY-A	92	11	57/2	✓	4	✗
AS-SUSY-B	128	11	75/2	✓	4	✗
AS-ST-A	22	12	51/2	✗	–	✗
AS-ST-B	166	12	63/2	✓	2	✗
AS-ST-C	76	12	57/2	✓	4	✗

Table 5.6: BSM matter configurations and whether they support gravitational fixed points or not. All solutions have negative Newton’s constant and therefore, they do not possess RG flows connecting the theory continuously to General Relativity in the IR.

in all cases. Since the running of Newton’s coupling vanishes for $g_N = 0$ independently of other interactions, RG trajectories cannot cross this line and thus, no smooth RG flows are available connecting the theory to General Relativity in the IR. A summary is provided in Table 5.6 indicating which models admit a numerically stable solution of the flow and the minimum number of relevant RG directions associated with those solutions. Overall, no physical fixed points are found for BSM models as all solutions have negative Newton’s constant, resulting from a large number of fermions and scalars in these models. The picture may change if non-minimal matter-gravity interactions are allowed. For example, it has already been noted that certain dimension five interaction terms, such as $R\bar{\psi}\gamma_5\psi$ can stabilise UV fixed points with fermions [227–230, 241].

5.5 Conclusions

New families of gravitational fixed points supporting asymptotic safety with SM matter have been identified in this study. No such solutions are available in the $f(R)$ theory, it is only when the $R_{\mu\nu}^2$ and $R_{\mu\nu\rho\sigma}^2$ operators are considered that stable fixed points can appear. Thus, these higher derivative curvature invariants play a crucial role in mediating a fixed point of gravity with matter.

The six solutions can be identified up to order $N = 101$ in the polynomial approximation. The bootstrap hypothesis is confirmed as no additional relevant RG directions

appear above $N = 7$. Thus, the theory remains predictive with 4-7 free parameters. The additional relevant directions can be explained due to interactions of the Riemann tensor and quantum matter fluctuations. The overall effect of SM matter is to shift the scaling dimensions towards more relevant values, explaining the additional relevant critical exponents compared to the theory without matter.

The theory remains predictive in the UV and is smoothly connected to a Gaussian regime compatible with General Relativity in the IR. Explicit RG flows have been identified up to $N = 4$ and are conjectured to exist at higher orders. These flows can naturally explain a vanishingly small and positive cosmological constant, and a small and positive Newton's coupling.

Nonetheless, there are some limitations to the results found. For instance, the approximations considered here have not uncovered global solutions of the action, although this could be further studied with other methods, such as Pade approximants, or could change due to neglected interactions. Chapter 7 will later show that global solutions can be found if there are many matter fields. Also, the equation of motion has no solutions within the radius of convergence for any of the six fixed points. Moreover, two of the solutions show limited convergence indicating they may not be approaching a fixed point of the full theory. Lastly, the same analysis has not found physical solutions for some selected BSM matter configurations as they appear with a negative Newton's coupling and hence, cannot be connected to General Relativity at low energies.

Overall, gravitational models which display asymptotic safety and are compatible with the Standard Model have been found. This represents a further advance towards combining quantum gravity and matter into a single fundamental theory. Future studies can explore further types of higher order interactions with Ricci and Riemann tensors, as they can become important for the high energy behaviour of the theory.

Chapter 6

Impact of SM matter on quantum gravitational fixed points

6.1 Introduction

This thesis has so far explored fixed points of gravity both without matter and with the SM field content. In the former case, highly stable solutions are found in an operator expansion with interactions of the Ricci and Riemann tensor present in the action (see Chapter 3). In the latter case, these higher order interactions counter the destabilising effect of matter fields and give rise to fixed points in various gravitational models (see Chapter 5). However, one cannot avoid but notice that three of the models which show remarkable stability in pure gravity do not admit fixed points in the presence of matter $((0, 1, 0), (1, 1, 1), (1, 0, 1))$. It would be interesting to understand why these solutions do not appear when matter fields are included in the system.

The aim of this study is to explore the fate of fixed points that are stable in pure gravity when matter is included in the system at high curvature order. In particular, the objective is to clearly establish whether the solution found in the absence of matter can be continuously connected to the SM field content beyond the Einstein-Hilbert approximation. To achieve this, a numerical variation analysis is performed in the spirit of the horizontal search of Chapter 3. The fixed point search takes the $f(R, Ric^2)$ theory starting from the pure gravity case and matter fields are gradually added in small steps, ending at the SM matter configuration.

The analysis is organised in five sections. Section 6.2 introduces the theoretical tools and lays out the methodology of the study. Section 6.3 presents the results of the fixed point search between the pure gravity scenario and the Standard Model case at high deriv-

ative order. Section 6.4 explains how scaling dimensions are affected by the presence of SM matter. Section 6.5 concerns relevant directions. Section 6.6 discusses some observations regarding lack of convergence in the extended solution. Finally, Section 6.7 presents a discussion of the findings and the conclusions.

6.2 Methodology

This chapter takes place in the same theoretical framework as the previous ones and the equations are not repeated anymore. Only the relevant notation for the parameter space is recalled. The flow equation of the models under investigation has six parameters besides from the approximation order N . Three specify the interactions present in the action, (a, b, c) , according to:

$$X = a R^2 + b R_{\mu\nu} R^{\mu\nu} + c R_{\mu\nu\rho\sigma} R^{\mu\nu\rho\sigma} \quad (6.1)$$

The other three are the matter field multiplicities, with N_S counting the number of real scalar fields, N_M the number of Maxwell vectors and N_D , the number of Dirac fermions. Additionally, the polynomial approximation is employed, where N specifies the approximation order, having $N = 2$ corresponding to the Einstein-Hilbert theory.

This analysis reuses the methods introduced in Chapter 3 to perform a horizontal search in the parameter space. However, this time, the gravitational parameters (a, b, c) are kept fixed, while the variation is applied in the matter parameter space (N_S, N_M, N_D) . This variation is performed in a linear manner by keeping the matter ratios fixed to that of the SM field content. Then, the path connecting the two points is characterized by one parameter interpolating from zero (no matter) to one (SM matter):

$$(N_S, N_M, N_D) = N_{mat} \times (4, 12, 45/2), \quad \forall N_{mat} \in [0, 1] \quad (6.2)$$

The gravitational parameters are fixed next. Chapter 3 found a one-parameter family of models where fixed points of pure gravity are highly stable to very high curvature orders and are virtually unchanged under variations of (a, b, c) . In particular, these models contain the points $(0, 1, 0)$, $(1, 1, 1)$ and $(1, 0, 1)$. Nonetheless, none of these three allowed a stable fixed point to appear when SM matter was introduced in Chapter 5. Since they all lie in the same line of stability, they are considered to be similar to each other and only one of them is chosen as a representative example for this analysis. Thus, the gravitational sector is specified as $(a, b, c) = (0, 1, 0)$.

There are only two free parameters remaining, (N, N_{mat}) , describing the approximation order and the matter content. Making use once more of the numerical toolkit developed by

the author, the fixed point search is performed at every order up to $N = 101$, segmented into 501 steps at each order. At each step, the flow equation is solved numerically with 100 digits of working precision using the *Wolfram Mathematica* software. The computations have been performed in the high performance computing cluster *Apollo* from University of Sussex. Scaling dimensions are computed every five steps in the interest of time efficiency. However, higher resolution has been employed whenever necessary to ensure the quality of the data. The main results are explained in the following sections.

6.3 Impact of matter on couplings

Starting from the pure gravity theory, a fixed point can be identified at each step in the numerical variation at every polynomial order. The variation in coupling values between consecutive steps is relatively small, thus, the solution can be regarded to be continuously connected between the two endpoints. A snapshot for the coupling values is shown in Figure 6.1 showing complementary views in terms of N and N_{mat} which is discussed in detail next.

The left panel of Figure 6.1 shows the absolute value of couplings from λ_0 (violet) to λ_{100} (red) at fixed order $N = 101$ while varying N_{mat} . Three regimes of different behaviour are identified in the plot from left to right. Close to the pure gravity scenario, the solution remains virtually unchanged for a small matter content. A cross-over regime is identified at $N_{mat} \approx 0.02 \sim 0.20$ where the rate of change with respect to N_{mat} significantly increases in the higher order couplings. As a result, these couplings switch from taking vanishingly small values to very large ones with increasing N_{mat} . Close to the SM matter configuration, the values seem to scale with powers of N_{mat} , a feature which will come up again when the large matter limit is discussed in Chapter 7. At this point, the curves have a very pronounced slope, indicating that small changes in the matter content, such as adding one extra BSM fermion or scalar, can lead to very large variations in the fixed point coordinates. This is summarised in Table 6.1 comparing the three regimes. Moreover, note that the higher order couplings display many changes in sign at large magnitude orders, indicated in the logarithmic plot by downward spikes in the curves. Small changes in the matter content in the cross-over regime push these couplings to wildly oscillate between very large positive and negative values. This suggests that the system is not numerically stable with respect to variations in the matter content. Special care has been taken to use enough resolution in the number of points and numerical precision in the computations to rule out the possibility that these fluctuations are due to numeric issues.

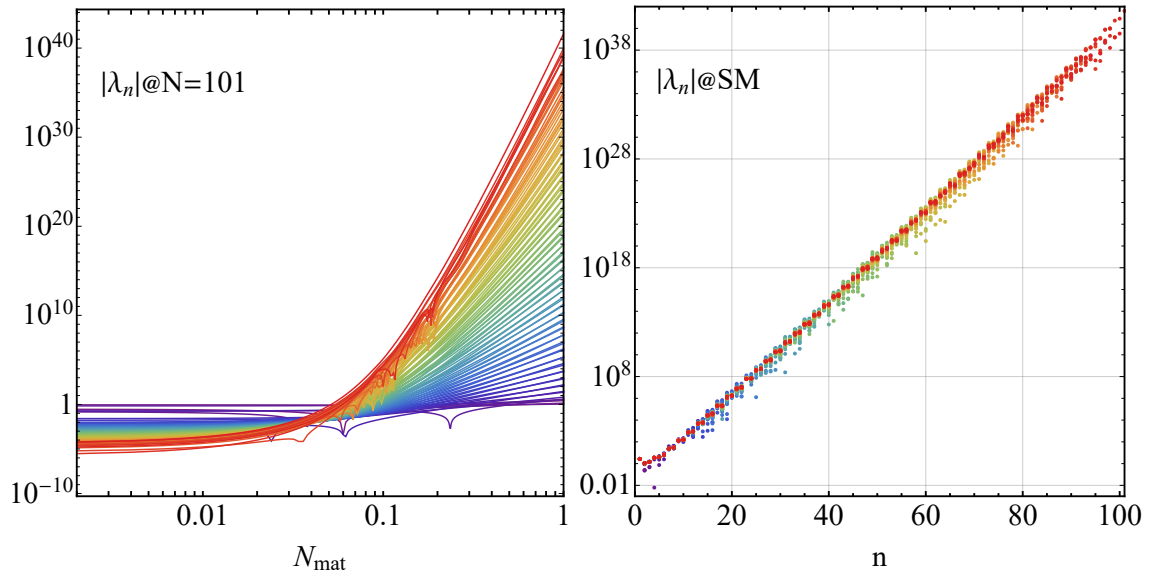


Figure 6.1: Absolute value of couplings λ_n at the fixed point. Left: Variation with respect to N_{mat} from pure gravity ($N_{mat} = 0$) to the SM ($N_{mat} = 1$) at $N = 101$ for λ_0 (violet) to λ_{100} (red). Right: variation with respect to N at the SM ($N_{mat} = 1$ fixed). Each vertical observation is a coupling with data points from $N = 2$ (violet) to $N = 101$ (red).

The right panel shows the transposed view, the absolute value of the couplings fixed at the SM matter configuration ($N_{mat} = 1$) at each order N . The horizontal axis indicates the index n of the couplings and each λ_n is a vertical observation. The data points in each column range from $N = 2$ (blue) to $N = 101$ (red). The spread for each of the observations can be used as a proxy to estimate the numerical stability in the value of each coupling towards higher truncation orders. A smaller spread is a sign of faster convergence towards their asymptotic value. Under this view, the first ten couplings show fast convergence. On the other hand, the rest show a larger spread, with fluctuations encompassing large orders of magnitude. Furthermore, the couplings appear in pairs of similar magnitude with an alternating sign. The sign cannot be appreciated in the logarithmic plot but can be read-off from Table E.1 in Appendix E, which presents the numeric values of couplings at $N = 101$ and $N_{mat} = 1$. The alternating signs are conventionally regarded as an indication of approaching convergence at high polynomial orders.

These two viewpoints show that although numerical stability in the values of the first few couplings at the SM matter configuration may be achieved at large N , the fixed point is highly susceptible to small variations in the matter content. Furthermore, the large spread in the higher order couplings indicates that it is necessary to retain a large number of higher derivative order operators in the action before these interactions approach their

Regime	N_{mat}	Couplings
Near pure gravity	< 0.02	Constant
Cross-over	$0.02 - 0.2$	Large oscillations
Gravity and matter	> 0.2	Exponential increase

Table 6.1: Qualitative behaviour of couplings between the pure gravity and the SM scenario.

asymptotic values. Thus, it may be concluded that the convergence properties of the fixed point found in the pure gravity regime greatly deteriorate once it is translated to the SM scenario.

6.4 Impact of matter on scaling dimensions

While in the pure gravity case the fixed point has three relevant directions and the scaling dimensions are found to follow a near-Gaussian scaling, the situation drastically changes once matter is included. Moreover, compared to the coupling values, convergence in the scaling dimensions is much slower. A comprehensive view of these values is shown in Figure 6.2 at the SM matter content for all orders N . The main findings are now discussed in detail.

The left panel of Figure 6.2 shows a transverse view of the scaling dimensions. The horizontal axis indicates the truncation order N and the data points at each of order are the real part of the critical exponents. The negative valued ones indicate relevant UV directions, while the positive, irrelevant ones. Lines join the data points ranked from relevant to irrelevant at each order. The first feature to notice is the persistent numerical variation which does not decrease at higher approximation orders. This aspect will be discussed in more detail further ahead. Second, the most relevant value is larger than four and seems to be slowly decreasing in magnitude at higher orders. This results from irrelevant operators becoming relevant due to matter, thus increasing the number of relevant RG directions. Furthermore, note that those values that are smallest in magnitude fluctuate between positive and negative sign, with a sign change appearing even at up to $N = 81$.

The right panel shows the transposed view. Similar to the format of the previous figure, here the vertical observations are the scaling dimensions ϑ_n with the horizontal

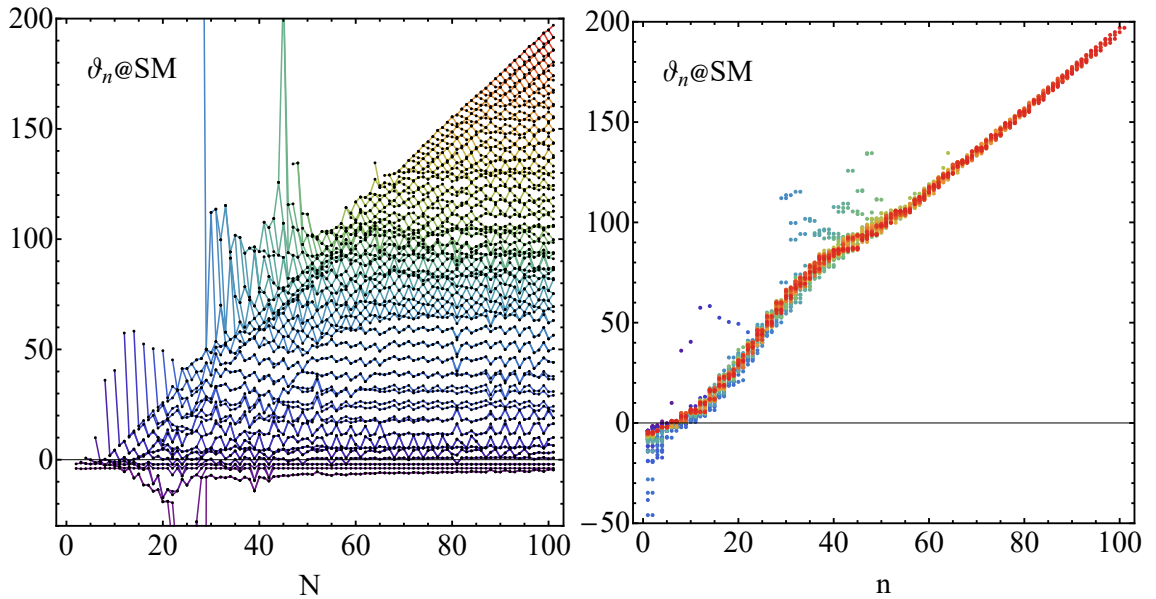


Figure 6.2: Eigenvalues of the stability matrix at the SM matter content at increasing order N . The left panel shows the trend of the eigenvalues ranked from relevant to irrelevant towards higher N . The right panel shows the variation of each eigenvalue at all orders from $N = 2$ (violet) to $N = 101$ (red).

axis giving the index n . Each data point is the value of the n th critical exponent, ranked from relevant to irrelevant, from $N = 2$ (violet) to $N = 101$ (red) at the SM matter configuration. The most important feature in this view is that at the highest order there are five relevant scaling dimensions, four of which come in complex conjugate pairs. Secondly, the difference between subsequent n values at a fixed order N (going from left to right for any fixed colour in the plot) is not constant, increasing for $\vartheta_{20} - \vartheta_{30}$ and decreasing for $\vartheta_{35} - \vartheta_{50}$. It is only for the higher order values that this difference seems to be constant and follow Gaussian scaling. However, it is the higher order values that are the least reliable as they will probably continue adjusting at higher polynomial orders. Although the bootstrap hypothesis still holds, this entails that matter is modifying the anomalous dimensions of different higher derivative operators in a non-uniform manner. Third, the spread on the values of the scaling dimensions across N is much wider than for the couplings values. Notably, the most relevant values show large fluctuations at lower orders. This is mainly because, at low orders, irrelevant directions become relevant and result in large scaling dimensions at the SM matter configuration. This can also be appreciated in the large fluctuations of the relevant values in the left panel and is further discussed in the next figure.

To complement the plots, the numeric values of the scaling dimensions at $N = 101$

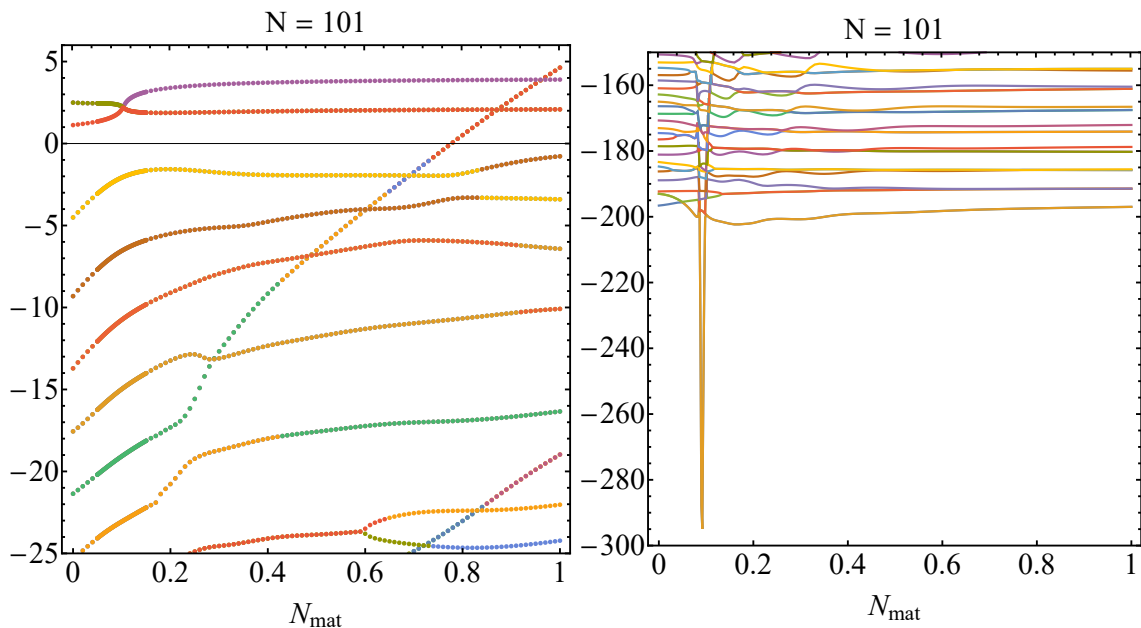


Figure 6.3: Scaling dimensions along the numerical variation at $N = 101$. The left panel shows the upper end (most relevant) of the scaling dimensions. The right panel shows the lower end (most irrelevant) of the scaling dimensions.

and $N_{mat} = 1$ are given in Tables E.2 and E.3 in Appendix E, separated by real and imaginary part, respectively. Note that the imaginary part of the two most relevant scaling dimensions is five times as large as their real part, indicating a strong spiraling trajectory in the phase diagram of the theory. The third one is real and close to four, while the fourth and fifth are close to two with a small complex part. These last three are similar to the ones found in the pure gravity case and the connection with relevant operators will be explored in the next subsection.

A third point of view is available by keeping the order N fixed and varying the matter content N_{mat} . The scaling dimensions undergo large fluctuations during the numerical variation. Furthermore, large variations are observed across different truncation orders. A snapshot is shown at $N = 101$ in Figure 6.3 (with a relative sign change with respect to the previous figure). The left panel displays the relevant scaling dimensions, where it can be clearly appreciated that a pair of complex irrelevant critical exponents become relevant as matter fields are added. The crossing point, denoted \tilde{N}_{mat} varies with N . The mean values of the crossing point are:

N	\tilde{N}_{mat}
≤ 25	0.643
26 – 51	0.699
52 – 76	0.702
77 – 101	0.749

No fixed point merger occurs as the eigenvalues cross the zero.

The right panel in Figure 6.3 shows the irrelevant end of the eigenspectrum, where a complex pair of scaling dimensions becomes very large for small matter content. This is consistently found in almost every order occurring at different values of N_{mat} , often within the cross over regime that was described in the previous section. Such large deviations indicate strong non-perturbative behaviour, thus these results should be treated carefully. This may be an artefact of the numerical variation path, other paths may avoid such large values. This could be checked in future studies.

Note that some stability is observed close to $N_{mat} = 1$ as the values do not change considerably. However, it has already been established in Figure 6.2 that these values, while stable in N_{mat} , fluctuate with N , meaning they stabilise to different values at each order.

Finally, it should be noted that the lower order approximations see a second complex pair of scaling dimensions becoming relevant closer towards the SM matter configuration and taking large values (not pictured). However, this tendency decreases at higher orders with the values staying irrelevant and close to zero. Nonetheless, this effect can still be found at up to order $N = 81$, producing an additional relevant direction, as was noted in the left panel of Figure 6.2. This explains the relatively large spread of the leading scaling dimensions in the right panel of the same figure.

6.5 Relevant directions

An additional pair of relevant scaling dimensions appears as matter is introduced in the system. A natural question is then, what are the RG directions associated to these critical exponents? This section attempts to shed some light on these question by revisiting the scaling dimensions and stability matrix. The technical details required to address this question are briefly explained first.

The eigenvalue equation for the stability matrix is:

$$M[V]^n = \vartheta_n[V]^n \tag{6.3}$$

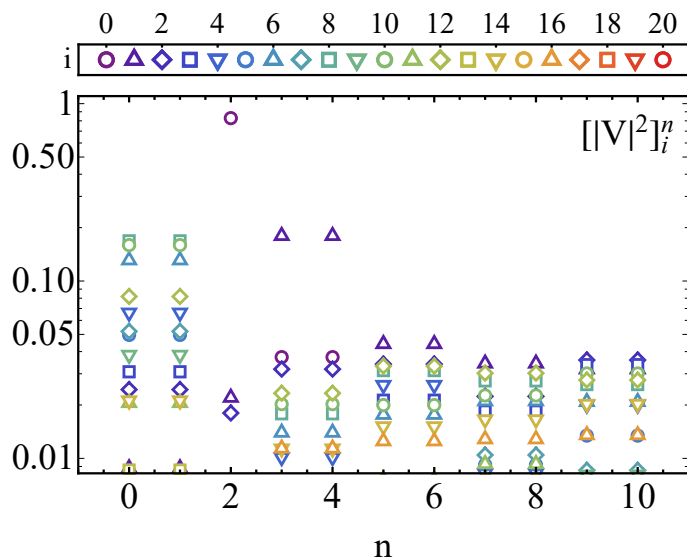


Figure 6.4: Eigenvectors of the stability matrix at the SM matter configuration and $N = 101$. The first five are relevant and the rest, irrelevant. The data points in each column indicate the elements of each eigenvector, associated with operators in the actions. The index i refers to the R^i operator.

The matrix of eigenvectors V of the stability matrix M contains in its columns the eigenvectors $[V]^n$ associated with the eigenvalues ϑ_n of M . The components $[V]^n_i$ are related to each of the running couplings λ_i that parametrise the interactions present in the action. This constitutes a space of running couplings, or space of operators, wherein RG flows exist. We put forward the interpretation that the components of the eigenvectors are the projections in the space of operators that the RG trajectories going into and out of the fixed point are associated with. In other words, the absolute value of the eigenvectors $[|V|^2]^n$ define the direction that RG flows point towards, around the fixed point, in the phase diagram of the theory.

To further disentangle the mixing of components due to large differences in the magnitude of couplings, V is transformed into a doubly-stochastic matrix, effectively projecting the eigenvectors into the unit sphere S^N , such that:

$$\sum_{i=0}^{N-1} [|V|^2]^n_i = \mathbf{1}^\top, \quad \sum_{n=0}^{N-1} [|V|^2]^n_i = \mathbf{1} \quad (6.4)$$

where $\mathbf{1}$ is a vector of all ones with N elements, the subscript denotes row and superscript denotes column, and the convention of taking the initial index as zero is adopted. This is equivalent to a similarity transformation of the stability matrix, corresponding to a linear transformation of the couplings, which leave the critical exponents unchanged.

The eigenvectors associated with the eleven most relevant scaling dimensions are shown

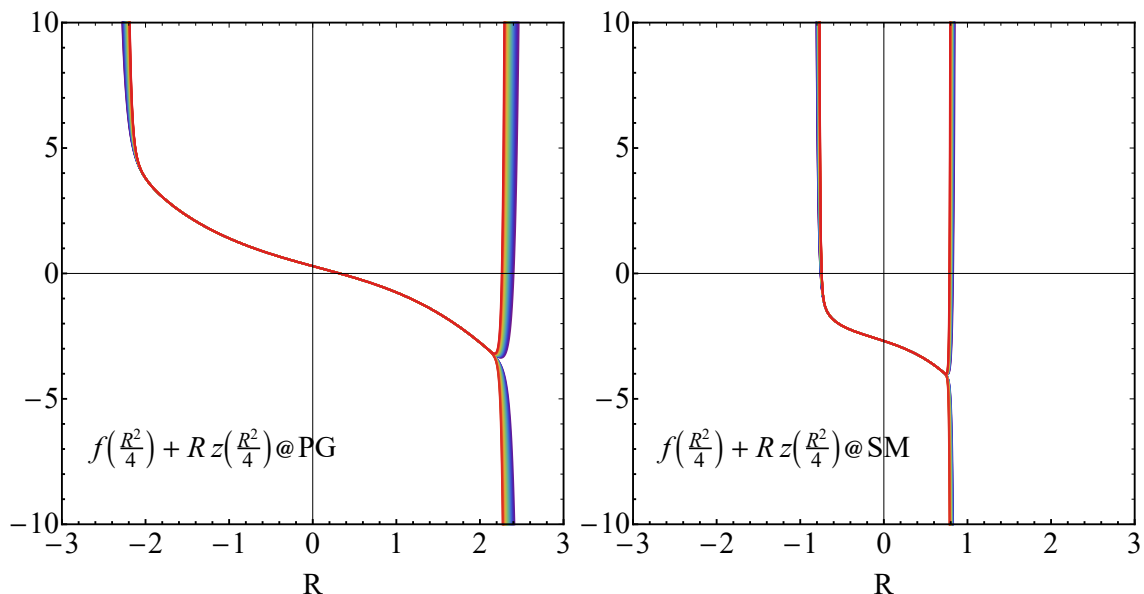


Figure 6.5: Polynomial action as a function of the scalar curvature at approximations $N = 51$ (violet) to $N = 101$ (red). The left panel shows the theory without matter, the right one, with SM matter.

in Figure 6.4 at the SM matter configuration and $N = 101$. The data points are the i components of each doubly-normalised squared eigenvector $[[V|^2]_i^n$, with the index n of the vector in the horizontal axis, ranked from relevant to irrelevant. The legend on the top associates data markers with the order in scalar curvature of the operators in the action. The plot reveals that the most relevant pair of critical exponents are associated to RG flows mainly projected on a combination of the $(R_{\mu\nu}R^{\mu\nu})^4$, $(R_{\mu\nu}R^{\mu\nu})^5$ and $(R_{\mu\nu}R^{\mu\nu})^3$ directions. The third exponent clearly corresponds to an RG flow in the direction of the cosmological constant. The fourth and fifth correspond to flows mostly projected on the R direction, while the rest show a mixture of directions.

The third through fifth RG trajectories are familiar from the theory without matter. The first and second are new and appear due to matter. Thus, matter has sourced new relevant RG flows to appear projected on the $((R_{\mu\nu}R^{\mu\nu})^4, (R_{\mu\nu}R^{\mu\nu})^5, (R_{\mu\nu}R^{\mu\nu})^3)$ directions. This, in turn, implies large anomalous scaling dimensions at the fixed point turning canonically irrelevant operators relevant in the UV.

6.6 Convergence

Owing to substantial changes in the coupling values, the domain of convergence of the polynomial approximation is heavily restricted in the presence of SM matter. Figure 6.5

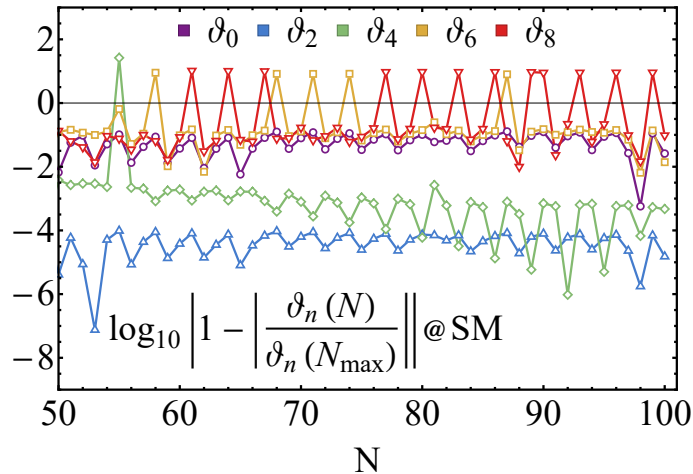


Figure 6.6: Rate of convergence of the scaling dimensions associated with the fixed point at the SM matter configuration.

shows the polynomial action as a function of R in the pure gravity theory (left panel) and with SM matter (right panel) for approximations $N > 50$. The action with SM matter is shifted down due to the cosmological constant becoming negative. Moreover, the large values of the higher order couplings lead to a substantial reduction in the radius of convergence with respect to the scalar curvature. While the pure gravity theory has a radius of convergence $R_C \approx 2$, this is narrowed to $R_C \approx 0.8$ in the theory with matter. Furthermore, the equation of motion does not admit any solutions within the radius of convergence (not pictured).

The convergence rate at higher polynomial orders can be quantitatively measured by counting the number of digits that stop changing in the scaling dimensions as the order N is increased. This is shown in Figure 6.6 on the negative axis for the first five scaling dimensions that differ in their real part (see Table E.2 in Appendix E) for $N > 50$. The plot elucidates that convergence is capped for all the values shown, reaching a maximum of five digits of convergence for ϑ_2 . The rate of convergence, indicating how many additional orders are required to achieve a further digit of accuracy, can in principle be extracted by taking the inverse of the slope of the linear fit of the data. However, no statistically significant estimate can be drawn from the shown data. Thus, this polynomial solution is most likely not approximating a physical fixed point of the full theory.

6.7 Conclusions

This study has employed a numerical variation analysis to show that the fixed point of $f(R, Ric^2)$ in pure gravity can be translated to the SM case, albeit at a great cost.

Numerical convergence towards higher approximation orders is heavily eroded for coupling values and is limited for scaling dimensions. Thus, critical exponents converge only to finite accuracy, indicating that the polynomial solution may not be approaching a fixed point of the full theory. Moreover, close to the SM matter configuration, coupling values are very sensitive to the matter content. This means that adding a few additional BSM matter fields can result in large changes of the higher order couplings.

The theory develops two additional relevant scaling dimensions due to quantum matter effects, resulting in a UV-critical surface that is five-dimensional. However, this is qualitatively different from other fixed points with SM matter that also display five relevant RG directions in two aspects (see Chapter 5). First, there are no Riemann interactions in this model that can source an additional relevant direction, meaning that both are due to quantum matter effects. Second, the new relevant RG directions originate from scaling dimensions which would be highly irrelevant in the pure gravity case. Moreover, these new values become even more relevant than the three commonly found relevant RG directions in gravity. The analysis of eigenvectors shows that these two new RG flows are associated with higher order operators. Thus, matter is inducing large anomalous scaling dimensions which turn highly irrelevant scaling dimensions into highly relevant ones.

Overall, the solution extrapolated to the SM case is not considered to be reliable. It would seem that the theories of pure gravity and the SM setting hold different families of fixed points which control the UV behaviour of each theory but which are not necessarily continuously connected. This is similar to the findings of Chapter 3 which explored the theory space of gravitational interactions. Then, fixed points of the theory appearing at some point in the parameter space may only be reliable within some domain of applicability close to that point. This is an hypothesis which can be further investigated in future studies. For example, the variational analysis could be performed in the reverse direction, translating the fixed points found with SM matter to the pure gravity case. A quick analysis at low orders finds that it may not be possible to translate these solutions to the pure gravity case in a simple manner. Further investigation is required and is left for future work.

Chapter 7

Gravitational fixed points in the large N limit

7.1 Introduction

The previous chapters have identified fixed points of pure gravity and of gravity with SM matter. These solutions have been shown to be stable up to very high orders in curvature, displaying fast numerical convergence at fixed field content. However, large variations in the matter field multiplicities can destabilise these solutions beyond the Einstein-Hilbert theory. Thus, it would seem that multiple families of fixed points can arise to control the UV behaviour of the theory in different regions of the parameter space. This chapter examines a further scenario where a new family of solutions appears, the large matter regime. Building on the results obtained so far, the computational toolbox previously developed is employed once more to investigate the large matter limit numerically.

The current understanding is that matter quantum fluctuations dominate over metric fluctuations in the large matter regime and can source a fixed point. The scenario was first considered perturbatively [39,40] and later non-perturbatively in the framework of the FRG [225,226]. However, graviton fluctuations were neglected in those studies, amounting to a semi-classical treatment, where gravity remained classical while matter is treated as a quantum field. Such an approach does not capture quantum gravitational effects. This has been improved upon in [210] using flat background approximations. There, it was shown that the Einstein-Hilbert theory in the large matter limit can have quantum gravity fixed points that scale with the number of matter fields. The present study accounts for the gravitational contributions to the flow equation beyond Einstein-Hilbert and looks for fixed points with many matter fields.

The investigation is organised in the following manner. Section 7.2 numerically looks for fixed points of the flow equation at large matter content, fully accounting for non-perturbative gravitational effects. The data suggests that an scaling limit of the couplings exists, which is investigated analytically in Section 7.3. Section 7.4 investigates critical exponents and renormalisation group flows of the theory. Section 7.5 considers scheme and parametrisation-independence of the results. Finally, Section 7.6 presents the conclusions.

7.2 Conformal window of matter-induced asymptotic safety

The large matter regime is investigated for the polynomial $f(R)$ gravitational theory. The flow equation of this theory has the general form:

$$\partial_t f(R) + 4f(R) - 2Rf'(R) = I_Q + I_M \quad (7.1)$$

The left-hand side is the classical part and the right-hand side arises due to quantum effects. The term I_Q encodes the corrections due to graviton interactions, I_M , those due to the matter fields and the prime notation $f'(R)$ denotes the derivative of the function with respect to the argument. Explicit expressions for I_Q have been derived in refs. [192, 263] and are reproduced in Appendix B. As before, free matter fields are considered; their contributions to the flow equation have been derived in Chapter 4. The matter multiplicities are free parameters of the flow equation and in this section they will be set to large finite values. It will be useful to fix the ratios of matter fields from the start and use N_{mat} to count the overall field multiplicities. Additionally, N (without subscript) is the order of the polynomial approximation as in previous chapters. Once the proportion of matter fields is fixed, the theory has only two free parameters, (N, N_{mat}) . The strategy of this search is to numerically solve the flow equation at a large and finite value of N_{mat} and then vary this parameter to understand how the solutions depend on the number of fields and what is the range where such fixed points are valid. Matter is incorporated in three steps, first adding only gauge bosons, then adding scalars and lastly, adding fermions.

Consider first a gravitational theory with only gauge bosons and $N_{mat} = 10^8$. The theory has two interesting fixed points, FP_2 and FP_3 with two and three relevant RG directions each and critical exponents being very close to the classical values. These solutions can be found at every approximation order N with virtually no numerical variation. This observation agrees with the notion that gravitational effects are suppressed in this scenario.

Once the fixed points are identified at an starting point, N_{mat} is reduced in finite

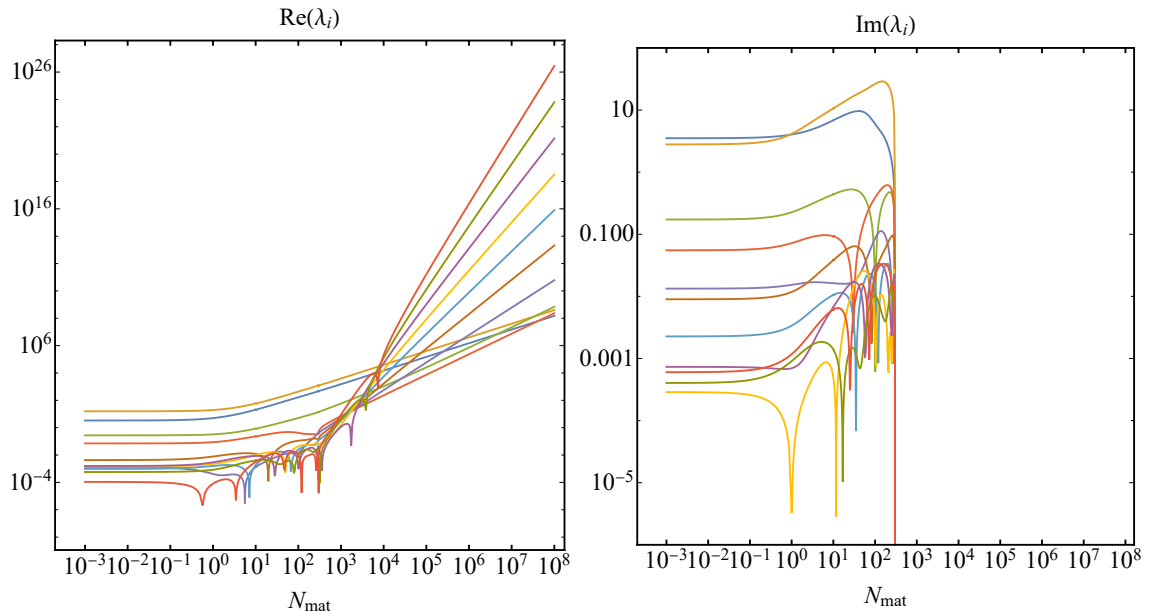


Figure 7.1: Real and imaginary parts of the couplings values of FP_2 , in a matter configuration with only gauge bosons, at $N = 11$.

steps following the solutions until all matter is removed from the system. This has been performed at up to order $N = 11$, using the same numerical variation algorithm employed in Chapter 6. At the highest order, 805 points were used with variable spacing, as higher resolution was required in regions of large numerical variations to ensure the quality of the data. The main results of this section are Figures 7.1 and 7.2, displaying the coupling values and critical exponents of FP_2 as a function of N_{mat} , respectively. These plots are discussed in detail now, noting that the results are qualitatively similar for FP_3 .

From right to left across N_{mat} , three distinct regimes can be identified in the plots where the behaviour of the fixed points changes. First, the couplings follow a linear relation at large N_{mat} in the logarithmic plot. This indicates a power-law scaling with N_{mat} , such that $\lambda_n \propto (N_{mat})^{\alpha_n}$, with α given by the slopes of the lines. The data suggests the following scaling for the couplings:

$$\lambda_n \propto \begin{cases} N_{mat}, & n = \{0, 1\} \\ (N_{mat})^{3/2}, & n = 2 \\ (N_{mat})^{n/2}, & n \geq 3 \end{cases} \quad (7.2)$$

Thus, in this regime, the fixed point is mostly determined by the matter field multiplicities up to a constant. The eigenvalues fall very close to the canonical dimensions and show little deviation.

As the number of matter fields is decreased, the solution enters a cross-over regime at

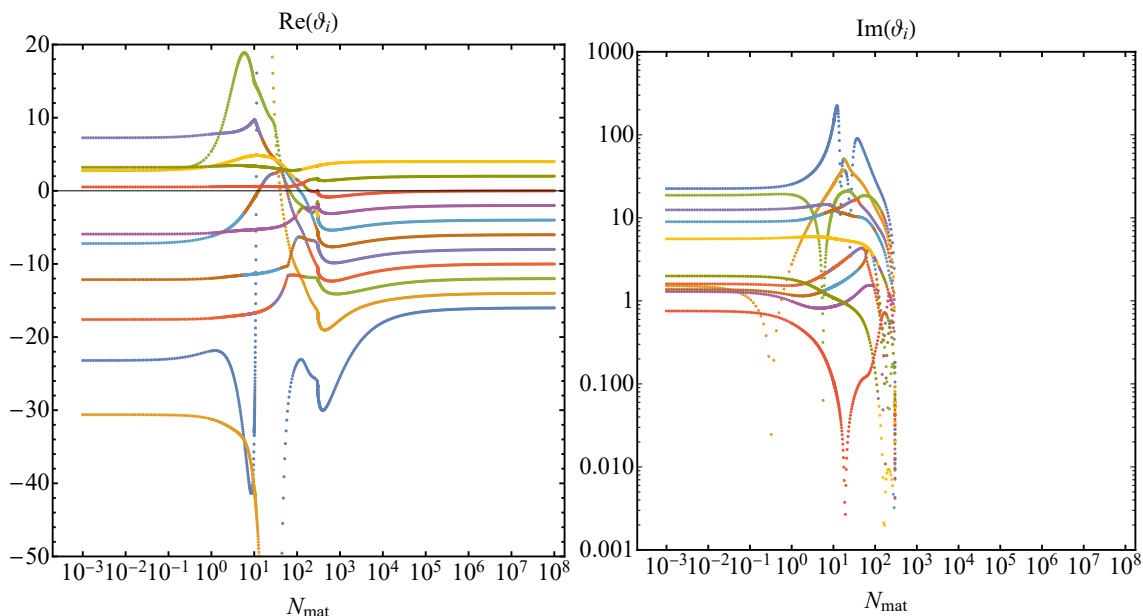


Figure 7.2: Real and imaginary parts of the eigenvalues of FP_2 , in a matter configuration with only gauge bosons, at $N = 11$.

$N_{mat} \approx 10^4$, where gravitational effects start to become more important. A fixed point merger appears, forcing the couplings into the complex plane at $N_M \approx 300$ for FP_2 and $N_M = 3850$ for FP_3 (not pictured). Thus, FP_2 and FP_3 get annihilated by other, probably spurious, solutions of the flow equation. This is shown in the right panel of Figure 7.1 where the couplings develop an imaginary part, and is also signalled by the marginally irrelevant eigenvalue approaching zero in the left panel of Figure 7.2 (third line from top to bottom on the right).

Following the now complex solution, a third regime is found below $N_M \approx 1$. Couplings and critical exponents remain roughly constant until all matter is removed. Fluctuations from the matter sector are negligible in this region because the number of matter fields is very small. The solution remains complex until all matter is removed, with eigenvalues falling away from Gaussian scaling.

Adding a small number of scalar fields into the system does not qualitatively change the behaviour but it does shift the merger towards higher N_{mat} , closing the conformal window. Fixing the ratio of scalars to gauge bosons at 1:3, the merger appears at $N_{mat} = 5900$ for FP_2 and $N_{mat} \approx 2.22 \times 10^5$ for FP_3 . This suggests that the spin-0 fields have a destabilising effect on these solutions.

However, fermions have an even more pronounced negative effect. As fermions are gradually added into the system, the solutions annihilate each other at a matter ratio $N_S:N_M:N_D$ of 1:3:2.125. In other words, only up to two fermions are allowed per one

$N_S:N_M:N_D$	$N_{crit.}^{(FP_2)}$	$N_{crit.}^{(FP_3)}$
0:1:0	299	3,850
1:3:0	5,900	221,780
1:3:2.125	∞	∞

Table 7.1: Boundary of the conformal window of the large N fixed point where solutions annihilate through a fixed point merger. The third row indicates the maximum proportion of fermions with the given scalar and gauge boson ratios. No real solution is available for the given ratios even in the formal $N \rightarrow \infty$ limit, as indicated by the LO solution, eq. (7.9).

scalar and three gauge bosons. Above this number, no physical solutions appear in the numerical search for any larger values of N_{mat} nor at higher approximation orders N . The boundary of the conformal window of the theory in these three scenarios is summarised in Table 7.1, indicating as $N_{crit.}$ the value where the merger appears.

7.3 Fixed points of the large matter regime

The power-law scaling observed in the couplings in the large matter regime suggests that an analytic scaling limit may exist. The different types of matter fields do not modify this scaling, although fermions do turn the solutions complex. It would be interesting then to find a physical justification for this scaling and understand if analytical expressions for these fixed points can be obtained. This section provides further insight into this limit by undertaking an analytic treatment of the flow equation in the large matter regime.

7.3.1 Enhanced quantum gravity fluctuations

The scaling of the couplings observed in the numerical analysis can be understood by considering the quantum corrections to the flow equation. The contributions due to the matter sector in a four dimensional spherical background can be written as

$$I_M = -A - B R - C R^2 \quad (7.3)$$

with

$$A = \frac{4N_D - 2N_M - N_S}{2\pi}, \quad B = \frac{-2N_D + 4N_M - N_S}{6\pi}, \quad C = \frac{11N_D + 62N_M - 29N_S}{2160\pi} \quad (7.4)$$

A minus sign has been extracted from the coefficients for later convenience and the quantities are multiplied by a factor of 16π according to the definition of the action employed here (see Appendix B). In the large matter limit, these terms are proportional to N_{mat} and must be cancelled for a fixed point to appear. Thus, the polynomial couplings λ_0 , λ_1 and λ_2 should naively be rescaled with a power of N_{mat} to participate at the same order as the matter terms. The beta functions for these rescaled couplings are then

$$\partial_t \lambda_0 = -A - 4\lambda_0, \quad \partial_t \lambda_1 = -B - 2\lambda_1, \quad \partial_t \lambda_2 = -C \quad (7.5)$$

From now on, a factor of N_{mat} is extracted from A , B and C , such that these are numbers of order one. This is the result found in ref. [225], where classical corrections due to the canonical mass dimension of the couplings balance with A and B . However, λ_2 is canonically marginal and has zero mass dimension. Therefore, it does not appear in the classical part of the flow equation and cannot cancel CR^2 .

The only way to achieve a complete cancellation of the matter contributions is if a term of order $N_{mat}R^2$ is generated from the quantum gravitational corrections. These contributions can be written as:

$$I_Q = V_a(R) + S_a(R) + T_g(R, F(R)) + S_g(R, F(R)) \quad (7.6)$$

The first two terms arise due to the gravitational ghosts and auxiliary fields introduced in the renormalisation process. They are independent of the action and will not play a meaningful role in this study. The other two, T_g and S_g , arise from the transverse traceless tensor and scalar modes of the metric fluctuation, respectively. They are non-linear functions of the action and contain terms that can potentially balance with the matter contributions. However, these terms are of order one if λ_2 is rescaled with N_{mat} and thus, cannot compete with $N_{mat}R^2$.

Consider instead the rescaling $\lambda_2 \rightarrow \lambda_2(N_{mat})^a$ with $a > 1$ an open real parameter. The contribution T_g can be expanded in a double series first on small R and then on small $1/N_{mat}$, finding at order R^2 the leading term $(N_{mat})^{2(-1+a)}$. Requiring this to be of order N_{mat} uniquely determines $a = 3/2$. In other words, the rescaling $\lambda_2 \rightarrow \lambda_2(N_{mat})^{3/2}$ enhances quantum corrections due to the physical tensor mode of the graviton to compete with matter terms at order $N_{mat}R^2$. Moreover, this scaling generates coefficients of order $(N_{mat})^{n/2}R^n$ for $n \geq 3$ in the quantum part of the equation. Therefore, the rescaling of the higher order couplings is also uniquely fixed such that these terms cancel, leading to

the proposed rescaled couplings:

$$\lambda_n \rightarrow \begin{cases} \lambda_n(N_{mat}) & n = \{0, 1\} \\ \lambda_n(N_{mat})^{3/2} & n = 2 \\ \lambda_n(N_{mat})^{n/2} & n \geq 3 \end{cases} \quad (7.7)$$

It is now briefly noted that expanding S_g can also source a term that competes with the matter contribution under a different scaling. However, this is not favoured for three reasons. First, S_g corresponds to fluctuations of the conformal mode of the graviton which is an unphysical degree of freedom, and this alternative scaling suppresses fluctuations from the physical transverse traceless mode. Second, the scaling only works if higher order couplings are present, implying a non-perturbative cancellation between higher curvature-order terms. Third, this solution can be found numerically but displays extremely large critical exponents that scale with N_{mat} and are deemed to be unphysical.

7.3.2 Fixed points in the infinite N limit

Under the new rescaling (7.7), the running of λ_2 is

$$\partial_t \lambda_2 = - \left(C + \frac{5}{3\pi} \frac{(B + 6\lambda_0)\lambda_2^2}{(\lambda_0 + \lambda_1)^3} \right) \frac{1}{\sqrt{N_{mat}}} \quad (7.8)$$

The gravitational quantum correction can now compete with the matter contribution C and source a non-trivial fixed point for all three couplings. Moreover, the running of this coupling is now suppressed by a factor of $1/\sqrt{N_{mat}}$. Thus, a large number of matter fields has the effect of *freezing* the running of this coupling. The fixed point coordinates can now be written explicitly in terms of the matter contributions:

$$\lambda_0^* = -\frac{A}{4}, \quad \lambda_1^* = -\frac{B}{2}, \quad \lambda_2^* = \pm \sqrt{\frac{3\pi}{160} \frac{(A + 2B)^3 C}{-3A + 2B}} \quad (7.9)$$

Coefficient B imposes a restriction in the matter configuration to obtain a positive Newton's coupling. Additionally, the squared root imposes a second constraint for the fixed point to be real-valued. It will be shortly shown that λ_2 modifies λ_0 and λ_1 at subleading orders, such that these couplings can also acquire a small but non-zero imaginary part if λ_2 becomes complex. The theories with only scalars or only fermions are ruled out by these constraints. Furthermore, the field content of the SM not only results in a negative Newton's constant but also leads to complex values, as was already pointed out in the numerical analysis. The numerical results are found to be in agreement with these expressions for large finite N_{mat} .

The running of the higher order couplings takes the generic form:

$$\partial_t \lambda_n = -(4 - 2n)\lambda_n - \frac{5 \times 2^{n-2}}{3\pi} \left(-\frac{\lambda_2}{\lambda_0 + \lambda_1} \right)^n \left(\frac{2(3\lambda_0 - \lambda_1) - \partial_t \lambda_1}{\lambda_0 + \lambda_1} \right) \quad (7.10)$$

for $n \geq 3$. The first term is the classical contribution due to the mass dimension of the couplings while the second term is the leading quantum effect. The beta functions are decoupled and thus, the fixed point of these couplings is completely determined by the value of λ_0 , λ_1 and λ_2 ,

$$\lambda_n = \frac{5 \times 2^{n-2}}{3\pi(n-2)} \left(\frac{3\lambda_0 - \lambda_1}{\lambda_0 + \lambda_1} \right) \left(-\frac{\lambda_2}{\lambda_0 + \lambda_1} \right)^n, \quad \text{for } n \geq 3 \quad (7.11)$$

where the star * notation is suppressed from now on. The two roots of λ_2 lead to solutions which differ in sign for odd index n . Thus, one fixed point has all couplings positive, while the other has couplings with alternating signs. Moreover, these infinitely many higher order couplings can be resummed into a compact expression,

$$\sum_{n=3}^{\infty} \lambda_n R^n = -\frac{5}{3\pi} \frac{(3\lambda_0 - \lambda_1)\lambda_2^2}{(\lambda_0 + \lambda_1)^3} R^2 \log \left(1 + \frac{2\lambda_2}{\lambda_0 + \lambda_1} R \right) \quad (7.12)$$

This amounts to recovering a Coleman-Weinberg gravitational potential where higher order interactions are encoded in the $R^2 \log(c + R)$ term, with c some constant. It is remarkable that although the polynomial approximation was assumed at the start, this scaling allows all higher derivative interactions to be collected into an expression which is valid for any curvature value.

7.3.3 Fixed points beyond the infinite N limit

The previous results represent the leading order (LO) in a large N_{mat} expansion. Now that the scaling with N_{mat} has been fixed to LO, subleading corrections can be computed by writing each coupling as a power series of $1/\sqrt{N_{mat}}$,

$$\begin{aligned} f(R) = & \sum_{j=1} \lambda_{0,j}(N_{mat})^{(3-j)/2} + \sum_{j=1} \lambda_{1,j}(N_{mat})^{(3-j)/2} R + \sum_{j=1} \lambda_{2,j}(N_{mat})^{(4-j)/2} R^2 \\ & + \sum_{n=3} \sum_{j=1} \lambda_{n,j}(N_{mat})^{(1+n-j)/2} R^n \end{aligned} \quad (7.13)$$

Where $\lambda_{n,1}$ can be identified with the previous expressions for λ_n at LO. At next-to-leading order (NLO), contributions from the other terms in the quantum corrections to the flow equation also come into play. Expanding the flow equation in R and $1/N_{mat}$, the

non-trivial NLO terms of the first three couplings are:

$$\lambda_{0,3} = -\frac{1}{12\pi} \frac{3\lambda_{0,1} - 7\lambda_{1,1}}{\lambda_{0,1} + \lambda_{1,1}} \quad (7.14)$$

$$\lambda_{1,2} = \frac{5}{6\pi} \frac{(3\lambda_{0,1} - \lambda_{1,1})\lambda_{2,1}}{(\lambda_{0,1} + \lambda_{1,1})^2} \quad (7.15)$$

$$\lambda_{2,2} = -\frac{6\lambda_{0,1}^2 + 19\lambda_{0,1}\lambda_{1,1} - 19\lambda_{1,1}^2}{24(3\lambda_{0,1} - \lambda_{1,1})} + \frac{\lambda_{2,1}^2}{6\pi(\lambda_{0,1} + \lambda_{1,1})^2} \quad (7.16)$$

where $\lambda_{0,2}$ has been omitted as it is zero. As mentioned above, λ_2 not only influences the higher order couplings at LO but also impacts λ_1 at NLO and it will impact λ_0 at (non-trivial) NNLO.

Writting down the factors of N_{mat} explicitly, the higher order couplings would lead to increasing powers of N_{mat} appearing in the action. These can be absorbed by defining a rescaled scalar curvature $\hat{R} = (N_{mat})^{1/2}R$. A global solution of the action can then be written to NLO in a $1/N_{mat}$ expansion,

$$\begin{aligned} f(\hat{R}) &= \lambda_0 N_{mat} + \lambda_1 (N_{mat})^{1/2} \hat{R} + \lambda_2 (N_{mat})^{1/2} \hat{R}^2 \\ &\quad - \frac{1}{12\pi} \frac{3\lambda_0 - 7\lambda_1}{\lambda_0 + \lambda_1} + \frac{5}{6\pi} \frac{(3\lambda_0 - \lambda_1)\lambda_2}{(\lambda_0 + \lambda_1)^2} \hat{R} \\ &\quad + \left(-\frac{6\lambda_0^2 + 19\lambda_0\lambda_1 - 19\lambda_1^2}{24(3\lambda_0 - \lambda_1)} + \frac{\lambda_2^2}{6\pi(\lambda_0 + \lambda_1)^2} \right) \hat{R}^2 \\ &\quad - \frac{5}{3\pi} \frac{(3\lambda_0 - \lambda_1)\lambda_2^2}{(\lambda_0 + \lambda_1)^3} \hat{R}^2 \log \left(1 + \frac{2\lambda_2}{\lambda_0 + \lambda_1} \hat{R} \right) + \mathcal{O}(N_{mat}^{-1/2}) \end{aligned} \quad (7.17)$$

The advantage of working with \hat{R} is that global solutions of the flow equation can be found order by order in a systematic $1/N_{mat}$ expansion by solving a first-order differential equation at each order. The results of these equations will contain exact resummed expressions of the higher order couplings. Integration constants proportional to R^2 appear at every order, which can be determined using the polynomial approximation. It should be noted that both approaches are equivalent and the rest of the study will continue using the polynomial approximation.

7.4 Critical behaviour

This section examines the scaling behaviour close to the fixed point. Expressions for the beta functions and critical exponents are derived in the polynomial approximation revealing near-Gaussian scaling. Renormalisation Group flows are found connecting the UV-safe theory to a Gaussian regime in the IR.

7.4.1 Beta functions

The beta functions can be expressed as a $1/N_{mat}$ series in the polynomial approximation:

$$\partial_t \lambda_i = \beta_i = \sum_{j=0} b_{i,j} N_{mat}^{-j/2} \quad (7.18)$$

This is similar in spirit to a loop expansion in any ordinary perturbative quantum field theory, wherein the small parameter is $1/N_{mat}$. The $b_{i,j}$ coefficients are the analogues of the j th loop order coefficient of the beta function of λ_i . The leading order coefficients $b_{i,0}$ were already determined in the previous section as well as $b_{2,1}$. The first subleading corrections to the running of λ_0 and λ_1 are

$$b_{0,2} = -4\lambda_{0,3} + \frac{3}{2\pi} - \frac{5}{12\pi} \frac{B + 6\lambda_{0,1}}{\lambda_{0,1} + \lambda_{1,1}} \quad (7.19)$$

$$b_{1,1} = -2\lambda_{1,2} + \frac{5}{6\pi} \frac{(B + 6\lambda_{0,1})\lambda_{2,1}}{(\lambda_{0,1} + \lambda_{1,1})^2} \quad (7.20)$$

The coefficient $b_{0,1}$ has been omitted as it is zero. These equations together with $b_{2,1}$ form a closed system as no higher order couplings appear at this order. The form of the coefficients $b_{n,1}$ for $n \geq 3$ takes a more complicated form but includes a term linear in the couplings,

$$b_{n,1} = -\frac{10n}{3\pi} \frac{(3\lambda_{0,1} - \lambda_{1,1} - \frac{1}{2}b_{1,0})\lambda_{2,1}}{(\lambda_{0,1} + \lambda_{1,1})^3} \lambda_{n,1} + \varepsilon \quad (7.21)$$

where ε stands for other terms that have been neglected. This term is shown explicitly because, as illustrated in the next subsection, it defines the diagonal part of the stability matrix and determines the critical exponents to NLO.

7.4.2 Scaling dimensions

The RG flow in the neighbourhood of a fixed point can be characterised to linear order by the stability matrix, defined as:

$$M_{i,j} = \left. \frac{\partial \beta_i}{\partial \lambda_j} \right|_* \quad (7.22)$$

The scaling dimensions are the negative of the eigenvalues of this matrix, which can be found via the eigenvalue equation:

$$\det(M - \vartheta_n I) = 0 \quad (7.23)$$

with ϑ_n being the eigenvalue associated to an eigenvector V_n and I the identity matrix. Taking the perturbative expansion of the beta functions (7.18), the stability matrix can be written in a similar manner:

$$M_{i,j} = m_{i,j}^{(1)} + m_{i,j}^{(2)} N_{mat}^{-1/2} + m_{i,j}^{(3)} N_{mat}^{-1} + \mathcal{O}(N_{mat}^{-3/2}) \quad (7.24)$$

Then, the eigenvalue equation immediately implies that the eigenvalues can also be written in such an expansion:

$$\vartheta_n = \vartheta_{n,1} + \vartheta_{n,2}N_{mat}^{-1/2} + \vartheta_{n,3}N_{mat}^{-1} + \mathcal{O}\left(N_{mat}^{-3/2}\right) \quad (7.25)$$

where the coefficients in this expression can be consistently computed order by order. A simple power-counting argument shows that the eigenvalues are completely determined by the diagonal part of the matrix to NLO. With the beta functions from the previous subsection, the eigenvalues can be written as:

$$\vartheta_n = (2n - 4) - n \frac{\chi}{\sqrt{N_{mat}}} + \mathcal{O}\left(N_{mat}^{-1}\right) \quad (7.26)$$

for $n \geq 0$, with:

$$\chi = \frac{10}{3\pi} \frac{(3\lambda_{0,1} - \lambda_{1,1})\lambda_{2,1}}{(\lambda_{0,1} + \lambda_{1,1})^3} \quad (7.27)$$

This is the anomalous scaling dimension that shifts the spectrum from Gaussian scaling due to weak interactions in the UV. The two stationary points have a two and three-dimensional UV critical surface, respectively. Note that $\vartheta_{0,2}$ is zero since $\lambda_{0,2}$ is itself zero. The leading non-zero anomalous dimension to this exponent appears at the next order.

The coefficients $\vartheta_{n,3}$ can be obtained by extending the analysis of the beta functions to NNLO. At this order, the eigenvalues also depend on the first sub and super-diagonals of the stability matrix. In general, denoting the index of the diagonal as d , where $d = 0$ is the main diagonal, at order $N^n LO$, the expressions depend on the diagonals $d = [-n+1, n-1]$, for $n > 0$. For the first six eigenvalues, these coefficients are:

$$\vartheta_{0,3} = -\frac{10\lambda_{1,1}}{3\pi(\lambda_{0,1} + \lambda_{1,1})^2} \quad (7.28)$$

$$\vartheta_{1,3} = \tau\chi - \frac{(6\lambda_{0,1}^2 + 31\lambda_{0,1}\lambda_{1,1} - 7\lambda_{1,1}^2)}{24(3\lambda_{0,1} - \lambda_{1,1})} \frac{\chi}{\lambda_{2,1}} - \frac{(19\lambda_{0,1} - 11\lambda_{1,1})}{10(3\lambda_{0,1} - \lambda_{1,1})} \chi^2 \quad (7.29)$$

$$\vartheta_{2,3} = 2\tau\chi - \frac{(6\lambda_{0,1}^2 + 19\lambda_{0,1}\lambda_{1,1} - 19\lambda_{1,1}^2)}{24(3\lambda_{0,1} - \lambda_{1,1})} \frac{2\chi}{\lambda_{2,1}} - \frac{2(8\lambda_{0,1} - 7\lambda_{1,1})}{5(3\lambda_{0,1} - \lambda_{1,1})} \chi^2 \quad (7.30)$$

$$\vartheta_{3,3} = 3\tau\chi - \frac{(6\lambda_{0,1}^2 + 15\lambda_{0,1}\lambda_{1,1} - 23\lambda_{1,1}^2)}{24(3\lambda_{0,1} - \lambda_{1,1})} \frac{3\chi}{\lambda_{2,1}} - \frac{3(8\lambda_{0,1} - 7\lambda_{1,1})}{5(3\lambda_{0,1} - \lambda_{1,1})} \chi^2 \quad (7.31)$$

$$\vartheta_{4,3} = 4\tau\chi - \frac{(6\lambda_{0,1}^2 + 13\lambda_{0,1}\lambda_{1,1} - 25\lambda_{1,1}^2)}{24(3\lambda_{0,1} - \lambda_{1,1})} \frac{4\chi}{\lambda_{2,1}} - \frac{2(19\lambda_{0,1} - 11\lambda_{1,1})}{5(3\lambda_{0,1} - \lambda_{1,1})} \chi^2 \quad (7.32)$$

$$\vartheta_{5,3} = 5\tau\chi - \frac{(6\lambda_{0,1}^2 + \frac{59}{5}\lambda_{0,1}\lambda_{1,1} - \frac{131}{5}\lambda_{1,1}^2)}{24(3\lambda_{0,1} - \lambda_{1,1})} \frac{5\chi}{\lambda_{2,1}} + \frac{(19\lambda_{0,1} + 34\lambda_{1,1})}{(3\lambda_{0,1} - \lambda_{1,1})} \chi^2 \quad (7.33)$$

with the auxiliary variable:

$$\tau = \left(\frac{3\lambda_{1,2}}{\lambda_{0,1} + \lambda_{1,1}} - \frac{\lambda_{2,2}}{\lambda_{2,1}} \right) \quad (7.34)$$

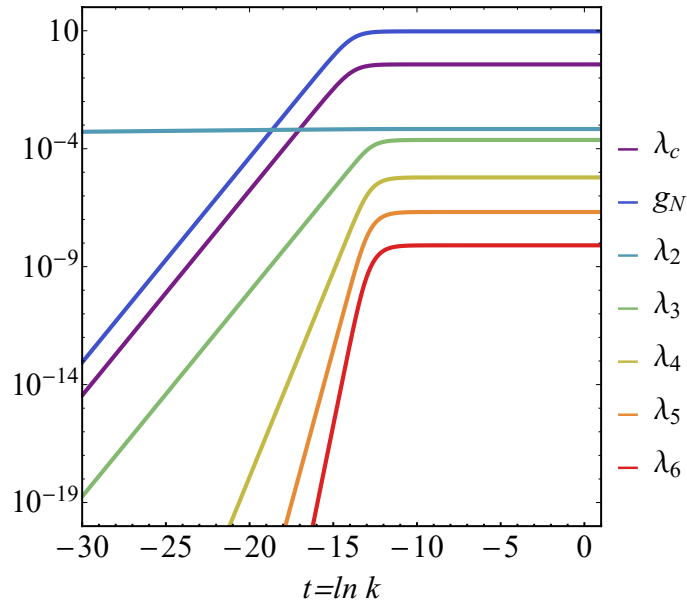


Figure 7.3: RG trajectory connecting the FP_2 with a Gaussian regime in the IR with $N_{mat} = 10^6$ gauge bosons. Only the first seven couplings are shown. The factors of N_{mat} have been extracted from the couplings in this plot to aid visualisation.

The subleading corrections to the eigenvalues can induce a sign change at a finite matter value $N_{crit.}$. This would correspond to the merger found in the numerical analysis. However, the estimate derived from these expressions is much lower than what was previously found. In a theory of only gauge bosons, the expressions at NLO predict $N_{crit.} \approx 45$ for FP_2 and $N_{crit.} \approx 403$ for FP_3 . At NNLO, these values shift to $N_{crit.} \approx 108$ for FP_2 and $N_{crit.} \approx 503$ for FP_3 . The bounds are smaller than the result of the numerical analysis by a factor of 3 and 9, respectively. This suggests that the $1/N_{mat}$ expansion is only applicable at extremely large N_{mat} and that strong quantum gravity effects are not being captured at NNLO.

7.4.3 UV-IR connecting trajectories

A fundamental theory can describe physics at all energy scales. Thus, there should exist RG flows that connect the UV fixed point to a regime compatible with GR in the IR and end at a finite point at infinite lengths. The flow of λ_c and g_N can be obtained by integrating their beta functions to leading order in the $1/\sqrt{N_{mat}}$ expansion:

$$\lambda_c(t) = -\frac{-\frac{A}{4} + c_0 e^{-4t}}{2(-\frac{B}{2} + c_1 e^{-2t})} + \mathcal{O}(N_{mat}^{-1/2}) \quad (7.35)$$

$$g_N(t) = -\frac{1}{-\frac{B}{2} + c_1 e^{-2t}} + \mathcal{O}(N_{mat}^{-1/2}) \quad (7.36)$$

where c_0 and c_1 are integration constants setting the measured values of couplings at a reference energy scale. The couplings flow into the fixed point at high energies, while at low energies, g_N vanishes and λ_c would apparently diverge. This is because the cosmological constant is an irrelevant direction of the Gaussian fixed point. However, the constants can be fixed to lie in the trajectory that flows exactly into the Gaussian.

It is not as straightforward to obtain a general expression for the fourth-derivative order coupling, as its beta function takes the form of a Riccati equation:

$$\frac{d\lambda_2}{dt} = - \left(C + \frac{5(B + 6\lambda_0(t))}{3\pi(\lambda_0(t) + \lambda_1(t))^3} (\lambda_2)^2 \right) \frac{1}{\sqrt{N_{mat}}} + \mathcal{O}(N_{mat}^{-1}) \quad (7.37)$$

One can instead focus on the asymptotic behaviour of the couplings within the interesting trajectories. In the deep UV, when λ_0 and λ_1 are at their fixed point values, the dependence on t drops out from the coefficient in front of $(\lambda_2)^2$ and the equation greatly simplifies, yielding:

$$\lambda_2(t)|_{UV} = -\lambda_2^* \tanh \left(\frac{C\lambda_2^{*3}}{\sqrt{N_{mat}}} (t - c_2) \right) \quad (7.38)$$

where c_2 is an integration constant setting the value of λ_2 at a reference scale. The hyperbolic tangent behaviour reflects the fact that λ_2 can flow from FP_2 to FP_3 . The signs unambiguously indicate that the negative-valued λ_2 is the fully stable UV attractor (FP_3) with the positive-valued one being meta-stable in the UV (FP_2).

At low energies, λ_c and g_N approach the Gaussian, thus the equation simplifies to:

$$\left. \frac{d\lambda_2}{dt} \right|_{IR} = - \frac{C}{\sqrt{N_{mat}}} \quad (7.39)$$

This result is similar to the running in the semi-classical approximation (7.5) but with an additional factor of $1/\sqrt{N_{mat}}$, which arises from the rescaling of λ_2 . This running indicates logarithmic growth towards lower energies for λ_2 . Note that in both (7.38) and (7.39), N_{mat} effectively rescales the RG time t , such that, as indicated before, matter slows down the flow of λ_2 across all energy scales.

Similarly, the beta functions of the higher order couplings simplify in these two regimes, leading to:

$$\lambda_j(t) \Big|_{IR} = c_j e^{(-4+2j)t} + \mathcal{O}(N_{mat}^{-1/2}) \quad (7.40)$$

$$\lambda_j(t) \Big|_{UV} = \lambda_j^* + c_j e^{(-4+2j)t} + \mathcal{O}(N_{mat}^{-1/2}) \quad (7.41)$$

valid for $j \geq 3$. As indicated by the critical exponents in the previous section, these are irrelevant couplings and their integration constants c_j must be set to zero to lie in

the trajectory that flows exactly into the fixed point in the UV. Their behaviour in the neighbourhood of the fixed point is dominated by the classical scaling dimensions.

The gap between the UV and IR expressions obtained above can be bridged by performing a numerical integration, producing the diagram of the running couplings shown in Figure 7.3 to LO. Starting at the UV FP in the right side of the plot, the couplings decrease in magnitude towards the IR to the left, with a short crossover regime in the middle. This cross-over regime was neglected by the previous expressions but does not display any behaviour out of the ordinary. The coupling λ_2 does not appear to move in the plot, however, this is due to the large number of matter fields in the system, with the plot showing the running with $N_M = 10^6$ gauge bosons and no scalars nor fermions. In fact, the coupling is running but its flow is bogged down by matter, with $\beta_2|_{IR}$ of order 10^{-9} . This is as indicated before, a large amount of matter has the effect of *freezing* the marginal coupling.

7.5 Scheme and parametrisation independence

This section briefly explores how the fixed point is modified by a change of regularisation scheme and fluctuation metric parametrisation. The effect of these changes amounts to subleading corrections and does not lead to qualitative modifications to the fixed point.

7.5.1 Higher order matter contributions

Matter corrections up to order R^2 have been considered so far. Nonetheless, there are other regularisation schemes where higher order corrections can appear. This can occur, for example, if an exponential regulator is used instead of the optimised profile function. Thus, it would be useful to understand the extent to which the obtained results are affected by scheme-dependence.

Consider a flow equation where matter quantum fluctuations of order N_{mat} contribute at every order in R . The rescaling (7.7) indicates that the higher order quantum gravity terms scale as $(N_{mat})^{n/2}R^n$, meanwhile, the matter terms scale only as $N_{mat}R^n$. Thus, the new matter contributions are increasingly subleading at each order and amount to only subleading corrections of the coupling values, with the largest correction being to λ_3 at NLO. Note, however, that λ_3 appears in the expression of the other couplings at NNLO. Therefore, couplings are implicitly modified at NNLO due to λ_3 . This is summarised in Table 7.2 which schematically denotes how matter terms of order R^3 and higher induce both explicit (E) and implicit (I) corrections to the couplings.

	LO	NLO	NNLO	NNNLO	N ⁴ LO	N ⁵ LO
λ_0	-	-	-	-	-	I
λ_1	-	-	-	I	I	I
λ_2	-	-	I	I	I	I
λ_3	-	E	I	I	I	I
λ_4	-	-	E	I	I	I
λ_5	-	-	I	E	I	I
λ_6	-	-	I	I	E	I
λ_7	-	-	I	I	I	E

Table 7.2: Schematic impact on the fixed point due to matter terms of order R^3 and higher. E indicates that matter explicitly appears in the equation of the corresponding term. I indicates that matter corrections appear implicitly through other couplings.

7.5.2 Parametrisation of graviton fluctuations

The expressions for the quantum corrections employed in this study have been derived using the linear parametrisation of the metric fluctuations. Another possible choice is the exponential parametrisation, where background and fluctuations are separated according to:

$$g_{\mu\nu} = \bar{g}_{\mu\rho}(e^h)^\rho{}_\nu \quad (7.42)$$

This has the advantage of preserving the sign of the metric for large fluctuations and allows to directly identify the conformal mode. The quantum corrections of the gravitational sector in this parametrisation have been computed in ref. [189] and result in only slight changes in the expressions compared to the linear parametrisation. The most significant difference for this analysis is that λ_0 drops out from the tensor mode of the graviton fluctuation and thus, is completely decoupled from the equations. Therefore, the value of λ_2 can be obtained by simply setting $\lambda_0 \rightarrow 0$ (or $A \rightarrow 0$) at LO:

$$\lambda_2^{(exp)} = \pm \sqrt{\frac{3\pi}{10} \left(-\frac{B}{2}\right)^2 C} \quad (7.43)$$

This modifies the constraint on the matter configurations by dropping A from this expression. The only qualitative difference is that the exponential split leads to complex solutions for the scalar-only theory, which was already excluded in the linear parametrisation because $g_N < 0$. The same replacement can be applied in (7.11) for the higher order

couplings at LO:

$$\lambda_{n,1}^{(exp)} = -\frac{5 \times 2^{n-2}}{3\pi(n-2)} \left(-\frac{\lambda_{2,1}^{(exp)}}{\lambda_{1,1}} \right)^n, \quad \text{for } n \geq 3 \quad (7.44)$$

The fluctuations due to the scalar mode of the trace and auxiliary fields come into play at NLO resulting in further modifications to the expressions. Defining $\Delta\lambda_{n,j} = \lambda_{n,j}^{(exp)} - \lambda_{n,j}^{(lin)}$, the remainder for λ_0 at NLO is:

$$\Delta\lambda_{0,3} = \frac{5\lambda_{0,1}}{6\pi(\lambda_{0,1} + \lambda_{1,1})} \quad (7.45)$$

As for the other couplings, setting $\lambda_0 \rightarrow 0$ leaves:

$$\Delta\lambda_{1,2} = 0 \quad (7.46)$$

$$\Delta\lambda_{2,2} = \frac{5}{8}\lambda_{1,1} + \frac{1}{2\pi} \left(\frac{\lambda_{2,1}^{(exp)}}{\lambda_{1,1}} \right)^2 \quad (7.47)$$

For the higher order interactions, the remainder after setting $\lambda_0 \rightarrow 0$ has the general form:

$$\Delta\lambda_{n,2} = u_n^{(1)} \left(\frac{\lambda_{2,1}^{(exp)}}{\lambda_{1,1}} \right)^{n-1} + \frac{u_n^{(2)}}{\lambda_{1,1}} \left(\frac{\lambda_{2,1}^{(exp)}}{\lambda_{1,1}} \right)^{n+1} \quad (7.48)$$

with $u_n^{(1)}$ and $u_n^{(2)}$ constants.

The beta functions only differ by a term proportional to λ_0 at LO, while further differences appear at NLO that do not vanish when λ_0 is set to zero. However, the diagonal part of the stability matrix remains structurally unchanged. The eq. (7.26) for the eigenvalues only gets modified by setting $\lambda_0 \rightarrow 0$ and replacing $\lambda_2^{(lin)} \rightarrow \lambda_2^{(exp)}$ in the exponential parametrisation. Thus, the expression for the eigenvalues remains structurally unchanged up to NLO.

7.6 Conclusions

This study has performed a systematic investigation of fixed points in the large matter regime in the $f(R)$ theory. A numerical analysis finds two fixed points with coupling values mostly determined by the number of matter fields in this setting. The critical exponents show only small deviations from classical scaling, with the marginal direction becoming either relevant or irrelevant. Moreover, couplings seem to follow a power-law scaling with the field multiplicities, suggesting the existence of an analytical scaling limit. Thus, a new scaling regime has been put forward based on this numerical observation.

An analytic treatment has found that quantum corrections arising from the tensor mode of the metric are enhanced under this rescaling in the large matter limit. This

enhancement allows metric fluctuations to balance with quantum matter corrections at leading order in a $1/N_{mat}$ expansion, leading to a non-trivial fixed point for the canonically marginal coupling. This coupling, in turn, sources a fixed point for all higher order interactions. Therefore, the numerical results can be understood to arise from a $1/N_{mat}$ expansion in this scaling limit. Analytic expressions for fixed point values can be systematically determined order by order in this expansion. Remarkably, higher order interactions can be resummed into a closed expression of the form of a Coleman-Weinberg potential. The result is valid for any value of the scalar curvature, defining a general solution of the action.

The new scaling limit also imposes restrictions on the matter content for the fixed point to be physical. The overall effect of scalar and fermion fields is to destabilise the solutions, bounding the conformal window at a finite value $N_{crit.}$. With sufficiently many fermions, the fixed points annihilate for any arbitrarily large N_{mat} . The bound on the conformal window can also be estimated from sign changes in the analytic expressions for critical exponents. However, the estimates for $N_{crit.}$ from these expressions are much smaller than the values observed in the numerical analysis. This suggests that the scaling limit has a limited domain of applicability and is only valid for very large N_{mat} .

Renormalisation group flows are available connecting the fixed points to a Gaussian regime in the IR. It is interesting to note that the running of the fourth derivative-order coupling is suppressed by a factor of $1/\sqrt{N_{mat}}$, meaning that its flow is parametrically slower than that of the other interactions. Finally, it's been shown that the solutions are largely insensitive to changes in the regularisation scheme and metric parametrisation. This is consistent with the notion that the fixed points are mostly driven by the physical metric fluctuations and quantum matter corrections, as these should be largely independent of details of the regularisation procedure.

Chapter 8

Conclusions

Formulating a consistent quantum theory of gravity compatible with the Standard Model faces many challenges. This thesis has studied the prospect for asymptotically safe extensions of gravity in the presence of matter fields and also exploring the role played by higher curvature invariants. Thereby, a number of new results have been achieved and are summarised now. A systematic search of fixed points in pure quantum gravity has been performed, including a scan over higher curvature interactions (Chapter 3). Notably, the Einstein-Hilbert fixed point becomes modified, often mildly, but sometimes more strongly, leading to a consistent higher curvature extension of the theory.

The focus has then been extended to the inclusion of matter, where technical aspects regarding their implementation have been clarified (Chapter 4). This has been followed by a comprehensive study of fixed points of quantum gravity with higher curvature invariants and Standard Model matter (Chapter 5). Several aspects are worth highlighting. Gravitational fixed points compatible with the Standard Model only arise if higher derivative curvature invariants involving Ricci and Riemann tensor interactions also appear in the action. The role of these operators is crucial and their importance cannot be stressed enough, as no physical solution with the Standard Model field content is available without them (within the approximations of this study). The result does depend on the type of matter fields, however, with free fermions tending to destabilise gravitational fixed points in the framework adopted here. Another noteworthy aspect is that scaling dimensions come out mostly real, unlike in the purely gravitational settings. Shifts in scaling dimensions are of the order of a few, in agreement with expectations and previous findings. In some settings, the presence of matter fields leads to new relevant eigenperturbations. This aspect is intriguing and would benefit from further scrutiny in the future. Theories admit well-defined UV-IR connecting trajectories, showing that these models can be viewed as

viable UV completions of the Standard Model with gravity.

The question of whether gravitational fixed points with and without Standard Model matter are connected has also been investigated, using the number of matter fields as interpolation parameters (Chapter 6). Perhaps surprisingly, the answer turns out to be negative. Moving away from pure gravity or gravity with SM matter rapidly makes either the fixed point disappear in the complex plane or generate unphysically large scaling dimensions which cannot be trusted. Moreover, limited convergence is observed in the scaling dimensions, casting doubt on the reliability of the fixed point. Therefore, it may be concluded that SM matter cannot be viewed as a small perturbation to a purely gravitational fixed point. In this light, pure quantum gravity and quantum gravity with SM matter are rather different theories and should be viewed as belonging to different universality classes.

Furthermore, the asymptotic limit of many matter fields ($N \rightarrow \infty$) coupled to higher curvature quantum gravity has been investigated (Chapter 7). Two key results are worth highlighting. First, a new scaling limit is found with near-Gaussian scaling exponents, both numerically and analytically. This scaling allows a systematic $1/\sqrt{N}$ expansion, establishing for the first time that large- N matter fluctuations can compete with fluctuations of the metric field to generate an asymptotically safe UV fixed point to all orders in Ricci curvature, including a global, closed expression for the UV fixed functional to the leading order in $1/N$. The UV conformal window of this new matter-gravity fixed point has been determined within an $f(R)$ approximation, as well as constraints on the matter content. This result opens a door for systematic fixed point searches in gravity-matter theories.

A new toolkit for numerical computations, developed by the author during the investigations performed in this thesis, allowed to investigate gravitational theories up to 100th curvature-order. Achieving such high polynomial order was important for two reasons. First, some solutions may seem reliable at low orders but destabilise later. Thus, more than a handful of spurious fixed points were discarded in the analysis of Chapter 6 narrowing the solutions to the ones presented there. Second, exploring high orders allowed to capture the asymptotic behaviour of the polynomial solutions. In some of the examples discussed here, this only sets in above the 60th polynomial order. Moreover, previous investigations were able to investigate only a few select models. The parallelisable nature of the algorithms employed allowed the author to explore hundreds of models with different gravitational interactions and matter content to very high polynomial order.

This thesis has argued that higher order interactions of curvature tensors can be key

elements to reconciling a fixed point of gravity with the Standard Model. Future investigations could consider other curvature invariants that have been left out from this study, as they may also become important at high energies. Other parametrisation choices can be explored to better understand the behaviour of the new solutions found in this investigation. Similarly, matter self-interactions and interactions with curvature can modify the constraints on the field content in the Einstein theory. It would thus be interesting to understand how such interactions could affect the dynamics when higher curvature interactions are included as well. Moreover, the new scaling limit uncovered here offers new settings where gravity can be renormalisable in four dimensions in a controlled expansion with a small parameter. A natural extension of this investigation would be to study the theory in a general background where the running of the three independent fourth-derivative order couplings can be untangled. Finally, many other models and generalisations can be considered to assess the reliability of the results. To conclude, the road to formulating a fundamental theory of quantum gravity with matter is long and tortuous. This thesis has aimed to bring the scientific effort a step closer towards achieving this goal.

Bibliography

- [1] S.L. Glashow. Partial Symmetries of Weak Interactions. *Nucl. Phys.*, 22:579–588, 1961. [1](#)
- [2] Steven Weinberg. A Model of Leptons. *Phys. Rev. Lett.*, 19:1264–1266, 1967. [1](#)
- [3] Abdus Salam. Weak and Electromagnetic Interactions. *Conf. Proc. C*, 680519:367–377, 1968. [1](#)
- [4] Peter W. Higgs. Broken Symmetries and the Masses of Gauge Bosons. *Phys. Rev. Lett.*, 13:508–509, 1964. [[160\(1964\)](#)]. [1](#)
- [5] David J. Gross and Frank Wilczek. Ultraviolet Behavior of Nonabelian Gauge Theories. *Phys. Rev. Lett.*, 30:1343–1346, 1973. [[271\(1973\)](#)]. [1](#)
- [6] H. David Politzer. Reliable Perturbative Results for Strong Interactions? *Phys. Rev. Lett.*, 30:1346–1349, 1973. [[274\(1973\)](#)]. [1](#)
- [7] M. Tanabashi et al. Review of Particle Physics. *Phys. Rev. D*, 98(3):030001, 2018. [1](#)
- [8] Georges Aad et al. Observation of a new particle in the search for the Standard Model Higgs boson with the ATLAS detector at the LHC. *Phys. Lett. B*, 716:1–29, 2012. [1](#)
- [9] Serguei Chatrchyan et al. Observation of a New Boson at a Mass of 125 GeV with the CMS Experiment at the LHC. *Phys. Lett. B*, 716:30–61, 2012. [1](#)
- [10] B.P. Abbott et al. Observation of Gravitational Waves from a Binary Black Hole Merger. *Phys. Rev. Lett.*, 116(6):061102, 2016. [1](#)
- [11] A.D. Sakharov. Violation of CP Invariance, C asymmetry, and baryon asymmetry of the universe. *Sov. Phys. Usp.*, 34(5):392–393, 1991. [1](#)

- [12] Y. Fukuda et al. Evidence for oscillation of atmospheric neutrinos. *Phys. Rev. Lett.*, 81:1562–1567, 1998. [1](#)
- [13] Q.R. Ahmad et al. Direct evidence for neutrino flavor transformation from neutral current interactions in the Sudbury Neutrino Observatory. *Phys. Rev. Lett.*, 89:011301, 2002. [1](#)
- [14] Giuseppe Degrandi, Stefano Di Vita, Joan Elias-Miro, Jose R. Espinosa, Gian F. Giudice, Gino Isidori, and Alessandro Strumia. Higgs mass and vacuum stability in the Standard Model at NNLO. *JHEP*, 08:098, 2012. [1](#)
- [15] Dario Buttazzo, Giuseppe Degrandi, Pier Paolo Giardino, Gian F. Giudice, Filippo Sala, Alberto Salvio, and Alessandro Strumia. Investigating the near-criticality of the Higgs boson. *JHEP*, 12:089, 2013. [1](#)
- [16] Steven Weinberg. The Cosmological Constant Problem. *Rev. Mod. Phys.*, 61:1–23, 1989. [1](#)
- [17] Gerard 't Hooft and M. J. G. Veltman. One loop divergencies in the theory of gravitation. *Ann. Inst. H. Poincare Phys. Theor.*, A20:69–94, 1974. [2](#)
- [18] S. M. Christensen and M. J. Duff. Quantizing Gravity with a Cosmological Constant. *Nucl. Phys.*, B170:480–506, 1980. [2](#)
- [19] Marc H. Goroff and Augusto Sagnotti. QUANTUM GRAVITY AT TWO LOOPS. *Phys. Lett.*, 160B:81–86, 1985. [2](#)
- [20] Marc H. Goroff and Augusto Sagnotti. The Ultraviolet Behavior of Einstein Gravity. *Nucl. Phys.*, B266:709–736, 1986. [2](#)
- [21] Stanley Deser and P. van Nieuwenhuizen. One Loop Divergences of Quantized Einstein-Maxwell Fields. *Phys. Rev. D*, 10:401, 1974. [2](#)
- [22] Stanley Deser, Hung-Sheng Tsao, and P. van Nieuwenhuizen. One Loop Divergences of the Einstein Yang-Mills System. *Phys. Rev. D*, 10:3337, 1974. [2](#)
- [23] Stanley Deser and P. van Nieuwenhuizen. Nonrenormalizability of the Quantized Dirac-Einstein System. *Phys. Rev. D*, 10:411, 1974. [2](#)
- [24] M.J. Duff. Observations on Conformal Anomalies. *Nucl. Phys. B*, 125:334–348, 1977. [2](#), [61](#)

- [25] J.S. Dowker and Raymond Critchley. The Stress Tensor Conformal Anomaly for Scalar and Spinor Fields. *Phys. Rev. D*, 16:3390, 1977. [2](#)
- [26] Hung-Sheng Tsao. Conformal Anomalies in a General Background Metric. *Phys. Lett. B*, 68:79–80, 1977. [2](#)
- [27] E. S. Fradkin and Arkady A. Tseytlin. Renormalizable asymptotically free quantum theory of gravity. *Nucl. Phys.*, B201:469–491, 1982. [2](#), [61](#)
- [28] K. S. Stelle. Renormalization of Higher Derivative Quantum Gravity. *Phys. Rev.*, D16:953–969, 1977. [2](#)
- [29] I.G. Avramidi and A.O. Barvinsky. ASYMPTOTIC FREEDOM IN HIGHER DERIVATIVE QUANTUM GRAVITY. *Phys. Lett. B*, 159:269–274, 1985. [2](#)
- [30] E.T. Tomboulis. Superrenormalizable gauge and gravitational theories. [2](#) 1997. [2](#), [34](#)
- [31] Leonardo Modesto. Super-renormalizable Quantum Gravity. *Phys. Rev. D*, 86:044005, 2012. [2](#)
- [32] Steven Weinberg. General Relativity: An Einstein Centenary Survey. In S Hawking and Werner Israel, editors, *General Relativity: An Einstein Centenary Survey*, chapter Ultraviole, pages 790–831. Cambridge University Press, Cambridge, 1979. [2](#), [5](#), [8](#)
- [33] K. G. Wilson and John B. Kogut. The Renormalization group and the epsilon expansion. *Phys. Rept.*, 12:75–199, 1974. [2](#), [4](#)
- [34] Kenneth G. Wilson. The Renormalization Group: Critical Phenomena and the Kondo Problem. *Rev. Mod. Phys.*, 47:773, 1975. [2](#), [4](#)
- [35] R. Gastmans, R. Kallosh, and C. Truffin. Quantum Gravity Near Two-Dimensions. *Nucl. Phys. B*, 133:417–434, 1978. [2](#)
- [36] S.M. Christensen and M.J. Duff. Quantum Gravity in Two + ϵ Dimensions. *Phys. Lett. B*, 79:213–216, 1978. [2](#)
- [37] Hikaru Kawai, Yoshihisa Kitazawa, and Masao Ninomiya. Scaling exponents in quantum gravity near two-dimensions. *Nucl. Phys. B*, 393:280–300, 1993. [2](#)

- [38] Hikaru Kawai, Yoshihisa Kitazawa, and Masao Ninomiya. Ultraviolet stable fixed point and scaling relations in $(2+\epsilon)$ -dimensional quantum gravity. *Nucl. Phys. B*, 404:684–716, 1993. [2](#)
- [39] Lee Smolin. A Fixed Point for Quantum Gravity. *Nucl. Phys.*, B208:439–466, 1982. [2](#), [34](#), [112](#)
- [40] E. Tomboulis. $1/N$ Expansion and Renormalization in Quantum Gravity. *Phys. Lett.*, 70B:361–364, 1977. [2](#), [112](#)
- [41] M. Reuter. Nonperturbative evolution equation for quantum gravity. *Phys. Rev. D*, 57:971–985, 1998. [2](#), [13](#), [25](#), [31](#), [54](#)
- [42] Jr. Callan, Curtis G. Broken scale invariance in scalar field theory. *Phys. Rev. D*, 2:1541–1547, 1970. [5](#)
- [43] K. Symanzik. Small distance behavior in field theory and power counting. *Commun. Math. Phys.*, 18:227–246, 1970. [5](#)
- [44] Didier Sornette. Discrete scale invariance and complex dimensions. *Phys. Rept.*, 297:239–270, 1998. [8](#)
- [45] V. Efimov. Energy levels arising from the resonant two-body forces in a three-body system. *Phys. Lett. B*, 33:563–564, 1970. [8](#)
- [46] T. Kraemer, M. Mark, P. Waldburger, J. G. Danzl, C. Chin, B. Engeser, A. D. Lange, K. Pilch, A. Jaakkola, H.-C. Nägerl, and R. Grimm. Evidence for Efimov quantum states in an ultracold gas of caesium atoms. *Nature*, 440:315–318, 2006. [8](#)
- [47] S. Knoop, F. Ferlaino, M. Mark, M. Berninger, H. Schöbel, H.-C. Nägerl, and R. Grimm. Observation of an Efimov-like trimer resonance in ultracold atom–dimer scattering. *Nature Physics*, 5, 2009. [8](#)
- [48] Scott E. Pollack, Daniel Dries, and Randall G. Hulet. Universality in three- and four-body bound states of ultracold atoms. *Science*, 326(5960):1683–1685, 2009. [8](#)
- [49] Daniel Litim and Alejandro Satz. Limit cycles and quantum gravity. 5 2012. [8](#)
- [50] Kenneth G. Wilson. Renormalization group and critical phenomena. 1. Renormalization group and the Kadanoff scaling picture. *Phys. Rev. B*, 4:3174–3183, 1971. [8](#)

- [51] Kenneth G. Wilson. Renormalization group and critical phenomena. 2. Phase space cell analysis of critical behavior. *Phys. Rev. B*, 4:3184–3205, 1971. [8](#)
- [52] Kenneth G. Wilson and Michael E. Fisher. Critical exponents in 3.99 dimensions. *Phys. Rev. Lett.*, 28:240–243, 1972. [8](#)
- [53] N. Tetradis and D.F. Litim. Analytical solutions of exact renormalization group equations. *Nucl. Phys. B*, 464:492–511, 1996. [8](#)
- [54] Astrid Eichhorn, David Mesterházy, and Michael M. Scherer. Multicritical behavior in models with two competing order parameters. *Phys. Rev. E*, 88:042141, 2013. [8](#)
- [55] Daniel F. Litim and Edouard Marchais. Critical $O(N)$ models in the complex field plane. *Phys. Rev. D*, 95(2):025026, 2017. [8](#)
- [56] Daniel F. Litim, Edouard Marchais, and Péter Mati. Fixed points and the spontaneous breaking of scale invariance. *Phys. Rev. D*, 95(12):125006, 2017. [8](#)
- [57] Andreas Jüttner, Daniel F. Litim, and Edouard Marchais. Global Wilson–Fisher fixed points. *Nucl. Phys. B*, 921:769–795, 2017. [8](#)
- [58] Daniel F. Litim and Matthew J. Trott. Asymptotic safety of scalar field theories. *Phys. Rev. D*, 98(12):125006, 2018. [8](#), [17](#)
- [59] David J. Gross and Andre Neveu. Dynamical Symmetry Breaking in Asymptotically Free Field Theories. *Phys. Rev. D*, 10:3235, 1974. [8](#)
- [60] K. Gawedzki and A. Kupiainen. Renormalization of a Nonrenormalizable Quantum Field Theory. *Nucl. Phys. B*, 262:33–48, 1985. [8](#)
- [61] Baruch Rosenstein, Brian J. Warr, and Seon H. Park. The Four Fermi Theory Is Renormalizable in (2+1)-Dimensions. *Phys. Rev. Lett.*, 62:1433–1436, 1989. [8](#)
- [62] C. de Calan, P.A. Faria da Veiga, J. Magnen, and R. Seneor. Constructing the three-dimensional Gross-Neveu model with a large number of flavor components. *Phys. Rev. Lett.*, 66:3233–3236, 1991. [8](#)
- [63] Jens Braun, Holger Gies, and Daniel D. Scherer. Asymptotic safety: a simple example. *Phys. Rev. D*, 83:085012, 2011. [8](#)
- [64] A. Jakovac and A. Patkos. Local potential approximation for the renormalization group flow of fermionic field theories. *Phys. Rev. D*, 88:065008, 2013. [8](#)

- [65] A. Jakovác, A. Patkós, and P. Pósfay. Non-Gaussian fixed points in fermionic field theories without auxiliary Bose-fields. *Eur. Phys. J. C*, 75(1):2, 2015. [8](#)
- [66] Tom Banks and A. Zaks. On the Phase Structure of Vector-Like Gauge Theories with Massless Fermions. *Nucl. Phys.*, B196:189–204, 1982. [8](#), [10](#)
- [67] David B. Kaplan, Jong-Wan Lee, Dam T. Son, and Mikhail A. Stephanov. Conformality Lost. *Phys. Rev. D*, 80:125005, 2009. [8](#)
- [68] Michael E. Peskin. CRITICAL POINT BEHAVIOR OF THE WILSON LOOP. *Phys. Lett. B*, 94:161–165, 1980. [8](#)
- [69] Holger Gies. Renormalizability of gauge theories in extra dimensions. *Phys. Rev. D*, 68:085015, 2003. [8](#)
- [70] Daniel F. Litim and Francesco Sannino. Asymptotic safety guaranteed. *JHEP*, 12:178, 2014. [9](#), [97](#)
- [71] Andrew D. Bond and Daniel F. Litim. More asymptotic safety guaranteed. *Phys. Rev. D*, 97(8):085008, 2018. [9](#), [12](#)
- [72] Andrew D. Bond and Daniel F. Litim. Theorems for Asymptotic Safety of Gauge Theories. *Eur. Phys. J.*, C77(6):429, 2017. [Erratum: *Eur. Phys. J.*C77,no.8,525(2017)]. [10](#)
- [73] Andrew D. Bond and Daniel F. Litim. Price of Asymptotic Safety. *Phys. Rev. Lett.*, 122(21):211601, 2019. [10](#)
- [74] Daniel F. Litim, Matin Mojaza, and Francesco Sannino. Vacuum stability of asymptotically safe gauge-Yukawa theories. *JHEP*, 01:081, 2016. [11](#)
- [75] Andrew D. Bond, Daniel F. Litim, Gustavo Medina Vazquez, and Tom Steudtner. UV conformal window for asymptotic safety. *Phys. Rev. D*, 97(3):036019, 2018. [11](#)
- [76] Daniel F. Litim and Gustavo Medina Vazquez. Closing in on conformal windows with finite N corrections. In preparation. [11](#)
- [77] Alessandro Codello, Kasper Langæble, Daniel F. Litim, and Francesco Sannino. Conformal Gauge-Yukawa Theories away From Four Dimensions. *JHEP*, 07:118, 2016. [11](#)
- [78] Andrew D. Bond and Daniel F. Litim. Asymptotic safety guaranteed in supersymmetry. *Phys. Rev. Lett.*, 119(21):211601, 2017. [11](#), [97](#)

- [79] Tugba Buyukbese and Daniel F. Litim. Asymptotic safety of gauge theories beyond marginal interactions. *PoS, LATTICE2016:233*, 2017. [12](#)
- [80] Andrew D. Bond, Daniel F. Litim, and Tom Steudtner. Asymptotic safety with Majorana fermions and new large N equivalences. *Phys. Rev. D*, 101(4):045006, 2020. [12](#)
- [81] Andrew D. Bond, Gudrun Hiller, Kamila Kowalska, and Daniel F. Litim. Directions for model building from asymptotic safety. *JHEP*, 08:004, 2017. [12](#)
- [82] Kamila Kowalska, Andrew Bond, Gudrun Hiller, and Daniel Litim. Towards an asymptotically safe completion of the Standard Model. *PoS, EPS-HEP2017:542*, 2017. [12](#)
- [83] Daniele Barducci, Marco Fabbrichesi, Carlos M. Nieto, Roberto Percacci, and Vedran Skrinjar. In search of a UV completion of the standard model — 378,000 models that don't work. *JHEP*, 11:057, 2018. [12](#)
- [84] Gudrun Hiller, Clara Hormigos-Feliu, Daniel F. Litim, and Tom Steudtner. Asymptotically safe extensions of the Standard Model with flavour phenomenology. In *54th Rencontres de Moriond on Electroweak Interactions and Unified Theories*, pages 415–418, 2019. [12](#), [97](#)
- [85] Gudrun Hiller, Clara Hormigos-Feliu, Daniel F. Litim, and Tom Steudtner. Model Building from Asymptotic Safety with Higgs and Flavor Portals. 8 2020. [12](#)
- [86] Gudrun Hiller, Clara Hormigos-Feliu, Daniel F. Litim, and Tom Steudtner. Anomalous magnetic moments from asymptotic safety. 10 2019. [12](#), [97](#)
- [87] A. Palanques-Mestre and P. Pascual. The $1/N_f$ Expansion of the γ and Beta Functions in QED. *Commun. Math. Phys.*, 95:277, 1984. [12](#)
- [88] J.A. Gracey. The QCD Beta function at $O(1/N(f))$. *Phys. Lett. B*, 373:178–184, 1996. [12](#)
- [89] B. Holdom. Large N flavor beta-functions: a recap. *Phys. Lett. B*, 694:74–79, 2011. [12](#)
- [90] Kamila Kowalska and Enrico Maria Sessolo. Gauge contribution to the $1/N_F$ expansion of the Yukawa coupling beta function. *JHEP*, 04:027, 2018. [12](#)

- [91] Oleg Antipin, Nicola Andrea Dondi, Francesco Sannino, Anders Eller Thomsen, and Zhi-Wei Wang. Gauge-Yukawa theories: Beta functions at large N_f . *Phys. Rev.*, D98(1):016003, 2018. [12](#)
- [92] J.A. Gracey. Large N_f quantum field theory. *Int. J. Mod. Phys. A*, 33(35):1830032, 2019. [12](#)
- [93] Claudio Pica and Francesco Sannino. UV and IR Zeros of Gauge Theories at The Four Loop Order and Beyond. *Phys. Rev. D*, 83:035013, 2011. [12](#)
- [94] Borut Bajc, Nicola Andrea Dondi, and Francesco Sannino. Safe SUSY. *JHEP*, 03:005, 2018. [12](#)
- [95] Steven Abel and Francesco Sannino. Framework for an asymptotically safe Standard Model via dynamical breaking. *Phys. Rev.*, D96(5):055021, 2017. [12](#)
- [96] Steven Abel and Francesco Sannino. Radiative symmetry breaking from interacting UV fixed points. *Phys. Rev. D*, 96(5):056028, 2017. [12](#)
- [97] E. Molinaro, F. Sannino, and Z.W. Wang. Asymptotically safe Pati-Salam theory. *Phys. Rev. D*, 98(11):115007, 2018. [12](#)
- [98] Giulio Maria Pelaggi, Alexis D. Plascencia, Alberto Salvio, Francesco Sannino, Juri Smirnov, and Alessandro Strumia. Asymptotically Safe Standard Model Extensions? *Phys. Rev. D*, 97(9):095013, 2018. [12](#)
- [99] Oleg Antipin and Francesco Sannino. Conformal Window 2.0: The large N_f safe story. *Phys. Rev. D*, 97(11):116007, 2018. [12](#)
- [100] Tommi Alanne, Simone Blasi, and Nicola Andrea Dondi. Critical Look at β - Function Singularities at Large N . *Phys. Rev. Lett.*, 123(13):131602, 2019. [12](#)
- [101] Francesco Sannino and Zhi-Wei Wang. Comment on "A critical look at β -function singularities at large N " by Alanne, Blasi and Dondi. 9 2019. [12](#)
- [102] Sean P. Robinson and Frank Wilczek. Gravitational correction to running of gauge couplings. *Phys. Rev. Lett.*, 96:231601, 2006. [12](#)
- [103] Artur R. Pietrykowski. Gauge dependence of gravitational correction to running of gauge couplings. *Phys. Rev. Lett.*, 98:061801, 2007. [12](#)

- [104] Dietmar Ebert, Jan Plefka, and Andreas Rodigast. Absence of gravitational contributions to the running Yang-Mills coupling. *Phys. Lett. B*, 660:579–582, 2008. [12](#)
- [105] David J. Toms. Quantum gravity and charge renormalization. *Phys. Rev. D*, 76:045015, 2007. [12](#)
- [106] David J. Toms. Cosmological constant and quantum gravitational corrections to the running fine structure constant. *Phys. Rev. Lett.*, 101:131301, 2008. [12](#)
- [107] Jan-Eric Daum, Ulrich Harst, and Martin Reuter. Running Gauge Coupling in Asymptotically Safe Quantum Gravity. *JHEP*, 01:084, 2010. [12](#), [54](#)
- [108] David J. Toms. Quantum gravity, gauge coupling constants, and the cosmological constant. *Phys. Rev. D*, 80:064040, 2009. [12](#)
- [109] David J. Toms. Quantum gravitational contributions to quantum electrodynamics. *Nature*, 468:56–59, 2010. [12](#)
- [110] Sarah Folkerts, Daniel F. Litim, and Jan M. Pawłowski. Asymptotic freedom of Yang-Mills theory with gravity. *Phys. Lett. B*, 709:234–241, 2012. [12](#), [35](#), [54](#)
- [111] U. Harst and M. Reuter. QED coupled to QEG. *JHEP*, 05:119, 2011. [12](#), [54](#)
- [112] David J. Toms. Quadratic divergences and quantum gravitational contributions to gauge coupling constants. *Phys. Rev. D*, 84:084016, 2011. [12](#)
- [113] Nicolai Christiansen and Astrid Eichhorn. An asymptotically safe solution to the U(1) triviality problem. *Phys. Lett. B*, 770:154–160, 2017. [12](#), [35](#)
- [114] Astrid Eichhorn and Fleur Versteegen. Upper bound on the Abelian gauge coupling from asymptotic safety. *JHEP*, 01:030, 2018. [12](#), [35](#), [36](#)
- [115] Astrid Eichhorn and Marc Schiffer. $d = 4$ as the critical dimensionality of asymptotically safe interactions. *Phys. Lett. B*, 793:383–389, 2019. [12](#)
- [116] Holger Gies and Jobst Ziebell. Asymptotically Safe QED. *Eur. Phys. J. C*, 80:607, 2020. [12](#)
- [117] Kin-ya Oda and Masatoshi Yamada. Non-minimal coupling in Higgs–Yukawa model with asymptotically safe gravity. *Class. Quant. Grav.*, 33(12):125011, 2016. [12](#), [35](#)

- [118] Yuta Hamada and Masatoshi Yamada. Asymptotic safety of higher derivative quantum gravity non-minimally coupled with a matter system. *JHEP*, 08:070, 2017. [12](#), [35](#)
- [119] O. Zanusso, L. Zambelli, G.P. Vacca, and R. Percacci. Gravitational corrections to Yukawa systems. *Phys. Lett. B*, 689:90–94, 2010. [12](#)
- [120] G.P. Vacca and O. Zanusso. Asymptotic Safety in Einstein Gravity and Scalar-Fermion Matter. *Phys. Rev. Lett.*, 105:231601, 2010. [12](#), [35](#)
- [121] Astrid Eichhorn, Aaron Held, and Jan M. Pawłowski. Quantum-gravity effects on a Higgs-Yukawa model. *Phys. Rev. D*, 94(10):104027, 2016. [12](#)
- [122] Nicolai Christiansen, Astrid Eichhorn, and Aaron Held. Is scale-invariance in gauge-Yukawa systems compatible with the graviton? *Phys. Rev. D*, 96(8):084021, 2017. [13](#)
- [123] Astrid Eichhorn and Aaron Held. Viability of quantum-gravity induced ultraviolet completions for matter. *Phys. Rev. D*, 96(8):086025, 2017. [13](#), [36](#)
- [124] Peter Kopietz, Lorenz Bartosch, and Florian Schütz. *Introduction to the functional renormalization group*, volume 798. 2010. [13](#)
- [125] Robert Percacci. *An Introduction to Covariant Quantum Gravity and Asymptotic Safety*, volume 3 of *100 Years of General Relativity*. World Scientific, 2017. [13](#), [26](#)
- [126] Martin Reuter and Frank Saueressig. *Quantum Gravity and the Functional Renormalization Group: The Road towards Asymptotic Safety*. Cambridge University Press, 1 2019. [13](#)
- [127] Joseph Polchinski. Renormalization and Effective Lagrangians. *Nucl. Phys. B*, 231:269–295, 1984. [14](#)
- [128] G. Keller and Christoph Kopper. Perturbative renormalization of QED via flow equations. *Phys. Lett. B*, 273:323–332, 1991. [14](#)
- [129] Tim R. Morris. The Exact renormalization group and approximate solutions. *Int. J. Mod. Phys.*, A9:2411–2450, 1994. [14](#), [17](#), [19](#), [54](#), [56](#)
- [130] Daniel F. Litim. Optimization of the exact renormalization group. *Phys. Lett. B*, 486:92–99, 2000. [15](#)

- [131] Daniel F. Litim. Optimized renormalization group flows. *Phys. Rev. D*, 64:105007, 2001. [15](#), [58](#)
- [132] Christof Wetterich. Exact evolution equation for the effective potential. *Phys. Lett.*, B301:90–94, 1993. [17](#), [54](#), [56](#)
- [133] Ulrich Ellwanger. FLOW equations for N point functions and bound states. pages 206–211, 9 1993. [17](#)
- [134] M. Bonini, M. D’Attanasio, and G. Marchesini. Perturbative renormalization and infrared finiteness in the Wilson renormalization group: The Massless scalar case. *Nucl. Phys.*, B409:441–464, 1993. [17](#)
- [135] Daniel F. Litim. Universality and the renormalisation group. *JHEP*, 07:005, 2005. [17](#)
- [136] C. Bagnuls and C. Bervillier. Exact renormalization group equations. An Introductory review. *Phys. Rept.*, 348:91, 2001. [18](#)
- [137] Juergen Berges, Nikolaos Tetradis, and Christof Wetterich. Nonperturbative renormalization flow in quantum field theory and statistical physics. *Phys. Rept.*, 363:223–386, 2002. [18](#)
- [138] Jan M. Pawłowski. Aspects of the functional renormalisation group. *Annals Phys.*, 322:2831–2915, 2007. [18](#)
- [139] Dario Benedetti and Francesco Caravelli. The Local potential approximation in quantum gravity. *JHEP*, 06:017, 2012. [Erratum: *JHEP* 10, 157 (2012)]. [18](#), [32](#), [54](#), [55](#), [57](#), [63](#), [75](#), [79](#)
- [140] J.-P. Blaizot, Ramon Mendez Galain, and Nicolas Wschebor. A New method to solve the non perturbative renormalization group equations. *Phys. Lett. B*, 632:571–578, 2006. [19](#)
- [141] Jean-Paul Blaizot, Ramon Mendez-Galain, and Nicolas Wschebor. Non perturbative renormalization group and momentum dependence of n-point functions. II. *Phys. Rev. E*, 74:051117, 2006. [19](#)
- [142] F. Benitez, J.-P. Blaizot, H. Chate, B. Delamotte, R. Mendez-Galain, and N. Wschebor. Solutions of renormalization group flow equations with full momentum dependence. *Phys. Rev. E*, 80:030103, 2009. [19](#)

- [143] Elisa Manrique and Martin Reuter. Bimetric Truncations for Quantum Einstein Gravity and Asymptotic Safety. *Annals Phys.*, 325:785–815, 2010. [19](#), [33](#)
- [144] Nicolai Christiansen, Daniel F. Litim, Jan M. Pawłowski, and Andreas Rodigast. Fixed points and infrared completion of quantum gravity. *Phys. Lett. B*, 728:114–117, 2014. [19](#), [33](#)
- [145] Nicolai Christiansen, Benjamin Knorr, Jan M. Pawłowski, and Andreas Rodigast. Global Flows in Quantum Gravity. *Phys. Rev. D*, 93(4):044036, 2016. [19](#), [33](#)
- [146] Kevin Falls. Renormalization of Newton’s constant. *Phys. Rev. D*, 92(12):124057, 2015. [20](#), [34](#)
- [147] Holger Gies, Benjamin Knorr, and Stefan Lippoldt. Generalized Parametrization Dependence in Quantum Gravity. *Phys. Rev. D*, 92(8):084020, 2015. [20](#), [23](#), [34](#), [41](#)
- [148] N. Ohta, R. Percacci, and A.D. Pereira. Gauges and functional measures in quantum gravity I: Einstein theory. *JHEP*, 06:115, 2016. [20](#), [34](#), [41](#)
- [149] N. Ohta, R. Percacci, and A.D. Pereira. Gauges and functional measures in quantum gravity II: Higher derivative gravity. *Eur. Phys. J. C*, 77(9):611, 2017. [20](#), [34](#), [41](#)
- [150] Gustavo P. De Brito, Nobuyoshi Ohta, Antonio D. Pereira, Anderson A. Tomaz, and Masatoshi Yamada. Asymptotic safety and field parametrization dependence in the $f(R)$ truncation. *Phys. Rev. D*, 98(2):026027, 2018. [20](#), [34](#), [41](#)
- [151] Daniel F. Litim and Jan M. Pawłowski. Flow equations for Yang-Mills theories in general axial gauges. *Phys. Lett. B*, 435:181–188, 1998. [22](#)
- [152] Alessandro Codello and Roberto Percacci. Fixed points of higher derivative gravity. *Phys. Rev. Lett.*, 97:221301, 2006. [22](#), [31](#)
- [153] Dario Benedetti, Pedro F. Machado, and Frank Saueressig. Asymptotic safety in higher-derivative gravity. *Mod. Phys. Lett. A*, 24:2233–2241, 2009. [22](#), [31](#), [54](#)
- [154] Nobuyoshi Ohta and Roberto Percacci. Higher Derivative Gravity and Asymptotic Safety in Diverse Dimensions. *Class. Quant. Grav.*, 31:015024, 2014. [22](#), [31](#)
- [155] Kevin Falls, Nobuyoshi Ohta, and Roberto Percacci. Towards the determination of the dimension of the critical surface in asymptotically safe gravity. 4 2020. [22](#), [31](#)

- [156] Jr. York, James W. Conformally invariant orthogonal decomposition of symmetric tensors on Riemannian manifolds and the initial value problem of general relativity. *J. Math. Phys.*, 14:456–464, 1973. [22](#)
- [157] Pedro F. Machado and Frank Saueressig. On the renormalization group flow of f(R)-gravity. *Phys. Rev. D*, 77:124045, 2008. [23](#), [31](#), [32](#), [54](#), [57](#), [79](#)
- [158] Djamel Dou and Roberto Percacci. The running gravitational couplings. *Class. Quant. Grav.*, 15:3449–3468, 1998. [23](#), [54](#)
- [159] Jan M. Pawłowski and Manuel Reichert. Quantum gravity: a fluctuating point of view. 7 2020. [25](#), [33](#)
- [160] Alessandro Codello, Roberto Percacci, and Christoph Rahmede. Investigating the Ultraviolet Properties of Gravity with a Wilsonian Renormalization Group Equation. *Annals Phys.*, 324:414–469, 2009. [26](#), [31](#), [41](#), [54](#), [57](#), [79](#)
- [161] Pietro Dona and Roberto Percacci. Functional renormalization with fermions and tetrads. *Phys. Rev. D*, 87(4):045002, 2013. [26](#), [35](#), [54](#), [58](#), [62](#)
- [162] Lando Bosma, Benjamin Knorr, and Frank Saueressig. Resolving Spacetime Singularities within Asymptotic Safety. *Phys. Rev. Lett.*, 123(10):101301, 2019. [30](#), [32](#)
- [163] Tom Draper, Benjamin Knorr, Chris Ripken, and Frank Saueressig. Finite Quantum Gravity Amplitudes – no strings attached. 7 2020. [30](#), [32](#)
- [164] Tom Draper, Benjamin Knorr, Chris Ripken, and Frank Saueressig. Graviton-Mediated Scattering Amplitudes from the Quantum Effective Action. 7 2020. [30](#), [32](#)
- [165] Benjamin Knorr, Chris Ripken, and Frank Saueressig. Form Factors in Asymptotic Safety: conceptual ideas and computational toolbox. *Class. Quant. Grav.*, 36(23):234001, 2019. [30](#), [32](#)
- [166] Wataru Souma. Nontrivial ultraviolet fixed point in quantum gravity. *Prog. Theor. Phys.*, 102:181–195, 1999. [31](#), [54](#)
- [167] M. Reuter and Frank Saueressig. Renormalization group flow of quantum gravity in the Einstein-Hilbert truncation. *Phys. Rev. D*, 65:065016, 2002. [31](#), [54](#)

- [168] O. Lauscher and M. Reuter. Is quantum Einstein gravity nonperturbatively renormalizable? *Class. Quant. Grav.*, 19:483–492, 2002. [31](#)
- [169] O. Lauscher and M. Reuter. Ultraviolet fixed point and generalized flow equation of quantum gravity. *Phys. Rev. D*, 65:025013, 2002. [31](#), [54](#)
- [170] Daniel F. Litim. Fixed points of quantum gravity. *Phys. Rev. Lett.*, 92:201301, 2004. [31](#)
- [171] Peter Fischer and Daniel F. Litim. Fixed points of quantum gravity in higher dimensions. *AIP Conf. Proc.*, 861(1):336–343, 2006. [31](#)
- [172] Peter Fischer and Daniel F. Litim. Fixed points of quantum gravity in extra dimensions. *Phys. Lett. B*, 638:497–502, 2006. [31](#)
- [173] Martin Reuter and Holger Weyer. Background Independence and Asymptotic Safety in Conformally Reduced Gravity. *Phys. Rev. D*, 79:105005, 2009. [31](#)
- [174] Martin Reuter and Holger Weyer. Conformal sector of Quantum Einstein Gravity in the local potential approximation: Non-Gaussian fixed point and a phase of unbroken diffeomorphism invariance. *Phys. Rev. D*, 80:025001, 2009. [31](#), [54](#), [55](#), [63](#)
- [175] Pedro F. Machado and R. Percacci. Conformally reduced quantum gravity revisited. *Phys. Rev. D*, 80:024020, 2009. [31](#)
- [176] Maximilian Demmel, Frank Saueressig, and Omar Zanusso. RG flows of Quantum Einstein Gravity on maximally symmetric spaces. *JHEP*, 06:026, 2014. [31](#), [32](#), [55](#), [57](#), [63](#), [75](#), [79](#)
- [177] M. Reuter and Frank Saueressig. A Class of nonlocal truncations in quantum Einstein gravity and its renormalization group behavior. *Phys. Rev. D*, 66:125001, 2002. [31](#)
- [178] Holger Gies, Benjamin Knorr, Stefan Lippoldt, and Frank Saueressig. Gravitational Two-Loop Counterterm Is Asymptotically Safe. *Phys. Rev. Lett.*, 116(21):211302, 2016. [31](#), [54](#)
- [179] Daniel F. Litim. Fixed Points of Quantum Gravity and the Renormalisation Group. *PoS*, QG-Ph:024, 2007. [31](#)
- [180] Daniel F. Litim. Renormalisation group and the Planck scale. *Phil. Trans. Roy. Soc. Lond. A*, 369:2759–2778, 2011. [31](#)

- [181] Martin Reuter and Frank Saueressig. Quantum Einstein Gravity. *New J. Phys.*, 14:055022, 2012. [31](#)
- [182] O. Lauscher and M. Reuter. Flow equation of quantum Einstein gravity in a higher derivative truncation. *Phys. Rev. D*, 66:025026, 2002. [31](#), [54](#)
- [183] Max R. Niedermaier. Gravitational Fixed Points from Perturbation Theory. *Phys. Rev. Lett.*, 103:101303, 2009. [31](#)
- [184] M. Niedermaier. Gravitational fixed points and asymptotic safety from perturbation theory. *Nucl. Phys. B*, 833:226–270, 2010. [31](#)
- [185] Juergen A. Dietz and Tim R. Morris. Asymptotic safety in the $f(R)$ approximation. *JHEP*, 01:108, 2013. [32](#), [57](#)
- [186] Kevin Falls, Daniel F. Litim, Kostas Nikolakopoulos, and Christoph Rahmede. On de Sitter solutions in asymptotically safe $f(R)$ theories. *Class. Quant. Grav.*, 35(13):135006, 2018. [32](#), [45](#), [57](#), [77](#)
- [187] Dario Benedetti. On the number of relevant operators in asymptotically safe gravity. *EPL*, 102(2):20007, 2013. [32](#)
- [188] Nobuyoshi Ohta, Roberto Percacci, and Gian Paolo Vacca. Flow equation for $f(R)$ gravity and some of its exact solutions. *Phys. Rev. D*, 92(6):061501, 2015. [32](#), [55](#), [59](#)
- [189] Nobuyoshi Ohta, Roberto Percacci, and Gian Paolo Vacca. Renormalization Group Equation and scaling solutions for $f(R)$ gravity in exponential parametrization. *Eur. Phys. J. C*, 76(2):46, 2016. [32](#), [55](#), [57](#), [63](#), [75](#), [126](#)
- [190] Alessandro Codello, Roberto Percacci, and Christoph Rahmede. Ultraviolet properties of $f(R)$ -gravity. *Int. J. Mod. Phys. A*, 23:143–150, 2008. [32](#)
- [191] K. Falls, D.F. Litim, K. Nikolakopoulos, and C. Rahmede. A bootstrap towards asymptotic safety. 1 2013. [32](#), [41](#)
- [192] Kevin Falls, Daniel F. Litim, Konstantinos Nikolakopoulos, and Christoph Rahmede. Further evidence for asymptotic safety of quantum gravity. *Phys. Rev. D*, 93(10):104022, 2016. [32](#), [34](#), [37](#), [41](#), [44](#), [45](#), [57](#), [75](#), [79](#), [86](#), [93](#), [113](#), [156](#)
- [193] Astrid Eichhorn. On unimodular quantum gravity. *Class. Quant. Grav.*, 30:115016, 2013. [32](#)

- [194] Astrid Eichhorn. The Renormalization Group flow of unimodular $f(R)$ gravity. *JHEP*, 04:096, 2015. [32](#), [57](#)
- [195] Kevin Falls, Callum R. King, Daniel F. Litim, Kostas Nikolakopoulos, and Christoph Rahmede. Asymptotic safety of quantum gravity beyond Ricci scalars. *Phys. Rev. D*, 97(8):086006, 2018. [32](#), [34](#), [37](#), [39](#), [41](#), [86](#), [93](#), [153](#)
- [196] Yannick Kluth and Daniel Litim. Fixed Points of Quantum Gravity and the Dimensionality of the UV Critical Surface. 8 2020. [32](#), [34](#), [37](#), [39](#), [41](#), [45](#), [51](#), [83](#), [87](#), [153](#)
- [197] Astrid Eichhorn, Holger Gies, and Michael M. Scherer. Asymptotically free scalar curvature-ghost coupling in Quantum Einstein Gravity. *Phys. Rev. D*, 80:104003, 2009. [32](#)
- [198] Kai Groh and Frank Saueressig. Ghost wave-function renormalization in Asymptotically Safe Quantum Gravity. *J. Phys. A*, 43:365403, 2010. [32](#)
- [199] Astrid Eichhorn and Holger Gies. Ghost anomalous dimension in asymptotically safe quantum gravity. *Phys. Rev. D*, 81:104010, 2010. [32](#)
- [200] Astrid Eichhorn. Faddeev-Popov ghosts in quantum gravity beyond perturbation theory. *Phys. Rev. D*, 87(12):124016, 2013. [32](#)
- [201] Alessandro Codello, Giulio D’Odorico, and Carlo Pagani. Consistent closure of renormalization group flow equations in quantum gravity. *Phys. Rev. D*, 89(8):081701, 2014. [32](#)
- [202] Elisa Manrique, Martin Reuter, and Frank Saueressig. Bimetric Renormalization Group Flows in Quantum Einstein Gravity. *Annals Phys.*, 326:463–485, 2011. [33](#)
- [203] Elisa Manrique, Martin Reuter, and Frank Saueressig. Matter Induced Bimetric Actions for Gravity. *Annals Phys.*, 326:440–462, 2011. [33](#)
- [204] Daniel Becker and Martin Reuter. En route to Background Independence: Broken split-symmetry, and how to restore it with bi-metric average actions. *Annals Phys.*, 350:225–301, 2014. [33](#)
- [205] Nicolai Christiansen, Benjamin Knorr, Jan Meibohm, Jan M. Pawłowski, and Manuel Reichert. Local Quantum Gravity. *Phys. Rev. D*, 92(12):121501, 2015. [33](#)

- [206] Nicolai Christiansen. Four-Derivative Quantum Gravity Beyond Perturbation Theory. 12 2016. [33](#)
- [207] Tobias Denz, Jan M. Pawłowski, and Manuel Reichert. Towards apparent convergence in asymptotically safe quantum gravity. *Eur. Phys. J. C*, 78(4):336, 2018. [33](#)
- [208] Astrid Eichhorn, Peter Labus, Jan M. Pawłowski, and Manuel Reichert. Effective universality in quantum gravity. *SciPost Phys.*, 5(4):031, 2018. [33](#), [35](#)
- [209] Jan Meibohm, Jan M. Pawłowski, and Manuel Reichert. Asymptotic safety of gravity-matter systems. *Phys. Rev. D*, 93(8):084035, 2016. [33](#), [35](#)
- [210] Nicolai Christiansen, Daniel F. Litim, Jan M. Pawłowski, and Manuel Reichert. Asymptotic safety of gravity with matter. *Phys. Rev. D*, 97(10):106012, 2018. [33](#), [35](#), [54](#), [112](#)
- [211] Astrid Eichhorn, Stefan Lippoldt, Jan M. Pawłowski, Manuel Reichert, and Marc Schiffer. How perturbative is quantum gravity? *Phys. Lett. B*, 792:310–314, 2019. [33](#)
- [212] Benjamin Bürger, Jan M. Pawłowski, Manuel Reichert, and Bernd-Jochen Schaefer. Curvature dependence of quantum gravity with scalars. 12 2019. [33](#), [35](#)
- [213] Nicolai Christiansen, Kevin Falls, Jan M. Pawłowski, and Manuel Reichert. Curvature dependence of quantum gravity. *Phys. Rev. D*, 97(4):046007, 2018. [33](#), [55](#)
- [214] Ivan Donkin and Jan M. Pawłowski. The phase diagram of quantum gravity from diffeomorphism-invariant RG-flows. 3 2012. [33](#)
- [215] Maximilian Demmel, Frank Saueressig, and Omar Zanusso. RG flows of Quantum Einstein Gravity in the linear-geometric approximation. *Annals Phys.*, 359:141–165, 2015. [33](#)
- [216] Elisa Manrique, Stefan Rechenberger, and Frank Saueressig. Asymptotically Safe Lorentzian Gravity. *Phys. Rev. Lett.*, 106:251302, 2011. [33](#)
- [217] Stefan Rechenberger and Frank Saueressig. A functional renormalization group equation for foliated spacetimes. *JHEP*, 03:010, 2013. [33](#)

- [218] S. Nagy, K. Sailer, and I. Steib. Renormalization of Lorentzian conformally reduced gravity. *Class. Quant. Grav.*, 36(15):155004, 2019. [33](#)
- [219] W.B. Houthoff, A. Kurov, and F. Saueressig. Impact of topology in foliated Quantum Einstein Gravity. *Eur. Phys. J. C*, 77:491, 2017. [33](#)
- [220] Adriano Contillo, Stefan Rechenberger, and Frank Saueressig. Renormalization group flow of Hořava-Lifshitz gravity at low energies. *JHEP*, 12:017, 2013. [33](#)
- [221] Jorn Biemans, Alessia Platania, and Frank Saueressig. Renormalization group fixed points of foliated gravity-matter systems. *JHEP*, 05:093, 2017. [33](#), [35](#), [54](#)
- [222] Benjamin Knorr. Lorentz symmetry is relevant. *Phys. Lett. B*, 792:142–148, 2019. [33](#)
- [223] Astrid Eichhorn, Alessia Platania, and Marc Schiffer. Lorentz invariance violations in the interplay of quantum gravity with matter. *Phys. Rev. D*, 102(2):026007, 2020. [33](#)
- [224] Kevin Falls. Background independent exact renormalisation. 4 2020. [34](#)
- [225] Roberto Percacci. Further evidence for a gravitational fixed point. *Phys. Rev. D*, 73:041501, 2006. [34](#), [54](#), [72](#), [112](#), [117](#)
- [226] Alessandro Codello. Large N Quantum Gravity. *New J. Phys.*, 14:015009, 2012. [34](#), [112](#)
- [227] Astrid Eichhorn and Holger Gies. Light fermions in quantum gravity. *New J. Phys.*, 13:125012, 2011. [34](#), [54](#), [98](#)
- [228] Astrid Eichhorn and Stefan Lippoldt. Quantum gravity and Standard-Model-like fermions. *Phys. Lett. B*, 767:142–146, 2017. [34](#), [98](#)
- [229] Jan Meibohm and Jan M. Pawłowski. Chiral fermions in asymptotically safe quantum gravity. *Eur. Phys. J. C*, 76(5):285, 2016. [34](#), [98](#)
- [230] Jesse Daas, Wouter Oosters, Frank Saueressig, and Jian Wang. Asymptotically Safe Gravity with Fermions. 5 2020. [35](#), [58](#), [98](#)
- [231] Roberto Percacci and Daniele Perini. Constraints on matter from asymptotic safety. *Phys. Rev. D*, 67:081503, 2003. [35](#)

- [232] Roberto Percacci and Daniele Perini. Asymptotic safety of gravity coupled to matter. *Phys. Rev. D*, 68:044018, 2003. [35](#)
- [233] Dario Benedetti, Pedro F. Machado, and Frank Saueressig. Taming perturbative divergences in asymptotically safe gravity. *Nucl. Phys. B*, 824:168–191, 2010. [35](#)
- [234] Gaurav Narain and Roberto Percacci. Renormalization Group Flow in Scalar-Tensor Theories. I. *Class. Quant. Grav.*, 27:075001, 2010. [35](#)
- [235] Gaurav Narain and Christoph Rahmede. Renormalization Group Flow in Scalar-Tensor Theories. II. *Class. Quant. Grav.*, 27:075002, 2010. [35](#)
- [236] Astrid Eichhorn. Quantum-gravity-induced matter self-interactions in the asymptotic-safety scenario. *Phys. Rev. D*, 86:105021, 2012. [35](#)
- [237] Peter Labus, Roberto Percacci, and Gian Paolo Vacca. Asymptotic safety in $O(N)$ scalar models coupled to gravity. *Phys. Lett. B*, 753:274–281, 2016. [35](#)
- [238] Roberto Percacci and Gian Paolo Vacca. Search of scaling solutions in scalar-tensor gravity. *Eur. Phys. J. C*, 75(5):188, 2015. [35](#)
- [239] Daniel Becker, Chris Ripken, and Frank Saueressig. On avoiding Ostrogradski instabilities within Asymptotic Safety. *JHEP*, 12:121, 2017. [35](#)
- [240] Astrid Eichhorn, Stefan Lippoldt, and Vedran Skrinjar. Nonminimal hints for asymptotic safety. *Phys. Rev. D*, 97(2):026002, 2018. [35](#)
- [241] Astrid Eichhorn, Stefan Lippoldt, and Marc Schiffer. Zooming in on fermions and quantum gravity. *Phys. Rev. D*, 99(8):086002, 2019. [35](#), [98](#)
- [242] Gustavo P. De Brito, Yuta Hamada, Antonio D. Pereira, and Masatoshi Yamada. On the impact of Majorana masses in gravity-matter systems. *JHEP*, 08:142, 2019. [35](#)
- [243] Jan Schröder. *Aspects of Quantum Gravity and Matter*. PhD thesis, Sussex U., 2015. [35](#), [44](#)
- [244] Pietro Donà, Astrid Eichhorn, and Roberto Percacci. Matter matters in asymptotically safe quantum gravity. *Phys. Rev. D*, 89(8):084035, 2014. [35](#), [41](#), [54](#)
- [245] Pietro Donà, Astrid Eichhorn, Peter Labus, and Roberto Percacci. Asymptotic safety in an interacting system of gravity and scalar matter. *Phys. Rev. D*, 93(4):044049, 2016. [Erratum: Phys.Rev.D 93, 129904 (2016)]. [35](#)

- [246] Natália Alkofer and Frank Saueressig. Asymptotically safe $f(R)$ -gravity coupled to matter I: the polynomial case. *Annals Phys.*, 396:173–201, 2018. [35](#), [41](#), [54](#), [55](#), [63](#), [65](#), [75](#)
- [247] Natália Alkofer. Asymptotically safe $f(R)$ -gravity coupled to matter II: Global solutions. *Phys. Lett. B*, 789:480–487, 2019. [35](#), [55](#), [59](#)
- [248] Mikhail Shaposhnikov and Christof Wetterich. Asymptotic safety of gravity and the Higgs boson mass. *Phys. Lett. B*, 683:196–200, 2010. [35](#), [36](#)
- [249] Astrid Eichhorn and Aaron Held. Top mass from asymptotic safety. *Phys. Lett. B*, 777:217–221, 2018. [35](#), [36](#)
- [250] Astrid Eichhorn and Aaron Held. Mass difference for charged quarks from asymptotically safe quantum gravity. *Phys. Rev. Lett.*, 121(15):151302, 2018. [35](#)
- [251] Astrid Eichhorn. Status of the asymptotic safety paradigm for quantum gravity and matter. *Found. Phys.*, 48(10):1407–1429, 2018. [36](#)
- [252] Astrid Eichhorn. An asymptotically safe guide to quantum gravity and matter. *Front. Astron. Space Sci.*, 5:47, 2019. [36](#)
- [253] Astrid Eichhorn and Aaron Held. Towards implications of asymptotically safe gravity for particle physics. In *An Alpine LHC Physics Summit 2019*, 7 2019. [36](#)
- [254] Kevin Falls, Daniel F. Litim, and Aarti Raghuraman. Black Holes and Asymptotically Safe Gravity. *Int. J. Mod. Phys. A*, 27:1250019, 2012. [36](#)
- [255] Kevin Falls and Daniel F. Litim. Black hole thermodynamics under the microscope. *Phys. Rev. D*, 89:084002, 2014. [36](#)
- [256] Benjamin Koch and Frank Saueressig. Structural aspects of asymptotically safe black holes. *Class. Quant. Grav.*, 31:015006, 2014. [36](#)
- [257] Alfio Bonanno, Adriano Contillo, and Roberto Percacci. Inflationary solutions in asymptotically safe $f(R)$ theories. *Class. Quant. Grav.*, 28:145026, 2011. [36](#)
- [258] Mark Hindmarsh, Daniel Litim, and Christoph Rahmede. Asymptotically Safe Cosmology. *JCAP*, 07:019, 2011. [36](#)
- [259] Giulia Gubitosi, Robin Ooijer, Chris Ripken, and Frank Saueressig. Consistent early and late time cosmology from the RG flow of gravity. *JCAP*, 12:004, 2018. [36](#)

- [260] Alfio Bonanno, Alessia Platania, and Frank Saueressig. Cosmological bounds on the field content of asymptotically safe gravity–matter models. *Phys. Lett. B*, 784:229–236, 2018. [36](#)
- [261] Alfio Bonanno and Frank Saueressig. Asymptotically safe cosmology – A status report. *Comptes Rendus Physique*, 18:254–264, 2017. [36](#)
- [262] Alessia Platania. From renormalization group flows to cosmology. *Front. in Phys.*, 8:188, 2020. [36](#)
- [263] Kevin G. Falls, Daniel F. Litim, and Jan Schröder. Aspects of asymptotic safety for quantum gravity. *Phys. Rev. D*, 99(12):126015, 2019. [37](#), [39](#), [41](#), [44](#), [57](#), [75](#), [86](#), [113](#), [154](#), [156](#), [157](#)
- [264] D.V. Vassilevich. Heat kernel expansion: User’s manual. *Phys. Rept.*, 388:279–360, 2003. [54](#), [60](#)
- [265] Ivan G. Avramidi. *Heat kernel and quantum gravity*. Lecture notes in physics. New series m, Monographs. Springer, Berlin, 2011. [54](#), [60](#)
- [266] Roberto Percacci and Ergin Sezgin. One Loop Beta Functions in Topologically Massive Gravity. *Class. Quant. Grav.*, 27:155009, 2010. [55](#), [62](#)
- [267] Dario Benedetti. Asymptotic safety goes on shell. *New J. Phys.*, 14:015005, 2012. [55](#), [63](#)
- [268] Raul Antonio Cuesta Ramos. *Quantum gravity and the renormalisation group: From the UV to the IR*. PhD thesis, Sussex U., 2016. [55](#)
- [269] Yannick Kluth and Daniel F. Litim. Heat kernel coefficients on the sphere in any dimension. *Eur. Phys. J. C*, 80(3):269, 2020. [60](#)

Appendix A

Flow equation of $f(X) + R z(X)$

The flow equation of $f(X) + Rz(X)$ theories with minimally coupled matter and in terms of the dimensionless functions $f(X) = k^{-d}\bar{F}(X)/(16\pi)$, $z(X) = k^{-d+2}\bar{Z}(X)/(16\pi)$ has the general form:

$$\partial_t f + R \partial_t z + 4f + 2z - 4X(f' + Rz') = I_Q + I_M \quad (\text{A.1})$$

The prime notation indicates the derivative with respect to the argument, I_Q contains the contributions due to metric field quantum fluctuations and I_M , that from matter fields. Expressions for the matter terms are given explicitly in (4.28)-(4.30) and (4.33)-(4.35). The quantum gravitational corrections have been computed in refs. [195, 196] and are written down explicitly next. The reader is directed to these references for details on the computation. The quantum gravity part can be written in the general form:

$$I_Q = \frac{1}{24\pi} (I_0 + \partial_t z I_1 + \partial_t f' I_2 + \partial_t z' I_3 + \partial_t f'' I_4 + \partial_t z'' I_5) \quad (\text{A.2})$$

Each of these terms can be further decomposed as follows:

$$I_0 = \frac{P_c^V}{D_c^V} + \frac{P_c^S}{D_c^S} + \frac{P_0^{Tz0} z + P_0^{Tf1} f' + P_0^{Tz1} z' + P_0^{T2} (f'' + Rz'')}{D^T} + \frac{P_0^{Sz0} z + P_0^{Sf1} f' + P_0^{Sz1} z' + P_0^{Sf2} f'' + P_0^{Sz2} z'' + P_0^{S3} (f^{(3)} + Rz^{(3)})}{D^S} \quad (\text{A.3})$$

$$I_1 = \frac{P_1^T}{D^T} + \frac{P_1^S}{D^S} \quad (\text{A.4})$$

$$I_2 = \frac{P_2^T}{D^T} + \frac{P_2^S}{D^S} \quad (\text{A.5})$$

$$I_3 = \frac{P_3^T}{D^T} + \frac{P_3^S}{D^S} \quad (\text{A.6})$$

$$I_4 = \frac{P_4^S}{D^S} \quad (\text{A.7})$$

$$I_5 = \frac{P_5^S}{D^S} \quad (\text{A.8})$$

The superscripts indicate whether each term arises from fluctuations of the the tensor (T), vector (V) or scalar (S) mode of the metric in the York decomposition. They also include the vector and scalar parts of auxiliary fields arising from the Jacobian of this decomposition. Using the treatment from ref. [263], the parts that are independent of the action are:

$$P_c^S = -12 - 12R + \frac{271}{90}R^2 \quad (\text{A.9})$$

$$P_c^V = -36 - 24R + \frac{191}{30}R^2 \quad (\text{A.10})$$

$$D_c^S = 1 \quad (\text{A.11})$$

$$D_c^V = 1 \quad (\text{A.12})$$

The other coefficients are:

$$D^T = -12(3f + (3 + 2R)z) \quad (\text{A.13})$$

$$+ (36(b + 4c) - 6(12a + b - 8c)R + (24a + 7b + 10c)R^2)(f' + Rz')$$

$$D^S = 36(2f + 3z) + 6 \left[-12(3a + b + c)(-3 + R) + (12a + 3b + 2c)R^2 f' \right. \\ \left. + (18(18a + 5b + 4c) - 12(15a + 4b + 3c)R + (12a + 3b + 2c)R^2)Rz' \right] \quad (\text{A.14})$$

$$+ (12a + 3b + 2c)^2(-3 + R)^2 R^2 (f'' + Rz'')$$

$$P_0^{Tz0} = -2880 + 1080R + 4R^2 - \frac{311}{63}R^3 \quad (\text{A.15})$$

$$P_0^{Tf1} = (-12(b + 4c) + (12a + b - 8c)R) \left(-360 + 120R + \frac{1}{3}R^2 \right) \quad (\text{A.16})$$

$$P_0^{Tz1} = 3240(b + 4c)R - 120(12a + 7b + 14c)R^2 - 2(61b + 304c)R^3 \quad (\text{A.17})$$

$$- \frac{(12a + 3b + 2c)}{3}R^4 + \frac{(14928a + 2597b - 3296c)}{756}R^5 \quad (\text{A.18})$$

$$P_0^{T2} = (12a + 3b + 2c)R^2 \left[-180(b + 4c) + 20(12a + 5b + 8c)R \right. \\ \left. - \frac{(360a + 29b - 244c)}{3}R^2 - \frac{(12a + b - 8c)}{18}R^3 \right. \\ \left. + \frac{(7464a + 731b - 4540c)}{4536}R^4 \right] \quad (\text{A.19})$$

$$P_0^{Sz0} = 1728 + 648R + \frac{348}{5}R^2 + \frac{37}{21}R^3 \quad (\text{A.20})$$

$$P_0^{Sf1} = -4(3a + b + c)(-6 + R) \left(216 + 72R + \frac{29}{5}R^2 \right) \quad (\text{A.21})$$

$$\begin{aligned}
P_0^{S_{z1}} = R & \left[1944(18a + 5b + 4c) + 72(12a + 5b + 6c)R \right. \\
& - \frac{6}{5}(1638a + 425b + 304c)R^2 - \frac{29(12a + 3b + 2c)}{5}R^3 \\
& \left. + \frac{(20442a + 5555b + 4296c)}{1260}R^4 \right] \tag{A.22}
\end{aligned}$$

$$\begin{aligned}
P_0^{S_{f2}} = (12a + 3b + 2c)R^2 & \left[108(6a, +b) - 48(3a + b + c)R + \frac{62(3a + b + c)}{5}R^2 \right. \\
& \left. + \frac{29(18a + 5b + 4c)}{15}R^3 + \frac{(24882a + 6665b + 5036c)}{7560}R^4 \right] \tag{A.23}
\end{aligned}$$

$$\begin{aligned}
P_0^{S_{z2}} = (12a + 3b + 2c)R^3 & \left[-54(24a + 7b + 6c) - 48(3a + b + c)R \right. \\
& + \frac{(3648a + 943b + 670c)}{10}R^2 + \frac{58(27a + 7b + 5c)}{15}R^3 \\
& \left. + \frac{(108408a + 27991b + 19846c)}{15120}R^4 \right] \tag{A.24}
\end{aligned}$$

$$P_0^{S^3} = (12a + 3b + 2c)^3 R^4 \left(-9 + \frac{91}{60}R^2 + \frac{29}{90}R^3 + \frac{181}{10080}R^4 \right) \tag{A.25}$$

$$P_1^T = -360 + 180R + R^2 - \frac{311}{126}R^3 \tag{A.26}$$

$$P_1^S = 216 + 108R + \frac{87}{5}R^2 + \frac{36}{42}R^3 \tag{A.27}$$

$$P_2^T = -\frac{3}{(12a + 3b + 2c)R^2} P_0^{T^2} \tag{A.28}$$

$$P_3^{T^3} = R P_2^T \tag{A.29}$$

$$P_2^S = (3a + b + c) \left(648 + 144R - \frac{186}{5}R^2 - \frac{58}{5}R^3 - \frac{127}{180}R^4 \right) \tag{A.30}$$

$$\begin{aligned}
P_3^S = R & \left[324(18a + 5b + 4c) + 144(3a + b + c)R - \frac{3(1278a + 335b + 244c)}{5}R^2 \right. \\
& \left. - \frac{58(15a + 4b + 3c)}{5}R^3 - \frac{(24882a + 6665b + 5036c)}{2520}R^4 \right] \tag{A.31}
\end{aligned}$$

$$P_4^S = -\frac{3}{(12a + 3b + 2c)R^2} P_0^{S^3} \tag{A.32}$$

$$P_5^S = R P_4^S \tag{A.33}$$

Appendix B

Flow equation of $f(R)$

The flow equation of $f(R)$ theories in four dimensions with minimally coupled matter and in terms of the dimensionless action $f(R) = k^{-4}\bar{f}(R)/(16\pi)$ has the general form:

$$\partial_t f(R) + 4f(R) - 2Rf'(R) = I_Q + I_M \quad (\text{B.1})$$

The prime notation indicates the derivative with respect to the argument, I_Q contains the contributions due to metric field quantum fluctuations and I_M , that from matter fields. Expressions for the matter terms are given explicitly in (4.28)-(4.30) and (4.33)-(4.35). The contributions due to the gravitational sector can be divided into three pieces (for details on the derivation, see refs. [192, 263]):

$$I_Q = \frac{1}{24\pi}(I_0 + \partial_t f' I_1 + \partial_t f'' I_2) \quad (\text{B.2})$$

where the argument of the functions has been suppressed and the factor of 24π is conventional, arising from the 16π introduced in the definition of the dimensionless action. The first piece can be further subdivided into four contributions:

$$I_0 = V_a + S_a + T_g + S_g \quad (\text{B.3})$$

The first two terms arise from the vector and scalar modes of the ghosts and auxiliary fields arising from the Jacobians of field decompositions. These contributions are:

$$V_a = \frac{P_C^V}{D_C^V} \quad (\text{B.4})$$

$$S_a = \frac{P_C^S}{D_C^S} \quad (\text{B.5})$$

and using the regularisation outlined in ref. [263]:

$$P_C^V = -36 - 24R + \frac{191}{30}R^2 \quad (\text{B.6})$$

$$P_C^S = -12 - 12R + \frac{271}{90}R^2 \quad (\text{B.7})$$

$$D_C^V = D_C^S = 1 \quad (\text{B.8})$$

The last two terms in I_0 represent the contributions due to the tensor and scalar modes of the graviton. These can be written schematically as:

$$T_g = \frac{P_0^{T1} f' + P_0^{T2} R f''}{D^T} \quad (\text{B.9})$$

$$S_g = \frac{P_0^{S1} f' + P_0^{S2} f'' + P_0^{S3} R f'''}{D^S} \quad (\text{B.10})$$

The other terms appearing in I_Q are similarly written as:

$$I_1 = \frac{P_1^T}{D^T} + \frac{P_1^S}{D^S} \quad (\text{B.11})$$

$$I_2 = \frac{P_2^S}{D^S} \quad (\text{B.12})$$

The denominators appearing in these terms depend on the action and its derivatives:

$$D^T = 3f - (R - 3)f' \quad (\text{B.13})$$

$$D^S = 2f + (3 - 2R)f' + (3 - R)^2 f'' \quad (\text{B.14})$$

while the coefficients in the numerators are independent of the action and arise from Heat Kernel coefficients:

$$P_0^{T1} = 240 - 90R - \frac{1}{3}R^2 + \frac{311}{756}R^3 \quad (\text{B.15})$$

$$P_0^{T2} = -60 + 30R + \frac{1}{6}R^2 - \frac{311}{756}R^3 \quad (\text{B.16})$$

$$P_0^{S1} = 48 + 18R + \frac{29}{15}R^2 + \frac{37}{756}R^3 \quad (\text{B.17})$$

$$P_0^{S2} = 216 - 12R - \frac{121}{5}R^2 - \frac{29}{10}R^3 - \frac{37}{756}R^4 \quad (\text{B.18})$$

$$P_0^{S3} = -54 + \frac{91}{10}R^2 + \frac{29}{15}R^3 + \frac{181}{1680}R^4 \quad (\text{B.19})$$

$$P_1^T = 30 - 15R - \frac{1}{12}R^2 + \frac{311}{1512}R^3 \quad (\text{B.20})$$

$$P_1^S = 6 + 3R + \frac{29}{60}R^2 + \frac{37}{1512}R^3 \quad (\text{B.21})$$

$$P_2^S = 27 - \frac{91}{20}R^2 - \frac{29}{30}R^3 - \frac{181}{3360}R^4 \quad (\text{B.22})$$

Appendix C

Additional figures for Chapter 3

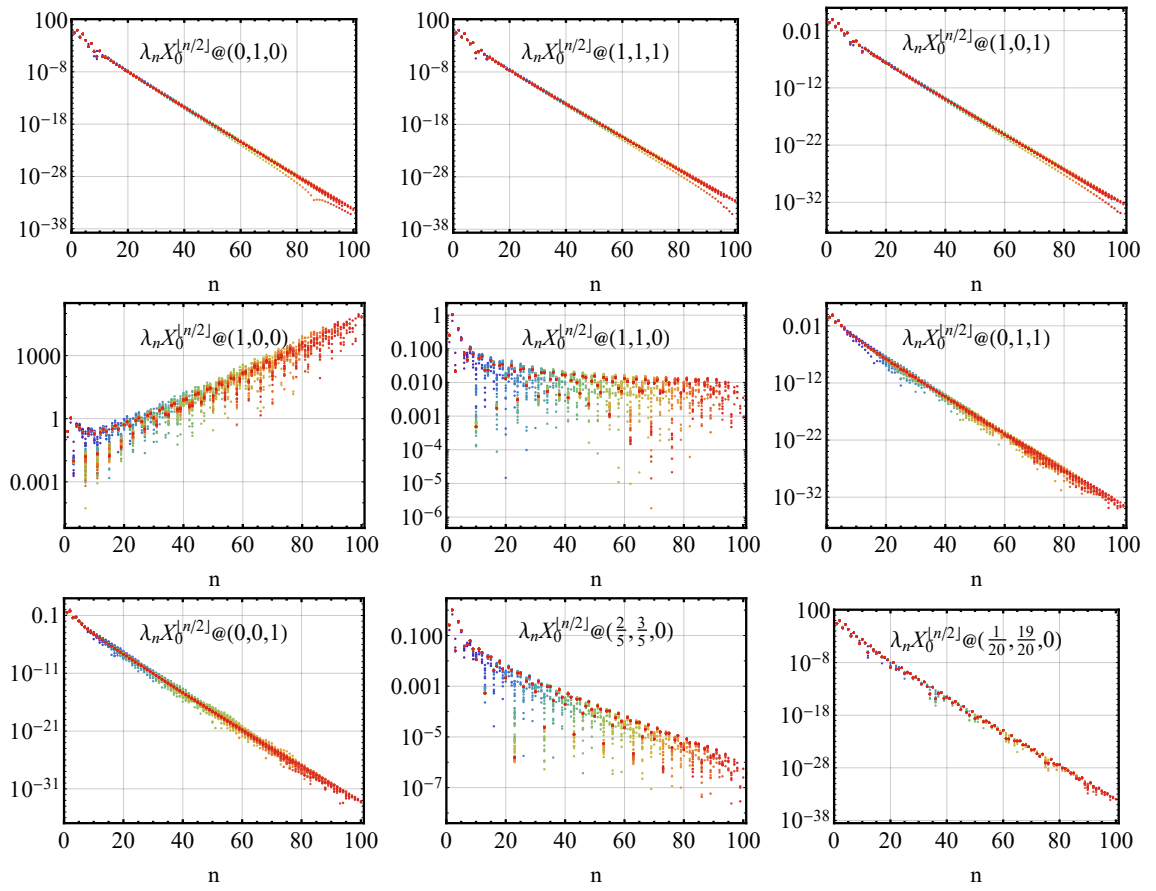


Figure C.1: Fixed points of pure gravity in various projections of the action.

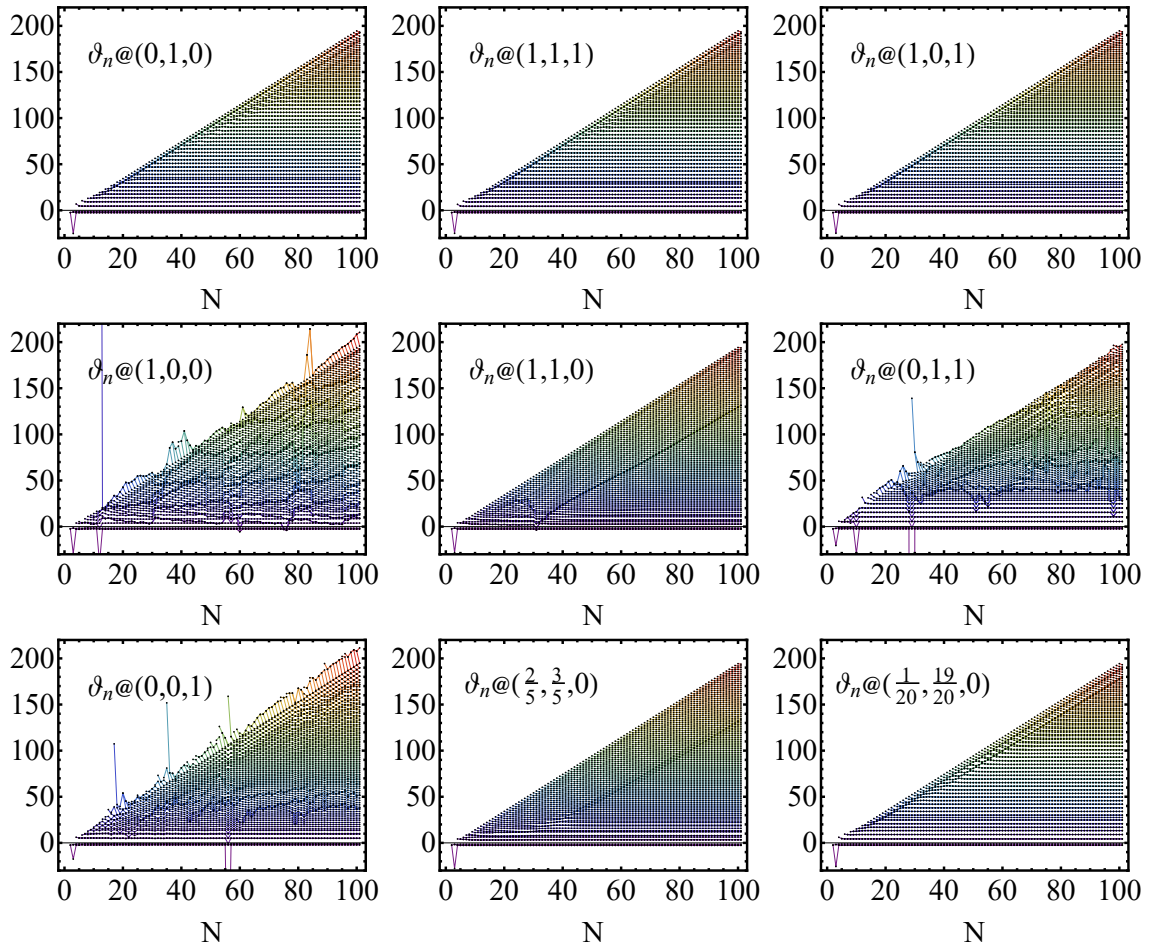


Figure C.2: Real part of scaling dimensions of gravitational fixed points in various projections of the action (view 1).

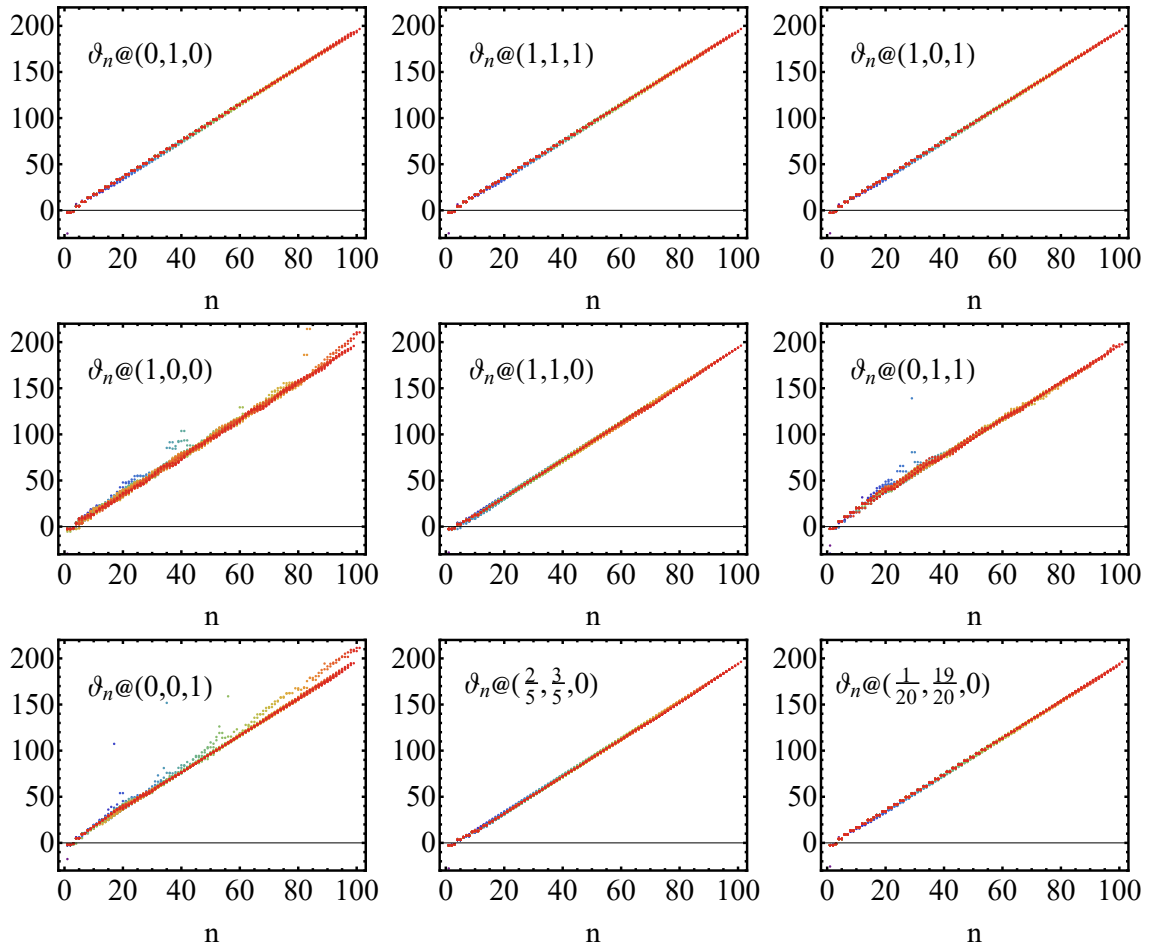


Figure C.3: Real part of scaling dimensions of gravitational fixed points in various projections of the action (view 2).

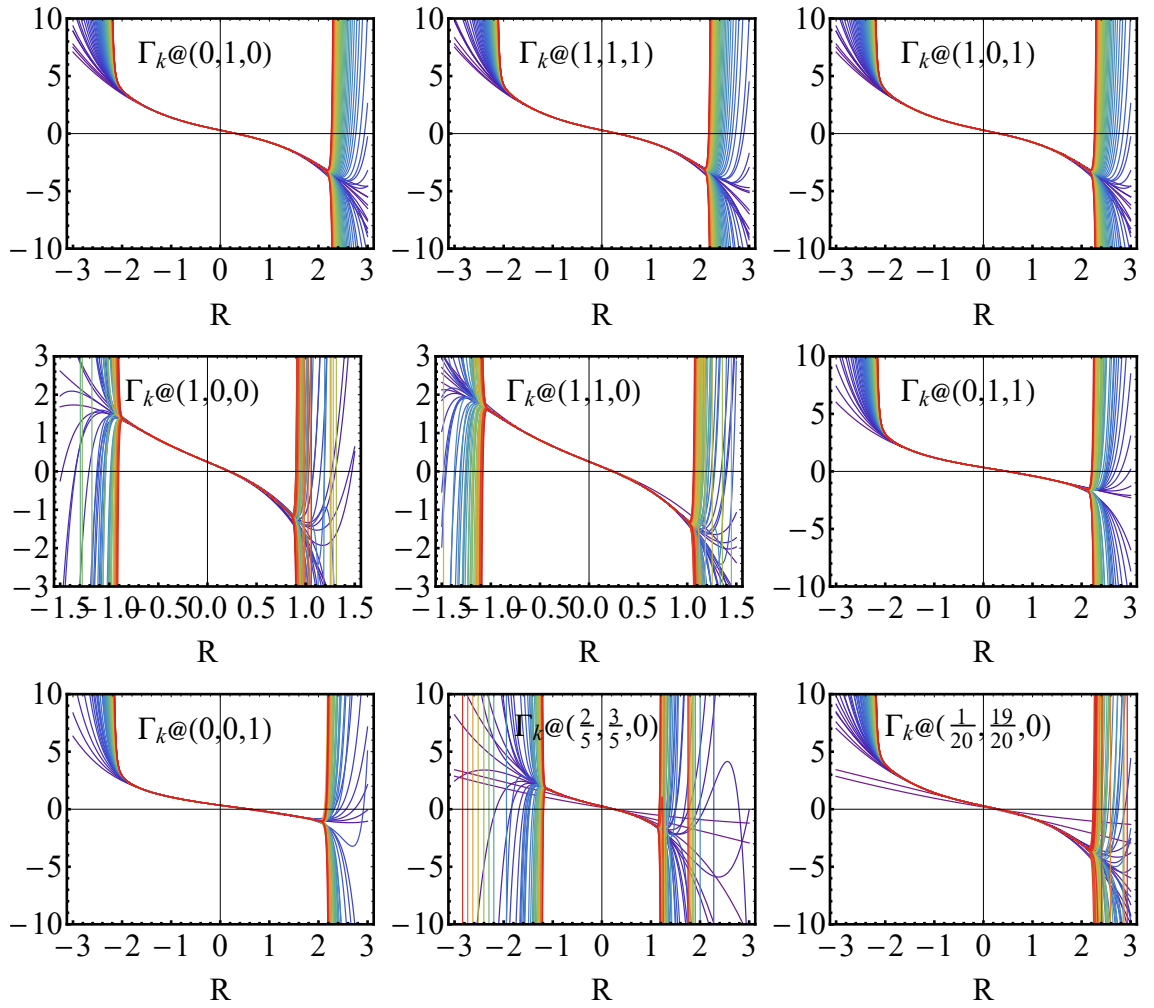


Figure C.4: Polynomial action as a function of R for various projections of the action in pure gravity.

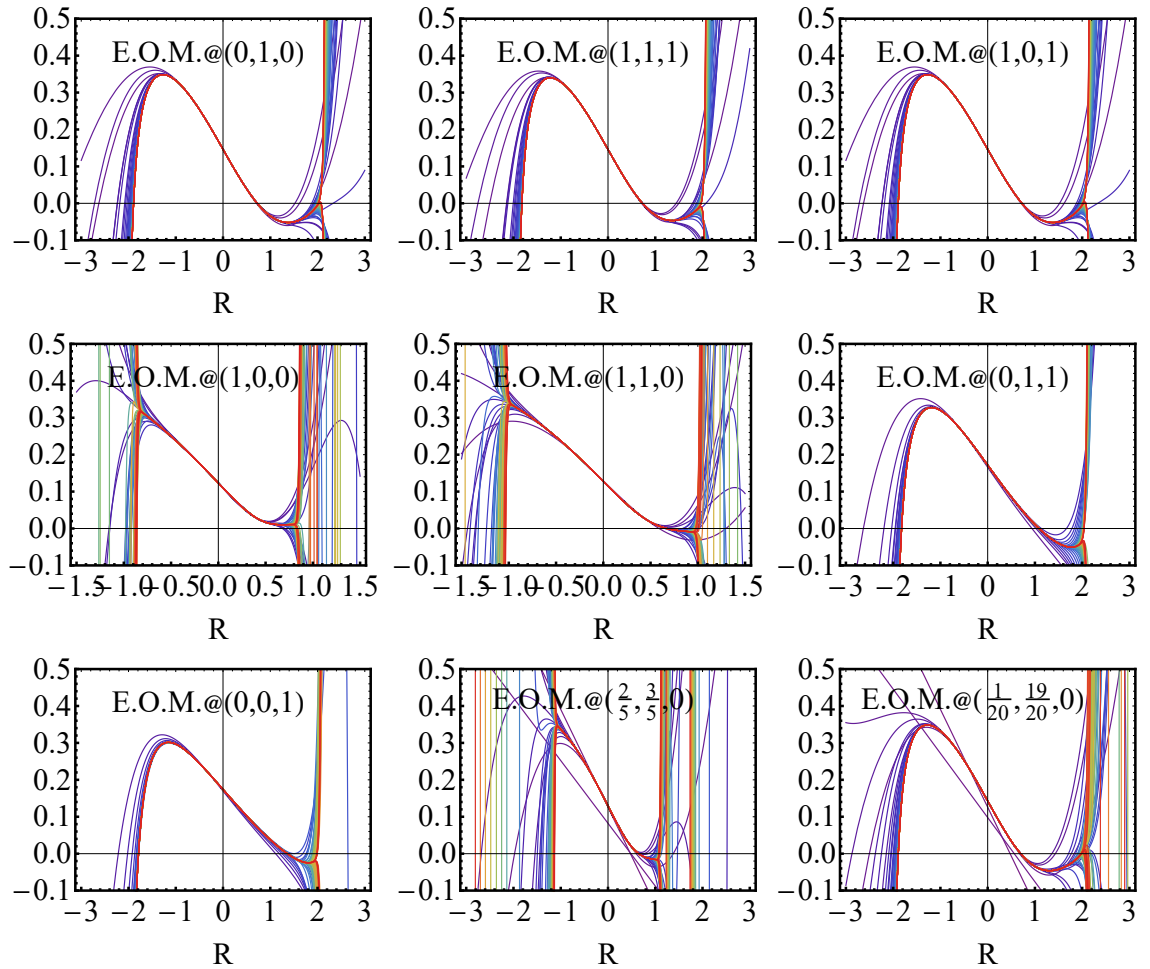


Figure C.5: Polynomial equation of motion as a function of R for various projections of the action in pure gravity.

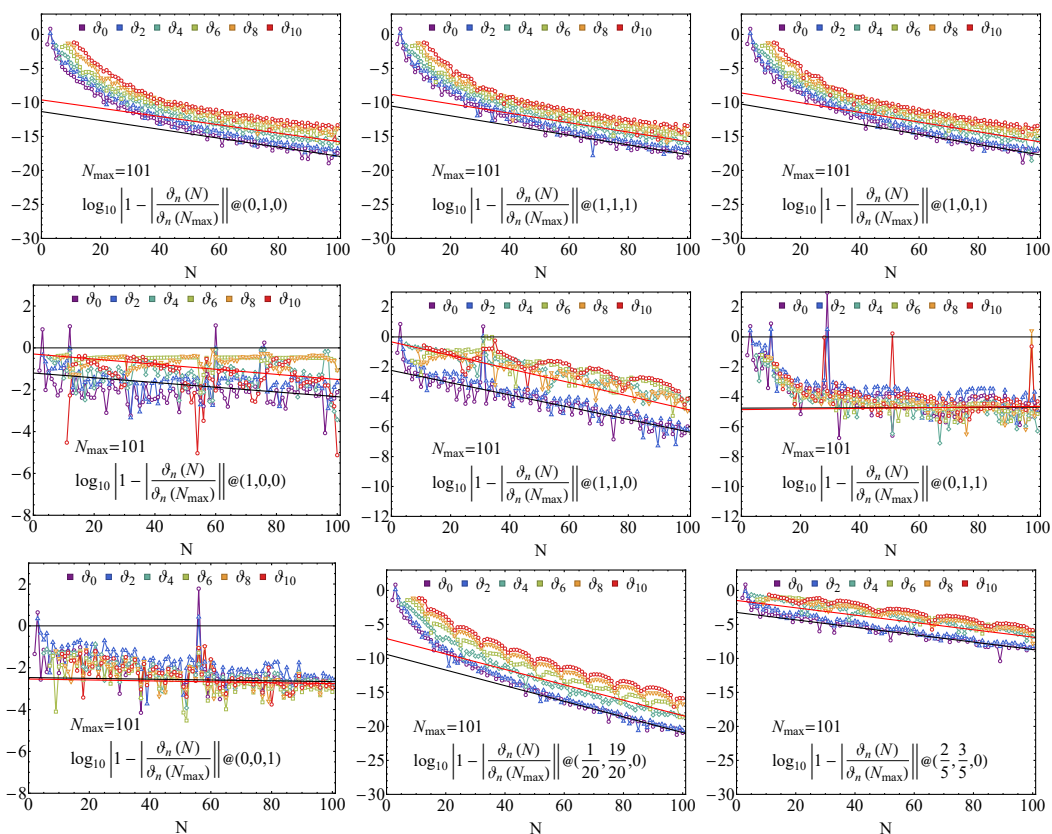


Figure C.6: Rate of convergence of scaling dimensions in various projections of the action in pure gravity with vanishing boundary conditions. The black line is the linear fit of ϑ_0 . The red line is the mean fit of the data shown for $N > 60$.

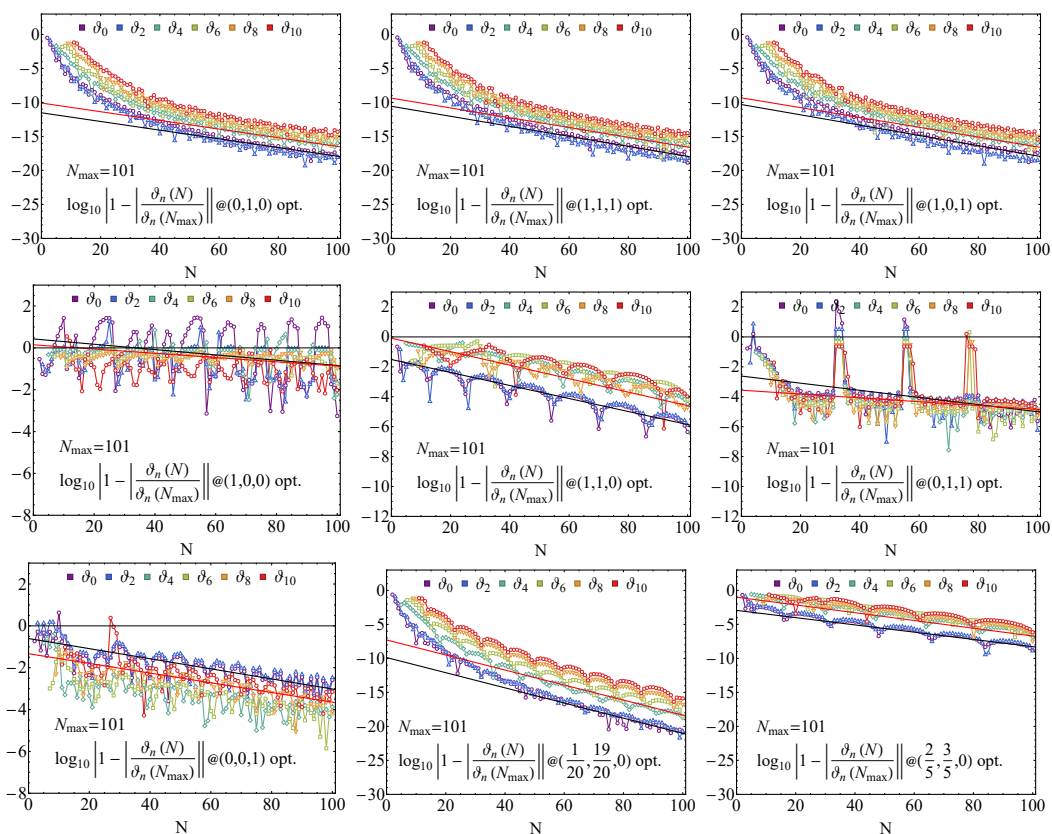


Figure C.7: Rate of convergence of scaling dimensions in various projections of the action in pure gravity with optimised boundary conditions. The black line is the linear fit of ϑ_0 . The red line is the mean fit of the data shown for $N > 60$.

Appendix D

Additional figures for Chapter 5

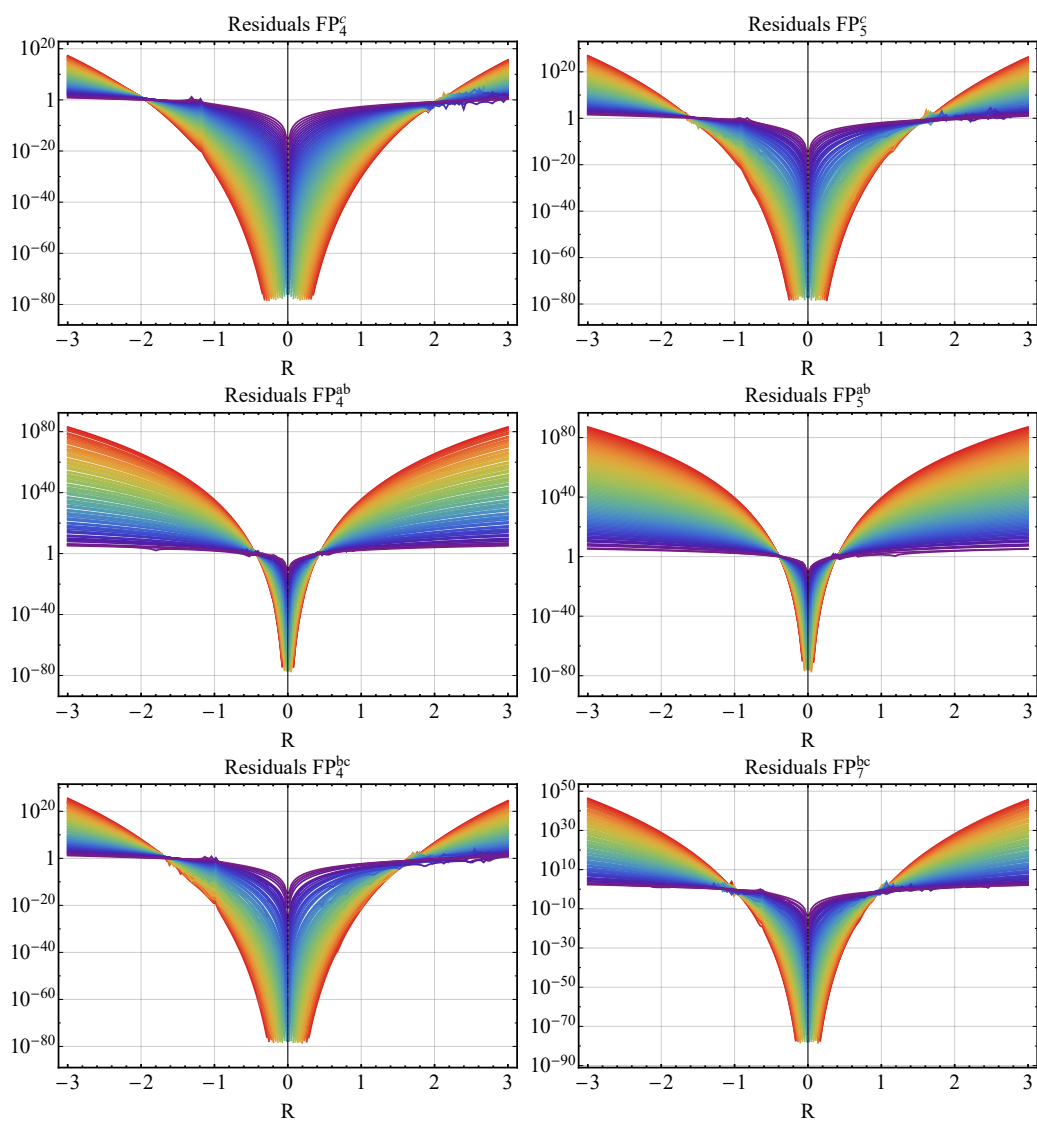


Figure D.1: Residuals of the polynomial solutions as a function of R with SM matter.

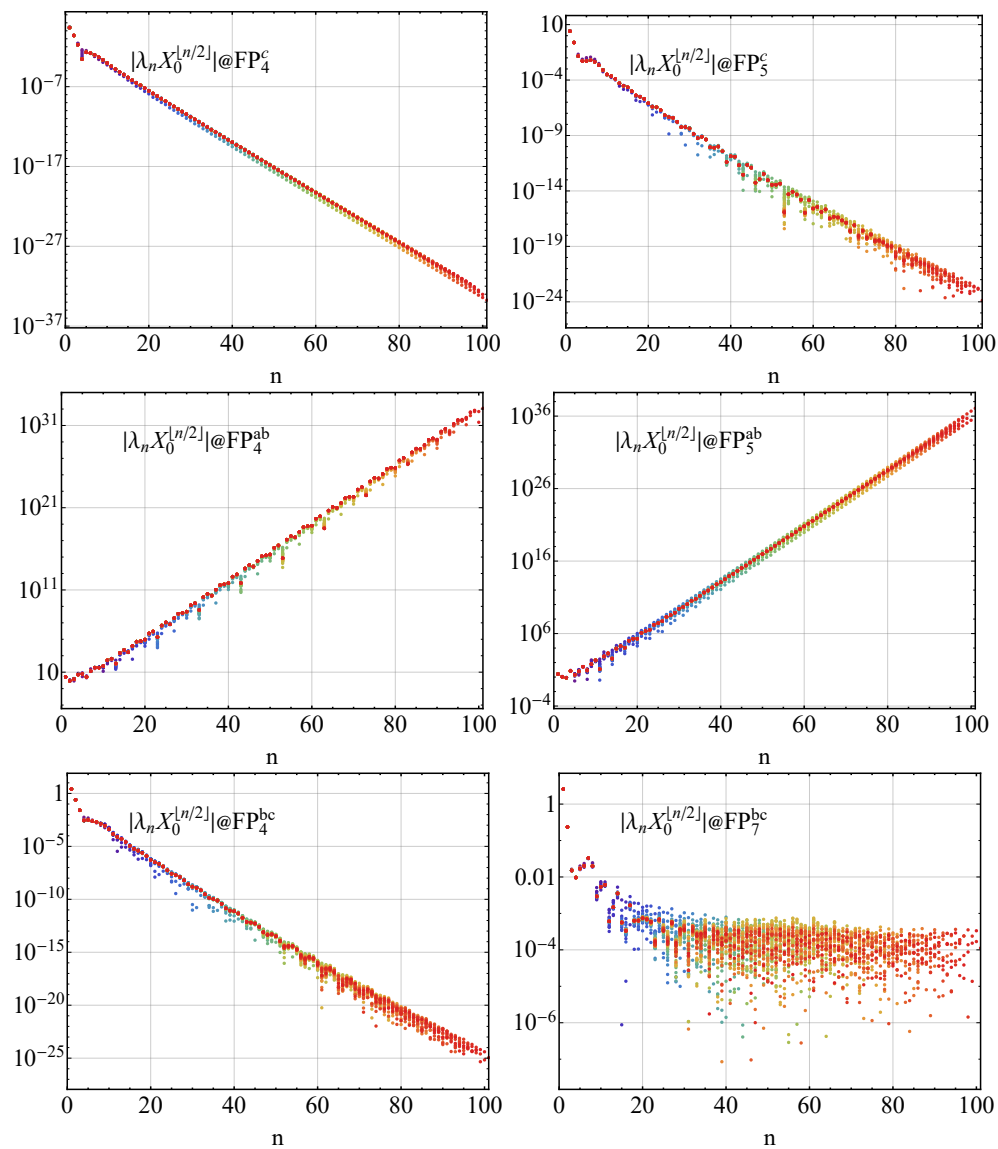


Figure D.2: Absolute value of effective couplings $|\lambda_n X_0^{[n/2]}|$ at the fixed point with SM matter.

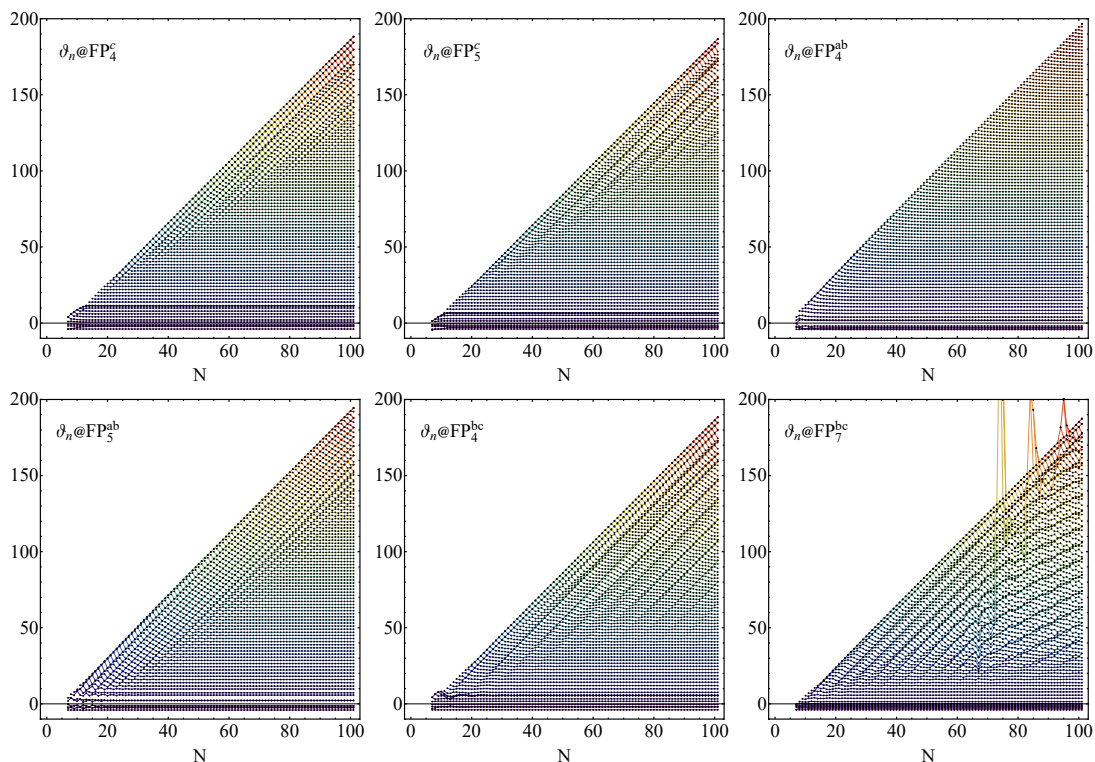


Figure D.3: Eigenvalues of the stability matrix for fixed points with SM matter. Negative values indicate relevant RG directions.

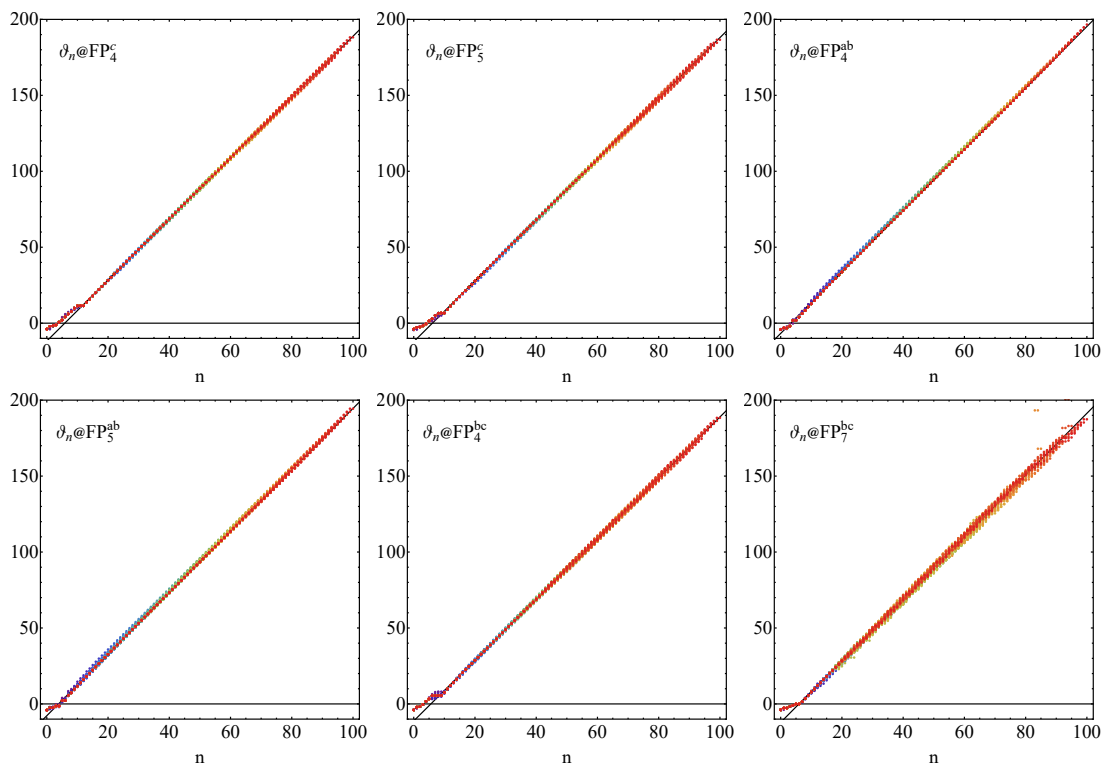


Figure D.4: Eigenvalues of the stability matrix superimposed at increasing N for fixed points with SM matter.

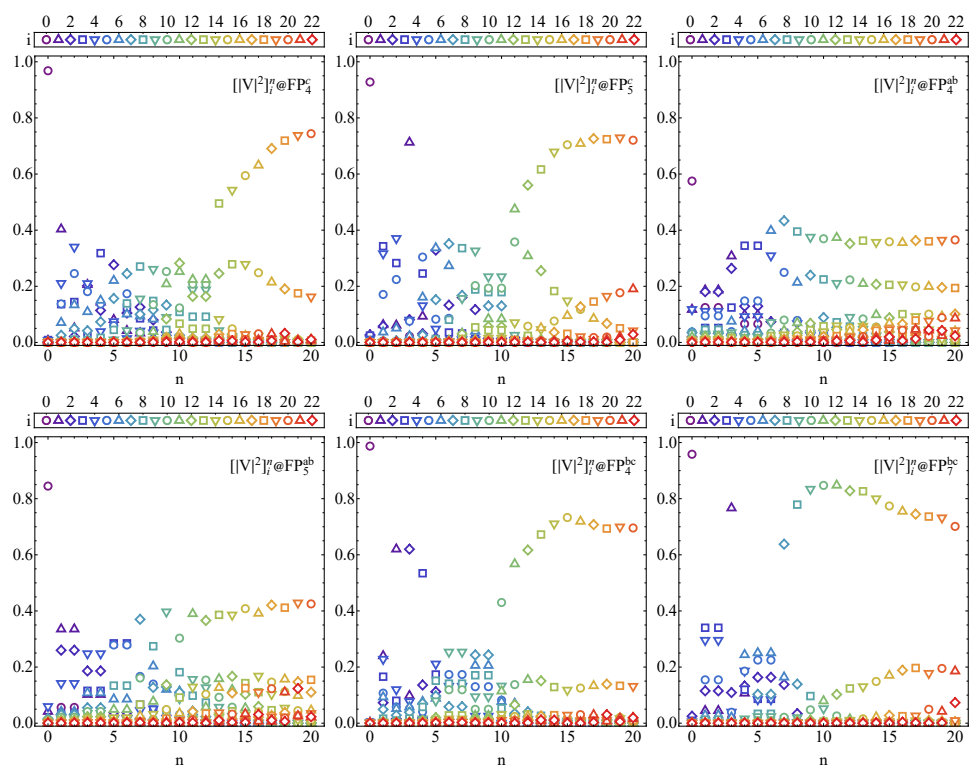


Figure D.5: Elements of the doubly-normalised eigenvectors of the stability matrix for fixed points with SM matter.

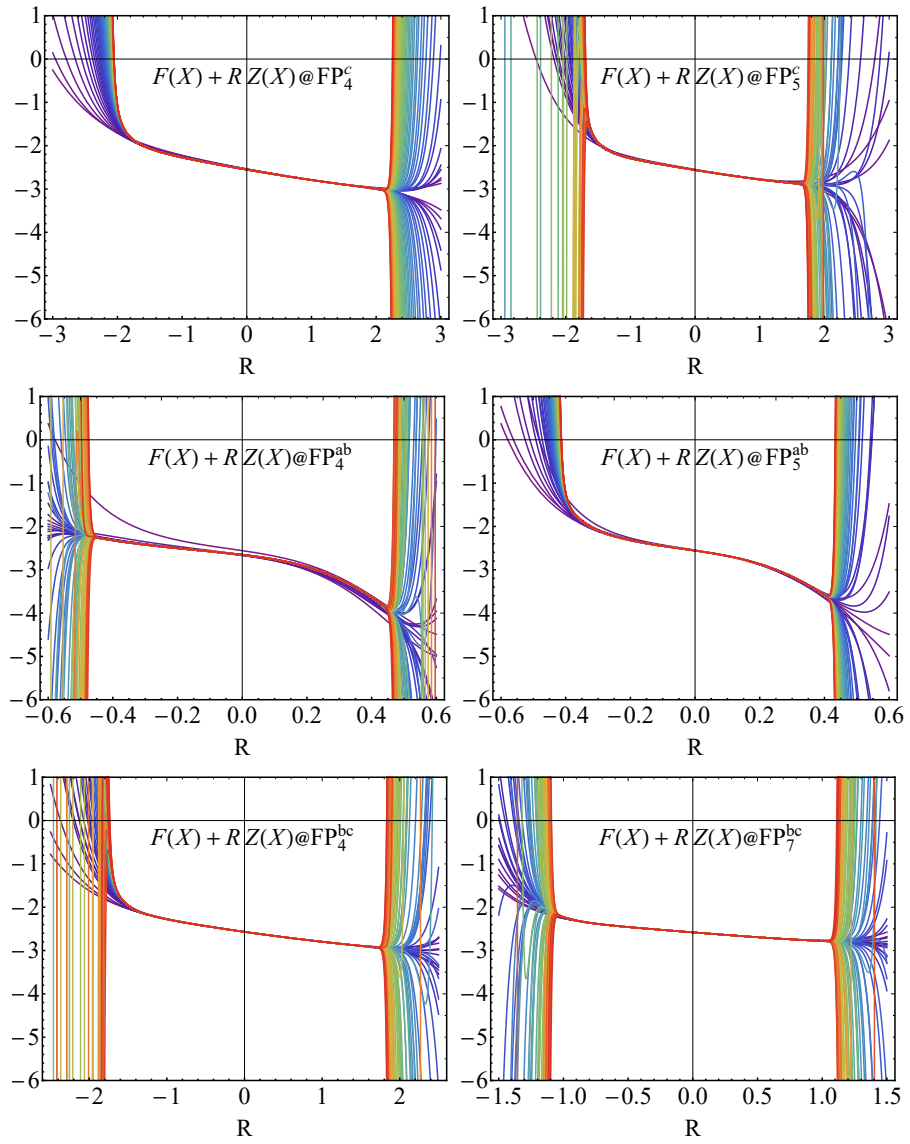


Figure D.6: Polynomial action for fixed points with SM matter.

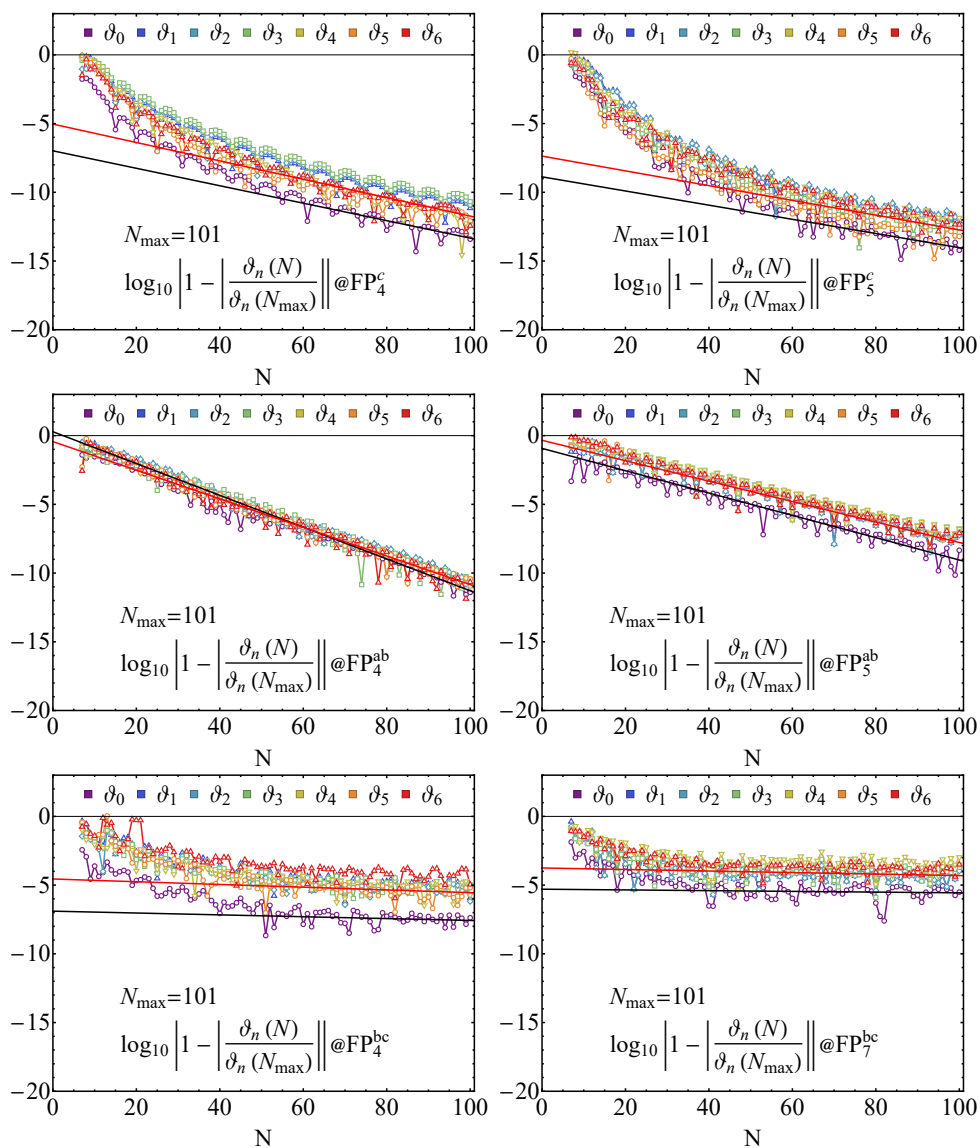


Figure D.7: Rate of convergence of scaling dimensions for fixed points with SM matter. The black line is the linear fit of ∂_0 . The red line is the mean fit of the data shown for $N > 50$.

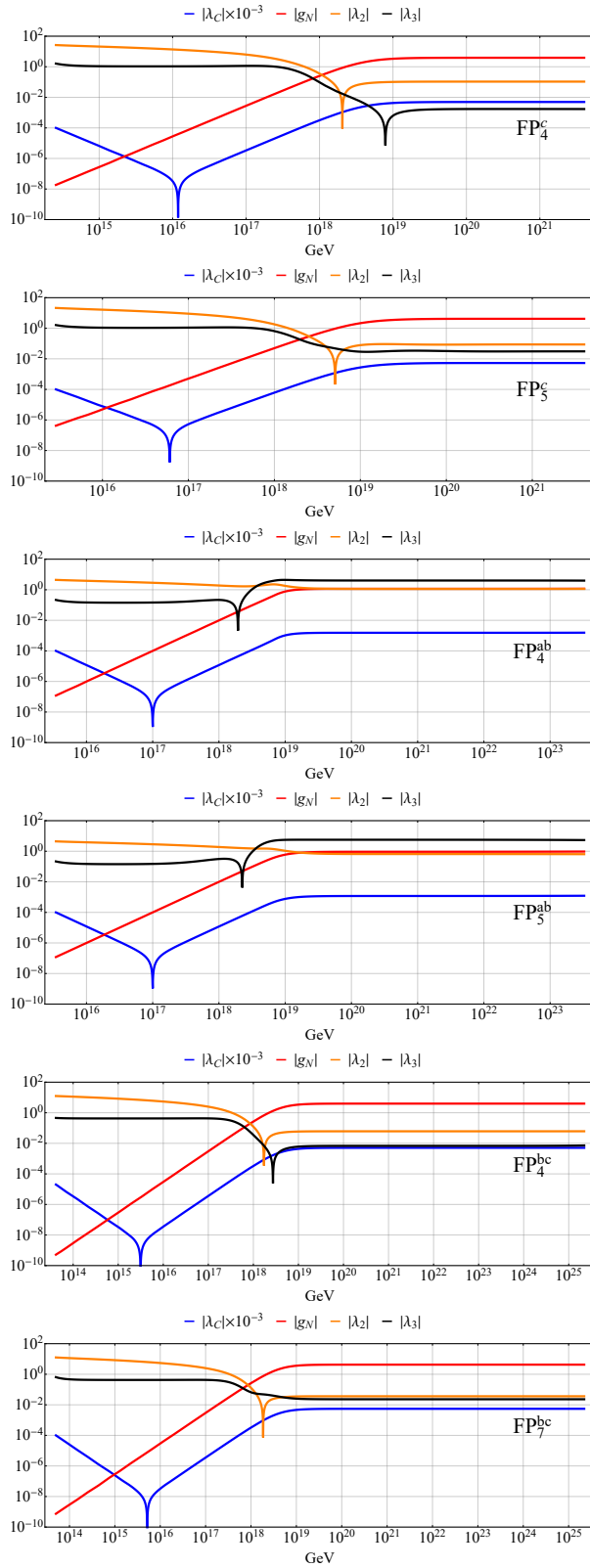


Figure D.8: RG flows connecting UV fixed points with SM matter to a Gaussian IR regime.

Appendix E

Tables for Chapter 6

Coupling values at the SM matter configuration and $N = 101$.					
λ_0	-2.6919	λ_{34}	6.8927×10^{12}	λ_{68}	1.4894×10^{27}
λ_1	-1.0956	λ_{35}	-6.9885×10^{12}	λ_{69}	-2.6376×10^{27}
λ_2	-1.4175	λ_{36}	4.3393×10^{13}	λ_{70}	2.2045×10^{28}
λ_3	-3.3816	λ_{37}	-6.4451×10^{13}	λ_{71}	-1.3967×10^{28}
λ_4	3.9746	λ_{38}	2.7265×10^{14}	λ_{72}	1.0544×10^{29}
λ_5	-6.5484	λ_{39}	-4.0845×10^{14}	λ_{73}	-2.2310×10^{29}
λ_6	23.747	λ_{40}	2.3777×10^{15}	λ_{74}	4.8005×10^{29}
λ_7	-29.160	λ_{41}	-2.5519×10^{15}	λ_{75}	-1.0335×10^{30}
λ_8	129.34	λ_{42}	1.6086×10^{16}	λ_{76}	9.4616×10^{30}
λ_9	-159.05	λ_{43}	-2.2433×10^{16}	λ_{77}	-4.0027×10^{30}
λ_{10}	737.45	λ_{44}	9.2385×10^{16}	λ_{78}	3.7584×10^{31}
λ_{11}	-905.52	λ_{45}	-1.5590×10^{17}	λ_{79}	-1.0111×10^{32}
λ_{12}	4.9217×10^3	λ_{46}	8.9439×10^{17}	λ_{80}	1.4799×10^{32}
λ_{13}	-5.5730×10^3	λ_{47}	-8.3610×10^{17}	λ_{81}	-3.2760×10^{32}
λ_{14}	2.6405×10^4	λ_{48}	5.8054×10^{18}	λ_{82}	4.2112×10^{33}
λ_{15}	-3.9614×10^4	λ_{49}	-8.9528×10^{18}	λ_{83}	-1.4421×10^{33}
λ_{16}	2.0346×10^5	λ_{50}	3.2321×10^{19}	λ_{84}	1.1849×10^{34}
λ_{17}	-1.9175×10^5	λ_{51}	-5.3330×10^{19}	λ_{85}	-4.3078×10^{34}
λ_{18}	1.3284×10^6	λ_{52}	3.4963×10^{20}	λ_{86}	5.1103×10^{34}
λ_{19}	-1.7423×10^6	λ_{53}	-3.1862×10^{20}	λ_{87}	-1.1420×10^{35}
λ_{20}	7.1215×10^6	λ_{54}	2.0443×10^{21}	λ_{88}	1.8093×10^{36}
λ_{21}	-1.0777×10^7	λ_{55}	-3.3330×10^{21}	λ_{89}	-3.5390×10^{35}
λ_{22}	6.1305×10^7	λ_{56}	1.2161×10^{22}	λ_{90}	4.1681×10^{36}
λ_{23}	-6.4386×10^7	λ_{57}	-2.0410×10^{22}	λ_{91}	-1.9785×10^{37}
λ_{24}	3.9302×10^8	λ_{58}	1.3096×10^{23}	λ_{92}	8.0244×10^{36}
λ_{25}	-5.0787×10^8	λ_{59}	-1.0868×10^{23}	λ_{93}	-3.2020×10^{37}
λ_{26}	2.4220×10^9	λ_{60}	8.0403×10^{23}	λ_{94}	8.7375×10^{38}
λ_{27}	-3.6116×10^9	λ_{61}	-1.3417×10^{24}	λ_{95}	-4.8706×10^{37}
λ_{28}	1.8536×10^{10}	λ_{62}	3.9062×10^{24}	λ_{96}	7.5277×10^{38}
λ_{29}	-2.0899×10^{10}	λ_{63}	-7.5335×10^{24}	λ_{97}	-9.4242×10^{39}
λ_{30}	1.3504×10^{11}	λ_{64}	5.5621×10^{25}	λ_{98}	1.5643×10^{39}
λ_{31}	-1.7606×10^{11}	λ_{65}	-3.7300×10^{25}	λ_{99}	-3.2952×10^{39}
λ_{32}	7.4951×10^{11}	λ_{66}	2.7605×10^{26}	λ_{100}	4.0116×10^{41}
λ_{33}	-1.2052×10^{12}	λ_{67}	-5.5844×10^{26}		

Table E.1: Couplings values of the non-Gaussian fixed point interpolated from pure gravity to the SM matter configuration at $N = 101$.

Real part of the scaling dimensions at the SM matter configuration and $N = 101$.

ϑ_0	4.6299	ϑ_{20}	-30.922	ϑ_{40}	-86.140	ϑ_{60}	-118.71	ϑ_{80}	-155.55
ϑ_1	4.6299	ϑ_{21}	-36.525	ϑ_{41}	-86.651	ϑ_{61}	-118.71	ϑ_{81}	-160.45
ϑ_2	3.8994	ϑ_{22}	-37.779	ϑ_{42}	-86.651	ϑ_{62}	-122.41	ϑ_{82}	-161.09
ϑ_3	2.0826	ϑ_{23}	-44.126	ϑ_{43}	-87.211	ϑ_{63}	-124.35	ϑ_{83}	-161.09
ϑ_4	2.0826	ϑ_{24}	-44.126	ϑ_{44}	-87.211	ϑ_{64}	-124.35	ϑ_{84}	-166.56
ϑ_5	-0.78005	ϑ_{25}	-50.401	ϑ_{45}	-91.123	ϑ_{65}	-127.75	ϑ_{85}	-167.54
ϑ_6	-0.78005	ϑ_{26}	-50.401	ϑ_{46}	-93.396	ϑ_{66}	-130.55	ϑ_{86}	-167.54
ϑ_7	-3.4032	ϑ_{27}	-56.439	ϑ_{47}	-93.863	ϑ_{67}	-130.55	ϑ_{87}	-172.08
ϑ_8	-3.4032	ϑ_{28}	-56.439	ϑ_{48}	-93.863	ϑ_{68}	-133.16	ϑ_{88}	-174.11
ϑ_9	-6.4214	ϑ_{29}	-63.161	ϑ_{49}	-98.491	ϑ_{69}	-137.04	ϑ_{89}	-174.11
ϑ_{10}	-6.4214	ϑ_{30}	-63.161	ϑ_{50}	-99.738	ϑ_{70}	-137.04	ϑ_{90}	-178.76
ϑ_{11}	-10.087	ϑ_{31}	-67.185	ϑ_{51}	-99.738	ϑ_{71}	-137.94	ϑ_{91}	-180.25
ϑ_{12}	-10.087	ϑ_{32}	-69.409	ϑ_{52}	-105.76	ϑ_{72}	-143.45	ϑ_{92}	-180.25
ϑ_{13}	-16.343	ϑ_{33}	-69.409	ϑ_{53}	-105.76	ϑ_{73}	-143.45	ϑ_{93}	-185.59
ϑ_{14}	-16.343	ϑ_{34}	-75.308	ϑ_{54}	-106.26	ϑ_{74}	-143.76	ϑ_{94}	-185.80
ϑ_{15}	-18.970	ϑ_{35}	-75.308	ϑ_{55}	-106.26	ϑ_{75}	-149.49	ϑ_{95}	-185.80
ϑ_{16}	-18.970	ϑ_{36}	-81.631	ϑ_{56}	-109.10	ϑ_{76}	-149.49	ϑ_{96}	-191.45
ϑ_{17}	-22.029	ϑ_{37}	-81.631	ϑ_{57}	-112.68	ϑ_{77}	-149.53	ϑ_{97}	-191.45
ϑ_{18}	-24.225	ϑ_{38}	-82.195	ϑ_{58}	-112.68	ϑ_{78}	-155.01	ϑ_{98}	-191.51
ϑ_{19}	-29.175	ϑ_{39}	-86.140	ϑ_{59}	-114.93	ϑ_{79}	-155.01	ϑ_{99}	-196.99
								ϑ_{100}	-196.99

Table E.2: Real part of the scaling dimensions of the non-Gaussian fixed point interpolated from pure gravity to the SM matter configuration at $N = 101$.

Imaginary part of the scaling dimensions at the SM matter configuration and $N = 101$.

ϑ_0	28.391	ϑ_{20}	0	ϑ_{40}	23.000	ϑ_{60}	-4.2334	ϑ_{80}	0
ϑ_1	-28.391	ϑ_{21}	0	ϑ_{41}	25.698	ϑ_{61}	4.2334	ϑ_{81}	0
ϑ_2	0	ϑ_{22}	0	ϑ_{42}	-25.698	ϑ_{62}	0	ϑ_{82}	-4.0156
ϑ_3	-0.72510	ϑ_{23}	1.5587	ϑ_{43}	-3.4045	ϑ_{63}	-4.0630	ϑ_{83}	4.0156
ϑ_4	0.72510	ϑ_{24}	-1.5587	ϑ_{44}	3.4045	ϑ_{64}	4.0630	ϑ_{84}	0
ϑ_5	6.2211	ϑ_{25}	-2.2389	ϑ_{45}	0	ϑ_{65}	0	ϑ_{85}	-3.7826
ϑ_6	-6.2211	ϑ_{26}	2.2389	ϑ_{46}	0	ϑ_{66}	3.6686	ϑ_{86}	3.7826
ϑ_7	4.5090	ϑ_{27}	-2.4632	ϑ_{47}	-3.9184	ϑ_{67}	-3.6686	ϑ_{87}	0
ϑ_8	-4.5090	ϑ_{28}	2.4632	ϑ_{48}	3.9184	ϑ_{68}	0	ϑ_{88}	-4.0273
ϑ_9	-9.1075	ϑ_{29}	-1.9980	ϑ_{49}	0	ϑ_{69}	3.5877	ϑ_{89}	4.0273
ϑ_{10}	9.1075	ϑ_{30}	1.9980	ϑ_{50}	2.7854	ϑ_{70}	-3.5877	ϑ_{90}	0
ϑ_{11}	2.7396	ϑ_{31}	0	ϑ_{51}	-2.7854	ϑ_{71}	0	ϑ_{91}	-4.5362
ϑ_{12}	-2.7396	ϑ_{32}	3.1326	ϑ_{52}	-10.609	ϑ_{72}	-3.8641	ϑ_{92}	4.5362
ϑ_{13}	-1.0346	ϑ_{33}	-3.1326	ϑ_{53}	10.609	ϑ_{73}	3.8641	ϑ_{93}	0
ϑ_{14}	1.0346	ϑ_{34}	-2.7126	ϑ_{54}	3.4668	ϑ_{74}	0	ϑ_{94}	-4.7098
ϑ_{15}	-59.822	ϑ_{35}	2.7126	ϑ_{55}	-3.4668	ϑ_{75}	4.4246	ϑ_{95}	4.7098
ϑ_{16}	59.822	ϑ_{36}	2.3902	ϑ_{56}	0	ϑ_{76}	-4.4246	ϑ_{96}	3.9309
ϑ_{17}	0	ϑ_{37}	-2.3902	ϑ_{57}	-3.7048	ϑ_{77}	0	ϑ_{97}	-3.9309
ϑ_{18}	0	ϑ_{38}	0	ϑ_{58}	3.7048	ϑ_{78}	4.4419	ϑ_{98}	0
ϑ_{19}	0	ϑ_{39}	-23.000	ϑ_{59}	0	ϑ_{79}	-4.4419	ϑ_{99}	7.0694
								ϑ_{100}	-7.0694

Table E.3: Imaginary part of the scaling dimensions of the non-Gaussian fixed point interpolated from pure gravity to the SM matter configuration at $N = 101$.